Doctoral Dissertation

Development of a Real-time Gamma-ray Energy Spectrum and Dose Rate Monitor for Radiation Therapy Facilities

VOULGARIS NIKOLAOS

October 2024

Graduate School of Engineering,
Osaka University

Acknowledgements

I would like to express my deepest gratitude to my supervisor Prof. Isao Murata for his constant support and guidance throughout my research. His introduction to various research topics and avenues greatly expanded my knowledge, helping me grow as a researcher and a person. It is an honor to work with him. I am also grateful to Prof. Shingo Tamaki for his invaluable assistance and warm support in both experimental and theoretical matters, as well as to Dr. Sachie Kusaka for her advice and encouragement during my years at the laboratory.

I want to thank Prof. Fuminobu Sato and Prof. Yoko Akiyama for being my secondary supervisors and providing me with valuable feedback on my work.

I am thankful to the Embassy of Japan in Greece and the Japanese Government for providing me with the MEXT scholarship, without which none of this would have been possible.

I would like to thank everyone at Murata Lab, both present and past students for their support and I wish them all the best in their endeavors.

To all my friends and family, thank you for your support and encouragement. I am grateful to my aunt, my brother and my mother for always cheering for me even if I am so many miles away. I want to express my appreciation to my late father, who always walks forwards with me. Finally, I want to thank my wife, for always being a pillar I can depend on, for discussing with me, helping and supporting me through everything. I would not have been able to do this without her.

Abstract

This thesis examines multiple aspects of the development of a portable gamma-ray monitor which can be used in radiotherapy facilities and is capable of measuring the energy spectrum and dose rate of gamma-rays in real time. In recent years, the growing use of radiation in medical applications has increased the complexity of medical radiation procedures and the risk of exposure for healthcare workers. While solutions such as training on radiation monitoring and shielding methods exist, the equipment used sometimes has shortcomings in terms of accuracy or portability. Therefore, having a device that is portable, easy to use, and is capable of providing accurate real-time information about radiation exposure and the radiation field to medical workers could significantly help in improving how they perceive their exposure and increase their awareness. This in turn can help in avoiding unnecessary exposure to radiation, which tends to be overlooked in environments where medical efficacy is the top priority, thus enhancing radiation protection. The monitor, which is also currently under development by EMF Japan Co. Ltd. for eventual commercial use, has proven to be accurate and versatile in a variety of gamma-ray fields, including background radiation conditions, standard sources, complex uncharacterised fields of gamma-rays, and gamma-rays of energies up to around 3 MeV. The device addresses the need for precise radiation exposure monitoring in medical environments, particularly where immediate data on radiation levels is crucial to ensure the safety of radiation workers. It combines the portability of a dosimeter with the spectral display capabilities of a spectrometer, displaying however not simply the pulse height spectrum but the unfolded (deconvoluted) energy spectrum of the incident gamma-rays. The prototype monitor consists mainly of a CsI (Tl) crystal, a Multi-Pixel Photon Counter (MPPC), an amplifier, and a DP5 digital pulse processor (DPP). Unfolding of the gamma-ray energy spectrum is realised continuously during measurement through an improved sequential Bayesian estimation method, named the $k{-}\alpha$ method and dose-rate estimation is made possible by applying a flux-to-dose conversion coefficient to the unfolded energy spectrum.

Historically, the device's accuracy in spectral reconstruction and dose estimation had been investigated for gamma-rays with energies up to 1.3 MeV. However this was realised with a resampling method, conducted post-measurement, in order to verify the moni-

tor's capabilities. Additionally, mainly one shape of the CsI(Tl) scintillator was utilised. Therefore, the objectives of this research aim to extend its capabilities, by investigating the performance of a few different crystal sizes, provide a comprehensive breakdown of the improved sequential Bayesian estimation, the $k{-}\alpha$ method, validating the monitor in true real-time measurements and verifying its performance for gamma-ray energies up to approximately 3 MeV. The goal for the future of this monitor includes application in various types of medical radiation environments, therefore initial steps are made to extend the dynamic measurement range to around 10 MeV, such as the extension of the response function to higher gamma-ray energies. Lastly, novel ideas are considered and discussed in order to enable use in neutron and gamma-ray mixed fields for prospective application in Boron Neutron Capture Therapy (BNCT).

Following comprehensive bibliographical investigation for previous established research regarding the above, in order to achieve these milestones, response functions were utilized for the required scintillator sizes and various gamma-ray standard source experiments were performed. Monte Carlo simulations with MCNP5 were utilized for detection efficiency calculations and the creation of response functions. The verification process up to 3 MeV for radiotherapy facility application, involved irradiating an Al foil with DT neutrons to induce the $^{27}\mathrm{Al}(n,\alpha)^{24}\mathrm{Na}$ reaction, with measurements taken using the prototype monitor alongside a Ge detector and an NaI survey meter. The results described in detail in this thesis overall illustrate a CsI(Tl) crystal size that can better balance portability and performance, establish the improvement of estimation that $k{-}\alpha$ method offers, and demonstrate the prototype's ability to accurately detect and display gamma-ray peaks in true real-time, with energy spectrum and dose-rate measurements showing good agreement with theoretical values up to 2.75 MeV. Therefore, since it has reached a level where it can be practically used, we are moving forward with its implementation and commercial development in collaboration with a company who develops detectors, EMF Japan Co., Ltd.

Contents

List of Figures

List of Tables

List of Abbreviations

MPPC ..... Multi-Pixel Photon Counter

CsI(Tl) ..... Cesium Iodide (Thallium-doped)

DPP ..... Digital Pulse Processor

IAEA ..... International Atomic Energy Agency

BNCT ..... Boron Neutron Capture Therapy

PET ..... Positron Emission Tomography

CT ..... Computed Tomography

EPDs ..... Electronic Personal Dosimeters

HPGe ..... High-Purity Germanium

MCA ..... Multi-Channel Analyzer

OSL ..... Optically Stimulated Luminescence

TSL ..... Thermally Stimulated Luminescence

RPL ..... Radiophotoluminescence

NaI(Tl) ..... Sodium Iodide (Thallium-doped)

SPECT ..... Single-Photon Emission Computed Tomography

GAGG(Ce) ... Gadolinium Aluminium Gallium Garnet (Cerium-doped)

MCNP ..... Monte Carlo N-Particle

AESJ ..... Atomic Energy Society of Japan

MPPC/SiPM . Multi-Pixel Photon Counter/Silicon Photomultiplier

ICRP ..... International Commission on Radiological Protection

LINAC ..... Linear Accelerator

Part I

Background and Objectives

1 | Introduction

1.1 Background

Radiation is widely used, in many fields, particularly in medical applications for both therapy and diagnosis [1]. As these technologies evolve and advance, so does the need for effective exposure monitoring devices that can keep up with the increasing complexity of radiation environments. Therapies include gamma knife and brachytherapy, as well as treatments utilizing different types of accelerators, such as electron accelerators which include medical linear accelerators (LINAC) for X-ray and electron beam therapy and particle accelerators. These therapies involves the use of charged particles such as protons and heavier ions such as carbon. Particle therapy centers in operation or under construction are based on cyclotrons and synchrotrons. For proton therapy, both cyclotrons and synchrotrons are in use, while synchrotrons are currently used for carbon ion therapy. Additionally, therapies using radionuclide teletherapy units with gamma-emitting sources such as ^{60}Co, as well as neutron irradiation based hybrid therapies like Boron Neutron Capture Therapy (BNCT), are employed for targeted radiotherapy [2]–[6]. Radiation has become an indispensable component of cancer treatment, with approximately 50% of all cancer patients requiring some form of radiotherapy during their care and overall it accounts for about 5% of the total cancer-related care budget globally. Worldwide, hundreds of accelerator based particle therapy centers and radionuclide treatment centers offer cancer therapy solutions not only in high income countries, but also in average to low income countries as well [7]. Diagnostics such as positron emission tomography (PET), computed tomography (CT), and radiopharmaceuticals comprise another major part of the medical applications of radiation [4].

To minimize exposure, apart from shielding, passive monitoring devices and proper staff training, precise and real-time monitoring is necessary to ensure safety for patients and staff alike [8]. During and after radiation treatment, not only is the patient exposed to the intended amount, but also sometimes unintended effects occur, such as through activation of materials. While there are guidelines in place to establish levels of doses that must not be exceeded, radiation workers are also exposed. However, guidelines are not uniform

for all medical radiation facilities and are continuously being scrutinized and amended. Especially for more complex treatments, such as BNCT, where high energy gamma-rays are present, there is a need for the medical staff to be aware of their exposure at all times. Specialized monitoring devices exist for improving the precision and effectiveness of treatment and also others for ensuring the safety of both patients and medical staff in complex radiation environments. While these workers are mainly shielded during operation, they are still exposed either by entering and leaving the irradiation room after treatment or due to leakages. Thus they are obligated by law and regulations to wear dosimeters at all times. These devices and other radiation monitors are examined in chapters 2 and 3. While advancements in radiation detection technologies have provided answers to many such monitoring needs, there is room for improvement. Traditionally used devices can exhibit shortcomings either in performance or in providing immediate and accurate feedback on radiation exposure, which is important in dynamic environments. Natural gamma-rays from the environment typically have energies up to around 3 MeV, which encompasses energy ranges relevant to radiopharmaceuticals and post-operation phases of medical accelerator facilities [9]. Most conventional gamma-ray spectrometry and dosimeters systems account with accuracy up to about 3 MeV, but they exclude a portion of higher energy gamma-rays. This limitation is relevant in environments of radiation medical facilities, such as neutron utilizing treatments of BNCT, or a medical LINAC room for example, where a broader range of gamma-ray energies may be present [10].

1.2 Motivation for this Study

Given the increasing prominence of radiation in medical applications, it is essential that radiation workers have access to the best possible monitoring devices. Broadly speaking, devices in use nowadays, typically either measure the cumulative dose exposure without offering real-time spectral data, are not capable of accurately measuring the dose rate of higher energy gamma rays up to 10 MeV, nor provide the true unfolded energy spectrum of gamma-rays, just the pulse height spectrum. There exists no device that is able to measure all of the above and remain lightweight as well. Those that show the dose rate and pulse height spectra, weigh usually over 1 kg, or suffer from precision issues over the range of 3 MeV. Other real time traditional dosimeters, have also shown issues such as

poor energy response over certain energies. These will be discussed later in more detail. At the same time, there are reports of physicians not always using dosimeters [11], [12] reinforcing the need for education and awareness. Active dosimeters, enhance feedback to the workers, improving their radiation protection according to the ALARA principle. Being able to see the measurements results in real-time, without the need to send them in for reading, is useful [13]. Therefore such active, real-time devices can help increase the workers awareness of their exposure. This is one main motivation for the development of the prototype monitor. It is designed to change the way medical radiation workers perceive their exposure by providing real-time, accurate feedback on the energy spectrum and dose rate, helping to enhance their safety awareness.

Another motivation of this study was the realisation of the potential of the sequential Bayesian estimation method, in real-time spectral unfolding and helping in creating a device thatcan help radiation workers understand better and faster their exposure risks. While drawing upon previous research and being designed mainly with medical radiation workers in mind, the result is a unique monitor that can be applied to virtually any field utilizing radiation, be it gamma-radiation and in the future hopefully a mixed field of neutrons and gamma-rays as well. The mixed neutron-gamma fields in complex radiation fields of advanced therapeutic environments, such as BNCT, require a monitoring solution that can accurately differentiate and measure both types of radiation simultaneously. It is therefore ideal to provide energy spectrum and dose rate solutions for a higher energy range, for a more accurate assessment of actual occupational radiation hazards in such settings.

Overall, the characteristics of the monitor described throughout this thesis combine the portability of a dosimeter and the detailed information provided by a spectrometer, with the added benefit of displaying the true gamma-ray energy spectrum, not just the pulse height distribution. Being able to apply such a versatile device in complex radiation field settings is beneficial for the future of radiation detection and protection. This thesis details the journey from the initial design and development of the prototype monitor to its application in complex environments. It includes calculations, simulations, and experiments that illustrate the monitor's capabilities and its potential to improve radiation safety in a variety of settings.

1.3 Overview of this Thesis

While the main object of this study is the development, investigation, verification and application of the prototype monitor, an effort was made to gather in one place information regarding radiation detection, medical radiation monitoring, radiotherapy facility guidelines as well as key concepts of Boron Neutron Capture Therapy (BNCT), a form of therapy whose guidelines are not yet strictly set and are still being improved upon. This thesis is split into two major parts:

Part 1: Background and Objectives and Part 2: Development and Application of the Prototype Monitor.

Part 1, focuses on providing the necessary theoretical background of radiation measurement, radiation detectors and guidelines, as well as set the background of various radiation therapy conditions. It also introduces the objectives for the study.

In Part 2, the study discusses the developmental steps of the prototype gamma-ray monitor, covering the investigations included in the referenced publications and additional studies. It investigates the applicability of the improved sequential Bayesian estimation method in various conditions and lays an important groundwork for its application radiation therapy environments, in terms of higher gamma-ray energy and neutron and gamma-ray discrimination considerations.

Part 1 consists of the following chapters:

- Chapter 1 - Introduction: This chapter introduces the context of the study, explaining the need for accurate radiation monitoring in medical applications.
- Chapter 2 - Physics of Radiation Measurement: This chapter describes the interactions of radiation with matter, the fundamentals of radiation detectors and monitors, and relevant applications. It delves into theoretical aspects that are crucial to the mechanisms of the prototype monitor such as radiation spectrum unfolding, scintillation detection theory, digital pulse processing and dose rate estimation.
- Chapter 3 - Radiation Therapy Facilities: This chapter outlines the guidelines, protocols, conditions and challenges associated with radiation monitoring during or after

treatment for various radiation therapies, closing with a focus on BNCT.

- Chapter 4- Objectives: This chapter defines the research goals, focusing on verifying the usability of the prototype monitor and investigating its application in actual radiation therapy settings.

Part 2 consists of the following chapters:

- Chapter 5 - Design and Development of Prototype Gamma-ray Monitor: This chapter details the design method of the prototype monitor, the methodologies used, and the major components, from the initial development to the present. The focus is mainly in regards to gamma-ray only fields, as it is one of the most common forms of ionizing radiation that needs to be monitored in radiotherapy facilities. Special emphasis is placed on the method for creating response functions and the principles of real-time operation. The newly proposed sequential Bayesian estimation method called the k—α method is also explained in detail. In the initial research, real-time measurement was achieved through resampling, but this thesis also describes the verification of true real-time measurement. After detailing the main materials used for the monitor, the measurement methods are explained. Since portability is crucial for the application of the prototype monitor, optimal design studies were also conducted. The relevant publications of evaluation of the sequential Bayesian estimation [14], CsI(Tl) scintillator size investigations [15] and true real time measurements [16] are explored in order.

- Chapter 6 - Application in Radiation Therapy Facilities: This chapter explores the application of the prototype monitor in settings with gamma-ray energies higher than the typical standard sources used until now in the laboratory environment. It mainly focuses on experimental investigations up to 2.75 MeV [17]. Then, the potential for use in mixed fields of neutrons and gamma rays, such as in BNCT, is explored. In this case, the maximum gamma-ray energy rises to around 10 MeV, so the response function of the monitor was extended to cover gamma rays up to 10 MeV, and the possibility of measuring in mixed radiation fields with neutrons and high-energy gamma rays is discussed.

- Chapter 7 - Discussion: This chapter discusses the methods used in this research,

the results of each section one by one and the challenges posed in the course of these investigations. It also outlines necessary future improvements.

- Chapter 8 - Conclusion: This chapter summarizes the findings of each part of this research, overall conclusions, its significance in radiation monitoring and highlights future directions.

2 | Physics of Radiation Measurement

2.1 Interactions of Radiation with Matter

The interaction of radiation with matter is a fundamental concept in radiation measurement. In the context of this thesis, the term radiation refers mainly to radiation originating from atomic or nuclear processes. Radiation can be categorized into charged type, including fast electrons and heavy charged particles, and uncharged, referring to electromagnetic radiation and neutrons. Electromagnetic radiation includes X-rays and gamma-rays, with the latter being the main focus of this thesis [18]. Understanding the interactions of radiation with matter, is a requirement for radiation detection research and detector development. The prototype monitor discussed in this study was developed for gamma-ray detection and neutron detection methods are also currently investigated. The following sections explore the interactions of gamma rays and neutrons, along with associated detection methods and challenges.

2.1.1 Gamma-ray Interactions

Electromagnetic radiation can be categorized based on its origin to gamma-rays, characteristic X-rays, annihilation radiation and bremsstrahlung. Gamma rays are electromagnetic waves emitted by an excited nucleus as it releases excess energy to stabilize. They are similar to X-rays but differ in origin since X-rays originate from electron interactions. Unlike other forms of decay, gamma emission does not change the nucleus into a different element. Regarding the interaction of gamma-rays with matter, when gamma-rays pass through materials, they interact through the processes of photoelectric effect (or photoelectric absorption), Compton scattering, and pair production [19]. All three of these processes involve either partial or complete transfer of the gamma-ray energy to electron energy. These processes are dominant in the cases of x-rays and bremsstrahlung as well [18]. In the photoelectric effect, a photon is completely absorbed by an absorber atom, and an energetic photoelectron is emitted by the atom. The energy of the ejected electron is given by the equation:

$$E_e = h\nu - E_b \tag{2.1}$$

where E_e is the kinetic energy of the ejected electron, h is Planck's constant, ν is the frequency of the incident photon, and E_b is the electron's binding energy. Such an interaction cannot take place with a free electron and always creates an ionized atom with a vacancy in one of the electron shells, with the K-shell being the most probable one to lose an electron [18]. Compton scattering occurs when a photon collides with an electron, producing a recoil electron and a scattered photon, with the incident energy split between them based on the scattering angle θ. The energy transferred to the recoil electron E_e (MeV) can be expressed as:

$$E_e = \frac{E^2(1-\cos\theta)}{0.511 + E(1-\cos\theta)} \tag{2.2}$$

$m_e c^2 = 0.511$ MeV is the rest mass energy of the electron.

Pair production happens when a photon is absorbed in the strong electric field around a nucleus, creating an electron-positron pair. When the positron's energy decreases to near the thermal energy level of ordinary electrons, it annihilates with an electron, producing two gamma rays in opposite directions, each with 0.511 MeV of energy. It is the primary mechanism of interaction for high energy photons, over around 2 MeV, with a threshold of 1.022 MeV.

The prevalence of these interactions—photoelectric effect, Compton scattering, and pair production—depends on the atomic number of the absorbing material and the gamma-ray energy, as illustrated in Figure 2.1. The left line shows the energy at which the probabilities of the photoelectric effect and Compton scattering are equal, relative to the atomic number Z of the material. The right line shows the energy at which the probabilities of Compton scattering and pair production are equal. Gamma-ray spectrum measurements rely on these interactions, with scintillation and semiconductor detectors being the primary tools used. These detectors generate signals when gamma rays interact with their sensitive components [18]. Following conversions through photodetectors and other components, a pulse height spectrum can be visualized, the value of the height of each pulse being proportional to the initial gamma-ray energy, which forms the basis of radiation detection, specifically in gamma-spectrometry.

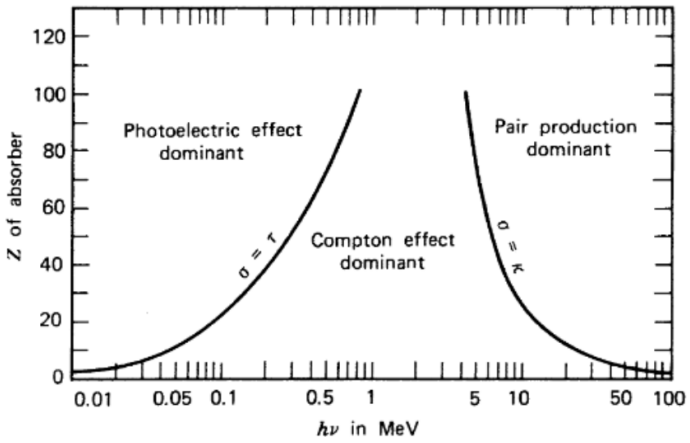

Figure 2.1: Diagram of regions where different gamma-ray interactions are dominant [18]

2.1.2 Neutron Interactions

Neutron interactions with matter are fundamentally different from those of gamma-rays, and neutron detection itself is challenging. Because neutrons lack charge, they do not interact directly with electrons in the material to which they are incident. Rather, interactions with atomic nuclei take place, and these interactions subsequently emit particles such as prompt gamma-rays. The process that occurs - elastic scattering, inelastic scattering, neutron-induced fission or neutron capture - depends on the incident neutron's energy and target nucleus. In the case of low-energy neutrons elastic scattering is a common interaction, where the neutron collides with a nucleus, transferring part of its kinetic energy to the nucleus whole total kinetic energy is conserved. This energy transfer can lead to the production of secondary charged particles, such as recoil protons. These events can be detected. Moderators such as water and paraffin take advantage of elastic scattering in order to slow down neutrons. In the case of inelastic scattering (mainly at higher than 0.5 MeV), the neutron transfers energy to the nucleus, causing the nucleus to become excited. This process plays an important role in fast neutron attenuation as well [20]. This excited nucleus subsequently emits gamma rays as it returns to its ground state. Neutron capture occurs when a neutron is absorbed by a nucleus, leading to the formation of a heavier isotope and the emission of energetic particles like gamma rays. Such reactions include (n, p), (n, 2n), (n, α) or (n, γ) reactions. The reaction alters the atomic number and/or atomic mass number of the nucleus.

While neutrons are classified according to energy, the classification is not always precise or consistent and changes slightly with application and field of research, but a recent classification by the IAEA[21] is as follows:

Neutron Classification	**Energy Range (eV)**
Cold Neutrons	$E < 0.005$ eV
Thermal Neutrons	$E < 0.5$ eV, $E \approx 0.025$ eV (at room temperature)
Hot Neutrons	0.1 eV $\leq E \leq$ 1 eV
Epithermal Neutrons	0.5 eV $\leq E \leq$ 10 keV
Fast Neutrons	$E > 10$ keV

Table 2.1: Classification of Neutrons According to Energy, courtesy of IAEA [21]

Additional sub-classifications such as cadmium (0.4 - 0.6 eV), epicadmium (0.6 - 1 eV), resonance (10 - 300 eV), intermediate (100 eV - 100 keV) and relativistic ($>$ 20 MeV) are also sometimes used [22], [23]. Depending on application or research team, fast neutrons can range starting from 1 keV and epithermal may encompass neutrons up to 0.1 keV, 1 keV or even 10 keV, the latter being the case for Boron Neutron Capture Therapy (BNCT) (0.5 eV to 10 keV) [21], [24].

Epithermal neutrons have energies between 0.025 eV and 1 keV. They are typically found in moderation processes where neutrons are slowing down but have not yet reached thermal energies. Epithermal neutrons are significant in applications like BNCT, as they can penetrate tissues deeper than thermal neutrons, providing therapeutic advantages in certain medical treatments [24]. Fast neutrons possess energies between 100 keV and 20 MeV. They are produced directly from fission or spallation reactions and are not significantly slowed down by interactions with matter. Fast neutrons are important in both reactor physics and radiation protection because their high energies make them more penetrating and capable of inducing additional nuclear reactions, including fission or neutron capture, depending on the target material. Fast neutrons primarily interact through elastic scattering, where energy is transferred from the neutron to the target nucleus. Fast neutrons slow down to thermal region following adequate scattering interactions until they are captured. In contrast, thermal neutrons often induce nuclear reactions, such as neutron capture and threshold reactions, with neutron activation being a notable outcome. Thermal neutrons, after being slowed down by a moderator, reach thermal equilibrium

with their surroundings, with their energy distribution following a Maxwell-Boltzmann energy distribution. These neutrons are utilized in reactor physics, representing an energy range where many nuclear reactions, such as fission or neutron capture, are most likely to occur. The energy dependency of the neutron capture cross-section and the time profile of neutron-induced radiations are crucial in various analytical applications.

In order to measure the dose from exposure to neutrons, depending on the energy range different devices are used like albedo dosimeters, track etch dosimeters, a bubble detectors or an electronic dosimeter [25]. Resonance foils have been widely used in neutron flux measurements, particularly for neutrons in the thermal and epithermal ranges. These foils absorb neutrons most efficiently at specific resonance energies, where the neutron absorption cross-section peaks. Neutrons with energies corresponding to the resonance energy of the foil are absorbed and the resulting activity (usually from decay) can be measured. By comparing the activity of foils with and without thermal absorbing material covers (like Cadmium (Cd)), the neutron flux in different energy regions can be determined. Cadmium ratio, refers to the activity of foil exposed to the neutron flux without cadmium to the activity with cadmium. It has been used to distinguish between thermal and epithermal neutron fluxes, as cadmium effectively absorbs thermal neutrons but not epithermal neutrons (see Table 2.1). This is because the cadmium cutoff energy is 0.5 eV, meaning only neutrons with kinetic energy below the cadmium cut-off energy are strongly absorbed by it. Depending on the thickness of the foil, interactions such as self-shielding (where neutrons are absorbed within the foil itself before interacting fully) and self-absorption of emitted particles can distort measurements and correction factors need to be applied to account for the foil's thickness [26].

Neutron activation occurs when a material absorbs a neutron, leading to the production of a radioactive isotope, as seen in reactions like (n,p). This process is significant for health physics because materials exposed to neutrons can become radioactive, posing a potential radiation hazard even after neutron exposure has ceased. Additionally, neutron activation allows for the measurement of neutron flux and enables quantitative analysis of unknown samples through spectroscopic examination of the resulting radiation. Resources on neutron energy spectra, neutron detectors and detection techniques as well as detector responses are widely available, including publications and technical documents of

the IAEA [27], [28]. Specifically, regarding neutron spectrometry, advancements include broad-energy detectors using thermal neutron detectors within moderators, various Bonner Sphere Spectrometer designs for real-time neutron monitoring, He-3 alternatives like boron-coated straw and liquid scintillators, and high-energy spectrometers utilizing PSD plastic scintillators [28].

2.2 Radiation Detectors and Monitors Fundamentals

In order to introduce the frame on which the prototype monitor is designed, and evaluate its performance with other currently used detector and monitoring systems, this chapter discusses theoretical aspects of scintillators and other detectors. Broadly speaking, radiation detectors can be categorized into scintillation detectors, gas-filled detectors and semiconductor detectors. Scintillator detectors, like the one used as the basis of this study will be examined specifically later on. A semiconductor detector is a device capable of counting incident radiation by measuring the ionization current generated when energy is transferred to electrons during interactions between photons and matter within the semiconductor. The energy required to generate one electron-hole pair is determined by the type of semiconductor. Since the magnitude of the current is proportional to the energy transferred to the electrons by the photons, by measuring this current, the amount of incident radiation energy can be measured. Detector systems vary in many parameters, from components to application, however most follow certain common key functions. An example showing the flow from radiation being incident on the detector's sensor until digitization to allow for pulse height analysis, can be seen in Figure 2.2.

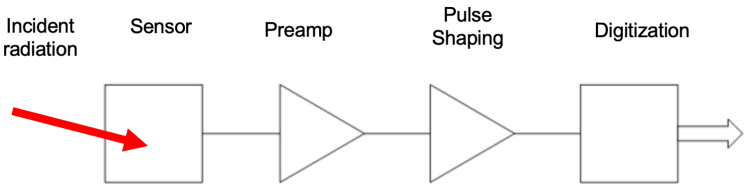

Figure 2.2: Diagram of fundamental functions of most detector electronics for pulse height analysis

Given a constant applied voltage, the magnitude of the output pulses consist the pulse height spectrum, or pulse height distribution. One of the standard sources that is

utilised commonly in radiation measurements, as well as this research, is that of ^{137}Cs. A common pulse height spectrum obtained using a CsI(Tl) cubic scintillation detector is shown in 2.3. In this case, the characteristic peak of 661.66 keV arises from the decay of ^{137}Cs, where the daughter nuclide ^{137m}Ba de-excites to its stable state ^{137}Ba.

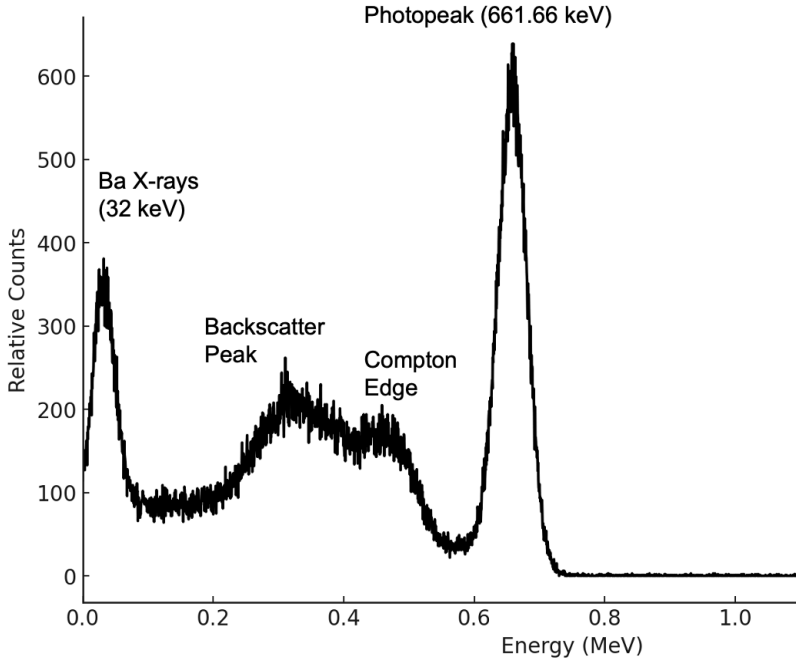

Figure 2.3: Pulse height spectrum of ^{137}Cs source, recorded from a CsI(Tl) scintillation detector, highlighting the photopeak, Compton edge, backscattering peak and characteristic X-ray peak

The peaks in a pulse height spectrum, called photopeaks, indicate the main gamma photon energy, mainly resulting from photoelectric absorption. In non-ideal detectors, the photopeak is not a sharp peak, but it is blurred, broadened as a result of statistical fluctuations in photon detection and conversion-to-signal mechanisms. This broadening is more prominent in scintillation detectors than semiconductor based detectors [29]. In identifying the areas in a pulse height spectrum, the Compton edge indicates the maximum energy of a single Compton scattering event. In Compton scattering, the maximum energy transferred to the scintillator, forming the Compton edge, is given by:

$$T_{\max} = \frac{2E^2}{m_e c^2 + 2E} \tag{2.3}$$

where $m_e c^2 = 0.511$ MeV is the rest mass energy of the electron. This is visible in Figure 2.3. The region on the left of the Compton edge, is the Compton plateau. In the figure, the characteristic X-rays of daughter nuclide ^{137m}Ba are visible at 32 keV, as well as the backscattering peak. The valley between the photopeak and the Compton edge is attributed to additional Compton scattering events, leading to the distribution of these pulses [18]. Pulse pile-up occurs when multiple gamma rays interact with the detector in quick succession, generating overlapping pulses before the initial pulse has fully attenuated. This results in the formation of several combined or "piled-up" pulses. As a consequence, the gamma-ray spectrum may show distorted peaks, often with tails on the higher energy side, and the detected count rates may be lower than the actual rates because some pulses are missed or merged. Additionally, sum peaks can appear, particularly in scenarios where multiple gamma-ray pulses coincide either randomly (random summing) or sequentially from the same event (coincidence summing). Such phenomena can affect the accuracy of both energy measurement and count rate in gamma-ray spectroscopy [29].

When measuring gamma-emitting radionuclides, the sample's gamma counts should be compared with those from a standard containing a known quantity of the radionuclide, using the same counting geometry. For gamma spectrometry, efficiency curves are created for different geometries using measurement standards, taking into account the relative yields of gamma emissions from various radionuclides [25]. Detection efficiency measures the ability of a detector to convert gamma-rays into useful signals. Meaning that better energy resolution is associated with better separation of adjacent energy peaks and identification of different radionuclides in a spectrum. Gamma-rays are detected after interacting with a detector. However, not all gamma rays interact with the detector, and as a result, the detection efficiency is less than 100%. Therefore, in order to relate the number of pulses counted to the number of photons incident on the detector, an accurate measurement of the detector's efficiency is required. There are two types of counting efficiencies: absolute efficiency (ε_{abs}) and intrinsic efficiency (ε_{int}), which are defined as follows:

$$\varepsilon_{\text{abs}} = \frac{\text{Number of recorded pulses}}{\text{Number of radiation quanta emitted by the source}}$$

$$\varepsilon_{\text{int}} = \frac{\text{Number of recorded pulses}}{\text{Number of quanta incident on the detector}}$$

Absolute efficiency is dependent on geometry, distance and intrinsic detector properties, while intrinsic efficiency is mainly dependent on detector material and incident energy. The latter is affected more on the path the radiation takes through the material medium of the detector, rather than the distance from the source. For an isotropic source, these two types of efficiency are related through the solid angle Ω by the following expression:

$$\varepsilon_{\text{int}} = \varepsilon_{\text{abs}} \cdot \frac{4\pi}{\Omega}$$

Counting efficiency can also be classified based on the nature of the recorded events into total efficiency and peak efficiency. Total efficiency is used when all pulses from the detector are considered, while peak efficiency refers only to interactions that contribute to the full-energy peak. This is why it is also referred to as full-energy peak efficiency as well. Peak efficiency is typically used for comparisons between different detectors.Most commonly in radiation detection, the peak efficiency (full-energy peak efficiency) is focused on. It is defined as the ratio of the number of counts in the photopeak, divided by the number of gamma rays emitted by the source [18], [23]. While many methods of calculation of detection efficiency can be conducted with Monte Carlo simulations and then compared with experimentally obtained efficiencies, other methodologies such as photon interaction probability integration calculations have been tested, providing fast results while also considering intricacies in geometry and photon path [30].

Energy resolution on the other hand, measures the ability of the detector to distinguish gamma-rays with close energies. The energy resolution of a detector is often expressed using the Full Width at Half Maximum (FWHM) of a peak in the energy spectrum. The equation for FWHM, related to the energy resolution, is given by:

$$R = \frac{\text{FWHM}}{E} \times 100\%$$

where:

- R is the energy resolution (expressed as a percentage),

- FWHM is the full width of the peak at half of its maximum height,
- E is the energy corresponding to the peak.

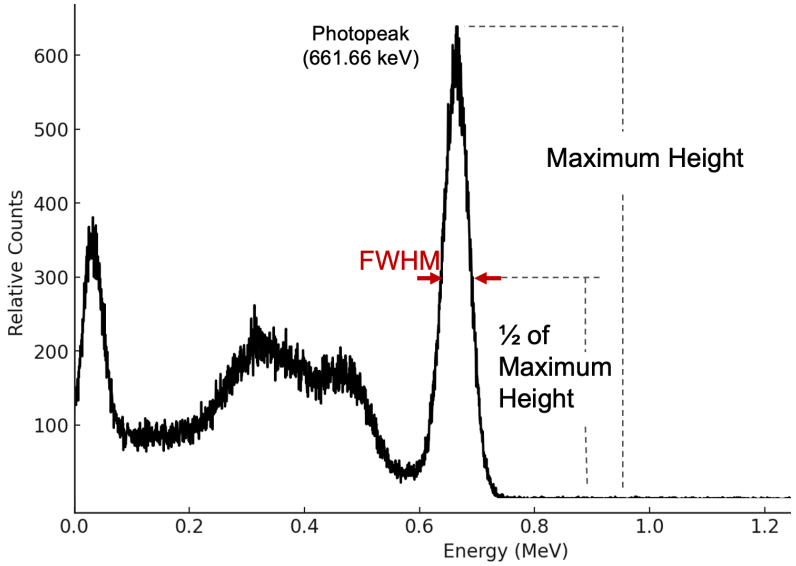

Figure 2.4: Pulse height spectrum of a ^{137}Cs source, recorded from a CsI(Tl) scintillation detector, highlighting the full width at half maximum height (FWHM) of the photopeak

Better energy resolution means its percentage value is lower and the photopeak is less broad [18]. The finite energy resolution of radiation detectors causes the 'blurring' of photopeaks, which can be approximated by a Gaussian distribution. In radiation detection research, this effect is commonly referred to as Gaussian smearing (or blurring) [31]. Energy resolution of a detector is affected by parameters such as statistical fluctuations in photons deposited in the crystal and those received by the photocathode and electrical noise of the system, especially within the photodetector component.

Most types of solid materials used for radiation detection are either semiconductors (like silicon or germanium), offering several benefits such as excellent energy resolution, and scintillators [32]. Both absorb ionizing radiation, however semiconductors convert this radiation directly into an electrical signal. Incident radiation excites electrons from the valence band to the conduction band, creating electron-hole pairs, the number of which is proportional to the energy deposited by the radiation.

2.2.1 Scintillation Detector Systems

Scintillation detectors are widely used for gamma-ray detection due to their high sensitivity and ability to detect a broad range of gamma-ray energies [33]. Gamma-rays, lacking charge do not ionize the material medium they are incident, thus detection depends on the interaction between the gamma-ray and the electrons of said material medium [18]. The term scintillator is generally used to describe the crystal material which converts the kinetic energy of the incident radiation into detectable light, while the term scintillation detector, usually refers to the scintillator coupled to a photodetector or photomultiplying device [34], [35]. Apart from gamma-ray and neutron related applications, scintillators have been used for beta particle detection and x-ray research as well, such as x-ray imaging [36]. Most scintillation detectors exhibit relatively lower detection efficiency and energy resolution when compared to systems like High Precision Germanium (HPGe) detectors. Various parameters contribute to the worsening of their attributes. However, they are relatively inexpensive per unit volume and their size can be adjusted. The energy resolution of scintillation detectors has been intensively investigated. Non-proportional response to incoming radiation, Landau fluctuations and secondary electrons as well as more complex parameters, such as slow component are among directions that have been pursued in investigating how energy resolution of scintillators like CsI and NaI is affected [37].

Overall, scintillators can be categorized to inorganic, exhibiting a crystalline structure and organic scintillators. Organic scintillators can mainly be organic crystals, plastic or liquid solutions.

Generally, inorganic scintillators are more expensive, have a higher atomic number Z, can be doped with other materials depending on intended usage and are commonalty used in nuclear and medical imaging. Organic scintillators have relative low Z, are usually doped and are overall inexpensive and easy to produce, while liquid scintillators have disadvantages like toxicity [18], [37]. Oftentimes, in order to alter the wavelength of the scintillation light which is to be detected, impurities known as activators are included in the scintillator crystal, creating levels within the forbidden band gap. Prominent examples include alkali halides like CsI(Tl) and NaI(Tl), Thallium activated (or doped) Cesium Iodide and Sodium Iodide respectively. Choice of scintillator is dependent on the type of

application, such as particle of interest alpha, beta, gamma-ray, the size limitations of the detector system and cost, among others. Scintillation behaviour depends on intrinsic characteristics of the scintillator, optical properties, surface reflectance as well as environmental conditions like temperature and humidity [18], [35]. Recently, compounds of inorganic and organic scintillators, such as perovskites, have been tested and found to exhibit high light yield and seemingly suitable for x-ray imaging, even though they are lacking in performance compared to most established detectors resolution and efficiency [38], [39].

If not properly covered with materials such as Teflon tape, scintillators may exhibit light losses [34]. If a charge particle enters the scintillator, the energy absorbed leads to the emission of light. The electrons in the scintillator are in the valence band and when they absorbed this energy, they jump to the conduction band. What follows is the de-excitation of the electron back to the valence band along with the emission of a low energetic photon. The intensity of the scintillation light produced after the incidence of the gamma-ray to the scintillator is proportional to the energy deposited by the incident gamma-ray. The scintillation light travels in the scintillator until it reaches the photodetector or escape. Light is converted into electrons on the photocathode of the photomultiplier tube or multi-pixel photon counter and is amplified electrically. As a result, a short current pulse is extracted, whose pulse height is proportional to the amount of detected light [35]. The frequency distribution of the heights of those pulses is the pulse height spectrum introduced in Section 2.2 and can be viewed when using a device such as a multi-channel analyzer (MCA). The role of the MCA is to allocate into a histogram of all the energies absorbed, by dividing the incoming signals, which are proportional to the initial energy, into channels. Each amplitude in the pulse height distribution represents a certain energy.

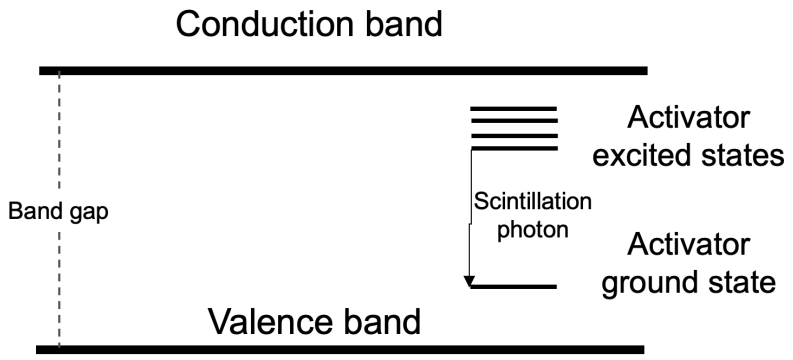

Figure 2.5: Structure of energy bands in a crystalline scintillator

A diagram of the basic connections used in this study, following the concept of a typical connection for a scintillation detector in principle, can be seen in Figure 5.5. The CsI(Tl) is couple to a Multi-pixel Photon Counter (MPPC), which is connected to the MCA after passing through an amplifier.

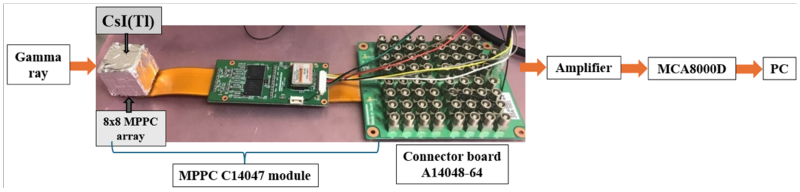

Figure 2.6: Standard setup for obtaining data for resampling calculations

An example spectrum that can be obtained, where many of the interactions described earlier can be observed, is shown in Figure 2.7. In this instance, the pulse height spectrum shown is mainly that of the 1369 keV and 2754 keV gamma rays emitted from ^{24}Na, as measured by an NaI(Tl) scintillation detector.

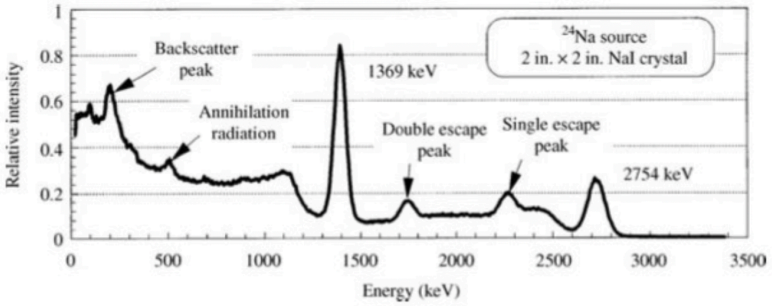

Figure 2.7: Pulse height spectrum of 24 Na obtained with a NaI(Tl) scintillation detector [18]

In figure 2.7, apart from the two major peaks at 1.37 MeV and 2.75 MeV, we can identify the backscatter peak, annihilation peak, and single and double escape peaks. The backscatter peak arises from gamma rays that are scattered back into the detector after interacting with surrounding materials. The annihilation peak occurs at 0.511 MeV, resulting from the annihilation of positrons with electrons. The single and double escape peaks are seen at energies lower than the primary peak of 2.75 MeV due to the escape of one or both of the annihilation photons produced in pair production events. Higher incident gamma-ray energies are associated with more prominent annihilation peaks. Utilizing 14 MeV neutrons to irradiate an aluminium (Al) foil and induce the reaction $^{27}\mathrm{Al}(n,\alpha)^{24}\mathrm{Na}$, a similar pulse height spectrum is obtained, the energy spectrum is unfolded, and the theoretical dose rate of the source is calculated in this thesis in Section 6.2.

The response function of scintillation detectors, is a matrix describing the way the detector responds to incoming photons and depends on crystal characteristics (type, size), photo fraction, incident gamma-ray energy, solid angle, overall experimental setup [40]. Response functions and radiation spectrum unfolding will be discussed later on in Section 2.7.1.

NaI scintillation survey meters are commonly used instruments that, despite their bulkiness and reduced accuracy when measuring gamma rays at energies different from the calibration point (such as 662 keV from Cs-137), provide a useful rough estimate of dose rate in medical, industrial, or research environments. Figure 2.8 illustrates the model used in this study.

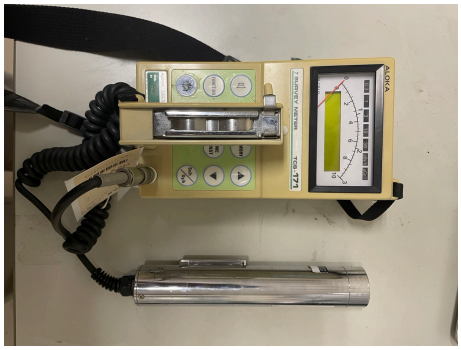

Figure 2.8: TCS-171 Aloka Hitachi NaI(Tl) survey meter used in this research

Table 2.2: Characteristics of some representative inorganic scintillators [18], [41]–[45]

Scintillator	**Density [g/cm^3]**	**Max Emission Wavelength [nm]**	**Decay Times [ns]**	**Light Yield [Photons/MeV]**	**Hygroscopic**	**Energy Resolution [% @ Cs-662 keV]**
NaI(Tl)	3.67	415	230	38,000	Yes	5.6
CsI(Tl)	4.51	550	1000, 1250	65,000	Slightly	5.7
CsI(Na)	4.51	420	460, 4180	39,000	Yes	6.0
$Bi_4Ge_3O_{12}$ (BGO)	7.13	480	300	8,200	No	12
$LaBr_3$(Ce)	5.08	380	16	70,000	Yes	2.6
GAGG(Ce)	6.63	520	88	60,000	No	6.3
LuAG(Pr)	6.7	312	20	22,000	No	4.2
CLYC	3.31	370	1, 50, 1000	20,000	Yes	5.0
CLLBC	4.0	410	25	45,000	Yes	4.0

Hygroscopicity, seen in Table 2.2, describes the tendency of a solid substance to absorb moisture from the surrounding atmosphere and environment [46]. For example, CsI(Tl) is compromised only when directly exposed to very high sources of humidity or water. Some sources regarding scintillator performance, confuse hygroscopicity with deliquescence, but it is important to note that deliquescence describes the quality of a substance to form an aqueous solution (dissolving completely) when absorbing water, whereas hygroscopic substances do not form an aqueous solution but absorb moisture from the air [47], [48].

It is well established that in general, larger scintillator crystals lead to better performance [18]. Increased efficiency in absorbing the photopeak is expected with crystal size increase (volume increase), as well as an increase in Compton peak and continuum. Consequently, thinner crystals (shorter optical path), when volume is constant, can enhance light-collection efficiency for events nearer to a photo-detecting surface. Previous studies on $LaCl_3$:Ce scintillators have reported light output losses in thicker crystals [49] and deteriorated timing resolutions [50]. Light output refers to the number of emitted photons per absorbed energy. In cases of BGO crystals, light output exhibits a decrease with an overall increase in size (volume) [51]. In testing various BGO scintillators with varying thickness, an intermediate thickness of 10 mm was found to be preferential in terms of energy resolution and spectrum performance characteristics like peak-to-Compton ratio [52]. Light collection efficiency for a scintillator describes the light that reaches the photodetector. This parameter, along with the intrinsic reflective characteristics and light absorption of the scintillator govern the amount of light that will be converted into meaningful signal after being detected by the photodetector [34]. Covering the detector to avoid light losses

with materials like Teflon tape is common practice [53]. Scintillation crystals can also experience losses and performance degradation if they are not polished [54]. Some other types of scintillators include GAGG and CLYC or CLLBC, 2.2, the later of which possess neutron and gamma-ray discrimination potential.

2.2.1.1 Scintillators for Neutron Detection

Scintillation detectors are also used for neutron detection. Materials used are neutron-sensitive converter materials that capture neutrons and produce charged particles that, in the case of scintillation detectors, convert the energy of these particles to scintillation light [55]. Scintillators used for neutron detection are often doped with materials such as lithium or boron, which have a high probability of capturing neutrons and producing secondary charged particles, such as alpha particles or protons. For example, from the decay of a neutron capture, the energy emitted can be detected by a scintillator. Specifically, following neutron capture and subsequent secondary emission, scintillation photons are emitted and scattered in the crystal and an amount of them collected by the coupled photodetector, similar to scintillators used in gamma-ray detection and gamma spectroscopy [55].

For neutron spectrometry, combinations of detectors are sometimes used such as combining NE-213 liquid scintillators with He-3 counters, to cover for energy ranges of 800 keV to 20 MeV and thermal to 1.5 MeV respectively. In one study, by using a 3-layered ^{10}B shield, the He-3 counter acts as a spectrometer, measuring in the range of 50 keV to above 800 keV. The response approximated the H*(10) curve, thus calculation of dose from thermal to 10 keV was also possible with this setup [56]. In order to increase the measurement range for neutron spectrometry, combinations of MPPC-coupled plastic scintillators, like the EJ-254, with scintillators, like the Thallium and Lithium doped NaI(Tl + Li), have been encased in Aluminium and Cadmium, in some studies. The former has been designed for fast neutron spectrometry while the latter for thermal and epithermal neutron measurements, with an overall weight of around 2.4 kg [57]. Gadolinium (Gd) based scintillators show lower output but less noise that their Lithium (Li) counterparts in investigations by Boillat et al. (2024). However, light output only dependence might produce incorrect results, highlighting the need for calculation of the quantum efficiency of

the detector as well [55]. Similarly, for scintillator screens for neutron imaging, boronated scintillators have shown increased detection efficiency in the thermal and epithermal region, in comparison to the commonly used Li based ^{6}LiF/ZnS scintillator [58]. Stilbene is an organic scintillator applicable for detection of fast neutrons. It is not hygroscopic and able to be manufactured at varying shapes. Such organic scintillators seem to provide advantages in performance, albeit at higher costs and availability constraints. Unlike detectors like He-3 neutron counters, which by the application of moderators change fast neutrons to thermal neutrons since they are highly sensitive to them, stilbene can detect fast neutrons as they are. Time, directional and energy information are retained, allowing for neutron imaging or source identification. Crystalline stilbene is confirmed to be able to discriminate between the neutron and gamma-ray contributions [59]–[61]. Attempts of manufacturing organic scintillators with mixtures of the materials diphenylacetylene (DPAC) and stilbene have been successful, exhibiting higher intensity emission in the range of 325–500 nm, with peaks around 363 and 380 nm, but little research has been done on the application of such combination of materials for neutron detection [61].

2.2.2 The CsI(Tl) Scintillator

Cesium Iodide activated with Thallium, CsI(Tl), is one of the most commonly utilized scintillator crystals. It is known to be compatible with MPPC in terms of maximum emission wavelength, as at around 500 nm it is read effectively by most photomultipliers [41]. It is only slightly hygroscopic and has an affordable price [18], [33]. CsI(Tl) is an established material, and multiple studies have confirmed its applicability in radiation detection systems. It does not have the highest energy resolution out of all the scintillators in its family [62]. CsI(Tl) does however possess the highest light yield of commonly used inorganic scintillators [35]. Additionally, it has been used both in portable dosimetric applications [63], [64]; and MPPC coupled pulse height spectrometry [65]. Overall many studies have confirmed its applicability with various types of radiation detection systems [32], [64], [66]. Main characteristics of a CsI(Tl) scintillator are shown in Table 2.3.

Table 2.3: Properties of the CsI(Tl) Scintillator [18], [41]

Property	**Value**
Light Yield (Photons / MeV)	45,000 $\sim$ 65,000
Effective Z_{eff}	51
Melting Point	621 °C
Hygroscopicity	Slightly
Decay Times (ns)	1000, 1250 nSec
Density	4.51 g/cm^3
Hardness [Mohs]	2
Peak Wavelength	540-550 nm
Refractive Index [@560 nm]	1.79

Figure 2.9 shows one type of CsI(Tl) scintillator used in the research that is described throughout this thesis.

Figure 2.9: 2.6 $\times$ 2.6 $\times$ 2.6 cm^3 CsI(Tl) scintillator

One study compared the performance of two handheld RadEYE detectors: one using a CsI crystal and the other a CLYC crystal [64]. Dynamic and static tests were conducted to evaluate their ability to detect and identify gamma rays and neutrons. The CsI detector outperformed the CLYC detector in gamma detection, particularly with high-energy sources like ^{60}Co, while the CLYC detector, though less sensitive for gamma detection, was capable of neutron detection, especially when used with a moderator. Overall, the CsI detector was faster and more sensitive for gamma rays, whereas the CLYC detector provided the added advantage of neutron detection. Pereira et al (2018) [67] have investigated the neutron detection capabilities of a CsI:Pb (Cesium Iodide doped with Lead) scintillator coupled with a photomultiplier tube (PMT). They focused on detecting fast and thermal neutrons, examining how the concentration of Pb dopant, along with the use of paraffin and Cd foil, influenced detection efficiency. Such investigations have utilized

paraffin to thermalize neutrons and cadmium to disregard scattered neutron contribution, for the purpose of elucidating how CsI scintillators interact with incident neutron [66]. It also has a larger absorption coefficient per-unit size, compared to NaI, making it easier to use in applications where smaller sizes are preferable [18].

2.2.3 Photodetection and Multi-pixel Photon Counters

To effectively utilize a scintillator for radiation detection, it is essential to employ a photodetector that can convert the scintillation light into an electrical signal. Photodetectors primarily fall into two categories: vacuum-based and solid-state devices. Vacuum photodetector operation is based on the photoelectric effect and the most important component is the photocathode. When photons with sufficient energy strike the surface of the photocathode, photoelectrons are emitted. These photoelectrons are directed towards an electrode (dynode) by an applied electric field, causing an emission of additional electrons through a process known as secondary electron emission. A commonly used vacuum photodetector is the photomultiplier tube (PMT), which uses a photocathode in combination with many dynodes for signal amplification [18].

Solid-state (semiconductor) photodetectors are light-sensitive devices made from semiconducting materials. These materials possess a distinct electronic band structure where photons of adequate energy can excite electrons from the valence band into the conduction band, leaving behind holes. In a pure semiconductor, electrons and holes exist in equal concentrations, but by introducing impurities, an excess of electrons (n-type) or holes (p-type) can be created, resulting in what is known as an extrinsic semiconductor. When n-type and p-type regions are placed together, electrons from the n-type diffuse into the p-type region, while holes move in the opposite direction. This diffusion creates an internal electric field across the p-n junction, forming a depletion region devoid of free carriers. This p-n junction acts as a diode, allowing the current to flow predominantly in one direction. Photon interactions within the depletion layer generate charge pairs, which are then separated by the internal electric field and collected as an electrical signal. Solid-state devices offer several advantages over their vacuum counterparts, including greater ruggedness, compact size, and lower cost. Main types of solid-state photodetectors include photodiodes, avalanche photodiodes (APDs), Geiger-mode avalanche photodiodes,

and the Silicon Photomultiplier (SiPM), also known as solid-state photomultiplier (SSPM) or Multi-pixel Photon Counter (MPPC).

MPPCs are photodetectors made of an array of hundreds or thousands pixels, which pixels are integrated single-photon avalanche diodes (SPADs). All pixels are square-shaped with edge length of a few µm, are connected to a common readout in parallel, with each one having its own quenching resistor. When a photon is detected, the SPAD generates a large electric output signal due to internal avalanche multiplication [68], [69]. A schematic and a photograph of an example MPPC array are shown in Figures 2.10 and 2.11 respectively. Each pixel can count a photon at the same time and then output a signal from all pixels as a summation [70]. MPPC module measurement range extends to the nW region from the photon counting region, and their main requirement for operation is a ±5 V power supply [70].

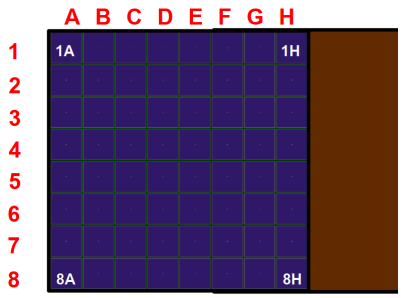

Figure 2.10: Arrangement of a 64 channel MPPC array [70]

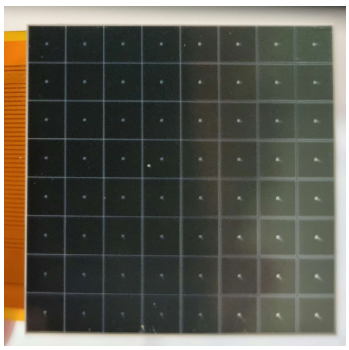

Figure 2.11: Light receiving area of the MPPC array

MPPCs have been widely coupled with various scintillators [71], [72], such as BGO and GAGG:Ce [52], including CsI(Tl) [63], [73]–[75], and have advantages in terms of their small size, being lightweight, being relatively inexpensive and having high signal

amplification gain while being insensitive to magnetic interference [71], [76]. They have high quantum efficiency and mechanical robustness, and are an energy-efficient alternative to traditional photomultiplier tubes (PMTs) with sensitivity across a wide wavelength range [77]. PMTs have less noise, but their need for high voltage supply and bulky size makes them unfit for portable radiation detection devices [63]. Usually an optical grease is applied when coupling, at the light receiving surface of the MPPC. Deterioration of the optical coupling grease can lead to worsening of the energy resolution of the detector. Investigations with CsI(Tl) scintillators showed that Gore-Tex Teflon and optical grease (OKEN-6262A) were optimal materials for shielding and coupling [78]. These materials are also used in research described in this thesis.

In applications using MPPCs, key considerations include the signal level, which is the amount of light detected, and noise, the intrinsic fluctuation in the signal. Linearity refers to how accurately the photodetector's output corresponds to its input. The dynamic range is the ratio between the maximum input signal that maintains linearity and the minimum detectable signal. The time response, indicated by rise and fall times, reflects how closely the detector's output matches the input signal over time, while time resolution is the uncertainty in determining the timing of detected events relative to a reference point [77]. The photon detection efficiency of an MPPC depends on wavelength of the incident light. In the case of coupling with a scintillator, it depends on the wavelength of the scintillation light. Figure 2.12 shows the photon detection efficiency curve as a function for wavelength for the C14047-0436 MPPC. A broad enough maximum peak that allows for applications with many scintillation detectors can be seen. For example, the emission of CsI(Tl) is located above 500 nm where it is effectively read out by the MPPC. In general, if the wavelength at which the MPPC has high detection efficiency matches the wavelength of the scintillation light, even a weak scintillation light intensity can produce a strong signal, resulting in high detection efficiency and good compatibility between the two.

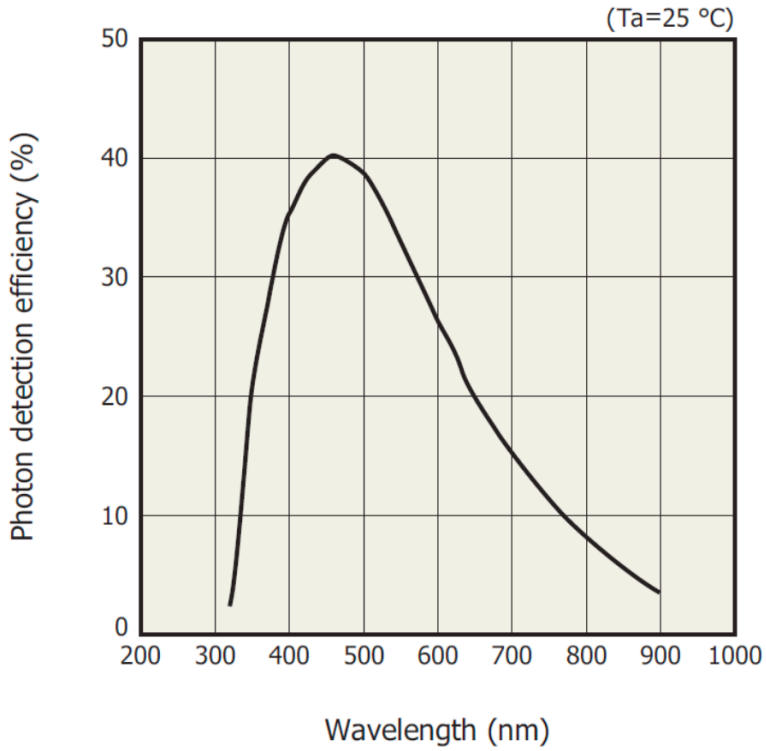

Figure 2.12: Photon detection efficiency as a function of wavelength for Hamamatsu C14047 series MPPC [79]

Overall, an MPPC is a solid choice in photodetector applications that require high precision photon counting, due to their high internal gain [80]. Even in cases of organic scintillators, like EJ-299-34 where PMTs are more standard, successful MPPC coupling and measurements have been conducted [81].

MPPCs can be applied to both studies involving neutrons and gamma-rays. Additionally, an MPPC can still function as a photon-counting device even when dark noise is significantly increased. Dark noise is "the noise produced in a photodetector when the photo-cathode is shielded from all external optical radiation and operating voltages are applied" [82]. Dark noise is associated with dark current, the small amount of baseline electrical current flowing through a photodetector, MPPC in this case, even in an absence of light, due to thermal excitation of electrons or other non-light-related processes. At the same time, findings of Mianowski et al, when testing GAGG coupled MPPCs, with PuBe continuous source (11 MeV) and mono-energetic 4.8 MeV neutrons, energy resolution degradation and detrimental increase in dark current as neutron fluence is increased

was displayed, leading to difficulties in distinguishing the photopeaks [83]. Such findings need to be considered in gamma-ray measurements with high neutron background.

2.3 Digital Pulse Processing

Digital pulse processing is an essential component of data acquisition in nuclear spectroscopy systems [84]. In order for the data of the signal produced by the photodetectors to be converted into a digital form for display and analysis, pulse processing is necessary. Pulse-type radiation detectors generate a burst of charge in response to radiation, which is proportional to the energy deposited. This charge is converted into a current pulse, which is processed to produce either a count rate or an energy spectrum. The signal processing chain typically includes a preamplifier that converts the current pulse into a voltage step proportional to the charge [18]. Separate properties of the pulse need separate processing, which leads to a separation in multiple signal chains, such as the fast and slow channels in a pulse processor. A traditional spectroscopic analog signal processing system involves processing the preamplifier signal using one channel for pulse detection (timing) and pile-up rejection (fast channel) and one for energy (pulse) measurements and by extension pulse height accuracy (slow channel) [85]. The processed analog signal is then digitized by an analog-to-digital converter (ADC) and stored in a multi-channel analyzer (MCA), which accumulates the input signals for each pulse height to enable counting. Older radiation detection systems sometimes employed one or multiple single channel analyzers (SCA), however MCAs are mainly the standard in modern applications.

In digital pulse processing (DPP), the detector or preamplifier signal is digitized immediately, with the fast and slow processes occurring in digital filters with the ADC. In the case of the DP5 digital pulse processor utilized in this study, the preamplifier signal is processed in real time and the digitally detected peak amplitude is binned as a histogram, which is used for the pulse height spectrum viewing with the included data acquisition and control software dppMCA. The slow channel provides pulse shaping with low noise for highly accurate pulse height measurements. The trapezoidal shape provided is beneficial in terms of limiting electronic noise and pulse pile-up. Shaping overall helps with limiting dead time, noise and pile-up, while also applying gain, and provides a balance between performance (accuracy) and speed [86]. In such applications, noise typically arises from

interference caused by energy coupling into the circuit from various connections. The fast channel rejects pulses that occur too close together to be distinguished by the slow channel [86]. A photograph of the DP5 system can be seen in Figure 2.13. It is small in size (8.89 × 6.35 cm^2) and lightweight (32 g) and requires only a power connection (+5 V), a communications connection (e.g. USB) and the signal input from the preamplifier. DP5 has been successfully implemented to solid state detector and scintillation detector systems [86], [87]. For some real-time applications, specialized DPP hardware can be used, incorporating field programmable gate arrays (FPGAs) or additional digital signal processors (DSPs).

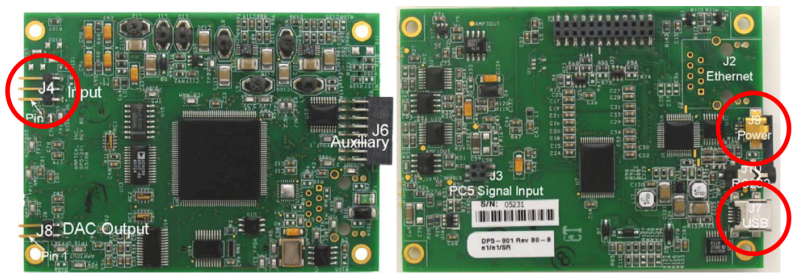

Figure 2.13: Front and back view of the DP5. Red circles indicate the main connections (input, power and communications)

In order to perform the above operations and process the output of the analog to digital converter continuously so as to generate the shaped pulse in real-time, the DP5 is comprised of an analog prefilter, ADC, digital pulse shaper, pulse selection logic and histogram logic components. These are shown in figure 2.14. Similar to an MCA, the DP5 creates an array from each pulse that contains information about the pulse's peak value, which contributes to the pulse height spectrum. This spectrum is the main output of the DP5.

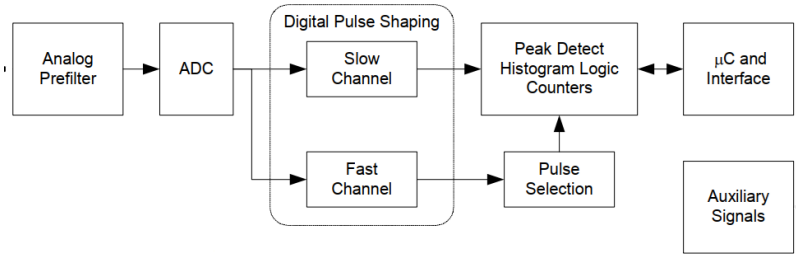

Figure 2.14: Block diagram of the DP5, illustrating the components for digital pulse processing (DPP) [86]

Overall, digital pulse processing offers several advantages over traditional analogue pulse processing, including improved stability, lower power consumption, higher resolution and fidelity of the original signal, and noise immunity since the processing occurs in the digital domain [88]. Time list data are preserved even when delaying signals due to the capability of first-in-first-out (FIFO) memory which retains the signal information without loss for tens of μs [85]. Section 5.5 describes the implementation of the DP5 with the current system of CsI(Tl) scintillator, MPPC and improved sequential Bayesian estimation for energy spectrum unfolding and dose rate estimation.

2.3.1 System Dead Time Consideration

Dead time is an important factor to consider in radiation measurement systems, as it affects the accuracy and reliability of the data collected. Dead time refers to the period during which a detector is converting gamma-rays into signals and is unable to record a new event because it is still processing the previous one. This means that the shortest time that separates two events so they are recorded, constitutes the dead time of the system [18]. Significantly increased dead time can lead to undercounting (counting loss) especially at high count rates, where events may be missed if they occur too close together. This appears as a measured count value, lower than the actual value. During this interval, the detector is considered 'dead.' Dead time is calculated by subtracting the live time from the total real time, which represents the actual time elapsed [29]. Dead time is affected by the response time of the system, intrinsic to the detector, pulse shaping time and data acquisition and processing time. In cases of significant but known dead time (dead time per pulse), the true count rate can be obtained through corrections processes. In the context of the DP5 digital pulse processor, dead time needs to be considered as well. The DP5's ability to process pulses rapidly minimizes dead time, but certain settings, such as the fast and slow thresholds, must be carefully adjusted to optimize performance [86]. Overall the impact of dead time is reduced compared to traditional analog systems. Unlike analog systems, where dead time is largely influenced by the MCA conversion time, the DP5 eliminates this factor, leading to more accurate count rate determinations even at high input count rates. Additionally, the DP5 incorporates advanced dead time correction algorithms, allowing it to effectively manage pulse pile-up and maintain accuracy[87].

2.4 Other types of Detectors and Dosimeters

As briefly mentioned earlier, apart from scintillation detectors, which offer advantages like portability, various types of detectors, monitors and dosimeters are widely used in radiation detection and protection.

Gamma-ray dosimeters measure the dose of gamma radiation by quantifying the amount of energy deposited in a detector material. Traditional passive dosimeters, such as film badges, Optically Stimulated Luminescent dosimeters (OSLs), Thermoluminescent dosimeters (TLDs) and radiophotoluminescence dosimeters (RPLs) while effective and have a wide dynamic range, do not provide real-time exposure information. Passive dosimeters are not continuously monitored. They are more suited to cases where workers are frequently exposed to low levels of radiation, without a danger of higher dose exposure increase [25]. These devices provide the total dose exposure over a set period, typically 1-3 months, in the form of a report for each individual worker [89]–[92]. They are lightweight, can be worn easily but are less suitable for situations where immediate feedback is necessary [93]. One example of a personal dosimeter can be seen in Figure 2.15.

Figure 2.15: Personal dosimeter for passive monitoring with monthly report of dose exposure

In cases where real-time monitoring is needed, in industrial or medical setting, active dosimeters are often preferred. Active dosimeters give instant feedback on dose and change of radiation exposure over time. Other modern dosimetry systems, such as electronic personal dosimeters (EPDs) and advanced scintillation-based dosimeters, are more suited for real-time data acquisition. Usually they measure personal dose equivalent [94], [95]. Electronic personal dosimeters (EPDs) have advanced significantly in size reduction and enhanced functionality such as dose rate alarms, yet can still face challenges such as accuracy and susceptibility to electromagnetic interference [96]. For example,

DKG-05D and DVS-02D dosimeters [97] (SPC Doza, Moscow, Russia, 2017) are relevant examples of supplementary dosimeters to be used along a passive dosimeter. The former is a direct-reading electronic personal gamma-radiation dosimeter that measures personal dose equivalent (radiation dose received by a person at a specific point on the body [mSv]) and dose equivalent rate (rate at which radiation dose is received [mSv/h]). The latter extends these capabilities to neutron radiation, measuring both neutron and integrated neutron/gamma radiation dose equivalents. Evaluations have shown acceptable performance, but poor display performance in temperatures below 5°C [98].

Spectrometers provide information about the pulse height spectrum of the radiation in real time and are useful in identifying radioactive sources [25]. Evaluation of dosimeters in mixed neutron and gamma-ray environments, testings of commercial personal dosimeters and assessment and improvement of neutron dosimeters are conducted by the IAEA. Results indicate that many personal dosimeters show significant under or overestimation, while passive systems were mostly consistent [13], [99].

Another main category of detectors is that of ionization chambers. These include Geiger-Muller (GM) counters, ion chambers and proportional counters. GM counters, the sensing element of which is the Geiger tube, have been a stable for environmental contamination detection. Pocket ionization chambers have been also used in radiation field work and provide dose reading in real-time. Table 2.4 compiles a few of monitoring systems for either pulse height spectroscopy or dose rate monitoring, including specifications in terms of size weight, performance and dynamic range.

Table 2.4: Specifications of a few commerical monitors and dosimeters

Monitor Name	Manufacturer	Capabilities	Weight	En.Range	Sv/h Response	Size	Special Note	Detector type	Date
RayMon 10	Kromek	PHS, dose rate, nuclide identif.	1.08 kg	30 keV to 3 MeV	Up to 1 mSv/h	21.6x20.5x4.5 cm	En. resol. 2-2.5% @ 662 keV	CZT	2019
RADEAGLET-R	ORTEC	Radioisotope, nuclide identif.	1.5 kg	15 keV-3 MeV / 45 keV-.5 MeV	10 nSv/h-250 Sv/h, >250 Sv/h-1 mSv/h	90 mm × 280 mm × 110 mm	Dual GM Det.	NaI, He-3	2022
DKG-09D	SPC Doza	Amb.dose equiv. rate	200 g	0.05 to 3 MeV Gamma:	0.1 Sv/h - 50 mSv/h	6.9x12.3x3.3 cm	Restore source spectrum	CsI(Tl)	2017
SPIR-Ace	Mirion	Radionuclide Identif.	1.45 kg	25 keV to 3 MeV, Neutron: 0.025 eV to 1 MeV	Gamma: 0.001 Sv/h to 100 mSv/h	206 mm x 153 mm x 57 mm	Fast nuclide identif.	NaI, LaBr3	2022
Inspector 1000	Canberra Industries	PHS, dose rate	2-7 kg	25 keV to 3 MeV	20,000 Sv/h (Probe 1), 10,000 Sv/h (Probe 2)	19x16.5x6.4 cm (alone), 25.4x24.1x14 cm (with probe)	±10%	NaI, GM Detector	2017
AMP 300	Mirion Technologies	Dose rate	340 g (meter), 131 g (detector)	70 keV to 2 MeV	1 mSv/h to 300 Sv/h	12x7.2x3.4 cm (meter), 2.45x14.3 cm (detector)	±10%	2 GM Detectors	2023
RDS 30	Mirion Technologies	Dose rate, measures dose	220 g	48 keV to 3 MeV	0.01 Sv/h to 100 mSv/h	78x126x32 mm	±5%3 mSv/h, en.response ±30%>3 MeV	GM Detector	2022
DMC 3000	Mirion Technologies	Dose rate, measures dose	88 g	15 keV to 10 MeV	1 Sv/h to 10 Sv/h	8.7x6x2.1 cm	±5% with Cs, +15% 0.15-1.5 MeV, ±20%<10 MeV	Semicond. based	2023
MBD-2	Mirion Technologies	Dose (gamma, neutron)	57 g	65 keV to 1.3 MeV	Dose up to 500 mSv (gamma rays)	5.3x5.6x2.3 cm	Measures dose, not dose rate		
miniTrace	Bertin Technologies	Dose rate	190-260g or 175-250g	42-2.8 MeV or 48-3 MeV	1 Sv/h - 100 mSv/h	8.4x2.4x13.9 cm	1s response time		2023

While the focus of this research is portable detectors, dosimeters and monitoring systems, the importance of semiconductor detectors cannot be overstated. This is mainly due to their exceptional energy resolution [100]. High Purity Germanium (HPGe) Detectors have many applications, including environmental monitoring and neutron activation analysis. Their measurement range covers low energy to high energy gamma-rays of the 10 MeV region and are cooled cryogenically, usually with liquid nitrogen or in some cases electro-mechanical cooling systems [101]. Due to the lead shielding usually utilized and the cooling system necessary, most HPGe detectors weight over 20 kg, however, portable systems of HPGe spectrometers have been developed. AMPTEK [102] and Mirion [103] for example offer at 11.1 kg and 16.6 kg respectively two of such accurate and relatively portable HPGe solutions.

2.5 Detectors in gamma-ray/neutron mixed fields

Distinguishing between neutron and gamma contributions, focusing on one of them, or extracting both contributions is important in radiation monitoring. ^{6}LiCaF is a scintillator primarily used for measuring gamma rays in a mixed radiation field. However, due to the high Q-value of the ^{6}Li(n,α)^{3}H reaction, approximately 4.78 MeV, the detector is less effective for measuring low-energy neutrons, particularly around 1 eV. The significant energy released during neutron capture by ^{6}Li makes it difficult to accurately detect and measure such low-energy neutrons, making ^{6}LiCaF more appropriate for gamma-ray detection in these environments. Eu:^{6}LiCaF onion-like single Bonner sphere neutron spectrometers have been used for neutron spectrum unfolding using Monte Carlo-calculated response functions, which are validated experimentally. However, the spectrum is unfolded post-measurement, rather than in real-time [104]. ^{6}LiI:Eu is a Eu doped promising material for the detection of thermal neutron, that can be coupled to an MPPC [105], [106]. However, such devices, are large in size and heavy, therefore cannot be incorporating into portable spectrometry. Alternatives to bulky Bonner sphere neutron spectrometers for use in medical accelerator facilities are being looked into, such as the In-MuNS (Indium Multi-shell Neutron Spectrometry system), that has been validated against simulation results [107].

Inorganic scintillators like $CeBr_3$, are more resistant to neutron radiation influence, and have many applications, such as plasma diagnostics in fusion research [108]. Plastic scintillators have been applied to neutron-gamma discrimination, by utilising PSD (pulse shape discrimination). Many advancements in neutron detection innovations, such as introducing ^{10}B or ^{6}Li into plastic scintillators and more, are described in publications by the IAEA [28]. In neutron detection, specifically regarding dose rate measurements, probes based on polyethylene moderators with a He-3 proportional counter can detect neutrons from thermal energies up to 20 MeV and follow ICRP recommendations [109]. He-3 counters in general are applicable in neutron measurements, since they combine good detection efficiency and can reject unwanted gamma-ray contribution [110]. Regarding real-time neutron spectrometry, the novel technique of Recoil-proton Track Imaging (RPTI) that combines gas scintillation with real-time imaging devices can optically record the tracks of recoil protons, enabling prompt analysis and unfolding of high energy (few

MeV) neutron spectra. In this method, collimated incoming neutrons scatter off hydrogen nuclei in a polyethylene foil, producing recoil protons. The energy of the recoil protons is related to the energy of the incident neutrons through the scattering angle.

The CLYC (Cs_2LiYCl_6) and CLLBC ($Cs_2LiLaBr_6$) elpasolite scintillators possess characteristics such as superior energy resolution to commonly used scintillators like CsI or NaI, dual discrimination capabilities, and enhanced performance for both gamma-ray and neutron detection [111]. These scintillators achieve an energy resolution of less than 5% at 662 keV for ^{137}Cs. CLLBC can achieve an energy resolution of approximately 4.1% at 662 keV [112]. Their scintillattion properties have been investigated and compiled in comprehensive reviews like that of Jin et al (2022) [45]. These crystals can be manufactured to custom sizes to meet specific detection requirements.A CLYC scintillator emits light within the wavelength range of 275-450 nm, with a peak scintillation wavelength at 390 nm. CLLBC emits light with a peak scintillation wavelength at 410 nm. Both allow them to be coupled most commonly with PMTs but also with some MPPCs [113]–[116]. Pulse shape discrimination in such coupling configurations has been achieved [113], [117]. These scintillators are particularly effective for neutron detection due to their enrichment. CLYC and CLLBC scintillators with 95% ^{6}Li enrichment are highly efficient for thermal neutron detection. CLLBC scintillators enriched with 99% ^{7}Li are well-suited for fast neutron spectroscopy. Additionally, they have dual discrimination capabilities allowing them to distinguish between different types of radiation through pulse-height and pulse-shape discrimination. Neutron and gamma-ray signals have distinct decay rates where gamma-rays decay faster. PSD is realised by calculating the ratio of tail area to front area of a pulse. These materials show potential in replacing certain high-energy gamma-ray detectors and He-3 tubes in various applications [113]. Despite the Li doping, CLYC scintillators have been applied to neutron spectrometer development, coupled with MPPCs, however not for energy ranges of thermal to few keV, where responses to different energies could not be distinguished [118]. The scintillation principle regarding neutron detection is based on a thermal neutron on a ^{6}Li atom producing two ionizing particles: a triton and an alpha particle that share the kinetic energy. These ionizing particles produce scintillations within the crystal. In the CLYC scintillator, unique signals for neutron interactions are produced through the ^{6}Li(n,α)^{3}H, ^{35}Cl(n,p)^{35}S, and ^{35}Cl(n,α)^{32}P reac-

tions, which are distinguishable from gamma-ray interactions based on the time profiles of the scintillation light. This allows for clear separation of neutron events from gamma events, effectively utilizing the pulse shape to reject gamma-ray signals [118]. Due to their high dynamic range and discrimination capabilities, these scintillators have been used for commercial handheld systems such as personal radiation detectors and radionuclide identification devices and have been effectively integrated with multi-channel analyzer (MCA) and digitizer systems, such as the eMorpho, for real-time data processing via field programmable gate arrays (FPGA) connected to PCs through USB interfaces. In recent publications such as that of Sakurai et al, the pulse timing and decay analysis techniques used for radiation type identification is highlighted, showcasing the advanced capabilities of these scintillators and reaching sufficient neutron and gamma-ray discrimination [119]. RMD (Radiation Monitoring Devices Co., Ltd.) has provided a comprehensive overview of the general advantages of CLYC and CLLBC in radiation detection [43]. In comparisons between CLYC and CsI(Tl) based portable dosimeters, while the former performed worse overall, the capability to account for both contributions of neutrons and gamma-rays, even if detection rate suffers in cases of unmoderated neutrons, is very beneficial in mixed fields [64]. CLLBC scintillator based detectors have also recently been tested with AmBe sources and fast neutron beams, utilizing standard pulse shape discrimination methods, as well as advanced artificial neural network algorithms to identify the pulse features and discriminate the neutron and gamma-ray signals with high accuracy [120]. Despite their numerous advantages, CLYC and CLLBC scintillators face challenges such as hygroscopicity, which necessitates encapsulation to prevent degradation. To address this, these scintillators are typically encapsulated in quartz or similar materials to protect them from moisture [119]. They have successfully been used in conjunction with PMTs to create portable, albeit bulky devices that show the pulse height spectra of gamma-rays and neutrons, as well as the dose-rate [121].

As introduced in Section 2.2.1.1, regarding fast neutron detection, various solutions including organic scintillators like stilbene can be used [60]. For this type of organic scintillators, pulse shape discrimination of neutron and gamma-ray contribution is feasible because the light it emits is characterised by an immediate and slow component depending on the type of incident particle.

Currently used portable detectors specialize in a specific radiation type and are used in combination with another, when measuring in a mixed field. Thus, regarding portable detectors in mixed radiation fields, the aforementioned scintillators are promising as they can detect thermal to fast neutrons and gamma-rays, while allowing for spectroscopical measurements and pulse shape discrimination.

Organic scintillators are utilized in fast neutron and gamma-ray discrimination, since it involves separating heavy charged particles scattered by neutrons like recoil protons from electrons excited by gamma-rays. Creating enclosure housing organic and plastic scintillators, such as stilbene and EJ-299-34, respectively, coupled with PMTs or MPPCs, with proper wrapping, digitization and pulse shape discrimination, can be used to measure and discriminate fast neutrons, up to around 10 MeV [81]. Similarly, with liquid scintillators like NE213, pulse shape discrimination in case of fast neutrons of energy around 5 MeV has been verified to be applicable for real-time measurements [122]. Another liquid scintillator, BC501A has been applied in spectrometry in mixed neutron and gamma-ray fields [123]. Morichi et al. used liquid organic scintillators (EJ309) and lithium-doped NaI(Tl) detectors with pulse shape discrimination (PSD) techniques to measure neutrons from thermal (0.025 eV) to fast (3 MeV) energies and gamma rays up to 662 keV [124]. Regarding MPPC coupling in thermal neutron detection ^{6}LiF/ZnS:Ag scintillation results have verified its applicability [81].

2.5.1 Pulse Shape Discrimination

As introduced in the previous section, pulse shape discrimination (PSD) is employed in mixed radiation fields, in order to separately measure the contribution of neutrons and gamma-rays. Neutron-gamma discrimination can be executed from detector response time difference, since the rise or decay times vary between a gamma-ray or a neutron pulse. Digital pulse processing algorithms successfully discriminate the necessary components from the incoming signal, in order to identify the neutron and gamma-ray contribution [56], [125], [126]. PSD techniques vary in terms of application and complexity, including techniques like wavelet transforms, neural networks and pulse correlation. PSD mainly utilizes differences in scintillation time profiles due to the interaction of different types of ionizing particles with a scintillator. As discussed earlier, scintillator molecules are excited

by the incident radiation and then de-excite by emitting photons. The scintillation light differs in time and intensity depending on the type of the incident radiation. Gamma-rays, mainly interacting via Compton scattering, subsequently producing high-energy electrons, result in a different scintillation profile than neutrons. This emerging relative timing of scintillation events is what allows PSD. Organic scintillators, such as solid crystals like stilbene, liquids, or plastics, exhibit a combination of prompt and delayed fluorescence, with the former occurring almost immediately after excitation, and the latter over a longer time period. The proportion of these components depends on the linear energy transfer (LET) of the interacting particle, with high LET particles, such as those involved in neutron interactions, tending to produce a more pronounced delayed component [60], [81]. When assuming that the pulse distributions are Gaussian shaped, the value commonly used to judge and compare PSD named figure of merit (FOM) is defined by:

$$\mathrm{FOM} = \frac{S}{\delta_{\mathrm{neutron}} + \delta_{\mathrm{gamma}}} \tag{2.4}$$

where S is the distance between the two peaks and $\delta_{\mathrm{neutron}}$ and $\delta_{\mathrm{neutron}}$ are the neutron and gamma-ray *FWHM* respectively. Figure 2.16 shows an example distribution.

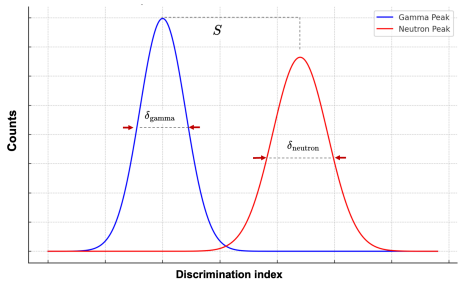

Figure 2.16: Example image of two Gaussian shape histograms of neutron and gamma-ray contributions, generated with sample data for the definition of components of figure of merit

Higher FOM values are associated with better PSD performance. For example FOM higher than around 1.3 are considered adequate for fast neutron detection and separation from gamma-rays [127]. Some organic scintillators like stilbenes have shown FOM values as high as 4.7, indicating strong discrimination performance [60]. CLLBC scintillators have shown FOM values of 0.9 for AmBe source discrimination and 1.3 for fast neutrons. Additionally, it has been found that FOM performances can be improved with methods

such as artificial neural networks yielding results on par or even better than those of the charge comparison technique [120]. CLYC scintillators coupled with PMTs or even with MPPCs have shown FOM values of 2.64 and 2.3 respectively [116]. The EJ-254 plastic scintillator and NaI(Tl+Li) combination has shown FOM of 2.57 and 2.90 [57]. Confirmations with stilbene single crystals coupled with MPPCs, have optimised PSD through a genetic algorithm (GA) optimisation of weighted integrations [128]. It has been suggested that optimisation of MPPCs with DPP can help achieve sufficient level of PSD on par with commonly used PMTs. This has already been achieved in the case of liquid scintillators. Pulse shape discrimination in neutron and gamma-ray mixed fields with organic scintillators (EJ-301 liquid scintillators) is achievable with methods like charge comparison, zero-crossing and linear filter algorithms. In such applications discrimination results are on par with other digital methods, with the charge comparison method leading with an advantage at higher neutron energies [129].

2.6 Capabilities and Limitations of Radiation Detectors and Dosimeters

In principle, dose rate measurement devices need to have a dose rate measurement range wide enough to cover the expected range of dose rates in practice and when exceeding said range, remain off scale and not underestimate the subsequent exposure [25]. The last characteristic ties in with the reports of dose underestimation or overall increase in inaccuracy when exceeding 3 MeV in the case of gamma-ray fields. In the context of medical environments using particle accelerators, the gamma-ray spectrum extends mainly up to about 3 MeV, as this range includes most of the gamma-rays produced after operation, such as due to the activation of accelerator components, and includes LINAC, accelerator-based neutron capture therapy, proton therapy, heavy ion therapy and others [5], [10], [130]. Additionally, the normalization of measurement ranges to a maximum of around 3 MeV, aligns with standard practices in radiation monitoring [131], emphasizing the need for measuring instruments to cover this range to ensure accuracy and reliability in various operational settings, like medical facilities. It is important to mention that 3 MeV has been set as the peak energy range for various commercial gamma-ray dose rate meters, such as the RDS-30 (Mirion Technologies, Atlanta, GA, USA, 2022), minitrace-

(Bertin Technologies, Paris, France, 2023), RadEye PRD series (Thermo-Fischer Scientific, Waltham, Massachusetts, USA) and DKG-09D15 (SPC Doza, Moscow, Russia, 2017) among others. Most gamma-ray emitting nuclides used as radiopharmaceuticals emit radiation below 1.3 MeV, which corresponds to the highest energy peak of ^{60}Co [29], [132]. However, there are exceptions such as ^{124}I, which emits gamma-rays up to 1.691 MeV [133]. Most commercial devices are well equipped to cover the range required for radiopharmaceuticals.

Dosimeters should be low-cost, lightweight, strong, easy to handle, have minimal maintenance requirements and be reliable, with convenient calibration and readout systems [25]. Despite their widespread use, many radiation detectors and dosimeters have inherent limitations, such as delayed data processing, limited energy resolution or bulky designs in the case of spectrometers. What is more, a significant limitation of many currently used monitoring devices is that they are often calibrated using a single source, such as ^{137}Cs (with a 0.662 MeV peak). These devices tend to exhibit poor response at energies either higher or lower than this calibration point, potentially leading to the underestimation or overestimation of the dose rate, respectively [134], [135]. This issue is present in NaI(Tl) scintillator survey meters. Inaccuracies have been documented by various research groups and observed throughout the course of this study through comparisons with theoretical values, where the NaI (TCS-171, ALOKA, Hitachi) survey meter was utilised. Another drawback of these devices is their size and weight. Furthermore, when performing measurements, a parameter known as the time constant must be set. The device must remain stationary for a period equal to three times the time constant to achieve a stable and accurate result. For instance, when the time constant is set to 30 seconds on the NaI survey meter, it requires $30 \times 3 = 90$ seconds to produce the most accurate result possible given its capabilities [136]. Of course less accurate values can be obtained with a time constant of 3 or 10 seconds, but this leads to the digits not stabilizing in the LED display.

Examining devices introduced earlier, spectrometers like the RayMon10 (Kromek, Durham, UK) and Radeaglet-R (ORTEC, Oak Ridge, USA) weigh over 1 kg but display the pulse height spectrum of gamma-rays and the dose rate. Those that only display the dose rate are much lighter, such as the DMC 3000, RDS 30 (Mirion Technologies, Atlanta, USA, 2023 and 2022 respectively) and DKG-09D15 (SPC Doza, Moscow, Russia, 2017),

weighing around 90 - 300 g but can exhibit high deviation at energies far from 0.662 MeV [25]. Spectrometers mentioned above can provide the pulse height spectrum, but they do not provide the true unfolded energy spectrum of the incident radiation. This sometimes can potentially hinder nuclide identification.

Neutron focused dosimeters usually are not adequate to accurately assess the personal dose equivalent due to neutron irradiation, especially considering the whole neutron energy range of interest. When neutrons are present, gamma-rays are also present, so for this reason neutron and photon dosimeters are used simultaneously in neutron fields. Complexity is added since neutron induced personal dose equivalents greatly vary. Depending on the energy range of interest different types of dosimeters are used because no dosimeter can measure thermal to fast neutron contribution at the same time. However apart from the issue of energy range, sensitivity and practical usefulness are reported to be lacking [25].

Regarding measurement accuracy issues, examples include dose underestimation and poor energy response, particularly at low energies below 100 keV [96]. Reports regarding inaccuracies in measurements [96] and overestimations or underestimations due to calibration [134], [135], [137], [138] have been documented. Evaluations, such as those conducted by the International Atomic Energy Agency (IAEA), have shown that there is room for improvement in accuracy, such as in the case of whole-body dosimeters [138]. Extensive reviews have shown limitations such as insensitivity to higher than background dose rates, unstable readings, and issues with display saturation. Some dosimeters have been deemed inadequate for use or nearly unsuitable for their intended applications.

Additionally, medical radiation workers sometimes misuse dosimeters or fail to wear them consistently, emphasizing the need for devices that are easy to use and that make their exposure apparent [11], [13], [139]–[141]. Overall, improvements in radiation protection are necessary, even when doses are within acceptable limits [142]. In terms of overall future directions, the IAEA recommends increasing the use of active dosimeters, as currently passive types are more commonly used [13]. Enhancing the understanding of medical professionals who are not knowledgeable in radiation safety is also highly desirable [13]. Real-time visual information regarding dose exposure has been shown to raise awareness among medical staff and contribute to a safer working environment [143]. Addressing

these issues is necessary for improving radiation safety in medical and industrial settings. Exactly because radiation monitoring and protection is so complicated, strict guidelines that have been set are constantly updated and improved for the sake of safety for the patients, staff and public.

2.7 Energy Spectrum Unfolding

The pulse height spectrum is transformed into an energy spectrum using a process known as unfolding, or spectral deconvolution. This technique requires the response function of the detector to be known with accuracy and extracts the true information of the original incident radiation by solving an inverse problem [18], [144], [145]. The response function is said to describe the relationship between the measured quantity and the incident radiation spectrum. Advances on radiation spectrum unfolding for neutrons and gamma-rays have been a topic of research for a long time, with significant advancements during the 1960s [28], [146]. This problem can be generally described by Equation 2.5:

$$y_i = R_{ij}\phi_j \tag{2.5}$$

where:

- y_i: pulse height spectrum of gamma-rays
- R_{ij}: response function of the detector
- ϕ_j: energy spectrum of incident gamma-rays

Many unfolding algorithms for various applications have been developed, and attempts at compiling them include those by Li et al. [147]. In this research, energy spectrum unfolding is conducted not only to extract the true gamma-ray energy spectrum, but also to estimate the dose-rate of gamma-rays, by applying a flux-to-dose coefficient. Some methods, like the *G(E)* function, compatible with scintillator based configurations like NaI(Tl), allow for dose-rate extraction based on Gaussian regression processes [148].

2.7.1 Theory of Radiation Spectrum Unfolding

The obtained pulse height spectrum is influenced by detector material, dimensions, and casing. Detector properties affect photon absorption and scattering. Partial energy detection and escape peaks can alter the measured spectrum. Therefore, radiation spectrum unfolding is used to reconstruct the undisturbed, true energy spectrum (fluence) and can be used for dose evaluations [149]. The theory behind radiation spectrum unfolding involves solving an inverse problem, where the goal is to reconstruct the original energy spectrum from the measured pulse height spectrum. This process requires knowing the detector response function, which describes how the detector responds to incident radiation, specifically meaning how the detector converts the incident radiation into measurable signal. In other words, from the easily obtained pulse height spectrum and knowing the detector's response when monoenergetic radiation is incident, a response function can be obtained, which can be used to unfold (deconvolute), and determine the true spectrum of the incident radiation [29]. The methodology utilized throughout this present research is a hybrid verified workflow, combining simulation data and experimental data, and is described in more detail in Section 5.6. The accuracy of the unfolding process depends on the quality of the response function and the stability of the unfolding algorithm. Theoretical advancements in spectrum unfolding have led to the development of various sophisticated algorithms. After removing various distortions and artifacts, the unfolded energy spectrum contains the true information of the incoming gamma-rays [145], which aids in understanding the exact conditions of the radiation field, allows for easy radionuclide identification and also serves as a means to calculate in real-time the dose rate, by applying a flux-to-dose conversion coefficient to the unfolded energy spectrum [29], [150], [151]. In gamma-spectroscopy, the need for deconvolution of the energy spectrum arose from the fact that detectors like scintillators have relatively low energy resolution and parameters like environment, shielding as well as escape peaks and effects like Compton scattering add to the complexity of the gamma-ray spectrum. Solving the forward problem involves the creation of a spectrum obtained through calculations and fitting, folded with the response function and evaluated by observational comparison to assess the agreement [152].

2.7.2 Unfolding Algorithms

Several unfolding algorithms have been developed for different applications, ranging from simple iterative methods to more complex Bayesian approaches. The choice of algorithm depends on factors such as the type of radiation being measured and the computational resources available. The application of Bayesian estimation in radiation spectrum unfolding is discussed in the following section. Efforts have been made to compile radiation spectrum unfolding algorithms, but do not encompass exactly all types and applications. Most methods utilize some sort of matrix inversion or an iterative approach [153]. Apart from the iterative Bayesian estimation, spectral and sequential type, which is key in this research, this chapter presents an overview of some algorithms and solutions used to solve the unfolding problem. For example, genetic algorithms have successfully been applied to radiation spectrum unfolding. These algorithms are based on continuously comparing generated results to derive the solution based on the "survival of the fittest" concept, without the need to provide an initial guess solution [145], [154]–[156]. Increased accuracy in neutron spectrum unfolding using genetic algorithms sees utilizing a multi objective optimization technique, taking into account prior information [157]. Another category is artificial neural network (ANN), whcih have been investigated through simulations of neutron spectra unfolding, with goals to expand to dose derivation [153].

Regarding the application of spectrum unfolding in this research, it can be described as follows. When gamma rays are incident on the detector crystal, they interact with the material, leading to the emission of scintillation photons. These photons are detected by the MPPC and converted into electrical signals [158]. After amplification, the signal is fed to an MCA (multi-channel analyzer), like the MCA8000D or a digital pulse processor (like the DP5) which performs the function of an MCA as well [86]. The obtained pulse-height spectrum can then be viewed on a PC. To estimate the energy spectrum in real time from the measured pulse-height spectrum, unfolding is performed. As mentioned earlier, unfolding can be achieved by solving the inverse problem linking the pulse-height spectrum, the energy spectrum, and the response function of the detector, and this can be described by Equation (2.6) [18], [135], [145], [159] . This equation shows how the energy spectrum ϕ_j and the measured pulse-height spectrum y_i are linearly related using the response function R_{ij} (with elements r_{ij}), which includes information about the detection

efficiency:

$$y_i = \sum_{j=1}^{n} R_{ij}\phi_j \tag{2.6}$$

- y_i: the pulse-height spectrum of incident gamma rays
- R_{ij}: the detector response function
- ϕ_j: the energy spectrum of incident gamma rays

$$\begin{bmatrix} y_1 \\ \vdots \\ y_i \\ \vdots \\ y_m \end{bmatrix} = \begin{bmatrix} r_{11} & \cdots & r_{1j} & \cdots & r_{1n} \\ \vdots & \ddots & \vdots & \ddots & \vdots \\ r_{i1} & \cdots & r_{ij} & \cdots & r_{in} \\ \vdots & \ddots & \vdots & \ddots & \vdots \\ r_{m1} & \cdots & r_{mj} & \cdots & r_{mn} \end{bmatrix} \cdot \begin{bmatrix} \phi_1 \\ \vdots \\ \phi_j \\ \vdots \\ \phi_n \end{bmatrix} \tag{2.7}$$

2.8 Bayesian Estimation in Radiation Measurement

Bayesian methods have been widely used in many areas of research regarding radiation, such as detection, internal and external dosimetry [160]. The application of the Bayesian estimation in radiation measurement states that the energy spectrum can be inferred, iteratively as the pulse-height data is received for each count by the detector [161]. Bayesian estimation theory is an approach that in general applies prior knowledge and observed data to estimate probability distributions. This method is well-suited when the goal is to refine an initial estimate of the energy spectrum based on the measured data. Specifically, this research is based on the sequential Bayesian estimation, also known as the α method, upon which our research group developed an improved version, named the $k{-}\alpha$ method. This refined method expedites the convergence process of determining the energy spectrum. First I introduce the basis of how Bayesian estimation can be applied in radiation measurements and gradually expand upon the current research.

As introduced above, Bayesian inference and its application to solving the unfolding problem has been investigated by many and from different perspectives such as Choudalakis [162], D'Agostini [163], Iwasaki [161], Dombrowski [164]. Differences in the methodology

and respective application should be noted. For example, the Fully Bayesian Unfolding[162] differs greatly from the iterative method described by D'Agostini [163]. Bayesian unfolding has been applied for x-ray spectra, for high intensity laser and matter interactions in the study of x-ray calorimeters [165]. It has been investigated in preliminary studies for neutron spectrum unfolding with scintillation detectors as well [166]. Some of the main reasons this method was chosen in this research was that the principle idea is straightforward in its application and allows for the required software creation for eventually realising real-time estimation. Additionally, the calculation of the response function of the detector is the major time-consuming constraint. Lastly, the inverse matrix which can lead to errors and instabilities does not need to be derived [167].

In order to properly introduce Bayesian estimation in radiation measurements we need to explain the basis of Bayesian estimation. For an event, a real number function P(A) the following is true:

$$P\left(\bigcup_{i=1}^{\infty} A_i\right) = \sum_{i=1}^{\infty} P(A_i)$$

when $P(A) \geq 0$, $A \in \Omega$ and $P(\Omega) = 1$ for mutually exclusive events $A_1, A_2, ..., A_i$. The conditional probability of A given B can be defined as:

$$P(A \mid B) = \frac{P(A \cap B)}{P(B)}, \quad \text{if } P(B) > 0$$

This can be rewritten as:

$$P(B \mid A) = \frac{P(A \cap B)}{P(A)}$$

The Bayes' theorem states:

$$P(A \mid B) = \frac{P(B \mid A) \cdot P(A)}{P(B)}$$

If B is divided into independent groups, the theorem can be generalized as:

$$P(A_j \mid B_i) = \frac{P(B_i \mid A_j) \cdot P(A_j)}{\sum_{k=1}^{n} P(A_k) \cdot P(B_i \mid A_k)}$$

Here, $P(A_j)$ is the prior probability, and $P(A_j \mid B_i)$ is the posterior probability, updated using event B_i. This iterative process is called Bayesian updating or Bayesian inference.

Using the obtained posterior probability as the new prior probability and repeating the Bayesian inference, $P(A_j)$ can be estimated.

To move to the context of radiation measurements, the following events and their corresponding probabilities are defined as :

- Sample space Ω: Events where radiation enters the detector
- $P(\Omega)$: The probability that radiation enters the detector.
- Event A_j: The event that energy belonging to the energy bin E_j enters the detector
- $P(A_j)$: The probability that the radiation that enters the detector belongs to energy bin E_j (**prior probability**).
- Event B_i: The event that radiation enters the detector and the detector gives a signal in channel i
- $P(B_i)$: The probability that the detector outputs a signal in the i-th channel when radiation enters.
- $P(A_j \mid B_i)$: The probability that when the detector give a signal in channel i, the energy of the radiation belongs to energy bin E_j (**posterior probability**).
- $P(B_i \mid A_j)$: The probability that when radiation with energy in energy bin E_j enters the detector, the detector gives a signal in channel i

Associating the Equations 2.7 and 2.8 , $P(B_i)$ corresponds to the pulse height spectrum y_i, $P(B_i \mid A_j)$ to the response function r_{ij}, $P(A_j)$ to the energy spectrum ϕ_j, and $P(A_j \mid B_i)$ to the revised energy spectrum. However, since these values do not satisfy the three axioms of probability, normalization is necessary. The sum of the response function elements r_{ij} over i, denoted as f_j, represents the intrinsic detection efficiency and the normalized response function elements r'_{ij} are described by:

$$f_j = \sum_{i=1}^{m} r_{ij}, \quad r'_{ij} = \frac{r_{ij}}{f_j}$$

The normalized response function elements r'_{ij} satisfy the following equation:

$$\sum_{i=1}^{m} r'_{ij} = 1 \tag{2.8}$$

The normalized response function matrix R' (with elements r'_{ij}) and the detection efficiency matrix F (with elements f_j) are expressed as follows:

$$R' = \begin{bmatrix} r'_{11} & \dots & r'_{1j} & \dots & r'_{1n} \\ \vdots & \ddots & \vdots & \ddots & \vdots \\ r'_{i1} & \dots & r'_{ij} & \dots & r'_{in} \\ \vdots & \ddots & \vdots & \ddots & \vdots \\ r'_{m1} & \dots & r'_{mj} & \dots & r'_{mn} \end{bmatrix}$$

$$F = \begin{bmatrix} f_1 & 0 & \dots & 0 \\ 0 & \ddots & \ddots & \vdots \\ \vdots & \ddots & \ddots & 0 \\ 0 & \dots & 0 & f_n \end{bmatrix}$$

From Equation 2.6:

$$\vec{y} = R' \cdot F \cdot \vec{\phi} \tag{2.9}$$

Using the sum of the elements of $F \cdot \vec{\phi}$, denoted as $|\Phi_F|$, the normalized corrected spectrum $\vec{\phi}'$:

$$|\Phi_F| = \sum_{j=1}^{n} f_j \cdot \phi_j$$

$$\vec{\phi}' = \frac{1}{|\Phi_F|} \cdot F \cdot \vec{\phi} = \frac{1}{|\Phi_F|} \cdot \begin{bmatrix} f_1 \cdot \phi_1 \\ \vdots \\ f_j \cdot \phi_j \\ \vdots \\ f_n \cdot \phi_n \end{bmatrix} = \begin{bmatrix} \phi'_1 \\ \vdots \\ \phi'_j \\ \vdots \\ \phi'_n \end{bmatrix} \quad , where : \sum_{j=1}^{n} \phi'_j = 1$$

Therefore:

$$\vec{\phi} = |\Phi_F| \cdot F^{-1} \cdot (\phi')\vec{\phi} \tag{2.10}$$

Substituting into Equation 2.9:

$$\vec{y} = |\Phi_F| \cdot R' \cdot (\phi')\vec{\phi} \tag{2.11}$$

Each element of this equation is expressed as follows:

$$y_i = |\Phi_F| \sum_{j=1}^{n} r'_{ij} \cdot \phi'_j \tag{2.12}$$

Taking the sum of y_i over i gives:

$$|y| = \sum_{i=1}^{m} y_i = \sum_{i=1}^{m} |\Phi_F| \sum_{j=1}^{n} r'_{ij} \cdot \phi'_j = |\Phi_F| \sum_{j=1}^{n} \phi'_j \cdot \sum_{i=1}^{m} r'_{ij} = |\Phi_F| \sum_{j=1}^{n} \phi'_j = |\Phi_F| \quad \text{(Eq. 2.22)}$$

Therefore, normalizing Equation 2.11 using $|y|$ and defining the normalized pulse height spectrum as $\vec{y'}$, we get:

$$\vec{y'} = \frac{\vec{y}}{|y|} = \frac{|\Phi_F| \cdot R' \cdot \vec{\phi'}}{|y|} = R' \cdot \vec{\phi'} \tag{2.13}$$

From Equation 2.13, Equation 2.7 can be finally transformed into the following equation:

$$\begin{bmatrix} y'_1 \\ \vdots \\ y'_i \\ \vdots \\ y'_m \end{bmatrix} = \begin{bmatrix} r'_{11} & \dots & r'_{1j} & \dots & r'_{1n} \\ \vdots & \ddots & \vdots & \ddots & \vdots \\ r'_{i1} & \dots & r'_{ij} & \dots & r'_{in} \\ \vdots & \ddots & \vdots & \ddots & \vdots \\ r'_{m1} & \dots & r'_{mj} & \dots & r'_{mn} \end{bmatrix} \cdot \begin{bmatrix} \phi'_1 \\ \vdots \\ \phi'_j \\ \vdots \\ \phi'_n \end{bmatrix}$$

The elements y'_i, r'_{ij}, and ϕ'_j all satisfy the three axioms of probability. This normalization allows the application of Bayes' theorem. From Equation 2.8, the posterior probability $\phi_j^{a'}$ of the energy spectrum in energy bin E_j can be expressed as:

$$\phi_j^{a'} = \frac{\phi'_j \cdot r'_{ij}}{\sum_{k=1}^{n} \phi'_k \cdot r'_{ik}} \tag{2.14}$$

and $P(B_i)$ corresponds to the normalized pulse height distribution $y'_i = \sum_{k=1}^{n} \phi'_k \cdot r'_{ik}$,

$P(B_i \mid A_j)$ to the normalized response function r'_{ij}, $P(A_j)$ to the normalized energy spectrum ϕ'_j, and $P(A_j \mid B_i)$ to the revised normalized energy spectrum $\phi_j^{a'}$. In analysis, arbitrary values are used as the initial spectrum for the prior probability $P(A_j)$, and Bayesian revision is repeated. This way Bayes' theorem can be applied to unfolding. The initial guess, that is, the initial spectrum is assumed to be a white spectrum.

Bayesian estimation can be categorized into two main types, spectral type and sequential type. Spectral type Bayesian estimation has been verified in radiation measurement [168]. In ideal cases where the measurement error does not exist, Nauchi et al (2014) have proven the convergence of the estimation. Nevertheless, previous published studies as well as the studies mentioned in this thesis have yielded promising results [14]–[17], [135], [169]. In the spectrum type, the initial pulse height spectrum is measured and converted into the energy spectrum post-measurement [170]. Therefore, it is not applicable for real-time spectral unfolding, only post measurement. Specifically, this is because the spectral Bayesian estimation method performs Bayesian revision for each channel of the pulse height distribution after measurement and sums the revised energy spectra weighted by the count numbers in the pulse height distribution. This process is repeated a set number of times to estimate the energy spectrum. On the other hand, the sequential Bayesian estimation method performs Bayesian revision for each detected radiation count and estimates the energy spectrum. In this study, the sequential Bayesian estimation method was adopted because the goal is to display the energy spectrum in real time. The details of the sequential Bayesian estimation method are described in the next section. The improved method coined $k{-}\alpha$, is introduced in Section 5.3 and a more detailed analysis and verification in Section 5.8.2.

2.8.1 Sequential Bayesian Estimation

This study is based on the sequential Bayesian estimation, which repeats for every count the process introduced in the spectrum type, thus being fitting for use in real-time. This method is also known as the α method. This approach in radiation measurement states that the energy spectrum can be deduced iteratively, as the gamma-ray pulse-height data are received for each count by the detector. Its effectiveness in radiation measurement has been validated by the foundational work of Iwasaki [161] and Nauchi [168]. Building

on this foundation, our research group has developed the $k{-}\alpha$ method, which expedites the convergence process of determining the energy spectrum. Developmental details of this method have been described in by Kobayashi [170], Nishimura [135], Voulgaris [16] and Murata [14]. When radiation is detected by a detector at pulse height channel i, the posterior probability of the energy spectrum at channel j, $P(j|i)$, can be derived using the response function R_{ij}, according to Equation 2.15:

$$P(j|i) = \frac{R_{ij}\phi_j}{\sum_{j=1}^{n} R_{ij}\phi_j} \tag{2.15}$$

where $P(j|i)$ is the posterior probability of the energy spectrum at channel j, given that radiation is detected at pulse height channel i.

The posterior probability of the energy spectrum is estimated whenever a new signal is counted. The posterior probability becomes the next prior probability used in the sequential Bayesian estimation. In the spectrum type Bayesian estimation, according to Bayes'theorem, the posterior probability is described by Equation (2.16):

$$\phi_j^{(N+1)} = \sum_{i=1}^{m} \left(\frac{y_i \cdot (R_{ij} \cdot \phi_j^{(N)})}{\sum_{j=1}^{n} (R_{ij} \cdot \phi_j^{(N)})} \right) \tag{2.16}$$

where:

- $\phi_j^{(N+1)}$: the energy spectrum revised by the latest detected count
- ϕ_j^N : the N-th estimation of ϕ_j, the estimated energy spectrum before the last count (prior probability)
- N: the count number.

The process described by Equation 2.16 is carried out post-measurement. The obtained posterior probability is used as the prior probability in the next estimation turn. This iterative calculation is performed until the estimation converges, which is proven to converge in case of no measurement error as discussed earlier [168]. For the sequential type however, the unfolding process is continuously performed in real time during measurement, where revision is conducted with each count (each pulse-height signal at channel

i). The posterior probability becomes the prior probability for the new data during these successive estimations. A contribution for each new detected count at channel i is added, which can be expressed by the following equation:

$$\phi'_j = \phi_j + \frac{R_{ij}\phi_j}{\sum_{j=1}^{n} R_{ij}\phi_j} \tag{2.17}$$

where ϕ_j is the estimated gamma-ray energy spectrum before the last count, and ϕ'_j is the energy spectrum revised by the presently detected count. This process allows for real-time estimation, however, the time until convergence is achieved is significantly slow. Therefore the α method is used in order to achieve faster convergence [161]. For this method, the energy spectrum ϕ_j is derived from:

$$\phi'_j = (1-\alpha)\phi_j + \alpha\frac{R_{ij}\phi_j}{\sum_{j=1}^{n} R_{ij}\phi_j} \tag{2.18}$$

where:

- α: Index related to the effect of prior on posterior probability
- ϕ'_j: Energy spectrum revised by the latest detected count
- ϕ_j: Estimated energy spectrum before the last count

Because the convergence of this method is slow for experimental applications, an improvement was made by introducing a parameter k that changes depending on the count rate, thus naming it the k–α method [14], [135]. Comparisons and evaluations of this are described in Sections 5.3 and 5.8.2.

2.9 Dose Rate Estimation

In order to derive the dose rate (μSv/h), Equation 2.19 is utilized:

$$D = \sum_{j=1}^{n} \frac{d_j \cdot C_j}{S \cdot T} \tag{2.19}$$

where:

- D: Dose rate [μSv/h]
- j: Indicates the energy bin
- d_j: Effective dose rate per unit fluence [(μSv/h)/(cm^{-2}·s^{-1})] (flux-to-dose conversion coefficient)
- C_j: Number of counts
- S: Area of the surface of the detector [cm^2]
- T: Time of measurement [s]

The flux-to-dose conversion factor exhibits monotonical increase with increasing energy of gamma-rays. This allows for accurate measurements, providing advantage over detectors that are calibrated with one source. In order to calculate the theoretical dose rates for each radionuclide, the effective dose rate constants for every standard source and Equation are used [171], [172]:

$$D = \frac{\Gamma \cdot Q}{r^2} \tag{2.20}$$

where:

- Γ: Gamma-ray effective dose rate constant at 1 cm $\left[\frac{\mu\text{Sv}\cdot\text{m}^2}{\text{MBq}\cdot\text{h}}\right]$
- Q: Radioactivity [MBq]
- r: Distance of the source from the detector, in our case, the distance to the halfway point in the CsI(Tl) crystal

Effective dose rate constant Γ takes into consideration the energy and emission probability of gamma-rays for each different radiation source. Table 2.5 [171], [173] shows some standard gamma-ray sources and their correspondent gamma-ray effective dose rate constants.

Table 2.5: Effective Dose Rate Constants for Standard Gamma-ray Sources

Gamma-ray Source	**Effective Dose Rate Constant [μSv m^2 / (MBq h)]**
^{137}Cs	0.0779
^{60}Co	0.306
^{133}Ba	0.0637
^{22}Na	0.284

Radioactivity is the process by which unstable atomic nuclei decay, releasing energy in the form of particles or electromagnetic waves. This decay leads to the transformation of the original nucleus into a different element or a different isotope of the same element. The rate of decay of a radioactive substance is described by the decay constant, λ, which is related to the half-life, $T_{1/2}$, by the equation:

$$T_{1/2} = \frac{\ln 2}{\lambda} \tag{2.21}$$

The activity, A, of a radioactive sample, which represents the number of decays per unit time, is given by:

$$A(t) = \lambda N(t) \tag{2.22}$$

where $N(t)$ is the number of undecayed nuclei at time t. The number of undecayed nuclei as a function of time can be expressed by the exponential decay law:

$$N(t) = N_0 e^{-\lambda t} \tag{2.23}$$

where N_0 is the initial number of nuclei at time $t = 0$. Activity also decreases over time according to:

$$A(t) = A_0 e^{-\lambda t} \tag{2.24}$$

where A_0 is the initial activity. As mentioned earlier, the method of *G(E)* function, which has been used with NaI(Tl) among others detectors for monitoring radiation in the environment allows for dose derivation from the pulse height spectrum. Even though the dose is derived fast, no spectral information are obtained. Results of both unfolding and *G(E)* function methods have been compared and found in agreement in cases of NaI(Tl) scintillation detectors [148], [174], [175]. It has also been applied to CsI(Tl)

scintillation detectors [176]–[178] for ambient dose equivalent derivation and for $CeBr_3$ based scintillation spectrometers [179].

3 | Radiation Therapy Facilities

3.1 Introduction

This chapter introduces radiation therapy conditions during and after treatment, along with guidelines, detectors, and areas for improvement in radiation monitoring. It also discusses the key features, challenges, and requirements for effective radiation monitoring in clinical settings. A later section introduces Boron Neutron Capture Therapy (BNCT), which involves the irradiation of tissues enriched with ^{10}B using low-energy neutrons. It is an advanced cancer treatment that utilizes the neutron capture reaction of boron to selectively destroy malignant cells.

3.2 Radiation Therapy Facility Guidelines and Protocols

3.2.1 Radiation Worker Associated Guidelines

Radiation protection and safety for workers are governed by frameworks of guidelines established by international bodies such as the International Atomic Energy Agency (IAEA) and the International Commission on Radiological Protection (ICRP). These guidelines are implemented through national regulatory bodies, such as Japan's Ministry of Health, Labor, and Welfare (MHLW) in the case of Japan, which adapt and enforce these recommendations to ensure optimal safety practices in various occupational settings, including the medical field and industries involving radioactive materials [91].The use of radioactive sources, accelerators, and radiation generators for therapeutic purposes, as well as X-ray generating equipment for diagnostics and interventions, are common practices that can result in high radiation doses to workers. Equipment engineers and maintenance workers are often referred to as itinerant workers. In general, these workers include radiological medical practitioners, medical physicists, medical radiation technologists, and industrial radiographers [25]. As briefly introduced in Chapter 2, to minimize exposure, apart from shielding and proper staff training, passive and active monitoring systems, in the form of dosimeters or radiation monitors are necessary to ensure safety for patients and staff alike [8]. While guidelines for training standards and requirements tend to vary by country or region, global education initiatives and sharing of knowledge are being coordinated,

mainly by the IAEA [7].

Guidelines are in place for radiation workers in both medical and non-medical fields, such as those involved in decontaminating objects contaminated with radioactive materials (e.g., soil, waste). These guidelines typically involve minimizing exposure by following the ALARA (As Low As Reasonably Achievable) principle introduced by the ICRP, measuring, monitoring, and recording doses (for field workers if ambient dose rate exceeds 2.5 μSv/h), and managing exposure limits. Limit for male and non-pregnant female workers is 100 mSv/(5 years) or 50 mSv/ (1 year). Such records may be kept as long as up to 30 years. This yearly limit of occupational exposure for example, corresponds to the IAEA safety standard: GSR Part 3 Req. 19. [180]. In this publication, exposure is generally categorized as public, occupational and medical. This is part of 52 Requirements, of which parts 34 - 42 are associated with medical exposure [180]. More publications by the IAEA currently in use today, like the "Fundamental Safety Principles", aim to optimize protection, limit risk to individuals and justify and optimize protective actions in order to reduce existing and unregulated radiation risks [181].

Specific publications for workers and occupational exposure exists, with the recent "Radiation Protection and Safety in Medical Uses of Ionizing Radiation" [8], "Occupational Radiation Protection" [25] as well as the proceedings "Occupational Radiation Protection: Enhancing the protection of workers - gaps, challenges and developments" which outline comprehensive safety standards aimed at minimizing radiation exposure and protecting workers [13]. In this medical setting related to radiotherapies, workers must undergo regular training and education to stay updated on the best practices in radiation safety. This includes the proper use of protective equipment, consistent dosimeter usage, understanding the risks associated with occupational exposure, and adhering to the established dose limits [13]. Some key points include the fact that to minimize external exposure from naturally occurring radioactive materials (NORM), implementing workplace protection measures like controlling occupancy time or adding shielding is effective [25]. For materials with low activity concentrations, which typically result in gamma dose rates of only a few μSv/h, restricting access by storing these materials in less occupied areas may suffice. However, in areas with higher activity concentrations, physical barriers and warning signs are required. The most common form of implementation of individual monitoring for the

assessment of external exposure is an integrating personal dosimeter.

In general, choices of type of personal dosimeters depend on the exact radiation conditions of the workplace, such as energy, directional distribution and expected dose rate values. Dosimeters like those mentioned in 2.4, like thermoluminescent dosimeters, optically stimulated luminescent dosimeters, photoluminescent glass dosimeters or photographic film dosimeters can be applied for gamma-ray fields and provide information on personal dose equivalent [25]. Given the diversity of radiation fields, beta-photon dosimeters. extremity focused dosimeters, eye lens dosimeters and neutron focused dosimeters are employed for workplace monitoring instruments for the assessment of external exposure. In addition, biokinetic models for the assessment of internal exposure are designed. In radiation fields in the medical and industrial field, sudden and significant increases in dose, is not something all dosimeters can handle, leading to inaccurate readings. For this reason active warning dosimeters are used in addition to main dosimeters, providing auditory warnings in such cases [25].

3.2.2 Conditions of Various Radiation Therapy Facilities

In reactor facilities, gamma-ray monitoring needs to consider gamma-rays of energies up to 10 MeV, even though a normalized measurement level is up to 3 MeV [131]. Meanwhile, as mentioned in the introduction, a common maximum energy range of many commercial detectors and monitors is 3 MeV in the medical radiation setting. This is mainly because this range covers radiopharmaceuticals as well as more complex processes such as decay gamma-rays in medical linear accelerator (LINAC) facilities for example, which can extend to 3 MeV and even beyond [10]. High-energy therapeutic photon and electron beams, commonly used in LINACs, can induce nuclear reactions that produce a broad spectrum of neutrons, particularly thermal and resonance neutrons (see Section 2.1.2). Nuclear reactions can occur in the collimators, targets, and filters of the accelerator. The energy spectra of these neutrons generally peaks in the range of several hundred keV, with significant contributions from thermal and resonance energies. Production of radioisotopes with half-lives of a few hours, can lead to additional exposure of the medical radiation workers [182]. These photonuclear reactions may lead to medical radiation worker exposure post treatment from decay-emitted gamma-rays or beta-rays or in the case of radiation leakage

at any point while operation is underway [6].

For LINACs operating at energies above 10 MV, contribution of neutrons and the subsequent capture gamma-rays needs to be considered, as shown by comprehensive neutron and photon dose equivalent investigations conducted at various points in such setups [183]. The neutron spectrum that is formed when operating at such energies, degrades from interactions and scattering with the various surfaces [109]. Since therapeutic beams over 10 MV are commonly used, a simulation-based investigation of radiological safety found that dose rates remained safely below the annual occupational limit of 20 mSv/year. This indicates that workers operating LINACs, as well as maintenance staff, do not face critical hazards [184]. However, with routine work, exposure levels may still increase significantly [130]. Dosimetry studies to understand the conditions in monoenergetic neutron fields formed from accelerator operation, have found prompt and secondary gamma-rays of energies up to 10 MeV [185]. Neutron capture processes can lead to the production of gamma-rays with energies in the range of 5 - 10 MeV [186]. Common shielding materials for such radiation include concrete and polyethylene, which moderate neutrons by scattering and reducing their speed before capture. Hydrogen is particularly effective at slowing neutrons due to its similar mass. Boron and cadmium are effective for thermal neutron capture because of their large cross sections.

Monitoring is also necessary when considering decommissioning of radiation therapy facilities, such as in the case of cyclotron based proton therapy, where specific radionuclides, like ^{152}Eu and ^{60}Co, need their activity to be monitored and recorded. They are a result of activation of materials within the treatment environment. Various detectors, such as $LaBr_3$, $CeBr_3$ and Ge spectrometers are used to measure the specific gamma-ray peaks. Activation of materials, like concrete, can occur from neutrons originating either from the device's nozzle or the patients themselves. Additionally, dose rate monitors like NaI(Tl) survey meters and ionization chambers, are used for radiation exposure assessment in both accelerator and treatment rooms. These monitoring systems are essential for evaluating residual radiation and ensuring proper radiation management of a facility until decommissioning [5].

Examples of high-energy gamma-ray spectra during accelerator operation can be found in investigations by various teams and one example is the phenomenon of skyshine,

that occurs in neutron utilizing facilities. This phenomenon is characterized by radiation leaks outside the facility, particularly from (n,γ) reactions [187], [188]. At facilities like OKTAVIAN (Osaka University, Japan), which hosts a DT 14 MeV intense neutron source [189], studies have measured secondary gamma-ray skyshine to understand the mechanisms of radiation escape and its impact on surrounding environments. High Purity Germanium (HPGe) detectors have been used to measure gamma rays up to 10 MeV, identifying specific nuclear reactions contributing to the leakage. This phenomenon occurs due to atmospheric scatter, ground reflection, and direct emissions from the facility. Shielding design and continuous monitoring to minimize external exposure to workers and the public are mandatory so that radiation levels remain within safety limits. Such evaluations are essential for the safe operation of high-energy radiation facilities, where continuous efforts are needed to minimize unintentional gamma-ray exposure [190], [191]. In order to adhere to the ALARA guideline, such contributions of primary and secondary gamma-ray skyshine, which can be present in the case of neutron irradiation or LINACs, ideally need to be considered and measured [192].

3.3 Guidelines and Monitors for BNCT

Similarly to other radiation therapy modalities, BNCT facilities are designed so that they adhere to the principle of ALARA. Apart from material selection, design and shielding, minimizing and monitoring dose to workers and patients is key to achieve this [24]. Even though set standards and strict guidelines have not been established explicitly only for BNCT, BNCT treatments follow, and alter where necessary, guidelines and protocols borrowed from other radiation therapies. Many similarities exist, while at the same time BNCT has various unique intricacies. Currently, the European project aims to establish a Code of Practice for BNCT dosimetry [193]. In practice, BNCT treatment facilities issue personal dosimeters (both universal and ring-type) to all staff, including radiotherapists and visitors such as nurses and patient relatives, in line with typical radiotherapy procedures. However, patients undergoing BNCT are exempt from these monitoring protocols, and their exposure is managed post-treatment through activation measurements of residual radioactivity [194]. Accurate radiation monitoring is essential for adhering to these protocols and for adjusting treatment parameters in real time. The IEC (International

Electrotechnical Commission) is developing international standards for BNCT treatment devices. The IAEA has published some recommendations for BNCT dosimetry and treatments. When a BNCT treatment device is approved for pharmaceutical affairs, guidelines are established and published by the Ministry. In Japan, BNCT device irradiation control is managed by measuring the current of the proton beam, not the generated neutrons. Neutron measurement is practiced in some countries but not adopted in Japan due to accuracy concerns. Regarding dosimeter usage, currently in BNCT facilities, mainly glass badges and pocket dosimeters are being used for medical staff radiation monitoring. Radiotherapists are typically equipped with finger dosimeters and personal dosimeters issued by the respective institutes, ensuring that their exposure remains well below regulatory limits. Thus far, radiation doses to staff members during BNCT treatments have remained within acceptable thresholds [194]. As mentioned in the previous section, the common upper energy range of many commercial detectors is 3 MeV. However, in BNCT, where neutrons are also present during irradiation, high energy gamma-rays are emitted. These gamma-rays need to be considered in order to adhere to the ALARA principle.

In BNCT facilities, interior surfaces are covered with lithiated or boronated plastic to efficiently absorb neutrons and walls are constructed with heavy concrete to absorb secondary gamma radiation [195]. Considerations regarding walls of BNCT facilities account for thermalized neutrons that can be reflected, and may result in additional dose delivered to the patient [24]. Regarding continuous monitoring of the condition in the treatment room, a gamma dose rate monitor alerts when residual dose rates are elevated [195]. The dose rate inside the treatment room needs to be able to be confirmed from the control room and operation is always indicated by lights [24]. It is important to measure both the flux at the patient position, but also the exact spectral conditions of the radiation field. Beam monitoring systems and back ups like fission chambers and GM tubes are in place, similar to other forms of radiotherapy [196]. Monitoring of the patient dose and knowledge of the dose distribution in the therapy room and awareness of potential leaking is necessary. It is known that typical neutron survey meters are not usable for example, due to significantly increased dose rates close to the collimator. Additionally, in the equipment room of the facility ionization chambers and HPGe detectors should be stored if needed [24].

Neutron flux can be measured using non-real-time methods, such as activation-based measurements. Real-time methods used in other therapies may be challenged by the high intensity of BNCT conditions. This has led to the development of LiCaF detectors with polyethylene moderators, expanding their sensitivity from the thermal neutron range, where LiCaF is primarily applicable, to also include epithermal and fast neutron ranges. The ability to calculate neutron flux and dose equivalents for all three major neutron ranges in real time within a water phantom is promising. [197]. Tanaka et al. [198] developed a real-time thermal neutron monitor array specifically for use in BNCT. The detector system combines an organic scintillator with a quartz fiber coated in polyimide. The scintillator is coupled with a ^{6}LiF neutron converter for gamma-ray discrimination and measures thermal neutron flux up to 10^{9} n/cm^{2}/s and performs two-dimensional neutron distribution measurements by employing a scanning method. The detector array is connected to a photomultiplier tube (PMT), with signals processed through an ADC and a scaler and is applicable both in nuclear reactor and accelerator-based neutron sources. $LiCaAlF_6$ based neutron spectrum viewing measurement system efforts, using PMT coupled optical fibers with digital pulse processing integration efforts have also been made [199]. Experimental measurements of neutron spectra is possible with Bonner spheres, with paraffin or polyethylene for thermal and epithermal neutron measurements specifically. The response is integrated over a specific energy range, determined by the activation cross section and the local neutron spectrum. Different activation materials are used to cover various energy intervals, and the measured reaction rate reflects the product of the neutron fluence rate [196], [200]. In line with efforts to improve monitoring and quality assurance in BNCT, a neutron energy spectrometry device (10^{-8} MeV to 1 MeV) using the CsI self-activation method is being researched for ABNS BNCT fields. Consisting of CsI scintillators combined with polyethylene (neutron moderation), Cd and B_4C filters (energy level dependent neutron absorption), the reaction ^{127}I(n, γ) $\rightarrow$ ^{128}I is utilized. ^{128}I (half-life 1500 seconds) decays by emitting β-rays, which can be detected, providing information about neutron intensity. This multi CsI scintillator utilizing setup managed to display neutron spectra after around 900 s [166]. Overall, detectors in BNCT setting are used for various purposes, such as assessing neutron dose during treatment and boron distribution of boron through prompt gamma-ray measurement [201]. Other investigations like those conducted by Kim et al. (2020), recommending LYSO and Cd:Te detectors

through preliminary results[148]. Additionally, owning to their applicability in thermal neutron capture, Cd containing detectors like CdTe have been applied in radiation therapy monitoring, including BNCT. [202].

3.3.1 Radiation Field During and After Treatment

Radiation monitoring for BNCT is focused on measuring neutron and gamma-ray components not just in and out of the treatment room but also the High Energy Beam Line (HEBL) and accelerator rooms, in the case of ABNS BNCT. Because the radiation field in these rooms is a mixed field of neutrons and gamma-rays and with intensity higher than capabilities of many commercial monitors, it is challenging to measure and monitor it completely. The high-energy gamma-ray component arises from neutron capture reactions, while the neutrons cover a wide range, mainly at the epithermal range where most neutron monitors are not well designed to handle [24]. Due to this, there is a need for monitors with good spectral response and that are able to tell apart the gamma-ray and neutron component contributions.

While great progress is made on Accelerator Based Neutron Sources (ABNS) for BNCT, such as proton, deuteron and even non-spallation production by smaller accelerators [24] , reactor based facilities generate neutron beams from the fission of ^{235}U in the reactor core. These beams contain not only neutrons of various energies but also gamma rays, which can deliver significant doses to healthy tissue [200]. Annihilation gamma-rays from the reactions between heavy materials and 2.22 MeV gamma-rays by $^{1}\mathrm{H}(n,\gamma)^{2}\mathrm{H}$ reactions are present [72]. Regarding ABNS for BNCT, unwanted fast neutron and neutron capture reaction generated gamma-rays are present. Glass dosimeters are one method utilized to understand the separate contributions of neutrons and gamma-rays to the patient in the treatment room. Overall, due to the mix of contributions the patient received in terms of dose, many methods and detectors like TLDs, gel dosimeters and others are used or and are continuously improved to monitor dose distribution [203]. Even though the energies of most commonly used radioactive sources are < 3 MeV, in BNCT, high energy gamma-rays are emitted during capture of thermal neutrons, reaching up to 8 MeV, some even higher. This is one of the reasons that in this thesis, the measurement goal is set at 10 MeV.

Regarding the beam, to optimise its properties and reduce unwanted neutrons and gamma rays, various materials (moderators, filters, attenuators) are used. These materials interact with the neutron beam, either slowing down neutrons, deflecting them, capturing them, or allowing preferred energy neutrons to pass through. High-energy neutron moderators include materials such as Al, Al_2O_3, D_2O, S, AlF_3, Fe, Be, BeO, Ti, PbF_2, Teflon, and Fluental. Gamma-attenuating materials include Bi, Ar, Pb, and PbF_2. Slow neutron eliminators can be materials such as ^{10}B, Cd, and ^{6}Li. [196], [200].

The Helsinki BNCT facility uses several dosimetry techniques to measure neutron and gamma radiation. The primary method for neutron flux dosimetry is neutron activation, where diluted Al-Au and Al-Mn activation foils are used to characterize the neutron beam and ensure daily quality control. The activity of the foils is measured with a high-purity germanium detector (HPGe) equipped with an integrated Cryo-cooling system and DSPEC-50 multi-channel analyzer, designed for high-resolution gamma spectrometry in the 40 keV to 2000 keV range [195]. For neutron and gamma dose measurements, the paired ionization chamber method is also employed, using a methane-based, tissue-equivalent (TE) gas-filled Exradin T2 chamber alongside an argon-filled magnesium-walled Exradin M2 chamber. This method is used for estimation of absorbed doses in tissues.

Neutrons are not generated while medical personnel are in the irradiation room, thus there is no need to consider exposure to neutrons for medical personnel before or after operation of the accelerator. During operation there are few neutrons over 1 MeV of energy [204]. Epithermal neutrons are categorized between 0.5 ev and 10 keV according to Sauerwein, and are most effective in treating a variety of tumour types [196]. Regarding the neutron beam characteristics, it can also vary depending on the target tumor type such as mainly thermal-epithermal for superficial cancers and epithermal for deep-seated cases[205]. Report on deliberation on the development of the BNCT Neucure machine, referring to the 2001 IAEA guidelines, set epithermal neutrons as between 0.5 eV and 40 keV. Using moderators, like lead or iron, fast neutrons are moderated down to epithermal neutron ranges [204]. However, the latest Advances in BNCT, address the absence of strict and universal definition, but set the standard for BNCT as below:

Table 3.1: Definition of neutron energy ranges used in BNCT. Courtesy of IAEA (2023) [24]

Range Name	**Neutron Energy**
Thermal	< 0.5 eV
Epithermal	0.5 eV - 10 keV
Fast	> 10 keV

Kakino et al. (2024) is among the comprehensive studies that measure and simulate the neutron and gamma-ray fields during BNCT operation. The study validates a Monte Carlo model of the entire treatment room, focusing on the distribution of thermal, epithermal, and fast neutrons, as well as gamma-ray dose rates, to assess whole-body doses and organ-at-risk (OAR) exposure. The findings highlight the significance of out-of-field radiation, which can increase doses even outside the direct treatment area [206]. While the main focus of many studies is to characterise the dose received by the patient, some studies have investigated the exposure of staff in various conditions and situations. Table 3.2 shows a typical BNCT-style beam characterized by Jahari et al. [207] and used in the study by Golshanian et al. [208] to define neutron and gamma sources for medical staff dose exposure calculations. They found that in emergency situations the medical worker's effective dose depends on their position and the specific situation during BNCT treatment. Critical positions in the therapy room varied from 4.7 mSv/s, to 25.5 mSv/s, emphasizing the need for proper radiation protection measures, including personal protective equipment, controlling access to the irradiation room, and potentially developing automated systems to remove patients in emergency conditions. Another find of their work showed that the presence of a patient was shown to reduce the absorbed dose for medical staff.

Table 3.2: Parameters typical of a BNCT source. Credit to [207], [208]

Source Strength ($\times 10^{10}$ s^{-1})										
Beam radius (cm)	0-1	1-2	2-3	3-4	4-5	5-6	6-7	7-8	8-9	9-10
Thermal	0.01	0.03	0.04	0.05	0.05	0.05	0.06	0.07	0.08	0.10
Epithermal	0.28	0.80	1.14	1.35	1.53	1.62	1.68	1.73	1.79	1.83
Fast	0.08	0.24	0.34	0.41	0.47	0.51	0.54	0.57	0.60	0.62
Total Neutron	**0.37**	**1.07**	**1.52**	**1.81**	**2.05**	**2.18**	**2.28**	**2.38**	**2.47**	**2.55**
Gamma	**0.02**	**0.06**	**0.07**	**0.05**	**0.04**	**0.03**	**0.02**	**0.02**	**0.01**	**0.01**

Based on calculations conducted with MCNP6, borated concrete as a wall material

significantly reduces the thermal neutron flux and overall radiation levels in the room, thus it is favored for the treatment room walls since activation and overall doses are reduced, ensuring safer environmental conditions [209]. Lead is used to shield gamma rays produced by the nuclear reactions induced, while polyethylene serves to block neutrons. At BNCT irradiation sites, the collimator incorporates polyethylene infused with lithium fluoride to lower neutron doses outside the targeted area, to minimize unnecessary radiation exposure for staff and patients [204].

As inroduced earlier, neutron activation is commonly utilized to calculate neutron flux [195]. Paired ionization chamber method is also utilized to estimate absorbed doses from neutron and gamma-rays in tissue. Regarding BNCT and neutron activation of materials, for in-room dosimetry, the following neutron activation reactions are generally considered: $^{27}\mathrm{Al}(n,\gamma)^{28}\mathrm{Al}$, $^{40}\mathrm{Ca}(n,\gamma)^{41}\mathrm{Ca}$, $^{58}\mathrm{Fe}(n,\gamma)^{59}\mathrm{Fe}$, $^{41}\mathrm{K}(n,\gamma)^{42}\mathrm{K}$, $^{26}\mathrm{Mg}(n,\gamma)^{27}\mathrm{Mg}$, and $^{23}\mathrm{Na}(n,\gamma)^{24}\mathrm{Na}$ [209]: Materials like aluminum fluoride $\mathrm{AlF_3}$ in the Beam Shaping Assembly (BSA) undergo neutron activation, leading to the production of radioactive isotopes such as ^{28}Al. The walls of the treatment room, especially if made of ordinary or borated concrete, can become activated by neutrons, producing isotopes like ^{41}Ca, ^{24}Na, and ^{59}Fe. Regarding air activation, neutron capture by argon (^{40}Ar) in the air produces the radioactive isotope ^{41}Ar, which contributes to the residual radioactivity in the treatment room. Many studies have investigated patient activation. For example, neutron capture reactions in the patient's tissues and fluids, such as $^{37}\mathrm{Cl(n,}\gamma)^{38}\mathrm{Cl}$ in chloride, can lead to the activation of biological elements, resulting in residual radioactivity in the patient's body after treatment.

4 | Objectives

4.1 Main Objectives of this Research

As mentioned in previous chapters, the primary goal of this study is to develop and validate a portable gamma-ray detector capable of real-time measurement of both the energy spectrum and dose rate of gamma rays. Initially, the project aims to confirm the prototype's accuracy in spectral reconstruction and dose estimation for gamma rays with energies up to approximately 3 MeV. This value was selected because it is common for many gamma-ray survey meters or dosimeters, reflecting the typical gamma-ray energies found after operating machines like particle accelerators for therapy, as well as from standard gamma-ray sources and radiopharmaceuticals. Verifying this capability is the main focus of this thesis and the corresponding publications. Following this, the research explores extending the device's measurement range to 10 MeV and introduces the challenge of neutron discrimination, specifically to address needs in neutron-based therapies like BNCT. To achieve these goals, the research is broken down into several smaller steps, each structured around key objectives.

Following the initial design and material selection for a prototype combining a CsI(Tl) crystal, a multi-pixel photon counter (MPPC), and a multi-channel analyzer (MCA), various post-measurement investigations were conducted. These investigations used a resampling methodology to confirm the feasibility of the improved sequential Bayesian estimation, the k–α method, to measure gamma-ray energy spectra and dose rates in real time. The studies included Monte Carlo simulations and experiments with standard gamma-ray sources to create a response function, as well as comparisons of scintillator shapes to determine the optimal size for performance and portability, focusing on detection efficiency and energy resolution. Within this scope, energy spectrum unfolding, dose rate estimation, and comparisons with theoretical values were also performed.

Verification of the measurement capabilities up to 3 MeV for radiation therapy applications was conducted. Extending the measurement range to 10 MeV was explored, as gamma rays with energies above 3 MeV are produced due to neutron-induced reactions whenever neutrons are present as introduced in the previous chapter. Simulation and ex-

perimental methods were used to develop an extended response function, up to 10 MeV. Additionally, initial discussions are made to explore the prototype monitor's use in mixed fields of neutrons and gamma-rays. This involves considering changes to the detector and shielding setup, response function, and other detector components.

The successful completion of these milestones and meaningful discussions of the challenges mark a significant advancement in radiation detection technology. Complementary to the investigations around the prototype monitor, in this research I compile the theory and background that is involved with scintillation detectors, gamma-ray and neutron detection as well as the conditions and guidelines surrounding radiation therapies and briefly BNCT as well, which have only recently starting to be set properly. Thus, apart from the points concerning the prototype monitor, this thesis aims to be a solid point of reference for all things considering similar detection devices as well as rules and guidelines for radiation therapy facilities exposure risk considerations.

4.2 Verification of Usability

Following the design concept of the prototype monitor, a key objective is verifying its usability in various scenarios. All the early verifications and evaluations of the potention of sequential Bayesian estimation were conducted using the resampling methodology using actual experimentally obtained data but performing estimation "real-time" post measurement, therefore experimental validation is necessary in true real-time scenarios to verify the usability of the monitor. Usability covers both accuracy of dose rate values, accuracy of energy spectrum unfolding and speed of convergence to a stable value for both. After verifying the $k{-}\alpha$ method through the resampling method, replacing the MCA component to the DP5 allowed for digital pulse processing and true real-time measurement. This meant comparing the true real-time measurement values to the resampling ones to verify the effectiveness of the $k{-}\alpha$ method. Experiments for the purpose of response function creation and verification experiments were mainly conducted using the gamma-ray sources available at the OKTAVIAN laboratory at Osaka University, such as ^{133}Ba, ^{137}Cs, ^{60}Co, and ^{22}Na.

4.3 Concept of Application in Radiation Therapy Facilities

A major part of this thesis discusses the conceptual application of the prototype monitor in a radiation therapy setting. Specifically, following the verification of the methodology and accurate measurements under various conditions (described in Chapter 5 and the introduction of key aspects such as current guidelines for different radiation therapies, including BNCT (in Chapter 3, the usability of the monitor was verified for gamma rays up to around 3 MeV. This is detailed in Section 6.2 and was achieved by analyzing gamma-ray spectra up to 2.75 MeV through irradiation of aluminum foil with DT neutrons, followed by comparison measurements with established detection technologies such as NaI survey meters and High Purity Germanium (HPGe) detectors. the former for comparison and the latter for theoretical dose rate calculation. The response function also is extended to 10 MeV and challenges in future applications of the monitor are discussed.

Part II

Development of the Prototype Monitor

5 | Design and Development of Prototype Gamma-ray Monitor

5.1 Introduction

The design flow of this prototype gamma-ray monitor involves the journey from conceptualization and design, to comprehensive measurement verifications. This chapter outlines the development process, including overview of the key components and the reasons for their selection, feasibility studies of the application of sequential Bayesian estimation with a scintillation detector and further experimental investigations. First the material used in the making of the scintillator are introduced and their selection is justified. Then, the $k{-}\alpha$ method is explained. The differences between the resampling and true real-time estimation is broken down. The response function creation methodology that is followed throughout this research is then explained, before delving into feasibility studies, crystal size evaluations and true real-time experimental verifications.

5.2 Overview and components

The current configuration of the prototype gamma-ray monitor consists of:

- a CsI(Tl) scintillator (provided by I.S.C.Lab. CO., LTD, Osaka, Japan)
- an MPPC [70] (C14047, Hamamatsu Photonics, Hamamatsu, Japan)
- a DP5 digital pulse processor (DPP) [86] or an MCA8000D multichannel analyser (Amptek Inc, Bedford, MA, USA) [210] in place of the DP5 in the case of resampling estimation
- an amplifier (ORTEC571/579 ORTEC/AMETEK, Oak Ridge, USA)
- a power supply, GWINSTEK GPD-33036
- a Personal Computer, for real-time viewing

As discussed earlier, the primary objective of this research is to cater to medical radiation workers and enhance their understanding and awareness of radiation exposure.

For this purpose, the monitor is designed to be lightweight and wearable, with the final size and weight estimated to be similar to a modern smartphone (∼250 g). The reason for the connection to PC instead of a LED monitor display is because currently the device is in the prototype stage. Figure 5.1 shows a simple conceptual design of the portable configuration of the monitor. As will be discussed in Sections 5.8.3 and 7.2.2, for enhanced portability and good performance, a non cubic scintillator is chosen, similar to the one EMF Japan [211], a company providing radiation detection solutions, is using in their development for future commercial use, showcased briefly in Appendix A.

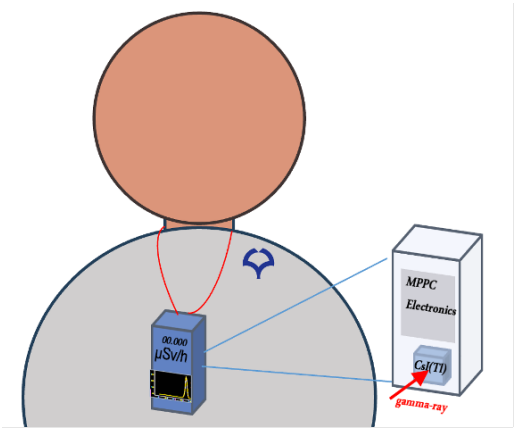

Figure 5.1: Proposed shape and configuration of the final conceptual design of the portable form of the prototype monitor

Each component plays a crucial role in detecting and processing radiation signals. The CsI scintillator converts gamma rays into scintillation light, as described in Chapter 2 and the MPPC detects this light. The analog signal produced by the MPPC module is amplified to a range of 0 - 10 V and is pulse-shaped using the amplifier. This input signal is discriminated by pulse height and counted by the MCA, either the MCA8000D or the MCA function of the DP5, across 1024 or 8192 channels respectively, visualising the pulse height spectrum. When using the DP5 digital pulse processor, it processes the signals to provide real-time dose rate and unfolded energy spectrum data. Details on the DP5 application can be found in Sections 5.5 and 5.9. To mitigate the mechanical noise occurring on the low-energy side, the lower 3% of the energy range is cut off by adjusting the MCA or DP5 settings, accessible from the dppMCA software. The MPPC array with specifications detailed in table 5.1 has 64 (8×8) output channels but becauseonly one output signal from the scintillator is required, the summed signal is extracted using the

connector board seen in Fig. 5.2.

Table 5.1: Basic Specifications of C14047-Series [79]

Number of Channels	64 ch (8 × 8)
Dimensions	38 × 90 mm + MPPC array + A14048
Power Consumption	Analog Circuit: ±200 mA Digital Circuit: +50 mA
Voltage	Analog Circuit: ±1.65 V (±50 mV) Digital Circuit: +5.0 V (±0.1 V)

Throughout the course of this research various sizes of CsI(Tl) crystals were investigated. The square configuration (2.6 × 2.6 × 2.6 cm^3) was chosen for the majority of experiments, mainly for its ease of use and simplicity of Monte Carlo simulation setup. Subsection 5.8.3 presents a more detailed analysis into results obtained from various sizes of scintillators. A diagram of the setup for true real-time estimation is presented in 5.2, where the main components can be identified, with the key difference from the schematic introduced in Figure 5.5 being the digital pulse processor DP5, which replaces the MCA of typical scintillation detector applications to allow for real-time estimation.

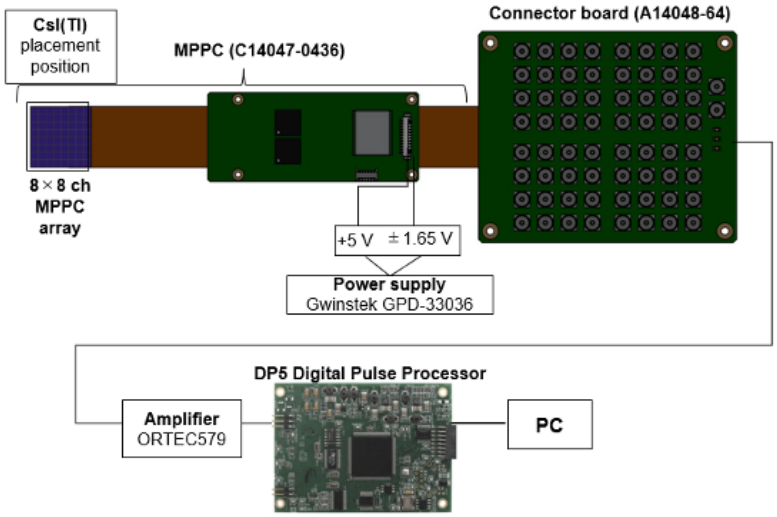

Figure 5.2: Schematic overview of the complete prototype monitor setup. (MPPC, C14047-0436, Hamamatsu photonics, Hamamatsu, Japan), and DP5 (Amptek Inc, Bedford, MA, USA)

The components chosen were so that the design would be compact and lightweight, making it practical for use by medical personnel, have sufficient detection efficiency and

good energy resolution, allowing for accurate reproduction of the gamma-ray energy spectra while being capable of measuring across a wide dynamic range. This range had an initial energy limit of 3 MeV, as this corresponds to a high enough gamma-ray energy range emitted by radioactive nuclides generated after the operation of particle radiation therapy accelerators or in the production of medical radioisotopes. A diagram of the CsI(Tl) - MPPC coupling is presented in Figure 5.3, where the main components can be identified. This coupling combination of CsI(Tl) - MPPC array and connector board - MCA/DP5 is the same for all evaluations reported in this chapter, while different CsI(Tl) crystal shapes are also evaluated.

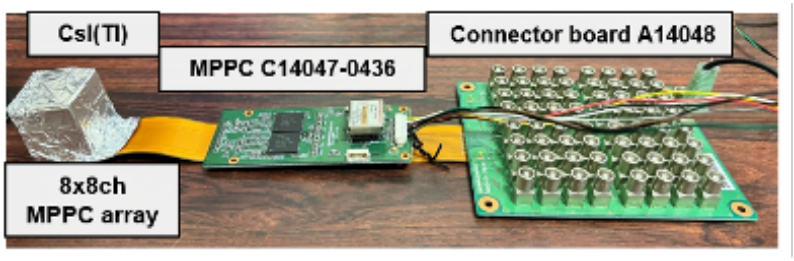

Figure 5.3: Annotated photograph of the main CsI(Tl) - MPPC scintillator setup.

In all instances described in the following sections, the CsI(Tl) scintillator is wrapped in white Teflon tape, black vinyl tape and lastly with aluminum. Teflon tape helps reduce light losses [34] and has been used with scintillation detectors like CsI(Tl) [53], [212]. Such wrapping aids in shielding light coming into the crystal [135]. The setup is always shielded from ambient room light [18] with a black cloth during measurement. For the optical coupling of the MPPC light receiving array and the scintillator, OKEN 6262 optical grease is carefully applied, prior to crystal wrapping in the tapes mentioned above. The specific type of optical grease has been used in such applications of scintillators before and has even been deemed optimal among others in certain cases [78]. As will be discussed in Chapter 3, the target energy range for all the applications in this chapter is 3 MeV and following guidelines for portable radiation monitors, a target dose rate range in development, is from background levels (0.05 Sv/h) to 1 mSv/h, with a final goal extending up to 10 mSv/h. Maximum count rate also designed to finally be at around 10,000 cps.

5.3 The k-α Method (Murata, Voulgaris et al., 2024)[14]

Expanding upon the foundation introduced in 2.8.1, this Section introduces the improved sequential Bayesian estimation method, named the k-α method. As discussed, in section 2.8.1, with the α method, by adjusting the value of α, convergence can be accelerated. However, there are instances when the energy spectrum has poor accuracy or the estimated spectrum does not converge at certain count rates. In the α method, a revision occurs with each detected count. For example, for $\alpha = 10^{-2}$, one percent of the total flux is revised per count, meaning after 100 counts ($= 1/\alpha$), a full revision (one round) is completed. With several rounds, the revision will eventually converge. In contrast, for $\alpha = 10^{-4}$, one round requires 10,000 counts, slowing the convergence. Thus, a larger α value speeds up convergence but may lead to instability. In simple terms, convergence can be described as the estimation (spectrum and dose rate) reaching the stable and correct value. In practice, the α value must be adjusted appropriately, sometimes larger, sometimes smaller, based on the count rate. A higher count rate requires a smaller α, indicating a suitable α value exists for each condition. While $\alpha < 10^{-3}$ is generally preferable, $\alpha = 10^{-4}$ slows convergence considerably. The continuous adjustment of α during measurement needs to be considered. For instance, if $\alpha = 1/N$, with N being count number, then $\alpha = 0.5$ after the second count and $\alpha = 0.33$ after the third. At N, the revision rate is $1/N$. While $\alpha = 1/N$ seems suitable, at large N (for instance, 10^6 counts), then $\alpha = 10^{-6}$ which results in a revision ratio of 0.001%, which is not feasible for application. To reiterate:

- when α is large, the energy spectrum is updated significantly as counts increase. While this is preferential early on in the estimation process, it leads to imprecise estimates later on
- when α is small, the energy spectrum is updated at a slow rate, improving accuracy to some extend but the convergence is too slow for application.

This indicates that α should ideally be high early on to accelerate the convergence and then decrease in order to stabilize at a constant value. Therefore the improvement to the α method was found to be possible by describing α as an index defined by a parameter k and the count number N. In this method, α initially decreases as $1/N$, but is then controlled

as it reaches a smaller value. Specifically, α changes continuously as follows:

$$\alpha = \frac{1+kN}{N} \quad (\alpha = 1, \text{ if } N < \frac{1}{1-k}) \tag{5.1}$$

where k is the convergence control factor ($0 < k < 1$). This method, coined $k{-}\alpha$ method, accelerates convergence while preventing an excessive decrease in α. As shown in Figure 5.4, α converges to k as number of counts (N) increases, with convergence occurring at $N > 1/k$. Consequently, with this addition, the Equation (5.2) seen in Chapter 5 becomes:

$$\phi'_j = (1-\alpha)\phi_j + \alpha \frac{R_{ij}\phi_j}{\sum_{j=1}^{n} R_{ij}\phi_j} \tag{5.2}$$

which can be updated to:

$$\phi'_j = (1-k)\,\frac{N-1}{N}\phi_j + \frac{1+kN}{N} \cdot \frac{R_{ij}\phi_j}{\sum_{j=1}^{n} R_{ij}\phi_j} \tag{5.3}$$

where:

- α : index related to the effect of prior to posterior probability, approaching k as N increases
- ϕ'_j : energy spectrum revised by the latest detected count
- ϕ_j : estimated energy spectrum before the last count (prior probability)
- N : count number.
- k: Parameter to accelerate convergence, which is dependent on count rate.

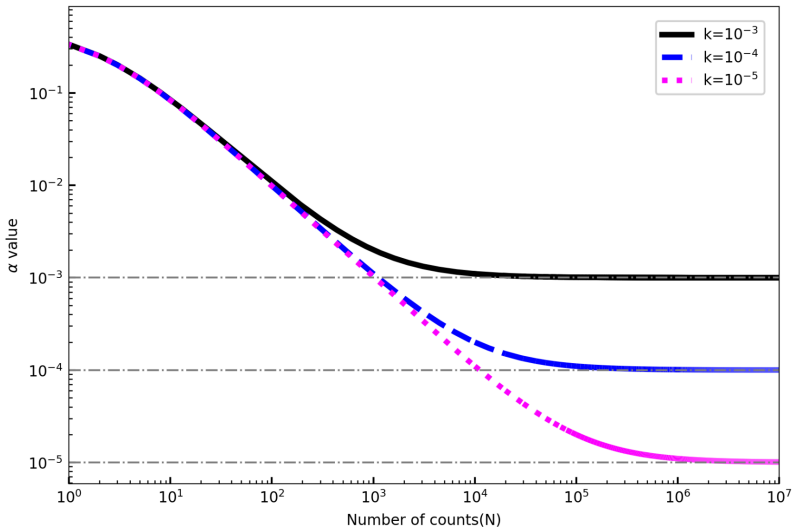

Figure 5.4: Visualization of the relation between parameter α and count number N

To summarize the key aspects of each of the main components forming this method:

Paremeter α controls how much weight the new measurement (posterior probability) has in updating the prior probability in Bayesian estimation. It is initially large to allow rapid updating, but as more data are accumulated (counts increase), α decreases to stabilize at an accurate energy spectrum estimate.

- When α is large (closer to 1), the prior probability is revised significantly with each new count. This can cause instability and a less accurate estimated value.
- When α is small (closer to 0), the updates are more gradual, stable and accurate, but at the cost of slowing down the convergence speed of the estimation.

Parameter k is introduced with the k−α method, to adjust how α changes with the number of counts. At a large number of counts, α approaches this value as seen in Figure 5.4. Appropriate k ensures that:

- At the beginning of the measurement, α is large for fast initial updating
- As the counts N increase, α gradually decreases (towards k) , which allows for a stable estimation of the energy spectrum.

This means that k depends on the count rate and it affects the balance between convergence speed and stability of the estimation. A larger k value results in faster convergence, while

a smaller one results more precise but slower convergence. The optimal value of k for any given count rate is not precisely and strictly known. However, prior investigations, for example, have shown that the values 10^{-3} and 10^{-4} are most suited for environments of approximately 0.08 Sv/h (background) in the case of the former and 2 Sv/h (front of nuclear fuel storage room) and 6 Sv/h (multiple standard gamma-ray sources) with the latter [135].

5.3.1 Convergence Parameter *I*

As the count number N increases, the number of revisions increases and the faster the estimated value converges. In the previous section the k—α method was examined from the point of view of k and α. From the point of view of the number of counts N:

- If N is large, the estimated result converges accurately even with a small k value with a small revision rate.
- If N is small, the revision will not proceed when k is small, so there is a risk that the accuracy will decrease.

This means it is necessary to increase the k value and increase the revision rate to increase the convergence speed. From Equation 5.1, if N is large, α converges to k. This can also be seen from Figure 5.4.

After $\frac{1}{\alpha}$ counts, 100% of ϕ_j is revised. In other words, based on the above, this occurs after $\frac{1}{k}$ counts. From this fact, we interpret $\frac{1}{k}$ counts as one cycle of revision and consider that the revision rate of the estimated value, that is, the degree of convergence, would be the same even if the k values were different but the cycle number is the same.

Revisiting the point mentioned throughout this chapter, if k is small, a large count number N is required for convergence (number of cycles = $\frac{N}{1/k}$), and conversely, if k is large, convergence (number of cycles = $\frac{N}{1/k}$) proceeds even with a small count number N. After $\frac{1}{k}$ counts, one complete revision (or "cycle") occurs, meaning the estimate is fully updated with new data. The number of cycles is calculated as $\frac{N}{1/k}$, indicating how many full updates of the estimate have occurred. Therefore, this number of cycles, dubbed I, represents a convergence metric that relates the count number N and parameter k to the

degree of convergence of the estimation. I is defined by:

$$I = \frac{N}{1/k} \tag{5.4}$$

I helps to standardize the degree of convergence for varying k values. Regardless of the specific value of k, if I is the same, the degree of convergence should also be similar. Larger k values require fewer counts N for convergence, while smaller k values need more counts.

5.4 Resampling method

Using the MCA8000D multi-channel analyzer for energy spectrum and dose estimation, the pulse height spectrum is converted to the energy spectrum post-measurement. The pulse height spectrum measured for a certain time is thus used as a population for the sequential Bayesian estimation and the signal is obtained for each revision by resampling from the population. This allows for many samples to be obtained in one experiment, but it is not a true real-time estimation that can be done during measurement. Figure 5.5 shows the standard setup configuration used for resampling research.

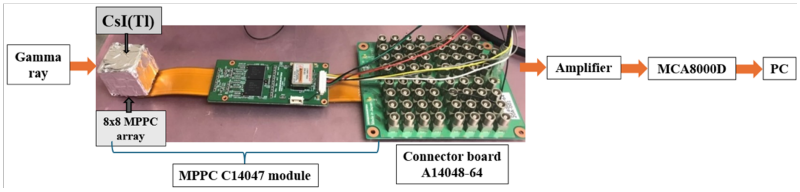

Figure 5.5: Standard setup for obtaining data for resampling calculations

This methodology was developed as a means to investigate real-time estimation, before implementing a digital pulse processor, like the DP5, which is capable of real-time digitization of the amplified MPPC signal. Using in-house programs to perform sequential Bayesian estimation, the input data required are the detector response file, a primary file which is a list of energies up to 3 MeV or 10 MeV, depending on the application and a measurement file, which contains data obtained from measurement. After the successful execution of the program of $k-\alpha$ method, visualization of the energy spectra, that is the gamma-ray flux is possible and also, calculation and visualization of the dose-rate after applying the flux-to-dose conversion coefficient. The advantages of this methodology and

reason for its use during development is the ability to evaluate the performance of the k−α method easily as well as its repeatability. Adjusting the algorithm or altering the code then executing the estimation process is time efficient.

5.5 True Real-time Measurements with Digital Pulse Processing

Achieving true real-time measurements with digital pulse processing by implementing the DP5 digital pulse processor [86], is a significant milestone in the development of the prototype gamma-ray monitor and verification of true real-time measurements with the k−α method. Compared to the initial concept of the prototype gamma-ray detector, like in Figure 5.5, the MCA part is changed from MCA8000D to DP5 (Figure 5.6) [86]. The MCA8000D can process and store pulse height data received from the MPPC in real-time, but it cannot store the input time of the pulse height data, preventing the application of sequential Bayesian estimation in true real-time. On the other hand, DP5 can store both pulse height data and input time as a list. Digital pulse processing offers other advantages compared to traditional analog systems, which often suffer from delays and reduced accuracy due to pulse pile-up or signal degradation. The list data of pulse heights and time stamps are stored internally [86], and are then sent to the PC, run through a series of custom in house programs to execute the k−α method, and the energy spectrum and dose rate are displayed in real-time.

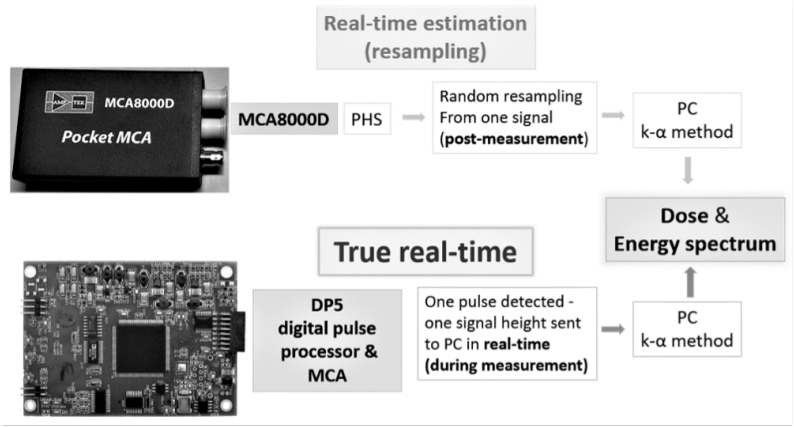

Figure 5.6: Overview of the two methods for derivation of energy spectrum and dose rate; resampling and true real-time

A flowchart of the main programs utilized can be seen in Fig. 5.7. Prior to initialization of the real-time measurement software, as mentioned in later Section 5.7, the values obtained through calibration with standard sources are input in the *json* file that contains pointers to all the resources required for the execution of the k—α method. Throughout all measurements utilizing the DP5, the internal gain was set to 1, specifically the closest possible value, 0.9999. Unlike the MCA, settings like internal gain can be adjusted for the DP5 through the interface of dppMCA. The gain is always adjusted manually by the amplifier. More specifically, the binary list data containing the required information on signal strength and time passes through the DP5's analog pre-filter, followed by its real-time digital pulse shaper, where digitization occurs, as introduced in Section 2.3. Thanks to the DP5's pulse selection logic and histogram memory capabilities, data for each event, along with the corresponding peak values, are output as an array. These form the basis of the pulse height spectrum viewed with the dppMCA program. In the real-time measurement case, these data are input to the program of *gccDppConsoleWin*, which retrieves the list data containing the pulse height and time information and sends it to be executed by the main program of *sequentialBayes*, carrying out the k—α method in real-time. If necessary, the frequency of the list data received from the DP5 can be altered by a simple command in the interface of the software.

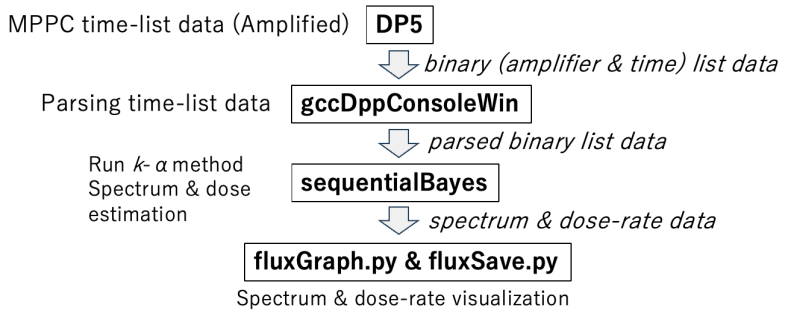

Figure 5.7: Overview and flow of the main programs utilized to realise real-time estimation through digital pulse processing with the DP5

Two other separate programs, *fluxGraph* and *fluxSave*, are implemented for the simultaneous visualization of the energy spectrum and dose-rate in true real-time and for saving the outputted data of the energy spectrum, dose rate and time, respectively. In more detail, the binary list of amplifier and time information containing data from the DP5 has been parsed by *gccDppConsoleWin*, run through the k—α method with *sequen-*

tialBayes and is able to be processed in order to output the estimated flux (/cm^2/sec) and dose rate (μSv/h). Terminating the program, automatically leads to the flux and dose rate data to be saved without a need to manually delete previous result data. Immediate restart of measurement is possible after termination of the software.

5.6 Response Function Creation

In order to perform unfolding (deconvolution) of the energy spectra, the response function unique to each detector configuration needs to be known. This could theoretically be done experimentally, however it is difficult to have specific monoenergetic gamma-ray sources for every single energy level in the energy range of interest and with small (few keV scale) increments in order to measure the detector's response to each one of them. Therefore simulations like Monte Carlo based methods are used [174]. Hybrid methods of experiment and simulation have been verified for the creation of accurate response functions, both by other researchers [213] and the research group in the authors laboratory [135], [170] . Throughout this research, MCNP5 (general purpose Monte Carlo N-Particle transport code version 5) [91], [214] is utilized, alongside with experimental data in order to account for the monitor's energy resolution. Various other programs, including PHITS and Geant4, are applicable and have functionalities of accounting for the full absorption (full-energy peak), single escape peak, double escape peak, Compton of the single and double escape gamma-rays and the internal and external scattering components [215]. In these calculations, the scintillator's effective center, which is used to determine the detector's output characteristics, is set as its geometric center. For the cubic 2.6 cm^3 crystal, this corresponds to a point 1.3 cm from each side. [29].

The process workflow generally includes the following steps:

- Using MCNP5 to model the experimental setup and perform simulations to create an initial response function for the measured energies
- Using standard gamma-ray sources (such as ^{137}Cs, ^{22}Na, ^{60}Co, ^{133}Ba) to measure the full width at half maximum (FWHM) of energy peaks (see Section 2.2). Pulse height spectra are accumulated until peaks have a 10,000-count net area, ideally excluding the background, in order to reduce uncertainty to 1% or less

- Establishing a relationship between the measured FWHM and energy peaks to calculate the standard deviation (σ) for the Gaussian distribution, modelling the detector' s energy resolution
- Applying the Gaussian distribution to blur (or "smear") the MCNP5-derived response functions according to the detector's energy resolution, resulting in a detector response function that accurately reflects its response to incident radiation
- Verifying the adjusted response functions against actual measurements for validation, then computing the response functions across the required energy range to form a comprehensive response matrix, which is used for the real-time unfolding of the gamma-ray energy spectrum.

The setup used for response function creation is shown in Figure 5.8.

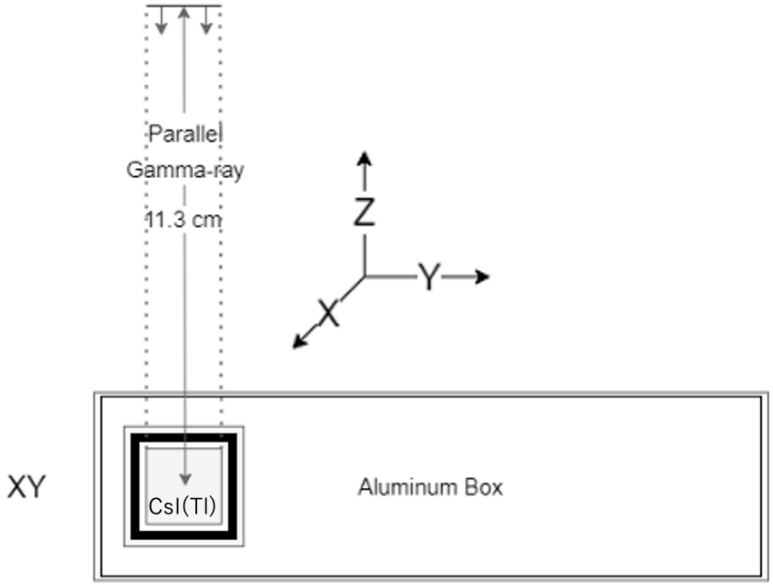

Figure 5.8: Schematics of simulation setup used for response function creation

In more detail, when a single energy H_0 is measured 2.4, the detector's energy resolution can be approximated by a Gaussian distribution with mean H_0 and standard deviation σ. The Gaussian distribution $G(H)$ (counts/source/MeV) is expressed by Equation 5.5.

$$G(H) = \frac{\mu}{\sqrt{2\pi\sigma^2}} \exp\left(-\frac{(H - H_0)^2}{2\sigma^2}\right) \tag{5.5}$$

Here, H is the energy, and μ is the net area under the peak. When the response function follows a Gaussian distribution, μ is the intrinsic detection efficiency (counts/source) at energy H_0. The relationship between σ and the FWHM is given as follows:

$$\text{FWHM} = 2\sqrt{2\ln 2} \cdot \sigma \tag{5.6}$$

Also, for the detector specific constants A and B, the relationship between the energy resolution R and the peak energy H_0 is expressed as:

$$R = \frac{\text{FWHM}}{H_0} = \frac{A \cdot H_0^B}{H_0} \tag{5.7}$$

$$\text{FWHM} = A \cdot H_0^B \tag{5.8}$$

Thus, once the detector-specific constants A and B are determined, σ for each H_0 can be obtained using Equations 5.6 and 5.8, allowing the calculation of the Gaussian distribution in Equation 5.5. To blur (or "smear") the response function using the obtained Gaussian distribution, the Gaussian function must be applied and integrated over each energy of the response function, as shown in the following equation:

$$F(H) = \sum_{H_0} \left(\frac{\mu(H_0)}{\sqrt{2\pi\sigma(H_0)^2}} \exp\left(-\frac{(H - H_0)^2}{2\sigma(H_0)^2} \right) \right) \cdot dH \tag{5.9}$$

Here, $F(H)$ (counts/source) is the response function blurred by the Gaussian distribution for each energy bin H. The intrinsic detection efficiency μ and the standard deviation σ are functions of H_0 and are expressed as $\mu(H_0)$ and $\sigma(H_0)$. To determine A and B, measurements are conducted using standard gamma sources with known energies and intensities, and the energy and FWHM of each peak are used to fit Equation 5.8. The least squares solution of this fitting provides the values for A and B. The methodology is the same for every investigation mentioned in the following sections. Here the sources and values of the main response function for the cubic configuration of the CsI(Tl) scintillator with dimensions 2.6 × 2.6 × 2.6 cm^3, used in the true real-time measurements with the DP5 are mentioned. For these evaluations, the detector-specific constants A and B were determined using energy resolutions obtained from standard gamma sources of ^{133}Ba, ^{22}Na, ^{137}Cs, and ^{60}Co, as shown in Table 5.7. Equation 5.10, where $A = 0.764$ and

$B = 0.4745$ is as follows:

$$\text{FWHM} = 0.764 H_0^{0.4745} \tag{5.10}$$

Next, to verify the accuracy of the response function derived from Equation 5.9, the pulse height spectra measured with standard gamma sources of ^{241}Am, ^{133}Ba, ^{22}Na, ^{137}Cs, and ^{60}Co seen in Table 5.2 were compared.

Table 5.2: Standard Gamma-ray Sources Used for Response Function Creation

Nuclide	Energy (keV)	Half-life	Radioactivity (Bq)
^{133}Ba	356.0134	10.52 y	6.84×10^5
^{22}Na	511	2.601 y	3.57×10^5
	1274.537		
^{137}Cs	661.657	30.07 y	2.50×10^5
^{60}Co	1173.228	5.271 y	6.84×10^5
	1332.49		
^{241}Am	59.5409	432.2 y	3.77×10^5

Figures 5.9 and 5.10 shows a comparison between the measured pulse height spectrum for ^{22}Na and ^{60}Co, two of the sources used, and the simulation results of the experimental setup using MCNP5. The full energy peaks at 0.511 MeV and 1.27 MeV from ^{22}Na gamma rays and the 1.173 MeV and 1.332 MeV from ^{60}Co can be clearly observed and there is good agreement between the experimental and simulated peak distributions. Similar agreement, especially in the full energy peaks, is present in the pulse height spectra of other gamma-ray standard sources as well.

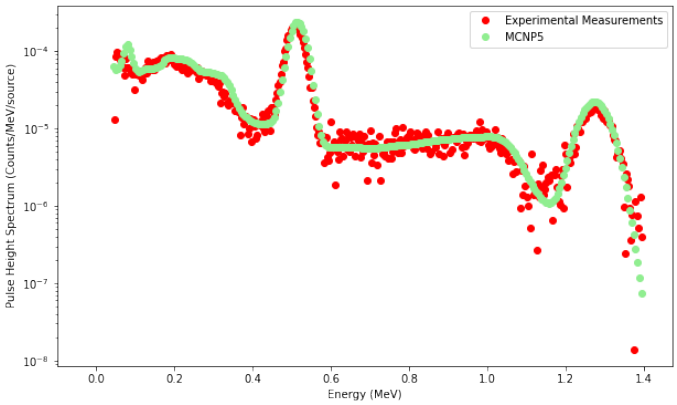

Figure 5.9: Pulse height spectrum of ^{22}Na measured using CsI(Tl) (MCA) and simulated using MCNP5

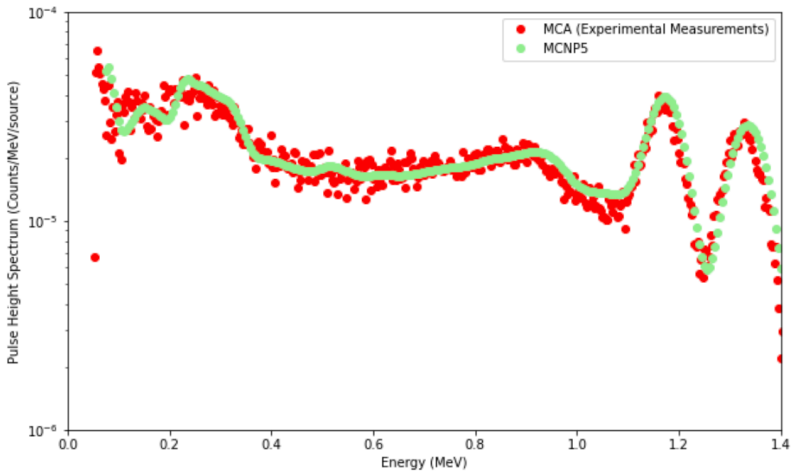

Figure 5.10: Pulse height spectrum of ^{60}Co measured using CsI(Tl) (MCA) and simulated using MCNP5

When simulating the surrounding materials of the detector in MCNP5, a backscatter peak around 0.2 MeV appears. This demonstrates that when gamma-ray scattering materials are present around the detector, simulating these materials is necessary to accurately reproduce the actual measurements. Including these materials in the simulation enables MCNP5 to create an accurate response function. After verifying that the measured and simulated values match, the response function was created for the required dynamic range of 10 - 3000 keV. The resulting response function matrix is shown in Figure 5.11.

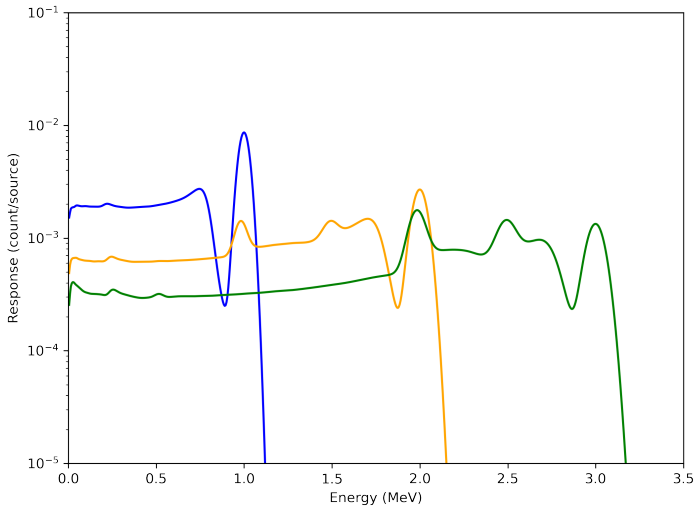

Figure 5.11: Response function to monoenergetic gamma-rays up to 3 MeV of a 2.6 x 2.6 x 2.6 cm^3 cubic CsI(Tl) scintillator, each colour blue, orange and green corresponding to the detector's response to 1, 2 and 3 MeV gamma-rays respectively [214]

For the response to 1 MeV incident gamma rays, a full absorption peak, Compton edge, and backscattering peak are observed. For the response to 2 MeV gamma rays, single and double escape peaks are seen. For 3 MeV gamma rays, the double escape peak is about the same as the full absorption peak. Table 5.3 shows the energy segmentation width chosen for the gamma-ray energy groups. The segmentation width was chosen to become larger after a certain point, due to worsening of the energy resolution. This means that the columns of the response function matrix are 185 bins corresponding to the incident gamma-ray energies covering the range seen in Table 5.3. To account for the broadening and deterioration of energy resolution, the response function matrix rows were 1024, from a range of 5 keV - 5 MeV.

Table 5.3: Energy Ranges and Intervals

Incident Energy Range (keV)	**Interval (segmentation width) (keV)**
10 - 700	10 keV
720 - 3000	20 keV

For the commercialization of the detector, detailed simulations of the detector housing are necessary to increase the accuracy of the response function, and by extention and

accuracy of the estimation.

5.7 Principle of Operation and Calibration

Apart from the detector components described above, and the implementation of the DP5 digital pulse processor and the custom programs developed in house, it is important to review the principles of operation of the prototype monitor in the current stage. Following the connections described in 5.2 the raw signal of the MPPC and the signal output from the amplifier are confirmed with an oscilloscope (Tektronix TBS 1152). The quality of the signal are confirmed for every measurement. After successful confirmation with the oscilloscope of the raw signal as well as the amplified and inverted signal, before starting the measurement, calibration with standard gamma-ray sources is performed, utilizing the AMPTEK dppMCA display and acquisition software. This software is utilized to control parameters of the DP5, such as internal gain, and is capable of regions of interest (ROI), calibrations and peak searching. Same standard gamma-ray sources and display and acquisition software is used in the case of measurements with the MCA8000D. In every calibration, a minimum of three points needs to be used, which is the majority of cases includes the peaks of ^{133}Ba, ^{137}Cs and ^{60}Co. The centroid positions of the peaks are input using the function of the dppMCA software. The error values are then confirmed to be within acceptable limits. In the case of using the DP5 digital pulse processor instead of the simple MCA, calibration equation values are then input into a .json file that contains information about all parameters required for real-time measurement and is read by the programs mentioned in Section 5.5, that execute the $k-\alpha$ method. When performing calibration, the counts corresponding to each photopeak of interest are accumulated until they reach 10,000 to reduce the relative error to 1% or lower. This is because the statistical uncertainty decreases with the square root of the number of counts, allowing for more accurate and reliable calibration of the energy peaks. By reaching 10,000 counts, the relative error is minimized, ensuring a precise calibration. Figure 5.12 shows an example of calibrating using the three gamma-ray sources of ^{133}Ba, ^{137}Cs and ^{60}Co, using the configuration of the prototype monitor with the DP5 digital pulse processor.

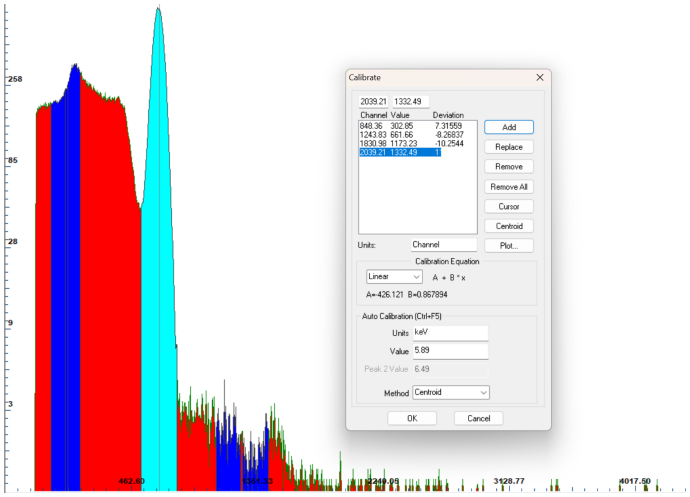

Figure 5.12: Calibration interface for ^{133}Ba ^{137}Cs and ^{60}Co

With the DppMCA software each channel of the DP5 is mapped to energy (keV). Equation 5.11 is provided from the linear relationship of the channels and energy:

$$y = A + B \cdot x \tag{5.11}$$

The above calibration methodology utilizing the dppMCA software and equation obtained through various standard gamma-ray sources is utilized in all measurement cases of the prototype monitor with the MCA8000D and the DP5 and also the HPGe detector used in later Section 6.2 which is also connected to a MCA8000D. However, it needs to be noted that in the resampling method using the MCA80000D, Equation 5.11 was used to convert the pulse height spectrum to energy (keV) after the fact, corresponding each MCA channel (ch) to the energy bins of the response function. For real-time measurement, the MCA channels are converted to energy (keV) in real-time and correspond them to the energy bins of the response function, which is the function conducted by the DP5. This was done using the following equation:

$$y = A + \frac{B}{2} \cdot x \quad (0 \leq x \leq 1024 \cdot 16\,\mathrm{ch}) \tag{5.12}$$

were x represents each pulse height channel of the DP5 or MCA8000D and y is the energy (keV) of a pulse height. Since the channel number is 1024×16 ch, the constant needs to become $B/2$. Additionally, bin_R is the energy width (keV) of each bin in the response

function R, which is 5 keV as mentioned in Section 5.6. *[x]* represents the floor function, truncating decimal points and x_R the energy bin (ch) of the response function R.

$$x_R = \left[\frac{y}{\mathrm{bin}_R} \right] \tag{5.13}$$

As introduced in Section 2.3.1, dead time can lead to inaccurate number or counts obtained, Throughout the course of all experiments, the dead time was confirmed and if need be, corrected for, by adjusting the threshold values. When faced with incredibly high dead time (>90%), the fast threshold can adjusted from the default value (normally set to 5) to a slightly higher value, such as 10, to reduce the dead time. Increasing the fast threshold can help in reducing noise and ensuring that the dead time with no source remains relatively low. It is important to note that the dead time displayed in the dppMCA software when using the DP5 is a rough estimate and at low count rates might not be accurate. Dead time is typically only shown if the input count rate exceeds 500 counts per second and is calculated using the ratio of input counts to total counts. Theoretically, with a very low count rate, the input counts should match the total counts, indicating minimal dead time. However, at higher count rates, some pile-up will inevitably occur, resulting in extra input counts compared to total counts. There should always be more input counts than total counts, which helps in identifying and compensating for dead time effects.

5.8 Flow of Development

The following sections present the story leading up to the current research efforts, starting from feasibility design to experimental and simulation results of present problematics.

5.8.1 Feasibility Studies

Following the initial design of combining the components described above, feasibility studies were conducted to evaluate the performance of the prototype monitor. Mainly described in the study by Kobayashi et al. (2017)[170], initial experimental investigations utilized a square CsI(Tl) scintillator sized $3 \times 3 \times 3$ cm^3. The detection efficiency and energy resolution were shown to be on the levels of most NaI(Tl) scintillators and the basic sequential Bayesian estimation was successfully applied to unfold gamma-ray energy spectra.

As mentioned in Chapter 2 the sequential Bayesian estimation can provide a good estimation of the gamma-ray dose and spectrum in real-time, something that the spectrum time Bayesian estimation cannot do. The precision of the sequential type was found to be on similar levels to the spectrum type. Following initial feasibility studies, measurements using the resampling method with the MCA8000D were conducted with standard gamma-ray sources (^{133}Ba, ^{137}Cs, ^{22}Na, and ^{60}Co) , in the background (0.07–0.08 Sv/h) and in front of a nuclear fuel storage room. Mainly described in [135], these experiments verified the accuracy of the dose-rate results by comparing them with theoretical values. With the $2.6 \times 2.6 \times 2.6$ cm^3 crystal, dose rates from standard gamma-ray sources (^{137}Cs, ^{22}Na, and ^{60}Co) could be immediately estimated. Additionally, the dose rate in background radiation conditions could be estimated in 20 s. The results also demonstrated that our measurements were more accurate compared with those obtained using a NaI survey meter. In that research, this was confirmed through comparisons with theoretical dose rates. Measurements in front of a nuclear fuel storage room (2 Sv/h), which contains 2 tons of UO_2 pellets that were fuel of a critical assembly in the past, confirmed that the unfolding process could be successfully performed in real time, even in more complex environments with a continuous spectrum and various gamma-ray peaks. Important results regarding the time needed for convergence of the energy spectrum and dose rate to stable values are summarized in table 5.4.

Table 5.4: Required time for estimation using the resampling method

Conditions	**Dose Rate (μSv/h)**	**Spectral convergence**	**Dose convergence**
Gamma-ray st. sources	6	30 s	Immediate
Fuel storage room	2	60 s	Few seconds
Background	0.08	7.5 mins	20 s

5.8.2 α and k-α Methods - Investigation of Estimation (Murata, Voulgaris et al., 2024) [14]

Much is discussed about the the α and k—α methods in the earlier chapter, but a comparison of the performance of the two is necessary. In order to investigate the estimation results of both methods, standard gamma-ray source experiments are performed and the dose rate is compared with theoretical and survey meter values. The overall convergence

performance is evaluated as well. Since monoenergetic sources are simpler and less realistic in actual measurement scenarios, in this verification gamma-ray measurements with a mixed source of ^{133}Ba, ^{137}Cs, and ^{60}Co were carried out to confirm the validity of the k-α method. Measurements were conducted using the prototype monitor described in Figure 5.13. Real-time measurements were simulated by sampling each count from a population obtained through long-duration measurements. This method ensures reproducibility and is valuable for debugging the data reduction system and developing the programs used in true real-time measurements. Initially, mono-energetic gamma-ray sources were considered, but in this study, multiple sources were combined to create an experimental radiation field simulating real conditions. The gamma-ray sources were placed 18 cm from the prototype monitor, which was positioned on a 1 cm thick aluminum plate, with a dose rate of approximately 6 μSv/h at the monitor location. The aluminum plate is utilized because when gamma-ray scattering materials are close to the detector, simulating these materials is necessary to accurately reproduce the actual measurements. Aluminium casing are commonly used for scintillation detectors, surrounding the scintillator and MPPC. Detector housing needs to be modeled as closely as possible to ensure accurate measurements. Table 5.5 summarizes the gamma-ray sources used.

Table 5.5: Nuclide properties of standard gamma-ray sources utilised, including half-life, gamma-ray energy, and intensity per decay.

Nuclide	**Half-life (years)**	**Gamma-ray energy (keV)**	**Intensity per decay (%)**
^{133}**Ba**	10.5	81	34
		276	7
		303	18
		356	62
		384	9
^{137}**Cs**	30	662	85
^{60}**Co**	5.3	1173	100
		1332	100

Figure 5.13 shows the experimental configuration used for these verification measurements.

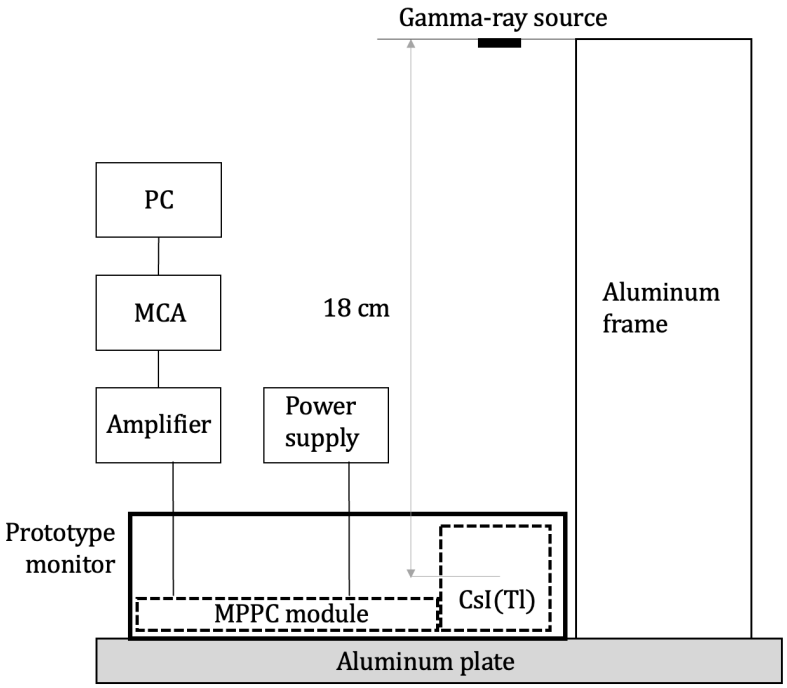

Figure 5.13: Experimental setup diagram used for the verification experiments

Figure 5.14 presents the pulse height spectrum measured by the monitor over 600 seconds. The count rate was 1500 counts per second (cps), and the total count reached 9.01×10^5 counts.

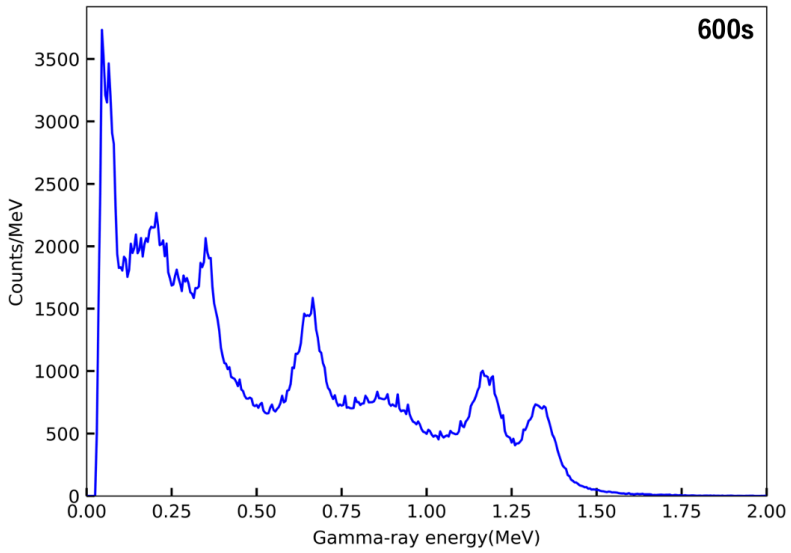

Figure 5.14: Pulse height spectrum measured by the prototype monitor for 600 s

The estimated spectrum for various α values at 30 and 300 seconds can be seen in Figures 5.15a and 5.15b respectively. The expected peaks appear for every α but the results are unstable when $\alpha = 10^{-2}$. As the α value decreases, the results improve, and while convergence has not been completely achieved for $\alpha = 10^{-4}$, considerable improvement is shown for $\alpha = 10^{-3}$. The estimated energy spectra for $\alpha = 10^{-3}$ and $\alpha = 10^{-4}$ have converged after 30 s and 300 s, respectively.

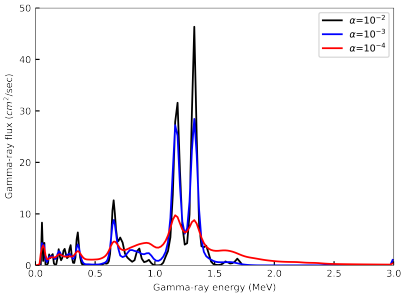

(a) ^{60}Co gamma-ray spectrum estimation (30s) for varying a $(10^{-2}, 10^{-3}, 10^{-4})$

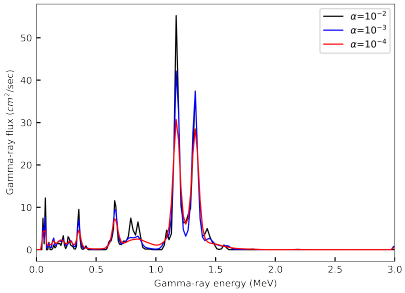

(b) ^{60}Co gamma-ray spectrum estimation (300s) for varying a $(10^{-2}, 10^{-3}, 10^{-4})$

Figure 5.15: Gamma-ray spectrum estimations for ^{60}Co for different durations and a values: (a) 30s and (b) 300s.

These graphs highlight what was discussed in Sections 5.3 and 5.8.2 regarding the α method. Careful selection of α can lead to convergence within few tens of seconds. Figure 5.16 shows the dose rate derived from the gamma-ray spectrum unfolding and application of flux-to-dose conversion coefficients [216], compared to the theoretical value (calculated with the effective dose rate constant [173]) and an NaI survey meter (TCS 171- Hitachi Aloka Medical, 2010). The survey meter's error margin was 11%. For $\alpha = 10^{-2}$, the estimated dose converged quickly but was very unstable and is not included in Figure 5.16. For $\alpha = 10^{-3}$, accuracy improved within 5 seconds, and for $\alpha = 10^{-4}$, it required about 40 seconds.

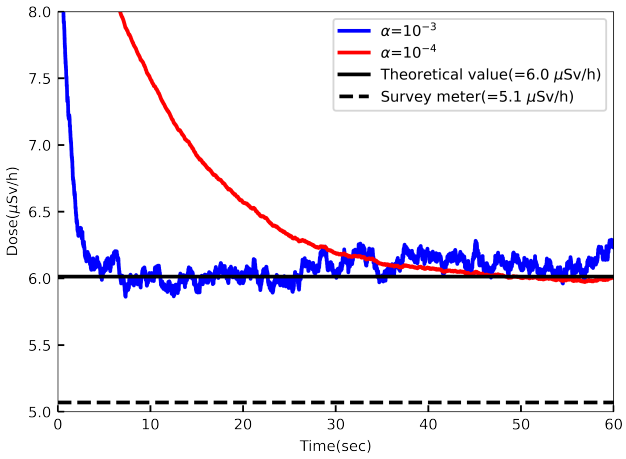

Figure 5.16: Dose rate comparison between the present method, theoretical results and NaI survey meter

Now, for validation of the k−α method, unfolding was performed with same experimental data from standard gamma-ray sources. The convergence improved with measuring time, and Figure 5.17 shows results at 300 seconds for $k = 10^{-4}$ and $\alpha = 10^{-4}$. Convergence is similar. Earlier on at 30 seconds, as seen in Figure 5.18, while neither is converged, the k−α method result shows a value much closer to the eventual final converged value.

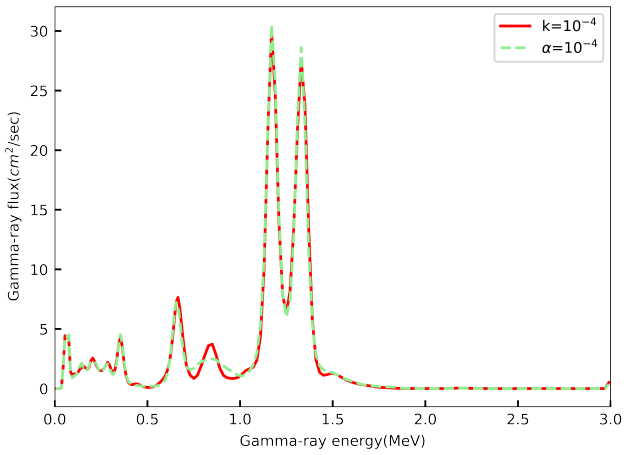

Figure 5.17: ^{60}Co gamma-ray energy spectrum at 300s ($k = 10^{-4}$ and $\alpha = 10^{-4}$)

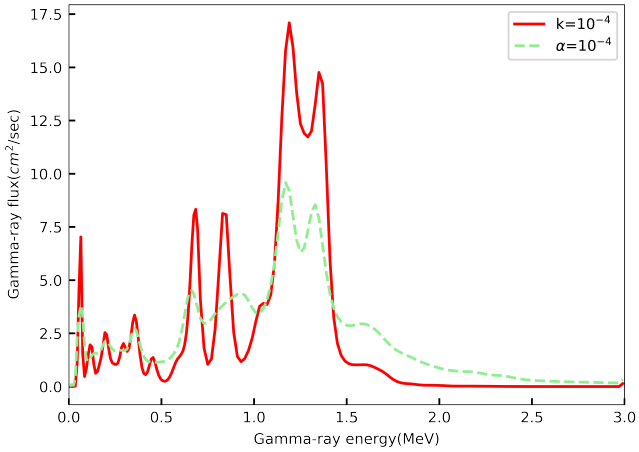

Figure 5.18: ^{60}Co gamma-ray energy spectrum at 30s ($k = 10^{-4}$ and $\alpha = 10^{-4}$)

Figure 5.19 considers the total error, a sum of absolute differences between the measured spectrum and the final converged spectrum (since it does not change after around 300 s), of both methods over time, reinforcing the fact that k—α method seems to give a faster and more accurate estimate of the final value.

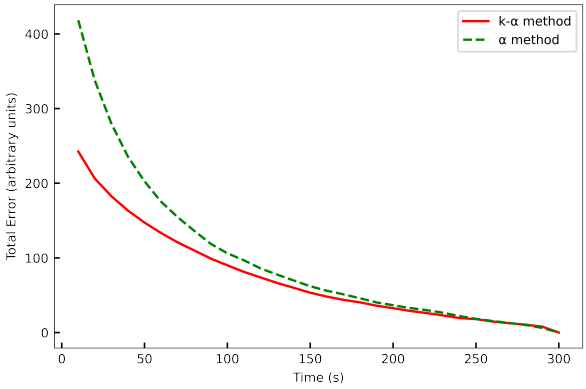

Figure 5.19: Total error between the measured spectrum and the final converged spectrum for k-α and α methods over time. The k-α method (red line) shows a faster reduction in error, suggesting quicker convergence ($k = 10^{-4}$ and $\alpha = 10^{-4}$)

It is necessary to examine the dose rate as well. Figure 5.20 showcases a comparison of dose rates between theoretical values, survey meter values and the k—α method when $k = 10^{-3}$, 10^{-4}, and 10^{-5}. For $k = 10^{-4}$, convergence to a stable value seems to require

less time than with the the α method seen in Figure 5.16. However, for $k = 10^{-5}$, the agreement with the theoretical value was not sufficient within the measurement time, likely due to very slow convergence.

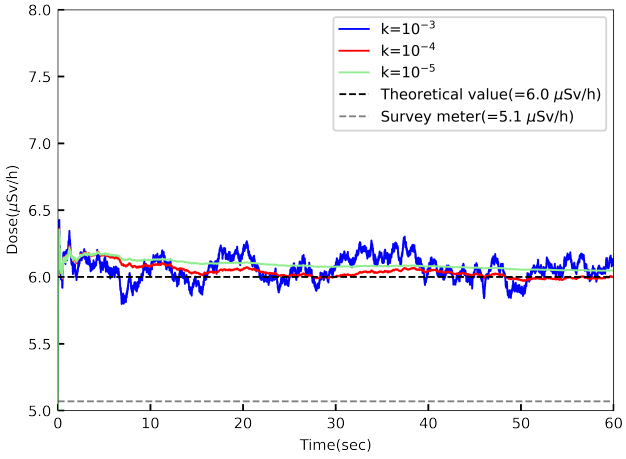

Figure 5.20: Dose rate estimation results for varying k, theoretical results and NaI survey meter

In conclusion, for radiation fields of approximately 6 μSv/h, the k–α method with $k = 10^{-4}$ can produce stable, accurate dose values within several seconds, and display the energy spectrum within tens of seconds. Table 5.6 shows dose rate results in the case of $k = 10^{-4}$, survey meter, and theoretical values. While for ^{137}Cs, results are close overall, this was not the case for ^{133}Ba and ^{60}Co. This is expected and is because the survey meter has been calibrated for ^{137}Cs (0.662 MeV), whereas the k–α method uses the measured gamma-ray energy spectrum and the flux-to-dose conversion coefficient for dose rate derivation as discussed.

Table 5.6: Comparison of doses for the present method, theoretical, and survey meter values for ^{133}Ba, ^{137}Cs, and ^{60}Co.

Isotope	**^{133}Ba**		**^{137}Cs**		**^{60}Co**	
Energy (keV)	356	81	303	662	1173	1332
Intensity per decay (%)	62	34	18	85	100	100
Flux-to-dose conversion coeff. (pSv·cm^2)	1.78	0.44	1.52	3.17	5.04	5.54
Survey meter (μSv/h)	0.27		0.57		4.23	
Theoretical value (μSv/h)	0.16		0.567		5.3	
Bayesian estimation (μSv/h)	0.165		0.569		5.28	

Overall, in this evaluation the prototype monitor successfully estimated the dose rate and the energy spectrum, allowing for precise measurements with the $k-\alpha$ method . Discussion of this study is expanded upon in Section 7.2.1.

5.8.3 CsI Crystal Size Investigation (Voulgaris et al., 2024) [15]

Since the aim of this research is to design a monitor that would be portable, the total size and weight of the device is very important, especially one of the aims is to make it wearable around the neck as seen in Section 5.2. As discussed in 2.2.1 the overall performance generally improves with an increase in scintillator size (volume) [18], [40], [53], [217], [218]. Thus one of the goals of this study is to also try to identify a scintillator shape that strikes a better balance between weight, volume, and performance. Response functions for a smaller cubic shaped ($2 \times 2 \times 2$ cm^3) and a flatter ($2.6 \times 2.6 \times 1.3$ cm^3) scintillator were created and compared with each other and the previously mentioned 2.6 $\times$ 2.6 $\times$ 2.6 cm^3 scintillator in term of detection efficiency, energy resolution, size, weight and speed of dose rate convergence. The dose rate comparison aimed to identify how quickly each one can provide a stable reading when measuring in a very low count rate environment, such as the background. Following the methodology of response function creation described earlier in section 5.6, the standard gamma-ray sources ^{137}Cs, ^{22}Na, and ^{60}Co were used to performed measurements 10 cm from the point of reference of the scintillators. The FWHM from the standard gamma-ray sources was measured to calculate the detector's energy resolution, and apply a Gaussian distribution to smear the MCNP5 derived response functions. This way, the created response matrix will accurately reflect how each detector setup "responds" to the incident gamma rays. The experimentally obtained pulse height spectrum and the one obtained from the simulation with MCNP5 matched especially in the photopeaks, so response functions of scintillators of the two additional sizes ($2 \times 2 \times 2$ cm^3, and $2.6 \times 2.6 \times 1.3$ cm^3) were created. Figures and showcase this agreement.The energy range of the response function was 10 keV to 3000 keV, same as the previous Section. The CsI(Tl) scintillator used up to this point ($2.6 \times 2.6 \times 2.6$ cm^3) has a weight of 80 g, while the $2 \times 2 \times 2$ cm^3, and $2.6 \times 2.6 \times 1.3$ cm^3 weight 39.6 g and 36.1 g respectively. Figure 5.21 shows the $2 \times 2 \times 2$ cm^3, and $2.6 \times 2.6 \times 1.3$ cm^3 CsI(Tl) scintillators [219].

(a) 2 × 2 × 2 cm^3 CsI(Tl) scintillator (b) 2.6 × 2.6 × 1.3 cm^3 CsI(Tl) scintillator

Figure 5.21: (a) 2 × 2 × 2 cm^3, and (b) 2.6 × 2.6 × 1.3 cm^3 CsI(Tl) scintillators with Teflon tape wrapping. I.S.C. Lab Co., Ltd

As mentioned earlier in Section 5.8.1, with a 2.6 × 2.6 × 2.6 cm^3 scintillator, the background dose was estimated in 20 s [135]. This raises the question, of if a considerably smaller scintillator can provide a stable dose at a very low count rate environment, in a reasonable amount of time. Before the experiment, using MCNP5 to model a point source of ^{137}Cs at 10 cm distance, the full-energy peak efficiency (see Section 2.2) change with crystal thickness was investigated. The peak efficiency for CsI(Tl) scintillators with constant volume but with thickness varying from 0.5 to 2.0 can be seen in figure 5.22. The experimentally obtained efficiencies at thicknesses of 1.3 cm and 2.0 cm are also included. Overall, around 1 –1.3 cm peak efficiency is slightly higher.

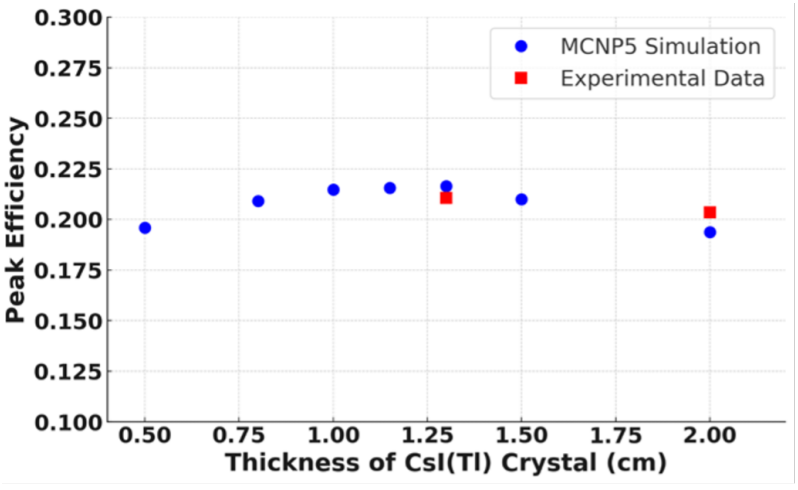

Figure 5.22: Peak efficiency of CsI(Tl) scintillators with constant volume but thickness ranging from 0.5 to 2.0 cm; simulations done with a ^{137}Cs point source 10 cm away from the CsI(Tl); Statistical error of simulation $< 1\%$

The experimental setup of the measurements with standard gamma-ray sources and $2.6 \times 2.6 \times 1.3$ cm^3 scintillator is shown in Figure 5.23.

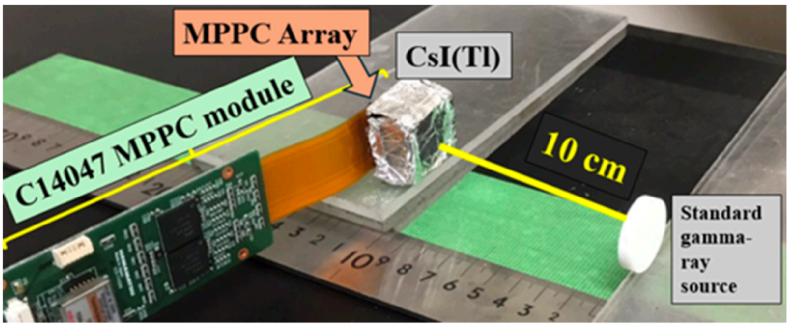

Figure 5.23: Experimental setup using the $2.6 \times 2.6 \times 1.3$ cm^3 CsI(Tl) crystal

The energy resolution for three different scintillator sizes are compiled in Figure 5.24. In the $2.6 \times 2.6 \times 1.3$ cm^3 crystal, the light-receiving unit of the MPPC was always mounted on the wide surface (2.6×2.6 cm^2); (① : wide gamma-ray incident surface ② thin gamma-ray incident surface).

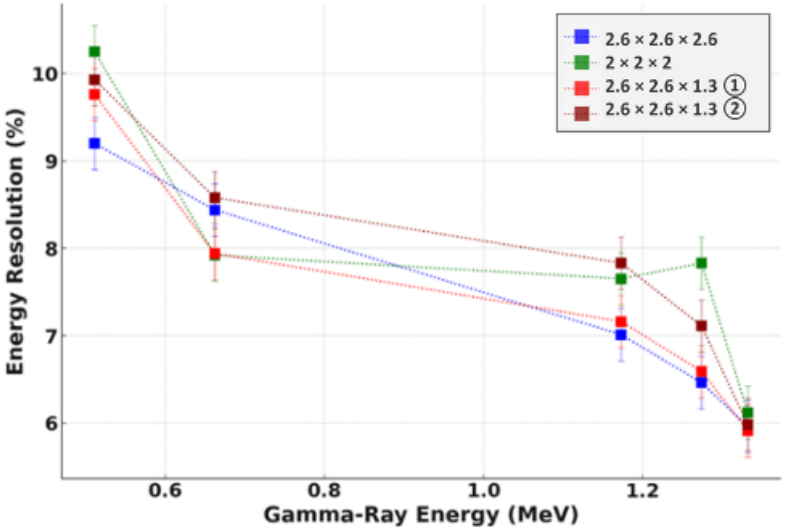

Figure 5.24: Energy resolution: size of CsI(Tl) crystal. For the $2.6 \times 2.6 \times 1.3$ cm^3 crystal, the MPPC was mounted on the wide surface (2.6×2.6 cm^2). ① and ② denote the incident gamma-ray surfaces (wide and thin, respectively). Sources: ^{137}Cs, ^{22}Na, and ^{60}Co at 10 cm distance

Experimentally measured pulse-height spectra are compared with those calculated using MCNP5 to ensure agreement [40].

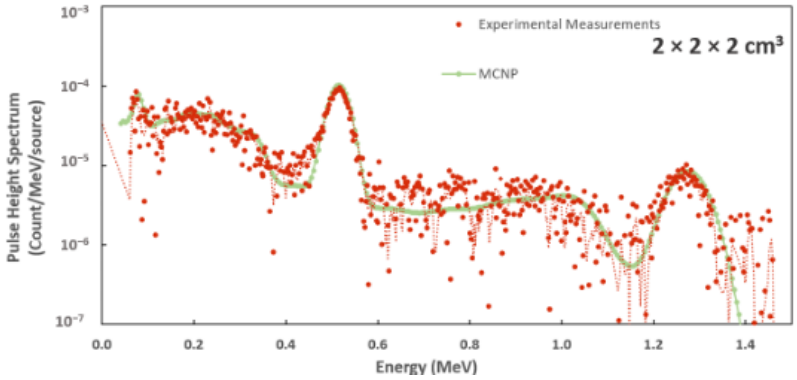

Figure 5.25: Experimentally obtained pulse-height spectrum of ^{22}Na at a 1 m distance and MCNP5 simulation results for 2 × 2 × 2 cm^3 CsI(Tl) scintillator

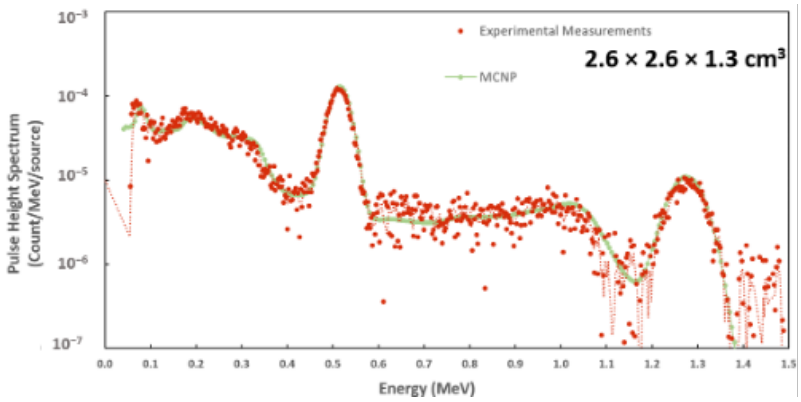

Figure 5.26: Experimentally obtained pulse-height spectrum of ^{22}Na at a 1 m distance and MCNP5 simulation results for 2.6 × 2.6 × 2.6 cm^3 CsI(Tl) scintillator

The photopeaks seem to match with high accuracy, while overall following a similar trend, as seen in Figures 5.25 and 5.26 for the case of a standard source of a standard source of ^{22}Na 1 m away from the CsI(Tl) scintillator. Figures 5.27a and 5.27b show, with 0.5 MeV increments, the newly created response functions. The main curves of 1, 2, and 3 MeV are specifically highlighted.

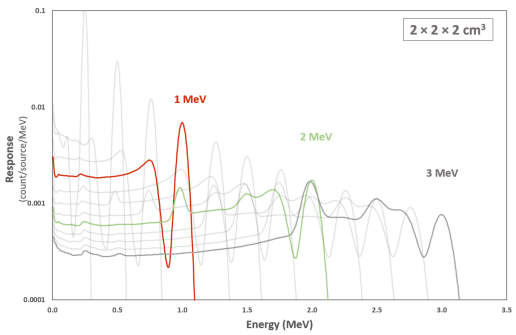

(a) Response functions using 2 × 2 × 2 cm^3 CsI(Tl) crystals

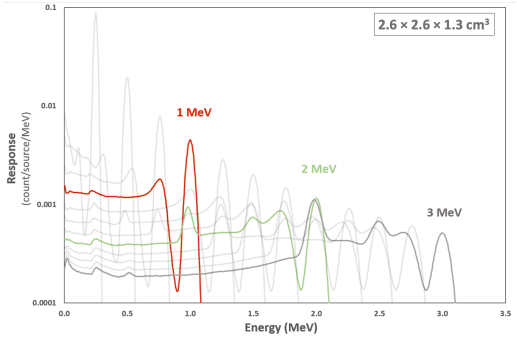

(b) Response functions using 2.6 × 2.6 × 1.3 cm^3 CsI(Tl) crystals

Figure 5.27: Response functions of the prototype gamma-ray monitor up to 3 MeV: (a) 2 × 2 × 2 cm^3 CsI(Tl) crystals and (b) 2.6 × 2.6 × 1.3 cm^3 CsI(Tl) crystals.

Figures 5.28a and 5.28b show the dose rate convergence over 120 seconds for the two new scintillator sizes, both indicating convergence around 35 s.

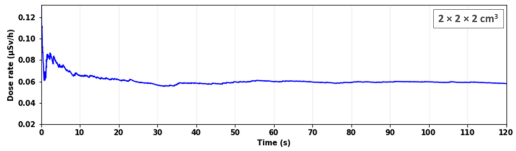

(a) Dose rate estimation for 2 × 2 × 2 cm^3 CsI(Tl). Convergence is achieved after around 35 s.

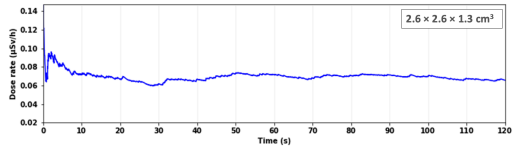

(b) Dose rate estimation for 2.6 × 2.6 × 1.3 cm^3 CsI(Tl). Convergence is achieved after around 35 s.

Figure 5.28: Dose rate estimation results in the background for different CsI(Tl) crystal sizes: (a) 2 × 2 × 2 cm^3 and (b) 2.6 × 2.6 × 1.3 cm^3.

Overall, the 2.6 × 2.6 × 1.3 cm^3 flat CsI(Tl) crystal showed better detection efficiency and energy resolution than the 2 × 2 × 2 cm^3 crystal while being nearly half the weight of the 2.6 × 2.6 × 2.6 cm^3 crystal. It achieved dose rate convergence in 35 seconds, compared to 20 seconds for the larger crystal, but offered a more portable design. Discussion on these results is expanded further in Section 7.2.2.

5.9 Verification of True Real-time measurements (Voulgaris et al., 2024) [16]

Achieving and confirming accurate real-time measurements is a fundamental goal of this research, since there is a need to provide immediate feedback regarding radiation exposure

to the medical staff. The integration of the DP5 digital pulse processor with the CsI(Tl) scintillator and MPPC, is what allowed this realization. The DP5, as discussed in Section 5.5, acts not only as a digital pulse processor but as a multichannel analyzer (MCA) at the same time. It digitizes the analog signals, processing and storing pulse height and time stamp information. This information is then transmitted to the connected PC [86], where the $k-\alpha$ method is applied and the real-time estimation results are displayed. Figure 5.29 shows the complete prototype experimental setup, introduced in Section 5.2, Figure 5.2.

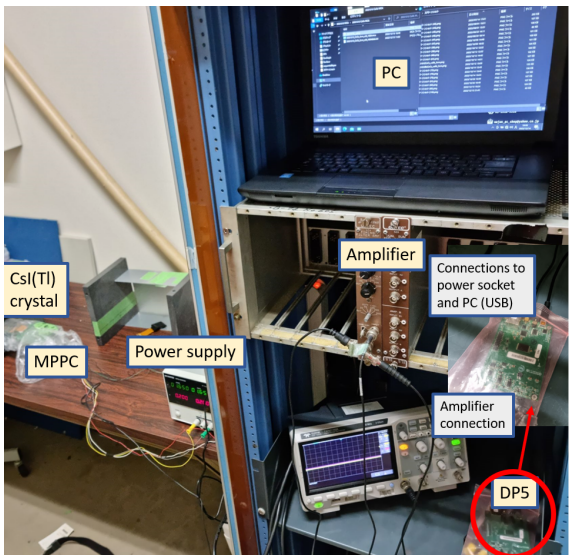

Figure 5.29: Complete experimental example setup for verification of prototype monitor

One of the key advantages of the DP5 is its ability to handle high count rates. This is particularly important in environments with varying radiation intensities, where traditional analog systems might struggle with data overload and signal degradation.The standard gamma-ray sources were used to compare the results of the $k-\alpha$ method with the post experimental, resampling-based real-time estimation, using the MCA8000D (see Section 5.4 and the results of the true real-time estimation, with the DP5 (see Section 5.5. Since the validity, accuracy and applicability of the former method has been verified, as described in5.8.2, matching results between the two methods can verify the applicability of the true-real time method.

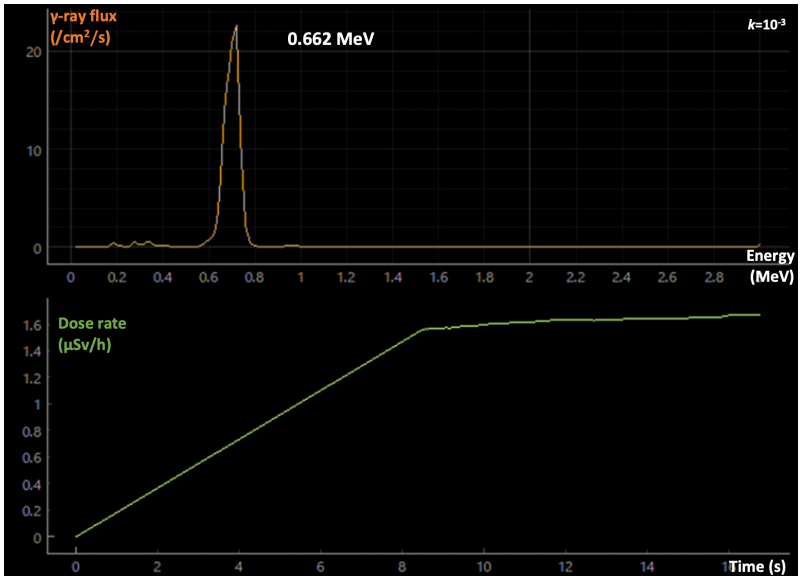

Figure 5.30: Annotated screenshot of the PC screen for real-time viewing of energy spectra and dose rate. ^{137}Cs source.

In this evaluation, the CsI(Tl) scintillator was placed 5 cm away from the gamma-ray sources, to obtain a high dose rate and reduce the contribution from the background. Measurement time was 600 s. The sources used are shown in Table 5.7. The setup of measurement is shown in Fig. .The gain of the amplifier was 5.2x on the ORTEC575A side and 1x on the DP5 side. As mentioned in Section 5.7 the internally set gain for the DP5 is always set to 1.

Table 5.7: Standard gamma-ray sources used in real-time evaluation experiments

Nuclide	**Energy (keV)**	**Half-life**	**Gamma-ray emission ratio (%)**	**Dose rate constant (μSv·m^2·MBq^{-1}·h^{-1})**	**Radioactivity (Bq)**
^{133}Ba	81.0 302.85 356.01	10.52 y	34.10 18.33 62.05	0.0637	6.38×10^4
^{137}Cs	661.657	30.07 y	85.10	0.0779	2.20×10^5
^{60}Co	1173.228 1332.49	5.271 y	99.85 99.98	0.305	1.27×10^4

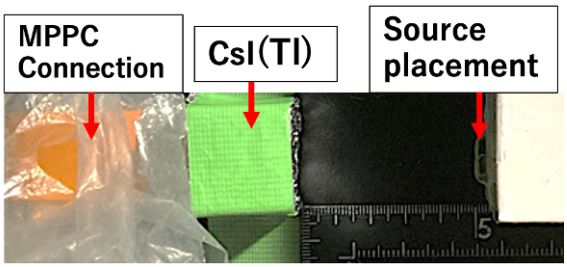

Figure 5.31: Setup of standard gamma-ray source measurement for verification of true real-time method. Source to detector distance 5 cm

The real time spectrum that was obtained in the case of measuring ^{137}Cs, it is shown in figure 5.30 in the form of a screenshot of the prototype monitor's PC interface.

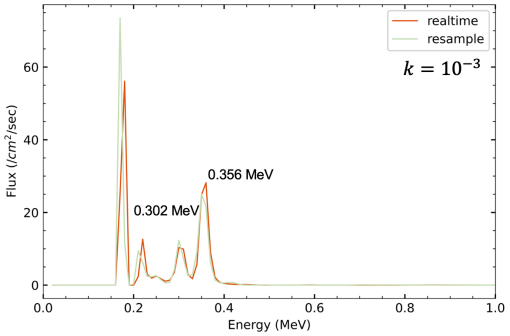

(a) Energy spectrum of ^{133}Ba for $k = 10^{-3}$, I = 40.

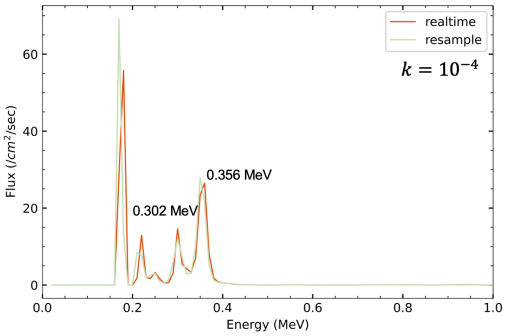

(b) Energy spectrum of ^{133}Ba for $k = 10^{-4}$, I = 40.

Figure 5.32: Energy spectrum estimation of ^{133}Ba for different values of k: (a) $k = 10^{-3}$ and (b) $k = 10^{-4}$, with $I = 40$.

From Figure 5.32 the total energy peaks of 302.85 and 356.01 keV of ^{133}Ba for both k values of 10^{-3} and 10^{-4} are clearly visible in the real-time and resampling estimated energy spectra. From Figures 5.33, the 0.662 MeV peak of ^{137}Cs is visible in the real-time and resampling estimated energy spectra. Lastly, from Figure 5.34, the 1.173 MeV and 1.332 MeV peaks are visible in the real-time and resampling estimated energy spectra. Additionally, the shapes of the spectra at the peaks match extremely well for all standard sources in Figures 5.32, 5.34 and 5.33. From the above results, it can be said that there is no difference between the real-time and resampling energy spectrum estimates for each one of ^{133}Ba, ^{137}Cs and ^{60}Co.

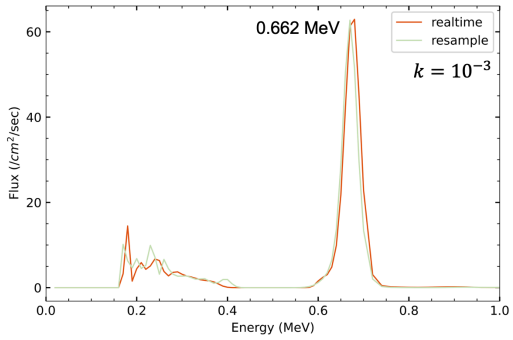

(a) Energy spectrum of ^{137}Cs for $k = 10^{-3}$, I = 40.

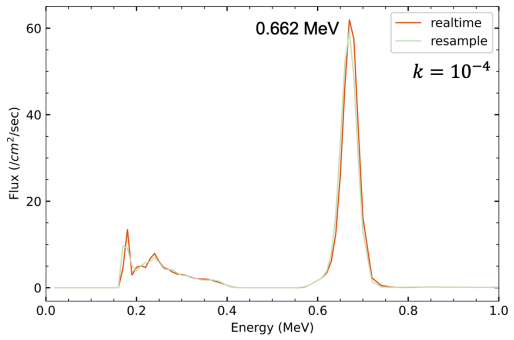

(b) Energy spectrum of ^{137}Cs for $k = 10^{-4}$, I = 40.

Figure 5.33: Energy spectrum estimation of ^{137}Cs for different values of k: (a) $k = 10^{-3}$ and (b) $k = 10^{-4}$, with $I = 40$.

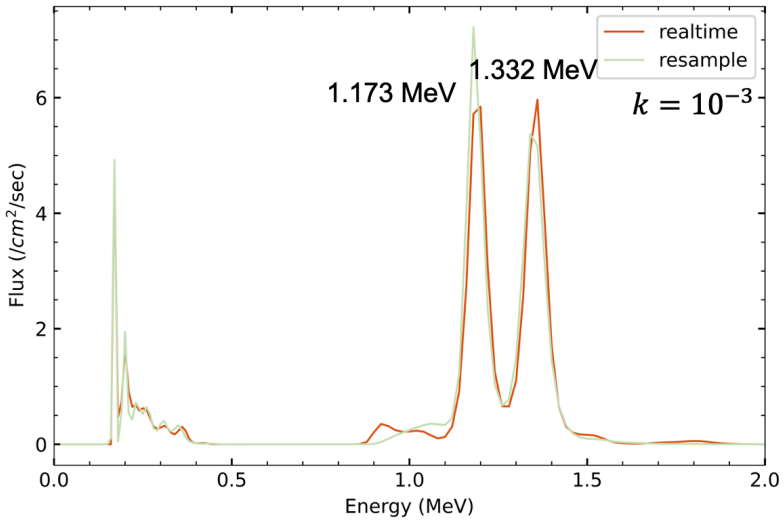

Figure 5.34: Energy spectrum of ^{60}Co for k=10^{-3} (left) and 10^{-4} (right) , I=40

The dose rate between the true real time method and the resampling method is compared in Figures 5.35, 5.36 and 5.37 over time up to 600 seconds. The horizontal axis is the measurement time (sec) and the vertical axis is the dose rate (μSv/h). In the graphs the theoretical value, and the NaI survey meter value are also included. Each standard gamma-ray source was measured 20 times, at a distance of 5 cm from the scintillator.

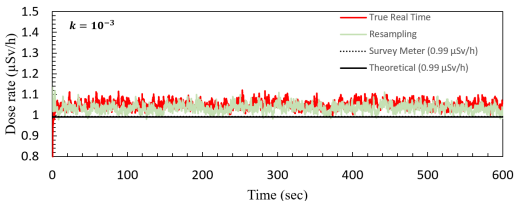

(a) Dose rate for ^{133}Ba, $k = 10^{-3}$.

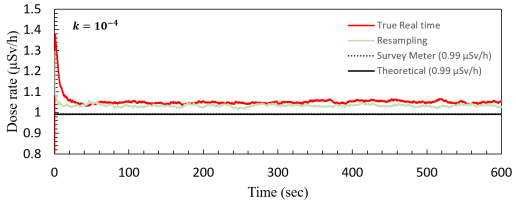

(b) Dose rate for ^{133}Ba, $k = 10^{-4}$.

Figure 5.35: Dose rate for ^{133}Ba: $k = 10^{-3}$ (a) and $k = 10^{-4}$ (b) (survey meter 2.5% relative standard deviation, 600 s measurement).

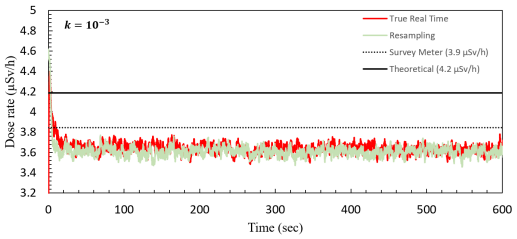

(a) Dose rate for ^{137}Cs, $k = 10^{-3}$.

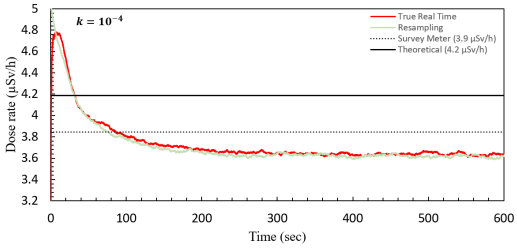

(b) Dose rate for ^{137}Cs, $k = 10^{-4}$.

Figure 5.36: Dose rate for ^{137}Cs: $k = 10^{-3}$ (a) and $k = 10^{-4}$ (b) (survey meter 2.2% relative standard deviation).

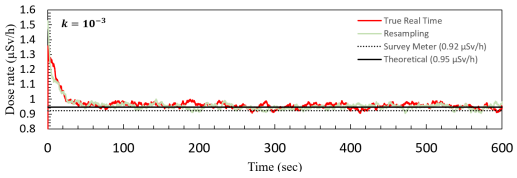

(a) Dose rate for ^{60}Co, $k = 10^{-3}$.

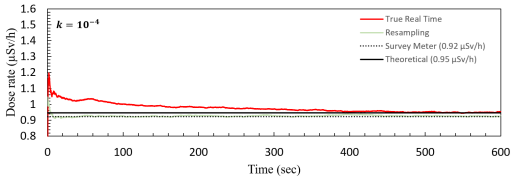

(b) Dose rate for ^{60}Co, $k = 10^{-4}$.

Figure 5.37: Dose rate for ^{60}Co: $k = 10^{-3}$ (a) and $k = 10^{-4}$ (b) (survey meter 4.8% relative standard deviation).

For ^{133}Ba, with $k = 10^{-3}$ and $k = 10^{-4}$, both real-time and resampling dose rate estimates converged almost immediately, matching the survey meter and theoretical values of 0.99 μSv/h, though a slight overestimation was noted with the prototype monitor. For ^{137}Cs, convergence occurred at 10 seconds for $k = 10^{-3}$ and 200 seconds for $k = 10^{-4}$, with a survey meter reading of 3.9 μSv/h and a theoretical value of 4.2 μSv/h, showing slight underestimation by the prototype. In the case of ^{60}Co, convergence took about 30 seconds for $k = 10^{-3}$, but was much slower for $k = 10^{-4}$. The survey meter reading was 0.92 μSv/h compared to the theoretical value of 0.95 μSv/h. Overall, for all gamma-ray standard sources and k value combinations, the true real-time dose rate agreed with the resampling

derived dose rate. Discrepancies, between the two such as in the case of ^{60}Co and k=10^{-4}, show that the convergence of the estimated value is very slow. For the same measurement time, I is smaller, and a larger count number is required for convergence. This can be confirmed from Equation 5.4. Additionally, discrepancies with the theoretical value arise from the fact that the distance between the radiation source and the scintillation crystal is only 5 cm. These points and more will be further discussed in Section 7.2.3.

6 | Application in Radiation Therapy Facilities

6.1 Introduction

As discussed earlier on, the application of the prototype gamma-ray monitor extends to various fields, medical or even industrial, however the focus of development is on medical facilities utilizing radiation. This includes commonly used modalities like LINAC-based ones, as well as Boron Neutron Capture Therapy (BNCT), where high energy gamma-rays are present from neutron induced reactions, and the energy spectra of neutrons cover a wide dynamic range from a few eV to a few MeV. To realistically consider applying this monitor to such practices, complementary measurements up to 3 MeV were needed, since the conducted standard gamma-ray source measurements (and some in complex fields [135]) have an upper limit of 1.3 MeV. This way the monitor would be on par with most similar monitoring systems and guidelines of many radiotherapies regarding measurements not during operation. As discussed, after radiological equipment, like accelerators, are turned off, primary particles such as protons and neutrons are no longer present. Meaning prior to or post-operation high energy gamma-rays are not a concern, and mainly decay gamma-rays from radioisotopes remain. These have a maximum energy of 3 MeV, a value which served as the initial goal of the energy limit for the monitor. Additionally, following guidelines for portable radiation monitors, a target dose rate range in development, is from background levels (0.05 μSv/h) to 1 mSv/h, with a final goal extending up to 10 mSv/h. Maximum count rate also is to be feasible at around 10,000 cps.

This chapter initially introduces the real-time estimation of the energy spectrum and dose rate of the gamma-rays emitted from the $^{27}\mathrm{Al}(n,\alpha)^{24}\mathrm{Na}$ reaction, which contain a peak of 2.755 MeV, utilizing the fact that neutron irradiated aluminum (Al) remains radioactive even for a few days post neutron irradiation [220], [221]. This chapter then presents the initial steps taken to extend the response function to cover gamma-ray energies up to 10 MeV, and discusses the conditions of neutron and gamma-ray mixed fields, including BNCT, in the context of this research. It explores how the prototype monitor could be applied in such settings, the challenges involved, and potential solutions for future improvements. Additionally, it reviews alternative methods and possible enhancements.

6.2 Verification up to 2.75 MeV (Voulgaris et.al., 2024) [17]

As a first step, it was needed to verify that the current orientation and setup of the monitor can be applied successfully to measure gamma-rays close to the established value of 3 MeV. For this purpose, a series of controlled irradiation experiments were conducted. The methodology involved calibrating the monitor with standard gamma-ray sources and comparing the results with theoretical calculations utilizing data derived from measurements with a high-purity germanium (HPGe) detector. NaI(Tl) (TCS-171, Aloka, Hitachi) survey meter comparisons were also performed for the sake of performance evaluation. The experiments were designed to assess the monitor's response to higher energy gamma rays than before, focusing on key parameters such accurate spectral unfolding, peak identification, speed of convergence and dose rate accuracy.

6.2.1 2.75 MeV Experiment Materials and Methodology

The components of the prototype monitor are mainly the same as introduced in Section 5.2, consisting of the cubic CsI(Tl) scintillator ($2.6 \times 2.6 \times 2.6$ cm^3, provided by I.S.C.Lab. CO.,LTD, Osaka, Japan[219]), a multi-pixel photon counter (MPPC, C14047-0436, Hamamatsu photonics, Hamamatsu, Japan), an amplifier (ORTEC575A, ORTEC/AMETEK, Oak Ridge, USA) and the DP5, a digital pulse processor and multi-channel analyzer (Amptek Inc, Bedford, MA, USA). Calibration was performed using a combination of ^{137}Cs, ^{60}Co sources, as well as the peaks of ^{24}Na from the irradiated Al foil, covering a range of energies up to 2.755 MeV, following the methodology and software introduced in Section 5.7. The pulse height spectra obtained from the monitor were then unfolded to derive the energy spectra in real time. The prototype monitor setup was encased in lead shielding, the source was placed 20 cm away from the surface of the scintillator, as seen in Figure 6.1,complemented by an additional layer of black cloth for enhanced shielding from light.

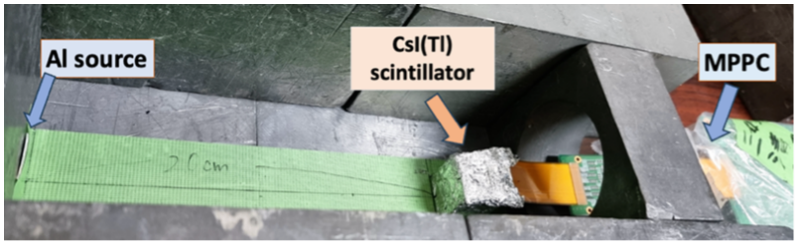

Figure 6.1: Setup for measurement with the prototype monitor. Sources were places 20 cm from the surface of the CsI(Tl) scintillator

More specifically, in order to induce the ^{27}Al$(n,\alpha)^{24}$Na reaction, a 2 × 2 × 0.1 cm^3, and Al foil was irradiated with a neutron source. Irradiation was performed at the OKTAVIAN facility in Osaka University, Japan, using a deuterium-tritium (D-T) neutron generator as depicted in Figure 6.2. This facility's neutron source has the capability to emit 3×10^{12} fusion neutrons per second [189].

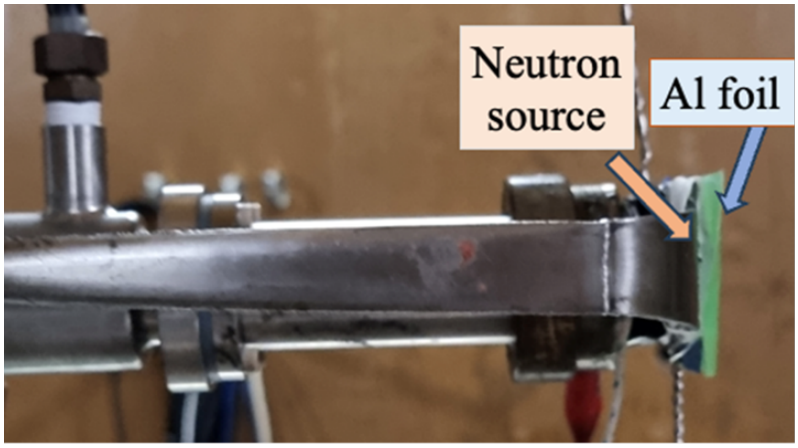

Figure 6.2: Placement of the Al directly in front of the D-T neutron source at OKTAVIAN facility

Regarding the induced reaction, the ^{27}Al$(n,\alpha)^{24}$Na reaction produces the radioactive isotope ^{24}Na, which decays by beta-particle emission into the second excited state of ^{24}Mg. Subsequent transitions to the first excited state and finally to the ground state of ^{24}Mg result in the emission of gamma-rays with energies of 2.755 MeV and 1.369 MeV, respectively[220], [222], [223]. The half-life of ^{24}Na is recorded as 14.9581 hours[224]. The ^{24}Na method was selected for its reproducibility as well as because it does not generate radioactive waste [225]. A reason for the close measurement distance and utilization of lead for the 2.75 MeV measurements is because when creating the source for the experiment

by irradiating the aluminum as just described, the activity of the created source is not always consistent, which has sometimes resulted in very weak sources. For this reason, the source is brought closer to the detector to increase the accuracy and ensure detectable signal levels. The standard gamma-ray sources used for the calibration of the prototype monitor are compiled in Table 6.1, focusing on higher gamma-ray energies.

Table 6.1: Standard gamma-ray sources used in prototype monitor calibration

Nuclide	**Energy (keV)**	**Half-life (y)**	**Radioactivity (Bq)**
^{137}Cs	661.657	30.07	1.04×10^6
^{60}Co	1173.228 1332.49	5.271	1.06×10^6

The dose rate is measured with the prototype monitor, an NaI survey meter and additionally, the theoretical dose rate value was calculated. They are compared with each other to finally confirm the effectiveness of the present monitor. The theoretical dose rate was calculated with the method introduced in 2.9 and detailed in the next Section, 6.2.2. Knowing the detection efficiency of a detector allows for the calculation of the absolute activity of a source. Thus, to calculate the radioactivity of ^{24}Na, calculating the detection efficiency was necessary [18]. Utilizing ^{24}Na for source activity calculation has been verified in various environments, like proton therapy facilities in regards to material activation [5]. The neutron irradiation time was 8.5 hours. After irradiation, the Al foil was retrieved, and measurements with the following devices were performed:

- Prototype real-time monitor: Measurements were conducted at a distance of 20 cm, with both the energy spectrum and dose rate recorded in video format, as well as saved in the form of .csv files.
- NaI(Tl) survey meter (TCS 171, Hitachi ALOKA, Tokyo, Japan): Multiple dose rate readings were recorded at the same distance of 20 cm.
- High Purity Germanium (HPGe) Radiation Detector: Measurements were conducted according to subsection 6.2.2 for the calculation of the activity of the Al sample, which is necessary in the extraction of the theoretical dose rates required for comparison.

6.2.2 High Purity Germanium (HPGe) Radiation Detector Methodology

HPGe semiconductor detectors are verified and tested instruments in gamma spectrometry and for radioactivity identification [18], [226], [227]. In order to use the HPGe detector, energy and efficiency calibration are conducted. Efficiency calculations are necessary because the signal count obtained from the HPGe detector includes factors such as geometric efficiency and the loss of accuracy as gamma-rays are transmitted. In gamma-ray measurements using an HPGe detector, the detector signal count C can be represented by Equation 6.1 [107]:

$$C = \frac{A}{\lambda}\left(1 - e^{-\lambda t}\right) I\gamma f\varepsilon \tag{6.1}$$

where:

- A [Bq]: the radioactivity of the radioactive nuclide
- λ: the decay constant of the nuclide
- t: the measurement time
- I: the branching ratio for the decay mode that emits gamma rays at the energy of interest
- γ: the gamma-ray branching ratio
- f: the self-attenuation factor
- ε: the detection efficiency of the detector for gamma rays

Thus, the gamma-ray detection efficiency during a measurement time t_m [s] can be calculated using Equation 6.2:

$$\varepsilon = \frac{C\lambda}{AI\gamma f\left(1 - e^{-\lambda t_m}\right)} \tag{6.2}$$

The source was placed 10 cm from the detector receiving surface, like in 6.3 and the setup was shielded with lead. Connected to the HPGe detector was an MCA8000D multi channel analyzer and the software dppMCA was used to obtain the pulse height spectrum.

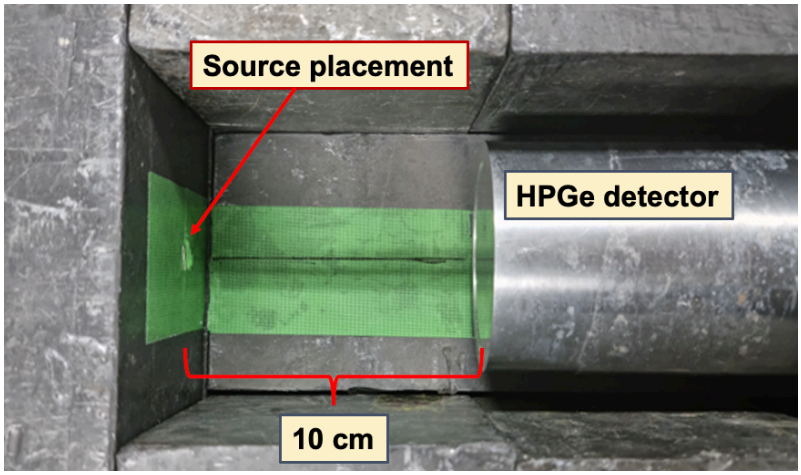

Figure 6.3: Setup for HPGe detector calibration and measurements. Source to detector distance was 10 cm

The detector was calibrated using the methodology introduced in Section 5.7, with standard sources of ^{137}Cs, ^{60}Co, and ^{22}Na, as seen in Table 6.2. Similar to measurements with the prototype monitor, in order to ensure a statistical error of less than 1%, the measurement continued until the net count of the primary peak reached 10^4 counts. With known activities and half-lives, the amount of gamma-rays produced was calculated. By calculating the detection efficiency of the detector for each energy and applying the least squares method, fitting of the 1.369 MeV peak of ^{24}Na was applied.

Table 6.2: Standard gamma-ray sources used for HPGe detector calibration

Nuclide	**Energy (keV)**	**Half-life (y)**	**Radioactivity (Bq)**
^{137}Cs	661.657	30.07	1.04×10^6
^{60}Co	1173.228 1332.49	5.271	4.41×10^5
^{22}Na	511.00 1274.54	2.6027	8.67×10^5

For gamma-ray energies above 100 keV, the interaction rate in the HPGe detector decreases as energy increases due to the declining attenuation coefficient of HPGe. Therefore, the detection efficiency is energy-dependent, assuming a constant source position. The standard gamma-ray sources used have known radioactivity, gamma-ray emission ratio, and decay branching ratio, assuming negligible self-attenuation. Using Equation 6.2, detection efficiency for each energy was calculated, and a power approximation curve

was fitted to represent the energy-efficiency relationship. By interpolating the desired desired gamma-ray energy point on the curve, the detection efficiency at 1.369 MeV was determined. Figure 6.4 shows the detection efficiency curve for the HPGe detector.

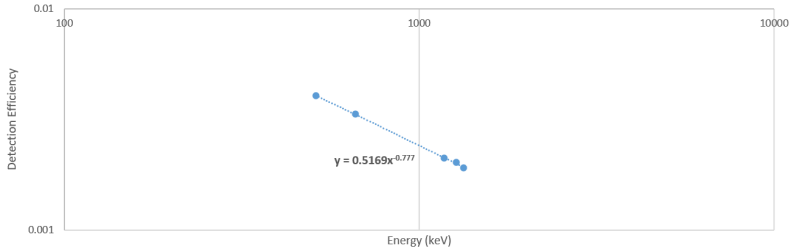

Figure 6.4: HPGe semiconductor detector detection efficiency curve from standard gamma-ray sources

When gamma rays of a specific energy are emitted from the radioactive nuclides produced within an activation foil, the intensity of the gamma rays decreases due to interactions within the foil. Therefore, the number of gamma rays measured by the HPGe detector is smaller than the number of emitted gamma rays. This is known as self-attenuation and needs to be accounted to achieve accurate measurements [228]. The intensity of gamma-rays, I_0 [s^{-1}] after traveling a distance x [cm] through a material, follows Equation (6.3):

$$I = I_0 e^{-\mu x} \tag{6.3}$$

Here, μ [cm^2/g] is the linear attenuation coefficient of the material through which the photons are passing. This value is specific to each material and the energy of the incident photons. According to Equation (6.3), when gamma rays produced within the foil pass through a foil with a thickness l [cm], the self-attenuation factor f due to the foil is expressed by Equation (6.4):

$$f = \frac{1 - e^{-\mu l}}{\mu l} \tag{6.4}$$

In this study, the linear attenuation coefficient was calculated by referring to the mass attenuation coefficient and multiplying by the density [229]. The Al foil used had a thickness of 0.1 [cm], a linear attenuation coefficient μ of 0.05245 [cm^2/g], and a density of 2.7 [g/cm^3], so the self-attenuation factor f_{Al} for the Al foil is given by Equation (6.5):

$$f_{\mathrm{Al}} = \frac{1 - e^{-\mu l}}{\mu l} = \frac{1 - e^{-0.05245 \times 2.7 \times 0.6}}{0.05245 \times 2.7 \times 0.1} = 0.9929 \tag{6.5}$$

For ε the detection efficiency of the Ge detector, f the self-attenuation factor, I_γ the gamma-ray emission ratio, and N the net area, then, the number of decays X of the radioactive nuclides during the measurement time can be expressed by Equation (6.6):

$$X = \frac{N}{\varepsilon \times f \times I_\gamma} \tag{6.6}$$

Furthermore, solving Equation 2.21 introduced in 2.9, for the decay constant λ when the half-life of the radioactive material is $T_{1/2}$ [s] it becomes:

$$\lambda = \frac{\ln(2)}{T_{1/2}} \tag{6.7}$$

At the start of the measurement using the Ge detector, the activity of the radioactive nuclide is A_0, and t_m is the measurement time.

$$A_0 = \frac{X\lambda}{(1 - e^{-\lambda t_m}) \times 10^6} \tag{6.8}$$

The radioactivity Q of Equation at the time measured by the prototype monitor was calculated by means of Equation 6.9 [226]:

$$Q = A_0 \cdot e^{-\lambda(t_2 - t_1)} \tag{6.9}$$

where:

- A_0: Activity at the start of measurement with the HPGe detector
- t_2: Prototype monitor measurement start time (s)
- t_1: HPGe detector measurement start time (s)
- λ: Radioactive decay constant

Therefore, if Γ is the gamma-ray effective dose rate constant $\left[\frac{\mu\text{Sv}\cdot\text{m}^2}{\text{MBq}\cdot\text{h}}\right]$ and r the distance of the source from the detector, then the dose rate can be calculated with Equation 6.10, as introduced in Section 2.9:

$$D = \frac{\Gamma \cdot Q}{r^2} \tag{6.10}$$

6.2.3 2.75 MeV Experiment Results

Figure 6.5 shows the pulse height spectrum obtained with the HPGe detector measurement due to the gamma-rays emitted from the ^{24}Na.

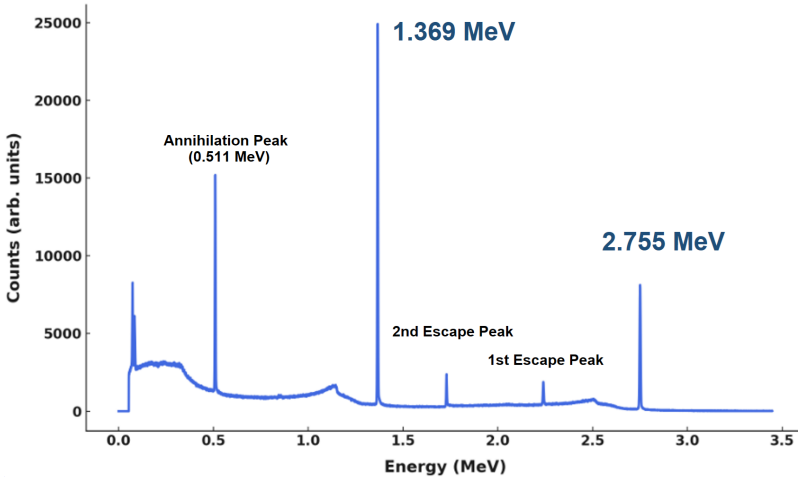

Figure 6.5: Pulse height spectra of ^{24}Na, obtained with the HPGe detector

After the HPGe detector measurements, the Al gamma-rays were measured with the prototype monitor and the energy peaks were accurately detected and observed in real-time. Figure 6.6 shows a screenshot of the prototype monitor. On the top half, the true information of the measured gamma-rays, the unfolded energy spectrum can be seen. Comparing with Figure 6.5, the two expected discrete gamma-rays from ^{24}Na are clearly observed in Figure 6.6. On the bottom half of Figure 6.6 the real-time graph of the estimated dose rate is shown.

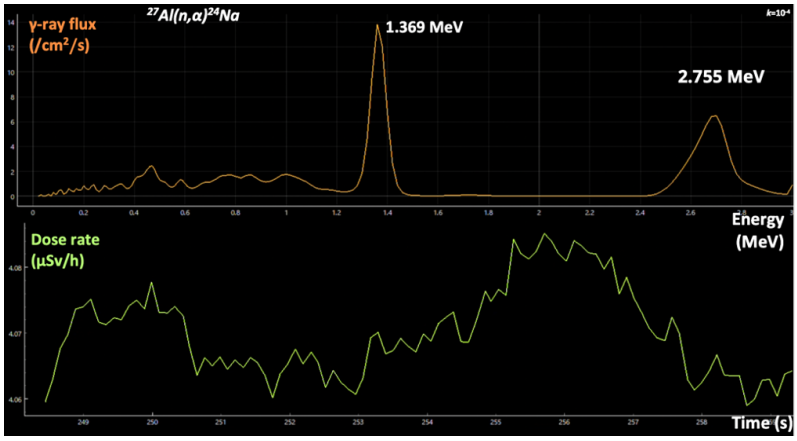

Figure 6.6: Screenshot of real-time measurement. Gamma-ray flux (top) and dose rate (bottom) are visualized in real-time (sec). The 1.369 and 2.755 MeV gamma-rays from ^{24}Na are clearly visible

Following the methodology detailed in Section 6.2.2, theoretical dose rate was calculated to be 4.05 μSv/h This value is compared with the experimental results obtained from real-time measurements (4.066 μSv/h with a standard deviation of 0.37% ($\pm$0.015)) and from the NaI survey meter (3.83 μSv/h), as shown in Fig. 6.7. The statistical error associated with the survey meter is 3.4%. The deviations from the theoretical value were found to be 0.4% for the prototype monitor and 5.43% for the survey meter.

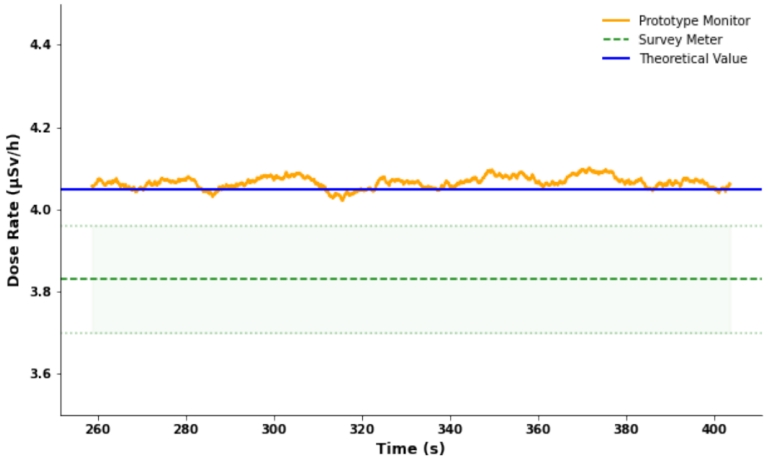

Figure 6.7: Comparison of measured dose rates: Prototype monitor, NaI survey meter, and theoretical value. Survey meter statistical error: 3.4%.

These findings suggest a consistency between the prototype monitor's readings and the theoretical calculations. Regarding the convergence time in these measurement conditions,

the dose rate stabilized after about 18-20 seconds, as shown in Figure 6.8, with k=10^{-3}. When setting k=10^{-3}, the dose rate converged after 130 s.

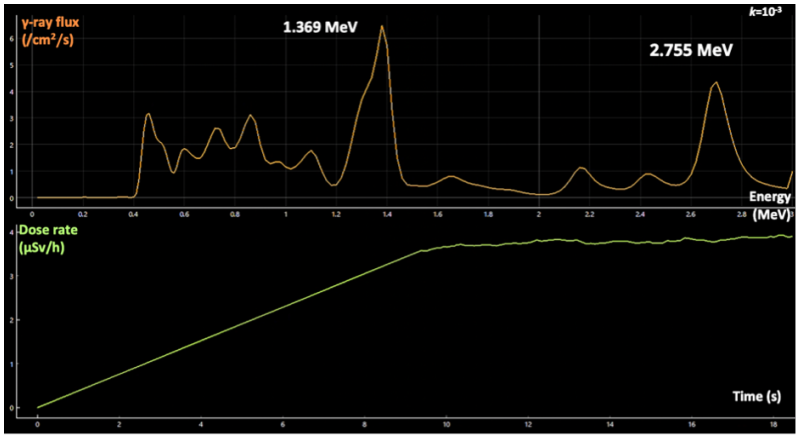

Figure 6.8: Screenshot of the start of measurement, after only a few seconds, during real-time unfolding. Gamma-ray flux and dose rate are visualized in real-time. Dose rate converges to the stable value

Overall the results showed that the prototype monitor can display the energy spectrum and dose rate of gamma-rays with energies up to around 3 MeV, with relative speed and good accuracy, better than an NaI survey meter as well. Further points of discussion are brought up in Subsection 7.3.1.

6.3 Current Research Problematics

Applying the present monitor to radiotherapy facilities, presents challenges, several of which have been successfully addressed so far. Verifying the monitor's performance in uncharacterized fields, determining a portable size small and capable enough for commercialization and confirming accuracy at around 3 MeV, a key value in radiotherapy settings. However, one of the more challenging aspects is the application to more complex forms of radiotherapy, like BNCT, is the accurate measurement of high energy gamma-rays and differentiation of neutron and gamma radiation contribution. Traditional dosimeters and radiation monitors struggle in measuring separately the dose contributions such conditions [203]. As mentioned in Chapter 3, combinations of detector and monitoring devices specialising in either contributions or specific particle energy ranges are commonly used for this exact reason.

The BNCT radiation field is complex, comprising of low energy neutrons, mainly epithermal, thermal neutrons and even some part fast neutrons, as well as high energy gamma-rays resulting from the neutron capture reaction and other interactions. The prototype gamma-ray monitor's ability to provide real-time data and detailed energy spectra would be very useful for informing the medical staff, while assisting in managing these radiation fields during BNCT procedures. Specifically for the prototype monitor the major challenges are:

- Neutron-Gamma Discrimination: The monitor must accurately differentiate between neutron and gamma events, particularly in the low-energy region where neutrons are dominant (mainly epithermal) and gamma-rays in the high energy region (up to around 10 MeV).
- Real-Time Data Processing: Adjusting the real-time data processing programs, including those that parse the data and execute the $k-\alpha$ method, so that it can handle the conditions of fields like those encountered in BNCT without introducing significant dead time or delays. In the case of increased dead time, corrections need to be applied.
- Portability: Ensuring that the monitor remains as lightweight and compact as possible, while integrating seamlessly with the added hardware necessary for operating in mixed fields conditions (increased weight and size due to addition of materials such as foils; addition of detector material in case of dual system etc.)

In this case, the epithermal neutrons can be captured by nuclei in the CsI(Tl) scintillator, leading to the emission of secondary radiation, such as beta or gamma-rays. This reaction can interfere with the detection of high-energy gamma rays by adding radiation contribution from the activated material itself, affecting the overall measurement. Apart from the neutron and gamma-ray discrimination, the designed monitor ideally needs to differentiate between thermal and epithermal neutron contribution. In environments with significant neutron dose contribution, accurate information of the neutron energy spectrum for each energy region can be beneficial and can even be used for dose reading corrections of various dosimeters [25]. Because the prototype monitor needs to measure in real-time, methods such as the one used by Hiramatsu et al., (2017) [203], utilizing attenuation of

neutrons and the ”lead filter” method for dose calculation of the two component are not applicable for real-time measurements.

6.4 Investigations for up to 10 MeV

In Section 6.2, regarding the verification of the prototype gamma-ray monitor's performance up to 3 MeV, the primary goal was to assess the accuracy and reliability in detecting gamma rays covering a range common in medical and industrial applications. In order to expand and cover gamma-rays of higher energies, the creation of an extended response function is necessary. By then applying the flux-to-dose conversion coefficient to the unfolded energy spectrum, given the accuracy of the created response function up to 10 MeV, accurate estimation can be realised. While as introduced in Chapter 2, most monitoring devices offer higher accuracy withing the 3 MeV range, research on response functions for detectors, including scintillator detectors, for gamma-rays up to 10 MeV have been created. Such as in the case of certain liquid scintillators [230]. Few background studies have tested the CsI(Tl) scintillator in applications with gamma-ray energies close to 10 MeV. Environmental spectrometry focused investigations, utilizing G(E) function based unfolding, have succeeded in creating 10 MeV response functions for various shapes and sizes of commonly used NaI(Tl) scintillation detectors [174]. Apart from the extension of the response function that is detailed in the following section, the in-house programs and primary files used were altered to accommodate for the new response matrix's larger size.

6.4.1 Response Function Extension and Further Considerations

The response function of the prototype monitor was extended to cover gamma rays up to 10 MeV. This extension involved mainly the same methodology described in Section 5.6, Monte Carlo simulations and experimental data usage, in order to accurately model the detector's response to high-energy gamma rays. When creating response functions up to 3 MeV, a response ”source” file is necessary, which covers the incident gamma-ray range and this was replaced to cover the new range. For the MCNP5 simulations the energy range was extended, retaining the early increments (energy widths). Figure 6.9 shows a part of the extended response matrix, specifically each response to every gamma-ray energy with 1 MeV increment up to 10 MeV.

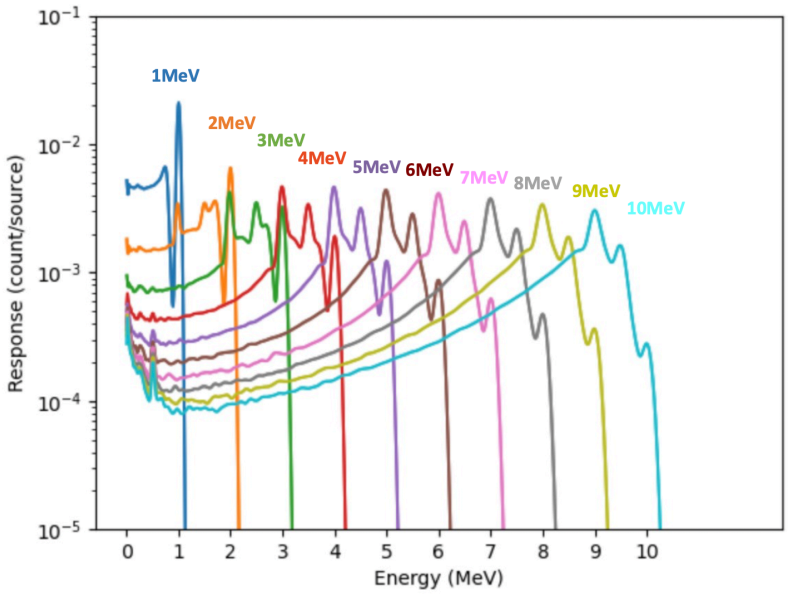

Figure 6.9: Response function of 2.6 x 2.6 x 2.6 cm^3 cubic CsI scintillator to monoenergetic gamma-rays up to 10 MeV

This means that while the previous response matrix's rows and columns covered a range of 3 MeV (incident gamma-ray energy) and 5 MeV (detector response) respectively, the updated matrix's rows and columns are 10 MeV and 12 MeV respectively. Discussion on the extended response function is elaborated upon in Section 7.4.1, however it can be seen that the performance might degrade after 4 MeV. Now, at higher energies, the risk of detector saturation increases, particularly if the flux of gamma rays is high. High-energy gamma rays can lead to pulse pile-up, where multiple events are recorded in quick succession, complicating the data analysis. The DP5's digital pulse processing capabilities are considered to be applicable in such conditions, due to allowing for dead time corrections [87]. MPPC investigations and inquiries with the manufacturing company, Hamamatsu photonics, suggest no preventing limitation in this scope regarding the performance of the MPPC if it is employed in such conditions, however a decline in energy resolution is expected.

Before discussing the mixed field problem in further detail, some future experimental considerations are briefly introduced. In terms of high energy gamma-ray only considerations, reactions such as (p,γ) resonance reactions, which can produce gamma-rays up to around 10 MeV and have been used for gamma-ray detector response function verifications

[230]. For example, the $^{13}C(p,\gamma)^{14}N$ gamma-rays cover a range of few hundreds of keV, with significant gamma-ray emissions at 2.31 MeV and 3.68 MeV, up to 9.17 MeV gamma-rays [231]. Additionally, the $^{19}F(p,\alpha\gamma)^{16}O$ reaction is notable for producing gamma-rays at 6.129 MeV and 7.115 MeV, which correspond to transitions within the ^{16}O nucleus as it de-excites. Regarding neutron utilizing experiments, experiments that involve the 4.44 MeV gamma-rays from an Am-Be source and a thick block of polyethylene, adjacent to a thinner Fe block, are considered. Additionally, $^{56}Fe(n,\gamma)$ reaction is known to produce 7.1 MeV gamma-rays [191]. To realise such a measurement, the CsI(Tl) scintillator crystal of the prototype monitor system may placed after them and be wrapped with either Cd or B containing foil. In contrast to the earlier experimental designs, using an Am-Be source introduces neutrons to the radiation field [232]. Similarly, the activation of water by fast neutrons, primarily through the $^{16}O(n,p)^{16}N$ reaction, results in the production of monoenergetic gamma-rays at 6.129 MeV and 7.115 MeV, contributing to significant high-energy gamma flux in neutron-rich environments [233], [234]. This activation is useful for understanding and simulating radiation fields in such mixed-field environments.

6.4.2 Investigation of Application of the Prototype monitor in mixed field and BNCT Practice

As mentioned in Chapters 2 and 3, there has been extensive research in developing radiation detection systems, dosimeters, spectrometers and monitors, for application in a mixed field of neutrons and gamma-rays. This chapter explores methods that the prototype monitor introduced in this dissertation and previous work, can operate at the conditions similar to a BNCT facility. In BNCT, apart from the wide range of gamma-rays that is present, a wide range of neutrons also poses a challenge in spectroscopy and dose calculation. The goal of the monitor is to be able to measure the neutron spectrum across these different energy regions introduced in Section 3.3.1. The thermal region could be measured using a single foil, providing a precise bin for thermal neutron detection. Regarding thermal neutrons, due to the Maxwell distribution that governs their energy distribution, this region cannot be effectively split into multiple energy subranges using different foils. This is why a single foil application is considered, and cadmium can fulfill this purpose because of its high cross-section for absorbing thermal neutrons. This ensures effective filtering and measurement of thermal neutrons. Beyond the thermal region, neutron energies can

be split into 6 to 10 bins, each corresponding to distinct energy ranges. The binning structure will be determined based on the response of the prototype monitor, with the goal of capturing neutron energies up to 1 MeV [56]. Epithermal neutrons, specifically in the region of 0.5 to 100 eV, materials with resonances within this range are needed to ensure accurate measurement. Gold (Au) and manganese (Mn) are good candidates as they exhibit strong resonance in the (n,γ) reaction. These materials allow for capturing neutrons within the epithermal range through neutron capture reactions, without direct radioactivation.

Regarding fast neutrons, very few neutrons over 1 MeV are present in BNCT [204]. Therefore, in the current iteration of the monitor, the measurement range was set at an upper limit of 1 to a few MeV. This decision was also made to align with the case of p-Li, where nuclear production reaction for ABNS is usually below 1 MeV (few hundred keV in the backward angle) [235]. However, in the case of p-Be reaction, the upper limit should be extended to 10 MeV. As mentioned throughout this thesis, direct neutron detection is challenging, therefore by "changing" the neutrons into gamma-rays, and measuring their contribution is a promising approach. Similar to a concept design by [156], where placing corresponding materials to induce certain prompt gamma-rays that will be detected by the scintillator. At the same time shielding the scintillator from direct interaction with neutrons is critical.

As introduced from the bibliography, cadmium is commonly used in nuclear measurements and in various applications in the nuclear industry, because of its property as an absorber of thermal neutrons. This property is a result of the element's very high cross-section for absorbing low-energy neutrons via the (n,γ) capture reaction. Cd can help in filtering neutron contribution [66]. For example in one of the applications described in Chapter 2, Cd is used because it absorbs thermal neutrons (below 0.4 eV), allowing only epithermal neutrons (1 eV - 1 keV) to pass, so the counts from the cadmium-covered detector (DCd) primarily reflect epithermal neutrons. Aluminium (Al) is also used allowing both thermal and epithermal neutron contributions and by applying mathematical corrections it is possible to differentiate and calculate the actual thermal and epithermal neutron counts based on the total readings [57]. Gadolinium and indium are also promising potential substitutes, but with some limitations in neutron absorption at specific energy

levels [236]. When considering the current scintillation detector, even with the use of Cd or B containing foils, not all necessary energy ranges are covered. Therefore the coupling with a scintillator such as NE-213 is considered. As discussed organic scintillators are mostly sensitive to fast neutrons. While usually coupled with bulkier PMTs, such scintillators types have been tested when coupled with MPPCs, increasing significantly their portability.

The capability of the DP5 for digital pulse processing is useful in the discrimination of neutron and gamma-ray contribution. Digital shaping is a verified way for pulse signal processing in mixed field cases [81]. Even though analog methods have more leeway in terms of dynamic range restrictions, performance is also dependent on the algorithm used. Since successful DPP approaches that utilize MPPC have been confirmed, the DP5 - MPPC pairing used in this research which is already optimized and well established for gamma-ray measurements, is promising. There is also precedent in NaI(Tl) - LiI(Eu) - DP5 pairing, albeit utilizing a PMT. In such a case, the advance pulse shape discrimination offered by the DP5 can distinguish between the gamma-ray and thermal neutron induced pulse shapes, the latter originating from the reaction with Li [237]. Therefore this computed optimization can potentially realise pulse shape discrimination in the future development of the prototype monitor.

6.4.3 CLYC, CLLBC Scintillators as Alternative Applicable Scintillators

In the process of investigating detector elements, many other scintillator materials, used in established detectors were examined and many were rejected. For example LiCaF cannot be used in this application due to the very low effective atomic number Z. A high effective atomic number is needed for successful neutron detection. Owning to the advantages described in Section 2.5, and having already been applied to BNCT in some capacity, the scintillators of the CLYC (Cs_2LiYCl_6) family are promising for incorporating into the prototype monitoring system. Scintillators of this family have been coupled successfully with MPPCs, used for neutron and gamma-ray discrimination and measuring the contribution of both components [111]. Spectrometers displaying both pulse height spectra and dose rate, as well as dosimeters, with sensitivity in both regions that were introduced in chapter 2, have been tested and commercialized. Furthermore, detectors in the CLYC family

have been investigated for fast neutron spectrometry in the energy range from approximately 1 MeV to 2 MeV using the ^{35}Cl(n,p)^{35}S reaction as the primary mechanism for proton generation, with successful implementation of pulse shape discrimination (PSD) techniques for separating neutron and gamma-ray signals [238]. Pulse digitization for eventual spectrometric applications have shown promising results albeit with PMT coupling [239]. However there are intricacies in applying these scintillators to the prototype monitor's configuration. The following points are considered:

- The scintillator must be compatible with multi-pixel photon counters (MPPCs) for effective neutron and gamma-ray discrimination, ensuring integration into the prototype monitoring system. Various researches have verified the effective coupling of this family of detectors with certain MPPCs [113], [115], [116], [118].
- Since the scintillator is hygroscopic, it requires quartz encapsulation to prevent moisture absorption. The encapsulation size should not hinder the overall portability of the monitor, ensuring that the detector remains compact and easy to transport.
- The scintillator should be compatible with digital pulse processors like the DP5, ensuring that the signal processing remains efficient and accurate for neutron and gamma-ray measurements. The DP5 - MPPC pairing used in this research is already well established and can perform PSD analysis in real-time with data stored in list mode for further analysis. With proper configuration, including adjustments to gain and shaping times, the DP5 can also handle CLYC scintillators, enabling effective neutron/gamma discrimination through their distinct pulse shapes and accurate energy resolution, even for slow decay times like those of CLYC.
- The setup must allow for applying sequential Bayesian estimation to the gamma-ray and neutron pulse height spectra (PHS) individually, enabling real-time unfolding of the energy spectra and calculation of the dose rate for each radiation component.

Alternatively, based on experimental results by various groups it could be applicable in specific neutron regions, such as fast neutrons [116], [240], to address current issues with fast neutron detection in the prototype monitoring configuration.

7 | Discussion

7.1 Introduction

This chapter discusses the findings compiled in this study, mainly in the order they were introduced, referencing other sections or prior relevant research when necessary.

7.2 Discussion on Design and Development

In this section the results, methodologies, conclusions and challenges introduced in Chapter 5 encompassing the published works [14]–[16] are discussed. Before delving into the discussion, the key concepts and points are reiterated:

- In simple terms, it is useful to have a device that can show the true unfolded energy spectrum and the dose rate, to the medical staff, in real-time. Seeing the actual information of the field is useful, and being aware of the dose rate at all times with high accuracy helps with awareness, protection and prevents unwanted exposure.
- In order to derive those two, unfolding of the energy spectrum is necessary. To reiterate, as introduced in Section 2.8, the basic concept of the usage of Bayesian estimation is to realise this unfolding process. This is achieved by associating the well known equation of the Bayes' theorem with the components of the basic form of the unfolding problem, that links the pulse height spectrum, the true gamma-ray energy spectrum, and the response function of the detector.
- For the derivation of the dose rate, a flux-to-dose conversion coefficient is applied.
- In order to achieve the above, the spectrum type Bayesian estimation forms the basis, but is not applicable as it revises the spectrum after the measurement to derive the energy spectrum.
- The sequential Bayesian estimation revises the energy spectrum for every count. The energy spectrum is thus continuously updated as new data come in, improving the estimation, as the estimated posterior probability become the prior probability for the next estimation.

- The parameter α is introduced to the sequential Bayesian estimation in order to speed up the convergence of the estimation to the stable value, however issues arise when the α is a set value, and thus the $k{-}\alpha$ method is introduced to ensure quick and stable updates of the energy spectrum as new data comes in, with a varying α value. The theory of this method was introduced in Section 5.3, the results of this investigation were presented in Section 5.8.2 and are further discussed in the following section.

7.2.1 *k*-α Method Verification discussion (Murata, Voulgaris et al., 2024) [14]

As illustrated by the results, a large α value leads to fast convergence (less counts needed for convergence) but the values are unstable, whereas a small α value leads to slower revision rate, but higher accuracy (stability) of the results. This indicates that early on (few counts), α needs to be larger and as counts increase α needs to become smaller. To achieve both fast convergence and high accuracy, the $k{-}\alpha$ method was introduced to update the α dynamically as counts increase and the two methods (α and $k{-}\alpha$) were evaluated and compared.

Comparing the estimated gamma-ray energy spectra of ^{60}Co in Figures 5.15a and 5.15b showed similar convergence (similar spectrum shape) for $\alpha = 10^{-3}$ and $\alpha = 10^{-4}$ for different times (30 s and 300 s respectively). This result highlights that adjusting α appropriately allows for an acceptably converged spectrum within few tens of seconds. Regarding the stability of estimation, it needs to be pointed out what has been discussed in bibliography as well, that for the spectrum type Bayesian estimation described mainly by Equation 2.16, significantly increasing iteration numbers can lead to over-revision, yielding unstable estimation results [241]. As a trait considered to be inherent to the method of applying Bayesian inference, at a high number of counts or at a big enough α value, this phenomenon seems to occur in the sequential Bayesian estimation as well, explaining potentially the less than ideal results in the case of $\alpha = 10^{-2}$. Since in all other cases, similar unstable results are not observed, the effect of this hypothesized over revision can be ignored for actual application, since it would need an incredibly long measuring time in medical application conditions for such over-revision to potentially occur when $\alpha \leqq 10^{-3}$.

Regarding the dose rate estimation, reading Figure 5.16, from the comparison with the theoretical and NaI survey meter values, for $\alpha = 10^{-3}$ and $\alpha = 10^{-4}$, accuracy improved within ~5 seconds and ~40 seconds respectively. The performance for $\alpha = 10^{-2}$ was not displayed and is unsuitable for application as it takes too long to converge. Choosing between $\alpha = 10^{-3}$ and $\alpha = 10^{-4}$ is related to the balance of accuracy and speed of results, that being, how fast the medical staff can get a fairly well converged accurate dose rate reading. This graph highlights the issue with the α method and the desire to allow for α to change dynamically, leading to the development of the $k{-}\alpha$ method.

For the $k{-}\alpha$ method investigation results, the same experimental values were used. Energy spectrum results at 300 seconds for $k = 10^{-4}$ and $\alpha = 10^{-4}$, shown in Figure 5.17, demonstrated similar performance. Comparing how the energy spectrum changes over time for the α and $k{-}\alpha$ methods shows that the energy spectrum reaches a value closer to the converged value faster with the latter. This is apparent when comparing Figures 5.17 and 5.18. At 30 s, the $k{-}\alpha$ method result is closer to the eventual converged value, while the α method result's shape is more stable. Supported by Figure 5.19 where the $k{-}\alpha$ method shows a much faster reduction in error, these results reinforce the fact that $k{-}\alpha$ method provides faster a good estimation of the spectrum early on until the eventual convergence.

However, judging the methods only with the shape of the spectrum can be challenging. A dose rate evaluation (an integral value of the spectrum), as a qualitative approach in discussion is more straightforward. When comparing the dose rate estimation results of the two methods in Figures 5.16 and 5.20, it is apparent that when $k = 10^{-4}$, convergence to the theoretical value is reached much faster than with the α method when α is 10^{-4}. Additionally, for $k = 10^{-5}$, the convergence was too slow, leading to a result for the dose rate that is not accurate enough in a reasonable time. Therefore, considering application for conditions of around 6 Sv/h, the $k{-}\alpha$ method with $k = 10^{-4}$ proved it can produce stable, accurate dose values within several seconds, and display the energy spectrum within tens of seconds.

Now, in order to judge not just the time it takes for estimation but also the accuracy of the dose rate values, Table 5.6 compared dose rates measured with the $k{-}\alpha$ method ($k = 10^{-4}$), survey meter, and theoretical values. For ^{137}Cs, all methods agreed, but

expected discrepancies were observed for the NaI survey meter for ^{133}Ba (overestimation) and ^{60}Co (underestimation). As mentioned throughout the investigations in this research, this is because the survey meter has been calibrated for ^{137}Cs, whereas the $k{-}\alpha$ method uses the measured gamma-ray energy spectrum and the flux-to-dose conversion coefficient, resulting in more accurate measurements for other sources even further away from the 662 keV peak of ^{137}Cs.

Overall, the findings showed that the $k{-}\alpha$ method demonstrated improved performance in dose estimation. Dose rates were accurately estimated as seen from the close values of $k{-}\alpha$ method and theoretical values. Using the obtained energy spectra and flux-to-dose conversion coefficients, stable values were obtained within a few seconds under measurement conditions of around 6 μSv/h. The energy spectrum was shown within tens of seconds. The case of $k = 10^{-4}$ provided a good balance between stability and speed, while $k = 10^{-2}$ exhibited critical instability. In the evaluations with ^{133}Ba, ^{137}Cs, and ^{60}Co, the monitor accurately reflected the dose contributions, even with complex energy spectra, making it suitable for real-time applications in environments with unknown gamma-ray distributions. As presented in Section 5.3.1, when k is small, the number of counts required for one round ($1/k$) are high. While in general measuring for increased time aids in agreement of estimation and theoretical values, what can be derived from the results of this investigation is that the value of k needs to be set according to the count rate present and by extension, it is important to consider the intensity of the radiation field at the application spot. While currently, as described in Section 5.5, the k value is input in a custom program before initiating measurement, effort is being made to make this process easier for the medical stuff by integrating a k value switch on the device, allowing for ease of choice on the spot, depending on the environment conditions, even when the spectrum is not known.

7.2.2 CsI(Tl) Crystal Size Evaluation Discussion (Voulgaris et al., 2024) [15]

This part of the research investigated the impact of different CsI(Tl) crystal sizes on the performance of the prototype monitor. Overall, this assessment helped to determine acceptable performance levels for the application, such as which size allows for faster

estimation, and evaluated the general practicality of the prototype monitor. Looking at the figure of scintillators of same volume but different thickness, a slight improvement in detection efficiency was observed for crystal thicknesses of 1 - 1.3 cm (Figure 5.22). In this region, sufficient material allows for absorption of gamma rays and minimizing internal scattering or losses. The optical path that needs to be travelled until light reaches the photo-receiving surface of the MPPC is short, but not too short. On the thinner side, (less than 1 cm), fewer material for gamma-ray interactions, likely leads to fewer events detected. At high thickness, light generated inside the crystal has a longer path to travel before reaching the MPPC . A longer optical path increases the chances of light scattering or being absorbed before detection, reducing efficiency. Also, because volume is constant, the gamma-ray incident surface area decreases. In terms of energy resolution, the 2.6 $\times$ 2.6 $\times$ 1.3 cm^3 crystal (with the gamma-rays incident on the wide surface) and the 2.6 $\times$ 2.6 $\times$ 2.6 cm^3 crystal showed better performance than the 2 $\times$ 2 $\times$ 2 cm^3 and thinner crystals (Figure 5.24). Table 7.1 summarizes in a simplified manner the main findings and conclusions of the scintillator size investigation.

Table 7.1: Summary of CsI(Tl) crystal size performance.

Crystal Size (cm^3)	**Volume (cm^3)**	**Detection Efficiency**	**Energy Resolution**	**Dose Rate Convergence (BG)**	**Portability**
2.6×2.6×2.6	17.6	Best	Best	20 s	Heaviest (80 g)
2.6×2.6×1.3	8.8	Slightly lower than 17.6cm^3 one	Near equal to 17.6 cm^3 one	35 s	Lighter (39.6 g)
2×2×2	8	Worst	Worst	35 s	Lightest (36.1 g)

The dose rate converged rapidly for standard gamma-ray sources, and background field evaluations showed a convergence time of 20 s for the 2.6 $\times$ 2.6 $\times$ 2.6 cm^3 crystal, while the 2 $\times$ 2 $\times$ 2 cm^3 and 2.6 $\times$ 2.6 $\times$ 1.3 cm^3 crystals converged in 35 s. The smaller crystals, though slightly slower in dose convergence speed, weighed half as much as the 2.6 $\times$ 2.6 $\times$ 2.6 cm^3 crystal, improving portability. Specifically, the 2.6 $\times$ 2.6 $\times$ 1.3 cm^3 and 2 $\times$ 2 $\times$ 2 cm^3 crystals weighed 39.6 g and 36.1 g, respectively, compared to 80 g for the 2.6 $\times$ 2.6 $\times$ 2.6 cm^3 crystal.

The similar volumes of the 2.6 $\times$ 2.6 $\times$ 1.3 cm^3 and 2 $\times$ 2 $\times$ 2 cm^3 crystals suggest that increasing surface area and reducing thickness enhanced light collection efficiency by shortening the scintillation light travel path. This agrees with studies reporting light loss or reports on timing resolution worsening in thicker crystals [49], [50]. For practical applications, considering size, weight, and performance, the 2.6 $\times$ 2.6 $\times$ 1.3 cm^3 crystal

is preferred, offering a balance between efficiency, resolution, and portability. EMF Japan who is currently developing the actual device, is utilizing a similar $2.5 \times 2.5 \times 1.25$ cm^3 crystal coupled to an S1416102302 MPPC. This development is important in the field of designing more effective and portable radiation monitors for medical radiation workers. More developmental schematics and details are included in Appendix A .

Since response functions play a core role in this research it is important to comment upon the shapes of the response functions shown in Figures 5.27a and 5.27a. In both cases, single and double escape peaks appear above 2 MeV, with the single escape peak at 3 MeV being similar in intensity to the full-energy peak, suggesting potential energy loss and affecting accurate gamma-ray spectrum reconstruction after 3 MeV.

7.2.3 Real-time verification discussion (Voulgaris et al., 2024) [16]

Since the population utilizing resampling methodology has been confirmed in previous studies [135] and Section 5.8.2, if the true real-time measurements with the DP5 digital pulse processor agree with the results of the verified method, then the true real-time methodology is one step closer to actual application. In the results presented in Section 5.9, the real-time estimated values obtained using the DP5 system were consistent with those from the resampling method performed with the MCA8000D, confirming the effectiveness of real-time gamma-ray spectrum and dose estimation using digital pulse processing and custom in-house developed software. While there were slight deviations compared to theoretical and survey meter values, these differences were attributed to the short distance (5 cm) between the radiation source and the scintillation crystal. To reiterate, the 5 cm distance between the source and the surface of the scintillator was even shorter than twice the size of one side of the scintillator, affecting the accuracy during data acquisition. The NaI survey meter—calibrated specifically for ^{137}Cs—showed differences compared to other sources such as ^{133}Ba where the value is overestimated and ^{60}Co where it is underestimated. This discrepancy of the NaI aligns with findings from previous studies [135] and in the Sections 5.8.2 and 7.2.1.

The short distance also affected the NaI survey meter and ^{137}Cs measurement, which should match with higher accuracy, since the survey meter is calibrated using the 662 keV peak of ^{137}Cs. The short distance was used to increase the counting rate and reduce

the background effects since the objective of this part of the research was to compare the true real-time estimation method with the verified resampling method; however, for more accurate comparisons between estimated and theoretical values, increasing the source-to-crystal distance reduces errors due to proximity. Additionally, error propagation in the Bayesian estimation process has yet to be fully resolved, and as a result, error bands were not plotted in the current analysis. In subsequent investigations of higher energies, the accuracy of this configuration is demonstrated as shown in Section 6.2 and discussed in the subsequent Section 7.3.1. Overall, the study successfully demonstrated that real-time gamma-ray spectrum and dose rate can be estimated using the DP5 system, providing a practical solution for real-time radiation monitoring, with the results matching those obtained through resampling post-measurement.

7.3 Discussion on Radiotherapy Facility Application

7.3.1 Verification of Experiments up to 3 MeV (Voulgaris et al.[Under Review] [17])

Regarding the energy spectrum estimation, as seen in the top graph of Figures 6.6 and 6.8, the unfolded spectrum was successfully visualized in real-time. Unwanted noise and peaks, such as the escape peaks visible in the pulse height distribution of the HpGe detector measurement, were removed and the true information of the incoming gamma-rays was restored. Overall, the dose rate measurements and calculations conducted, support the potential of the prototype monitor. The monitor's measured dose rate closely matched with the theoretical value, while the NaI survey meter showed expected differences when compared to them, due to its calibration using a ^{137}Cs source at 0.662 MeV. As demonstrated in Figure 6.7, the NaI survey meter underestimated the dose rate for higher energy gamma-rays. As discussed throughout these investigations, devices calibrated at a single energy point tend to overestimate dose rates at energies below the calibration point and underestimate at energies above it, but the prototype monitor is not subject to these calibration constraints due to its capacity for direct, real-time energy spectrum measurement and application of flux-to-dose conversion coefficient, allowing for accurate dose estimation across a broad range of gamma-ray energies. By setting the parameter k of the $k-\alpha$

method accordingly, convergence to a stable value is achieved in around 18-20 s as shown in Figure 6.8. For comparison, when setting the time constant to 30 s in the NaI survey meter, it requires $30 \times 3 = 90$ seconds to produce a stable result that is as accurate as its functions allow. Faster readings can be provided by the survey meter by adjusting the time constant, however, it was set to 30 s in order to increase accuracy for the sake of comparison and provide a stable result, as has been done in existing research as well [136]. Overall, the results highlight the prototype monitor's advantage in environments with gamma-rays close to 3 MeV. Even with slight deviations, the successful unfolding of high energy gamma-ray spectra, speed and accuracy are promising in terms of actual application.

In all gamma-ray energy spectra derived from real-time unfolding, when compared to pulse height spectra of the HpGe detector for example, the annihilation gamma-rays are not visible, such as when comparing Figures 6.5 and 6.6. This is because the 511 keV annihilation gamma-rays are included in the response function of the monitor. The 511 keV peak does not appear independently; it appears when energies over 1.022 are present. For the creation of the response function, sources over 1.022 MeV were utilized, which lead to the production of annihilation gamma-rays outside the detector. The HPGe measurement shows the raw pulse height distribution without unfolding. Therefore, the 511 keV peak from annihilation gamma-rays is distinctly visible as a separate peak. In contrast, the unfolding process for the spectrum in Figure 6.6 uses the response function, which already incorporates the effects of these annihilation events. As a result, the 511 keV peak does not appear independently in the unfolded spectrum.This difference arises because the unfolding process aims to reconstruct the incident gamma-ray spectrum as accurately as possible by deconvoluting the detected signals based on the response function, which inherently includes the effects of secondary gamma-rays such as the 511 keV annihilation peak. This stands true also in the case of measurements with ^{60}Co, where energies over 1.022 are present, and in the pulse height spectra an annihilation peak is visible, however, in the unfolded spectra, apart from the main photopeaks, only the backscattering peak remains. Similarly, the two Compton edges, one for each photopeak of ^{60}Cs, are not visible in the unfolded spectrum, as expected.

7.4 Challenges and Improvements of current research

In the development of this prototype monitor, several significant challenges had to be overcome, but some more still need to be addressed in the future, mainly regarding the intricacies of the error propagation in Bayesian inference and the implementation of necessary components for use in a mixed field of neutrons and gamma-rays, in order to consider all aspects for application during irradiation, such as in the case of Accelerator Based BNCT.

7.4.1 Regarding Energy Extension and Mixed Field Investigation

As shown in Section 6.4, Figure 6.9, even with monoenergetic gamma-ray irradiation, at high gamma-ray energies, three peaks become visible, and the photoelectric peak no longer is the main peak. A single escape peak and a double escape peak appear due to pair production starting from 2 MeV. At 3 MeV, there is not a significant difference between the photoelectric peak and the escape peaks. Furthermore, when observing the detector' s response to gamma-rays of 4 MeV and higher, it becomes clear that as the energy increases, the response at the photoelectric peak decreases gradually but significantly, while the response at the escape peaks increases notably. This reduction in the photoelectric peak response at higher energies could be attributed to factors such Compton scattering spreading the deposited energy over a wide range, resulting in a broad continuum rather than a distinct peak, which reduces the prominence of the photoelectric peak. Significantly high double and single escape peaks could be caused by the more active pair production at higher energies. In contrast, when creating response functions up to 3 MeV, for the various sizes and shapes of CsI(Tl) scintillators, the shape of the response functions was very simple, as seen in Figure 5.11. Additionally, as seen by the shape of the extended response function, additional changes to the software need to be made to account for the altered programs and accurately unfold the energy spectra.

Furthermore, apart from the extension of the response function, one of the primary challenges is the detection of neutrons in the energy range of 1-10 keV as introduced in Section 7.4.1. Introducing another scintillator material, a resonance foil or a secondary digital pulse processing systems leads to additional complexities, such as increased weight

and potential issues with detector sensitivity and response time. This additional weight can be a significant drawback in the portability which is one of the most important aspects of the monitor in order to consider eventual application in mixed field scenarios. Furthermore, ensuring the accuracy of measurements when the detector is moved between locations with different radiation intensities presents another set of challenges. With the DP5 implementation, the integration of real-time digital pulse processing techniques, while offering significant advantages in terms of accuracy and speed, introduces challenges related to pulse pile-up in high count rate scenarios. Managing these aspects is needed to ensuring that the system can provide accurate dose rate and energy spectrum readings in fields far more complex than the already tested and verified gamma-ray only environments.

8 | Conclusion

In conclusion, this thesis presents the successful development and validation of a prototype real-time gamma-ray monitor capable of measuring the energy spectrum and dose rate of gamma-rays in real-time, in complex radiation environments. The device, primarily built around a CsI(Tl) scintillator, an MPPC, and a DP5 digital pulse processor, addresses a significant need in radiation therapy facilities for accurate and portable monitoring. Through a series of experiments and simulations, the prototype monitor demonstrated its ability to provide reliable data, making it suitable for use in many medical radiotherapy environments, outside of during operation. The improved Bayesian estimation method $k{-}\alpha$ method was successfully verified and compared with the α method, highlighting its advantages. Among a few scintillator configurations, the most optimal one was found, which is also used in actual developmental application this moment. These results allowed for the realization of true real-time estimation with digital pulse processing, in scenarios which reached almost 3 MeV energy of gamma-rays.

The research validated the device's performance in true real-time through several key experiments, notably the ^{24}Na irradiation experiment using aluminum foil at the DT neutron source in OKTAVIAN facility, in Osaka University. In this experiment, the gamma-ray spectra were successfully unfolded in real-time and the 1.369 MeV and 2.754 MeV peaks identified. The dose rate values also were also highly accurate. These findings confirmed the prototype monitor's ability to measure gamma rays up to 2.754 MeV with accuracy. Furthermore, the response function creation extended beyond 3 MeV, reaching 10 MeV and discussions were introduced regarding high energy applications. These initial steps mark a significant step in preparing the monitor for application in mixed radiation fields of neutrons and gamma-rays, where high energy gamma-rays are present. This aims to eventually adapting the monitor for potential use in environments such as Boron Neutron Capture Therapy (BNCT).

While the prototype monitor demonstrated promising results, there are still challenges to overcome, particularly in achieving precise measurements in mixed neutron-gamma fields. Future improvements should focus on refining the monitor's neutron detection capabilities, enhancing the accuracy of dose rate measurements for gamma rays beyond 3

MeV, and further validating its performance in real-world radiation therapy settings.

In summary, the development of this real-time gamma-ray monitor is an important advancement in radiation monitoring technology. The actual device is being produced and refined by EMF Japan Co. Ltd., while optimizations and improvements are constantly being made. By providing accurate real-time dose and energy spectrum measurements in a portable format, the monitor holds great potential for improving radiation safety in medical, industrial, and research environments. The initial direction taken toward high-energy and mixed-field applications, along with the creation of response functions for gamma rays up to 10 MeV, pave the way for further advancements that will hopefully enhance the device's utility and applicability.

Bibliography

[1] T. Henriksen, H. D. Maillie, and T. Henriksen, *Radiation and health*, Engl. ed., 1. publ. London: Taylor & Francis, 2003, 226 pp., ISBN: 978-0-415-27162-2 978-0-415-27161-5.

[2] IAEA. "The IAEA directory of radiotherapy centres (DIRAC)." (), [Online]. Available: https:/dirac.iaea.org/ (visited on 01/08/2024).

[3] U. Amaldi, R. Bonomi, S. Braccini, *et al.*, "Accelerators for hadrontherapy: From lawrence cyclotrons to linacs," *Nuclear Instruments and Methods in Physics Research Section A: Accelerators, Spectrometers, Detectors and Associated Equipment*, vol. 620, no. 2, pp. 563–577, Aug. 2010, ISSN: 01689002. DOI: 10.1016/j.nima.2010.03.130. [Online]. Available: https://linkinghub.elsevier.com/retrieve/pii/S0168900210007357 (visited on 09/06/2024).

[4] M. Sasaki and T. Fujibuchi, "Development of the system of radiological protection and medical exposure: Basic information and trends," *Radiation Environment and Medicine*, vol. Vol.9, no. 2, pp. 105–110, 2020.

[5] H. Matsumura, G. Yoshida, A. Toyoda, *et al.*, "Investigation of concrete radioactivation in cyclotron type proton therapy facilities using in situ ^{24}na measurement method," *Radiation Safety Management*, vol. 21, no. 0, pp. 13–25, 2022, ISSN: 1347-1511, 1884-9520. DOI: 10.12950/rsm.200909. [Online]. Available: https://www.jstage.jst.go.jp/article/rsm/21/0/21_200909/_article (visited on 04/23/2024).

[6] L. Donadille, F. Trompier, I. Robbes, *et al.*, "Radiation protection of workers associated with secondary neutrons produced by medical linear accelerators," *Radiation Measurements*, vol. 43, no. 2, pp. 939–943, Feb. 2008, ISSN: 13504487. DOI: 10.1016/j.radmeas.2008.01.018. [Online]. Available: https://linkinghub.elsevier.com/retrieve/pii/S1350448708000371 (visited on 04/23/2024).

[7] M. Abdel-Wahab, S. S. Gondhowiardjo, A. A. Rosa, *et al.*, "Global radiotherapy: Current status and future directions—white paper," *JCO Global Oncology*, no. 7, pp. 827–842, Dec. 2021, ISSN: 2687-8941. DOI: 10.1200/GO.21.00029. [Online]. Available: https://ascopubs.org/doi/10.1200/GO.21.00029 (visited on 08/30/2024).

[8] IAEA, *Radiation Protection and Safety in Medical Uses of Ionizing Radiation: Specific Safety Guide*. Vienna: IAEA, 2018, OCLC: 1108568089, ISBN: 978-92-0-101717-8.

[9] S. Sharma and M. S. Sarkar, "Measurement and simulation of gamma-ray background in a low energy accelerator facility," *Journal of Instrumentation*, vol. 15, no. 9, T09003–T09003, Sep. 7, 2020, ISSN: 1748-0221. DOI: 10.1088/1748-0221/15/09/T09003. [Online]. Available: https://iopscience.iop.org/article/10.1088/1748-0221/15/09/T09003 (visited on 05/06/2024).

[10] K. Polaczek-Grelik, A. Kawa-Iwanicka, M. Rygielski, and Ł. Michalecki, "Gamma radiation in the vicinity of the entrance to linac radiotherapy room," in *Use of Gamma Radiation Techniques in Peaceful Applications*, B. A. Almayah, Ed., IntechOpen, Oct. 2, 2019. DOI: 10.5772/intechopen.82726. [Online]. Available: https://www.intechopen.com/books/use-of-gamma-radiation-techniques-in-peaceful-applications/gamma-radiation-in-the-vicinity-of-the-entrance-to-linac-radiotherapy-room (visited on 04/24/2024).

[11] F. Qureshi, A. Ramprasad, and B. Derylo, "Radiation monitoring using personal dosimeter devices in terms of long-term compliance and creating a culture of safety," *Cureus*, Aug. 14, 2022, ISSN: 2168-8184. DOI: 10.7759/cureus.27999. [Online]. Available: https://www.cureus.com/articles/103833-radiation-monitoring-using-personal-dosimeter-devices-in-terms-of-long-term-compliance-and-creating-a-culture-of-safety (visited on 05/01/2024).

[12] E. Lee, C.-W. Lee, and G. Cho, "Radiation safety analysis for the a-BNCT facility in korea," *Applied Radiation and Isotopes*, vol. 142, pp. 92–103, Dec. 2018, ISSN: 09698043. DOI: 10.1016/j.apradiso.2018.09.022. [Online]. Available: https://linkinghub.elsevier.com/retrieve/pii/S0969804318304664 (visited on 04/23/2024).

[13] IAEA, *Occupational Radiation Protection: Enhancing the Protection of Workers – Gaps, Challenges and Developments : proceeding of an international conference organized by the International Atomic Energy Agency, co-sponsored by the International Labour Organization and held in Vienna, 1-5 December 2014*. Vienna: International Atomic Energy Agency, 2022, OCLC: 1349865049, ISBN: 978-92-0-122422-4.

[14] I. Murata, N. Voulgaris, T. Miyoshi, *et al.*, "Real-time gamma-ray energy spectrum / dose monitor with k- method based on sequential bayesian estimation," *Applied Radiation and Isotopes*, vol. 212, p. 111 454, Oct. 2024, ISSN: 09698043. DOI: 10.1016/j.apradiso.2024.111454. [Online]. Available: https://linkinghub.elsevier.com/retrieve/pii/S0969804324002823 (visited on 08/18/2024).

[15] N. Voulgaris, H. Nishimura, S. Tamaki, S. Kusaka, and I. Murata, "Balancing performance and portability: A study on CsI(tl) crystal sizes for real-time gamma-ray spectrum and dose monitoring," *Radiation*, vol. 4, no. 3, pp. 213–223, Jul. 3, 2024, ISSN: 2673-592X. DOI: 10.3390/radiation4030016. [Online]. Available: https://www.mdpi.com/2673-592X/4/3/16 (visited on 09/05/2024).

[16] N. Voulgaris, T. Miyoshi, S. Tamaki, S. Kusaka, and I. Murata, "Development of real-time gamma-ray spectrum and dose monitor investigation of true real-time convergence," in *Proceedings of the 37th Workshop on Radiation Detectors and their uses*, Tsukuba, Ibaraki, Japan: High Energy Accelerator Research Organization (KEK), 2024, pp. 30–42.

[17] N. Voulgaris, S. Tamaki, J. Qiu, S. Kusaka, and I. Murata, "Simultaneous measurement of gamma-ray energy spectrum and dose in real-time up to 3 MeV with sequential bayesian estimation and CsI(tl) scintillator-based prototype monitor," *[Under Review]*,

[18] G. F. Knoll, *Radiation detection and measurement*, 4th ed. Hoboken, N.J: John Wiley, 2010, 830 pp., OCLC: ocn612350364, ISBN: 978-0-470-13148-0.

[19] E. B. Podgoršak and International Atomic Energy Agency, Eds., *Radiation oncology physics: a handbook for teachers and students*, OCLC: ocm61877454, Vienna: International Atomic Energy Agency, 2005, 657 pp., ISBN: 978-92-0-107304-4.

[20] R. E. Faw and J. Shultis, "Radiation sources," in *Encyclopedia of Physical Science and Technology*, Elsevier, 2003, pp. 613–631, ISBN: 978-0-12-227410-7. DOI: 10.1016/B0-12-227410-5/00636-0. [Online]. Available: https://linkinghub.elsevier.com/retrieve/pii/B0122274105006360 (visited on 09/03/2024).

[21] IAEA, *Cold Neutron Sources: Practical Considerations and Modern Research* (TECDOC Series 2025). Vienna: INTERNATIONAL ATOMIC ENERGY AGENCY, 2023, ISBN: 978-92-0-139423-1. [Online]. Available: https://www.iaea.org/

publications/15409/cold-neutron-sources-practical-considerations-and-modern-research.

[22] IAEA, "Interactions of radiation with matter- neutron shielding."

[23] M. F. L'Annunziata, *Handbook of radioactivity analysis*, 2nd ed. San Diego: Academic Press, 2003, ISBN: 978-0-12-436603-9.

[24] IAEA, *Advances in Boron Neutron Capture Therapy*. Vienna: International Atomic Energy Agency, 2023, OCLC: 1406409333, ISBN: 978-92-0-132623-2.

[25] IAEA, *Occupational Radiation Protection: General Safety Guide*. Vienna: IAEA, 2018, OCLC: 1108531988, ISBN: 978-92-0-102917-1.

[26] A. Furuhashi, K. Matsumoto, and M. Obu, "Measuring the Ratio of Epi-thermal to Thermal Neutron Densities Using Thick Gold Foils," *Journal of the Atomic Energy Society of Japan / Atomic Energy Society of Japan*, vol. 2, no. 7, pp. 394–400, 1960, ISSN: 0004-7120. DOI: 10.3327/jaesj.2.394. [Online]. Available: http://www.jstage.jst.go.jp/article/jaesj1959/2/7/2_7_394/_article/-char/ja/ (visited on 09/03/2024).

[27] IAEA, Ed., *Compendium of neutron spectra and detector responses for radiation protection purposes: supplement to Technical reports series no. 318*, Technical reports series / International Atomic Energy Agency 403, Vienna: IAEA, 2001, 337 pp., ISBN: 978-92-0-102201-1.

[28] IAEA, "Modern neutron detection proceedings of a technical meeting," IAEA-TECDOC–1935 52019798, 2020. [Online]. Available: https://www-pub.iaea.org/MTCD/Publications/PDF/TE-1935_web.pdf.

[29] Nuclear Regulation Authority, *Method for Measurement of Environmental Gamma-rays with a Continuous Monitor, "Environmental Radioactivity and Radiation in Japan."* (The series of environmental radioactivity measuring methods 17). Radiation Monitoring Division Radiation Monitoring Department Nuclear Regulation Authority, 2017, 156 pp. [Online]. Available: https://www.kankyo-hoshano.go.jp/en/library-en/series-en/ (visited on 04/20/2024).

[30] K. Boukeffoussa and K. Bouakaz, "Analytical method for calculating the efficiency and solid angle of an NaI(tl) detector," *Applied Radiation and Isotopes*, vol. 173, p. 109 708, Jul. 2021, ISSN: 09698043. DOI: 10.1016/j.apradiso.2021.

109708. [Online]. Available: https://linkinghub.elsevier.com/retrieve/pii/S0969804321001160 (visited on 05/10/2024).

[31] J.-H. Cheng, Z. Wang, L. Lebanowski, G.-L. Lin, and S. Chen, "Determination of the total absorption peak in an electromagnetic calorimeter," *Nuclear Instruments and Methods in Physics Research Section A: Accelerators, Spectrometers, Detectors and Associated Equipment*, vol. 827, pp. 165–170, Aug. 2016, ISSN: 01689002. DOI: 10.1016/j.nima.2016.05.010. [Online]. Available: https://linkinghub.elsevier.com/retrieve/pii/S0168900216303680 (visited on 05/12/2024).

[32] T. Yanagida, "Inorganic scintillating materials and scintillation detectors," *Proceedings of the Japan Academy, Series B*, vol. 94, no. 2, pp. 75–97, 2018, ISSN: 0386-2208, 1349-2896. DOI: 10.2183/pjab.94.007. [Online]. Available: https://www.jstage.jst.go.jp/article/pjab/94/2/94_PJA9402B-02/_article (visited on 04/22/2024).

[33] R. Hawrami, E. Ariesanti, A. Farsoni, D. Szydel, and H. Sabet, "Growth and evaluation of improved CsI:tl and NaI:tl scintillators," *Crystals*, vol. 12, no. 11, p. 1517, Oct. 25, 2022, ISSN: 2073-4352. DOI: 10.3390/cryst12111517. [Online]. Available: https://www.mdpi.com/2073-4352/12/11/1517 (visited on 04/24/2024).

[34] F. Gramuglia, S. Frasca, E. Ripiccini, *et al.*, "Light extraction enhancement techniques for inorganic scintillators," *Crystals*, vol. 11, no. 4, p. 362, Mar. 30, 2021, ISSN: 2073-4352. DOI: 10.3390/cryst11040362. [Online]. Available: https://www.mdpi.com/2073-4352/11/4/362 (visited on 04/24/2024).

[35] E. Roncali, M. A. Mosleh-Shirazi, and A. Badano, "Modelling the transport of optical photons in scintillation detectors for diagnostic and radiotherapy imaging," *Physics in Medicine & Biology*, vol. 62, no. 20, R207–R235, Oct. 4, 2017, ISSN: 1361-6560. DOI: 10.1088/1361-6560/aa8b31. [Online]. Available: https://iopscience.iop.org/article/10.1088/1361-6560/aa8b31 (visited on 09/01/2024).

[36] A. Sahlholm, O. Svenonius, and C. Nasga, "SELECTION OF DIMENSIONS AND GEOMETRY OF a STRUCTURED SCINTILLATOR FOR x-RAY IMAGING,"

[37] M. Moszynski, "Energy resolution and non-proportionality of scintillation detectors," *MRS Proceedings*, vol. 1038, 1038–O07–02, 2007, ISSN: 0272-9172, 1946-4274.

DOI: 10.1557/PROC-1038-007-02. [Online]. Available: http://link.springer.com/10.1557/PROC-1038-007-02 (visited on 06/20/2024).

[38] N. Kawano, M. Koshimizu, G. Okada, *et al.*, "Scintillating organic–inorganic layered perovskite-type compounds and the gamma-ray detection capabilities," *Scientific Reports*, vol. 7, no. 1, p. 14 754, Nov. 7, 2017, ISSN: 2045-2322. DOI: 10.1038/s41598-017-15268-x. [Online]. Available: https://www.nature.com/articles/s41598-017-15268-x (visited on 06/05/2024).

[39] A. Wibowo, M. A. K. Sheikh, L. J. Diguna, *et al.*, "Development and challenges in perovskite scintillators for high-resolution imaging and timing applications," *Communications Materials*, vol. 4, no. 1, p. 21, Mar. 13, 2023, ISSN: 2662-4443. DOI: 10.1038/s43246-023-00348-5. [Online]. Available: https://www.nature.com/articles/s43246-023-00348-5 (visited on 09/01/2024).

[40] I. Singh, B. Singh, B. S. Sandhu, and A. D. Sabharwal, "Comparative study for intermediate crystal size of NaI(tl) scintillation detector," *Review of Scientific Instruments*, vol. 91, no. 7, p. 073 105, Jul. 1, 2020, ISSN: 0034-6748, 1089-7623. DOI: 10.1063/5.0005243. [Online]. Available: https://pubs.aip.org/rsi/article/91/7/073105/966031/Comparative-study-for-intermediate-crystal-size-of (visited on 05/07/2024).

[41] B. N. Corp. "(CsI) cesium iodide scintillation detectors-TECHNICAL RESOURCES." (), [Online]. Available: https://www.berkeleynucleonics.com/cesium-iodide (visited on 05/08/2024).

[42] B. N. Corp. "LaBr3 lanthanum bromide scintillation detector." (2023), [Online]. Available: https://www.berkeleynucleonics.com/lanthanum-bromide.

[43] R. M. Deviced. "CLYC gamma-neutron scintillator: Properties and brochures." (), [Online]. Available: https://www.rmdinc.com/product-category/products/clyc-gamma-neutron-scintillators/.

[44] A. UK. "Lutetium aluminium garnet - LuAG(pr)." (), [Online]. Available: https://www.advatech-uk.co.uk/luag_pr.html.

[45] T. Jin, S. Hao, Y. Shang, Z. Lei, and C. Yang, "Recent trends in elpasolite single crystal scintillators for radiation detection," *Crystals*, vol. 12, no. 7, p. 887, Jun. 22, 2022, ISSN: 2073-4352. DOI: 10.3390/cryst12070887. [Online]. Available: https://www.mdpi.com/2073-4352/12/7/887 (visited on 08/14/2024).

[46] E. Gregorich, L. W. Turchenek, M. Carter, and D. A. Angers, Eds., *Soil and Environmental Science Dictionary*, 0th ed., CRC Press, Jun. 22, 2001, ISBN: 978-1-4200-3778-4. DOI: 10.1201/9780849331152. [Online]. Available: https://www.taylorfrancis.com/books/9781420037784.

[47] A. G. Tereshchenko, "Deliquescence: Hygroscopicity of water-soluble crystalline solids," *Journal of Pharmaceutical Sciences*, vol. 104, no. 11, pp. 3639–3652, Nov. 2015, ISSN: 00223549. DOI: 10.1002/jps.24589. [Online]. Available: https://linkinghub.elsevier.com/retrieve/pii/S0022354916301526 (visited on 09/22/2024).

[48] A.-M. Helmenstine. "Hygroscopic definition in chemistry." (2021), [Online]. Available: thoughtco.com/definition-of-hygroscopic-605230.

[49] R. Pani, M. Cinti, F. De Notaristefani, *et al.*, "Imaging performances of LaCl/sub 3/:ce scintillation crystals in SPECT," in *IEEE Symposium Conference Record Nuclear Science 2004.*, vol. 4, Rome, Italy: IEEE, 2004, pp. 2283–2287, ISBN: 978-0-7803-8700-3. DOI: 10.1109/NSSMIC.2004.1462715. [Online]. Available: http://ieeexplore.ieee.org/document/1462715/ (visited on 05/12/2024).

[50] W. Moses, W.-S. Choong, and S. Derenzo, "Modeling time dispersion due to optical path length differences in scintillation detectors," *Acta Physica Polonica B Proceedings Supplement*, vol. 7, no. 4, p. 725, 2014, ISSN: 1899-2358, 2082-7865. DOI: 10.5506/APhysPolBSupp.7.725. [Online]. Available: http://www.actaphys.uj.edu.pl/sup7/abs/s7p0725 (visited on 04/17/2024).

[51] M. Sasano, H. Nishioka, S. Okuyama, *et al.*, "Geometry dependence of the light collection efficiency of BGO crystal scintillators read out by avalanche photo diodes," *Nuclear Instruments and Methods in Physics Research Section A: Accelerators, Spectrometers, Detectors and Associated Equipment*, vol. 715, pp. 105–111, Jul. 2013, ISSN: 01689002. DOI: 10.1016/j.nima.2013.03.022. [Online]. Available: https://linkinghub.elsevier.com/retrieve/pii/S0168900213003070 (visited on 05/16/2024).

[52] S. Park, M. D. Hammig, and M. Jeong, "Comparison of characteristics of gamma-ray imager based on coded aperture by varying the thickness of the BGO scintillator," *Journal of Radiation Protection and Research*, vol. 47, no. 4, pp. 214–225, Dec. 30, 2022, ISSN: 2508-1888, 2466-2461. DOI: 10.14407/jrpr.2022.00122. [On-

line]. Available: http://jrpr.org/journal/view.php?doi=10.14407/jrpr.2022.00122 (visited on 05/16/2024).

[53] A. Wagner, W. Tan, K. Chalut, *et al.*, "Energy resolution and energy–light response of CsI(tl) scintillators for charged particle detection," *Nuclear Instruments and Methods in Physics Research Section A: Accelerators, Spectrometers, Detectors and Associated Equipment*, vol. 456, no. 3, pp. 290–299, Jan. 2001, ISSN: 01689002. DOI: 10.1016/S0168-9002(00)00542-8. [Online]. Available: https://linkinghub.elsevier.com/retrieve/pii/S0168900200005428 (visited on 05/16/2024).

[54] M. Stockhoff, S. Jan, A. Dubois, S. R. Cherry, and E. Roncali, "Advanced optical simulation of scintillation detectors in GATE v8.0: First implementation of a reflectance model based on measured data," *Physics in Medicine and Biology*, vol. 62, no. 12, pp. L1–L8, Jun. 21, 2017, ISSN: 0031-9155, 1361-6560. DOI: 10.1088/1361-6560/aa7007. [Online]. Available: https://iopscience.iop.org/article/10.1088/1361-6560/aa7007 (visited on 09/01/2024).

[55] P. Boillat, P. Trtik, E. H. Lehmann, *et al.*, "Who made the noise? systematic approach for the assessment of neutron imaging scintillators," *Optics Express*, vol. 32, no. 8, p. 14 471, Apr. 8, 2024, ISSN: 1094-4087. DOI: 10.1364/OE.511939. [Online]. Available: https://opg.optica.org/abstract.cfm?URI=oe-32-8-14471 (visited on 09/01/2024).

[56] H. Ing, S. Djeffal, T. Clifford, R. Machrafi, and R. Noulty, "Portable spectroscopic neutron probe," *Radiation Protection Dosimetry*, vol. 126, no. 1, pp. 238–243, May 13, 2007, ISSN: 0144-8420, 1742-3406. DOI: 10.1093/rpd/ncm049. [Online]. Available: https://academic.oup.com/rpd/article-lookup/doi/10.1093/rpd/ncm049 (visited on 08/22/2024).

[57] J. Li, P. Fan, C. Zhu, M. Wang, Z. Wei, and Y. Xia, "Design and performance evaluation of a compact thermal and fast neutron spectrometer," *Nuclear Instruments and Methods in Physics Research Section A: Accelerators, Spectrometers, Detectors and Associated Equipment*, vol. 1063, p. 169 247, Jun. 2024, ISSN: 01689002. DOI: 10.1016/j.nima.2024.169247. [Online]. Available: https://linkinghub.elsevier.com/retrieve/pii/S0168900224001736 (visited on 09/22/2024).

[58] W. Chuirazzi, A. Craft, B. Schillinger, S. Cool, and A. Tengattini, "Boron-based neutron scintillator screens for neutron imaging," *Journal of Imaging*, vol. 6, no. 11,

p. 124, Nov. 19, 2020, ISSN: 2313-433X. DOI: 10.3390/jimaging6110124. [Online]. Available: https://www.mdpi.com/2313-433X/6/11/124 (visited on 09/01/2024).

[59] U. D. of Homeland Security. "Stilbene, an organic scintillator for fast neutron detection." (2024), [Online]. Available: https://www.dhs.gov/archive/fast-neutron-detection (visited on 08/19/2024).

[60] I. Optics, *Scintinel™ stilbene for fast neutron detection*, 2020. [Online]. Available: https://inradoptics.com/pdfs/Inrad_AN_Stilbene.pdf (visited on 01/06/2024).

[61] A. K. D. and R. S. Babu, "Single crystal grown with stilbenex diphenylacetylene1-x for scintillation application," *Optik*, vol. 248, p. 168 098, Dec. 2021, ISSN: 00304026. DOI: 10.1016/j.ijleo.2021.168098. [Online]. Available: https://linkinghub.elsevier.com/retrieve/pii/S0030402621016478 (visited on 09/15/2024).

[62] B. Stríbrnský and R. Hinca, "The comparison of energy resolution fitting functions for 1.5 NaI:tl, CsI:tl, LaBr3:ce, and CeBr3 scintillation detectors," presented at the APPLIED PHYSICS OF CONDENSED MATTER (APCOM 2021), Štrbske Pleso, Slovak Republic, 2021, p. 070 005. DOI: 10.1063/5.0067390. [Online]. Available: https://pubs.aip.org/aip/acp/article/687035 (visited on 09/01/2024).

[63] P. Buzhan, A. Karakash, and Y. Teverovskiy, "Silicon photomultiplier and CsI(tl) scintillator in application to portable h*(10) dosimeter," *Nuclear Instruments and Methods in Physics Research Section A: Accelerators, Spectrometers, Detectors and Associated Equipment*, vol. 912, pp. 245–247, Dec. 2018, ISSN: 01689002. DOI: 10.1016/j.nima.2017.11.067. [Online]. Available: https://linkinghub.elsevier.com/retrieve/pii/S016890021731313X (visited on 04/24/2024).

[64] M. Risse, H. Friedrich, J. Glabian, T. Köble, O. Schumann, and T. Teuteberg, "Comparison of CLYC vs. CsI in a hand-held detector," *EPJ Web of Conferences*, vol. 288, A. Lyoussi, F. D'Errico, M. Carette, *et al.*, Eds., p. 10 009, 2023, ISSN: 2100-014X. DOI: 10.1051/epjconf/202328810009. [Online]. Available: https://www.epj-conferences.org/10.1051/epjconf/202328810009 (visited on 04/24/2024).

[65] T. Nakao, "Developing a gamma-ray spectrometer using a scintillator and an MPPC (multi-pixel photon counter)," Ph.D. dissertation, Hiroshima University, 2014.

[66] M. d. C. C. Pereira, T. Madi Filho, V. M. Lopes, J. R. Berretta, and J. P. N. Cardenas, "Scintillation response of CsI: Tl crystal under neutron, gamma, alpha particles and beta excitations," presented at the international nuclear atlantic conference. Brazilian nuclear program. State policy for a sustainable world, Sao Paulo, SP (Brazil): Associacao Brasileira de Energia Nuclear (ABEN), Rio de Janeiro, RJ (Brazil), 2015.

[67] M. D. C. Costa Pereira, T. M. Filho, J. R. Berretta, J. P. Náhuel Cárdenas, and A. C. Iglesias Rodrigues, "RESPONSE OF CsI:pb SCINTILLATOR CRYSTAL TO NEUTRON RADIATION," *EPJ Web of Conferences*, vol. 170, A. Lyoussi, M. Carette, M. Giot, *et al.*, Eds., p. 01 005, 2018, ISSN: 2100-014X. DOI: 10.1051/epjconf/201817001005. [Online]. Available: https://www.epj-conferences.org/10.1051/epjconf/201817001005 (visited on 05/02/2024).

[68] S. Gundacker and A. Heering, "The silicon photomultiplier: Fundamentals and applications of a modern solid-state photon detector," *Physics in Medicine & Biology*, vol. 65, no. 17, 17TR01, Sep. 7, 2020, ISSN: 0031-9155, 1361-6560. DOI: 10.1088/1361-6560/ab7b2d. [Online]. Available: https://iopscience.iop.org/article/10.1088/1361-6560/ab7b2d (visited on 08/12/2024).

[69] F. Acerbi and S. Gundacker, "Understanding and simulating SiPMs," *Nuclear Instruments and Methods in Physics Research Section A: Accelerators, Spectrometers, Detectors and Associated Equipment*, vol. 926, pp. 16–35, May 2019, ISSN: 01689002. DOI: 10.1016/j.nima.2018.11.118. [Online]. Available: https://linkinghub.elsevier.com/retrieve/pii/S0168900218317704 (visited on 09/04/2024).

[70] H. Photonics. "MPPC array module documentation." (), [Online]. Available: https://www.hamamatsu.com/jp/en/product/optical-sensors/mppc/mppc_mppc-array/related_documents.html.

[71] T. Kato, J. Kataoka, T. Nakamori, *et al.*, "A novel gamma-ray detector with sub-millimeter resolutions using a monolithic MPPC array with pixelized ce:LYSO and ce:GGAG crystals," *Nuclear Instruments and Methods in Physics Research Section A: Accelerators, Spectrometers, Detectors and Associated Equipment*, vol. 699, pp. 235–241, Jan. 2013, ISSN: 01689002. DOI: 10.1016/j.nima.2012.04.008. [On-

line]. Available: https://linkinghub.elsevier.com/retrieve/pii/S0168900212003609 (visited on 06/09/2024).

[72] K. Okazaki, H. Tanaka, T. Takata, *et al.*, "Development of a prompt gamma-ray detector with an 8 × 8 array LaBr 3(ce) scintillator and a multi-pixel photon counter for boron neutron capture therapy," *Nuclear Instruments and Methods in Physics Research Section A: Accelerators, Spectrometers, Detectors and Associated Equipment*, vol. 1055, p. 168 546, Oct. 2023, ISSN: 01689002. DOI: 10.1016/j.nima.2023.168546. [Online]. Available: https://linkinghub.elsevier.com/retrieve/pii/S0168900223005363 (visited on 06/02/2024).

[73] J. Guo, X. Pang, J. Cai, *et al.*, "Compact MPPC-based coded aperture imaging camera for dual-particle detection," *Radiation Detection Technology and Methods*, vol. 5, no. 1, pp. 61–70, Mar. 2021, ISSN: 2509-9930, 2509-9949. DOI: 10.1007/s41605-020-00218-5. [Online]. Available: https://link.springer.com/10.1007/s41605-020-00218-5 (visited on 08/11/2024).

[74] K. Torigoe, Y. Fukazawa, G. Galgóczi, *et al.*, "Performance study of a large CsI(tl) scintillator with an MPPC readout for nanosatellites used to localize gamma-ray bursts," *Nuclear Instruments and Methods in Physics Research Section A: Accelerators, Spectrometers, Detectors and Associated Equipment*, vol. 924, pp. 316–320, Apr. 2019, ISSN: 01689002. DOI: 10.1016/j.nima.2018.08.039. [Online]. Available: https://linkinghub.elsevier.com/retrieve/pii/S0168900218309926 (visited on 06/09/2024).

[75] A. A. Jasni, Y. Yap, I. H. Hashim, N. E. Ahmad, and N. Ramlee, "Two dimensional array of MPPC and CsI(tl) for radiation monitoring prototype," *IOP Conference Series: Materials Science and Engineering*, vol. 1106, no. 1, p. 012 028, Mar. 1, 2021, ISSN: 1757-8981, 1757-899X. DOI: 10.1088/1757-899X/1106/1/012028. [Online]. Available: https://iopscience.iop.org/article/10.1088/1757-899X/1106/1/012028 (visited on 05/02/2024).

[76] J. Kataoka, A. Kishimoto, T. Fujita, *et al.*, "Recent progress of MPPC-based scintillation detectors in high precision x-ray and gamma-ray imaging," *Nuclear Instruments and Methods in Physics Research Section A: Accelerators, Spectrometers, Detectors and Associated Equipment*, vol. 784, pp. 248–254, Jun. 2015, ISSN: 01689002. DOI: 10.1016/j.nima.2014.11.004. [Online]. Available: https:

//linkinghub.elsevier.com/retrieve/pii/S0168900214012522 (visited on 06/09/2024).

[77] A. Ghassemi, K. Sato, and K. Kobayashi, *MPPC technical information - literature*, 2022. [Online]. Available: https://www.hamamatsu.com/jp/en/product/optical-sensors/mppc/power-supply_driver-circuit/related_documents.html.

[78] Y. Jin, "Study of a scintillation counter consisting of a pure CsI crystal and avalanche photodiodes," University of Tokyo, 2015.

[79] H. Photonics, *C14047-0436 MPPC array module*.

[80] P. Slawomir. Physics and Operation of an MPPC. (2014), [Online]. Available: https://hub.hamamatsu.com/us/en/technical-notes/mppc-sipms/physics-and-operation-of-the-MPPC-silicon-photomultiplier.html.

[81] R. M. Preston, J. E. Eberhardt, and J. R. Tickner, "Neutron-gamma pulse shape discrimination using organic scintillators with silicon photomultiplier readout," *IEEE Transactions on Nuclear Science*, vol. 61, no. 4, pp. 2410–2418, Aug. 2014, ISSN: 0018-9499, 1558-1578. DOI: 10.1109/TNS.2014.2335208. [Online]. Available: http://ieeexplore.ieee.org/document/6870459/ (visited on 09/02/2024).

[82] N. Desai and D. J. Valentino, "A software tool for quality assurance of computed/digital radiography (CR/DR) systems," presented at the SPIE Medical Imaging, N. J. Pelc, E. Samei, and R. M. Nishikawa, Eds., Lake Buena Vista, Florida, Mar. 3, 2011, 79614E. DOI: 10.1117/12.878345. [Online]. Available: http://proceedings.spiedigitallibrary.org/proceeding.aspx?doi=10.1117/12.878345 (visited on 08/12/2024).

[83] S. Mianowski, J. Baszak, Y. Gledenov, *et al.*, "Study of MPPC damage induced by neutrons," *Nuclear Instruments and Methods in Physics Research Section A: Accelerators, Spectrometers, Detectors and Associated Equipment*, vol. 906, pp. 30–36, Oct. 2018, ISSN: 01689002. DOI: 10.1016/j.nima.2018.07.080. [Online]. Available: https://linkinghub.elsevier.com/retrieve/pii/S0168900218309161 (visited on 08/12/2024).

[84] R. Grzywacz, "Applications of digital pulse processing in nuclear spectroscopy," *Nuclear Instruments and Methods in Physics Research Section B: Beam Interactions with Materials and Atoms*, vol. 204, pp. 649–659, May 2003, ISSN: 0168583X. DOI:

10.1016/S0168-583X(02)02146-8. [Online]. Available: https://linkinghub.elsevier.com/retrieve/pii/S0168583X02021468 (visited on 08/25/2024).

[85] W. Warburton, M. Momayezi, B. Hubbard-Nelson, and W. Skulski, "Digital pulse processing: New possibilities in nuclear spectroscopy," *Applied Radiation and Isotopes*, vol. 53, no. 4, pp. 913–920, Nov. 2000, ISSN: 09698043. DOI: 10.1016/S0969-8043(00)00247-5. [Online]. Available: https://linkinghub.elsevier.com/retrieve/pii/S0969804300002475 (visited on 08/25/2024).

[86] AMPTEK. "DP5 OEM digital pulse processor & MCA –amptek –x-ray detectors and electronics," Amptek - DP5 OEM Digital Pulse Processor & MCA. (), [Online]. Available: https://www.amptek.com/products/digital-pulse-processors/dp5-digital-pulse-processor-and-mca.

[87] R. H. Redus, A. C. Huber, and D. J. Sperry, "Dead time correction in the DP5 digital pulse processor," in *2008 IEEE Nuclear Science Symposium Conference Record*, Dresden, Germany: IEEE, Oct. 2008, pp. 3416–3420, ISBN: 978-1-4244-2714-7. DOI: 10.1109/NSSMIC.2008.4775075. [Online]. Available: http://ieeexplore.ieee.org/document/4775075/ (visited on 07/11/2024).

[88] J. Simões and C. M. Correia, "Pulse processing architectures," *Nuclear Instruments and Methods in Physics Research Section A: Accelerators, Spectrometers, Detectors and Associated Equipment*, vol. 422, no. 1, pp. 405–410, Feb. 1999, ISSN: 01689002. DOI: 10.1016/S0168-9002(98)00992-9. [Online]. Available: https://linkinghub.elsevier.com/retrieve/pii/S0168900298009929 (visited on 08/25/2024).

[89] O. Lakhwani, V. Dalal, M. Jindal, and A. Nagala, "Radiation protection and standardization," *Journal of Clinical Orthopaedics and Trauma*, vol. 10, no. 4, pp. 738–743, Jul. 2019, ISSN: 09765662. DOI: 10.1016/j.jcot.2018.08.010. [Online]. Available: https://linkinghub.elsevier.com/retrieve/pii/S097656621830167X (visited on 05/01/2024).

[90] T. Yamamoto, Y. Yanagida-Miyamoto, T. Iida, and H. Nanto, "Current status and future prospect of RPL glass dosimeter," *Radiation Measurements*, vol. 136, p. 106 363, Aug. 2020, ISSN: 13504487. DOI: 10.1016/j.radmeas.2020.106363. [Online]. Available: https://linkinghub.elsevier.com/retrieve/pii/S135044872030127X (visited on 05/01/2024).

[91] W. Ministry of Health Labour, *Guidelines on prevention of radiation hazards for workers engaged in decontamination works*, 2018. [Online]. Available: https://www.mhlw.go.jp/english/topics/2011eq/workers/ri/index.html.

[92] T. Yanagida, G. Okada, T. Kato, D. Nakauchi, and N. Kawaguchi, "A review and future of RPL dosimetry," *Radiation Measurements*, vol. 158, p. 106 847, Nov. 2022, ISSN: 13504487. DOI: 10.1016/j.radmeas.2022.106847. [Online]. Available: https://linkinghub.elsevier.com/retrieve/pii/S135044872200138X (visited on 05/01/2024).

[93] K. Hattori, Y. Inaba, T. Kato, *et al.*, "Evaluation of a new real-time dosimeter sensor for interventional radiology staff," *Sensors*, vol. 23, no. 1, p. 512, Jan. 3, 2023, ISSN: 1424-8220. DOI: 10.3390/s23010512. [Online]. Available: https://www.mdpi.com/1424-8220/23/1/512 (visited on 04/17/2024).

[94] B. Buddemeier, S. Musolino, and G. Klemic, "Preventive rad/nuc detection equipment categorization for consequence management," LLNL–TR-732941, 1366955, Jun. 1, 2017, LLNL–TR–732 941, 1 366 955. DOI: 10.2172/1366955. [Online]. Available: https://www.osti.gov/servlets/purl/1366955/ (visited on 09/27/2024).

[95] National Council on Radiation Protection and Measurements, Ed., *Guidance for emergency response dosimetry*, NCRP report no. 179, Bethesda, MD: National Council on Radiation Protection and Measurements, 171 pp., ISBN: 978-0-913392-10-2.

[96] X. Ortega and M. Ginjaume, "Advantages and limitations of electronic devices for primary occupational dosimetry," in *International ISOE Symposia*, Tarragona, Spain: ISOE, 2000. [Online]. Available: https://www.isoe-network.net/publications/pub-proceedings/symposia/international-symposia/tarragona-spain-april-2000/papers-18/171-ortega2000/file.html.

[97] S. Doza. "Medical radiation monitoring systems," SPC Doza MEDICINE. (2024), [Online]. Available: https://www.doza.ru/en/application/meditsina/.

[98] R. Piper and R. Scherpelz, "Functional evaluation of the DOZA DKG-05d electronic dosimeter system," Pacific Northwest National Laboratory., Richland, WA, 2009.

[99] IAEA, "Assessment of occupational exposure due to external radiation sources-neutron dosimetry."

[100] R. Cooper, M. Amman, P. Luke, and K. Vetter, "A prototype high purity germanium detector for high resolution gamma-ray spectroscopy at high count rates," *Nuclear Instruments and Methods in Physics Research Section A: Accelerators, Spectrometers, Detectors and Associated Equipment*, vol. 795, pp. 167–173, Sep. 2015, ISSN: 01689002. DOI: 10.1016/j.nima.2015.05.053. [Online]. Available: https://linkinghub.elsevier.com/retrieve/pii/S0168900215007123 (visited on 09/15/2024).

[101] ORTEC/AMETEK. "HPGe radiation detector types." (), [Online]. Available: https://www.ortec-online.com/products/radiation-detectors/high-purity-germanium-hpge-radiation-detectors/hpge-radiation-detector-types-how-choose (visited on 08/18/2024).

[102] V. A. ORTEC/AMETEK. "Trans-SPEC-DX-100t battery powered, portable, LN2 free, HPGe gamma spectrometer." (), [Online]. Available: https://www.ortec-online.com/products/radiation-detectors/gamma-spectroscopy-systems/all-in-one-spectrometers/trans-spec-dx-100t.

[103] M. Technologies, *Aegis portable HPGe spectrometer*, 2022. [Online]. Available: https://assets-mirion.mirion.com/prod-20220822/cms4_mirion/files/pdf/spec-sheets/spc-194-en-e-aegis-spec-sheet.pdf (visited on 10/08/2024).

[104] K. Watanabe, T. Mizukoshi, A. Yamazaki, *et al.*, "Response evaluation of onion-like single bonner sphere neutron spectrometer using TRUST eu:LiCAF scintillator," *Progress in Nuclear Science and Technology*, vol. 6, no. 0, pp. 122–125, Jan. 31, 2019, ISSN: 2185-4823. DOI: 10.15669/pnst.6.122. [Online]. Available: https://www.aesj.net/document/pnst006/data/122_125.pdf (visited on 08/24/2024).

[105] M. Foster and D. Ramsden, "A compact neutron detector based on the use of a SiPM detector," in *2008 IEEE Nuclear Science Symposium Conference Record*, Dresden, Germany: IEEE, Oct. 2008, pp. 1882–1886, ISBN: 978-1-4244-2714-7. DOI: 10.1109/NSSMIC.2008.4774758. [Online]. Available: http://ieeexplore.ieee.org/document/4774758/ (visited on 08/26/2024).

[106] K. Watanabe, T. Yanagida, K. Fukuda, A. Koike, T. Aoki, and A. Uritani, "Portable neutron detector using ce:LiCaAlF6 scintillator," *Sensors and Materials*, vol. 27, no. 3, 2015.

[107] A. Asuncion-Astronomo, C. V. Balderas, F. C. Hila, *et al.*, "Validation of an indium-based multi-shell neutron spectrometer," *Applied Radiation and Isotopes*, vol. 170, p. 109 629, Apr. 2021, ISSN: 09698043. DOI: 10.1016/j.apradiso.2021.109629. [Online]. Available: https://linkinghub.elsevier.com/retrieve/pii/S0969804321000439 (visited on 09/22/2024).

[108] L. Swiderski, A. Gojska, M. Grodzicka, *et al.*, "Scintillators for high-temperature plasma diagnostics," in *Proceedings of 1st EPS conference on Plasma Diagnostics —PoS(ECPD2015)*, Frascati, Italy: Sissa Medialab, Oct. 26, 2016, p. 162. DOI: 10.22323/1.240.0162. [Online]. Available: https://pos.sissa.it/240/162 (visited on 05/16/2024).

[109] S. Andersson, "Evaluation of the radiation protection at the new radiotherapy treatment department at the university hospital of umeå," MSc, Umeå University, 2010.

[110] J. Choi, J. Park, J. Son, and Y. K. Kim, "Study of n/ discrimination using 3he proportional chamber in high gamma-ray fields," *Nuclear Engineering and Technology*, vol. 51, no. 1, pp. 263–268, Feb. 2019, ISSN: 17385733. DOI: 10.1016/j.net.2018.08.013. [Online]. Available: https://linkinghub.elsevier.com/retrieve/pii/S1738573318301050 (visited on 09/06/2024).

[111] R. Song, X. Yan, J. Han, *et al.*, "Simultaneous detection of energy and flux for neutron and gamma by CLYC scintillator," *IEEE Transactions on Nuclear Science*, vol. 70, no. 8, pp. 2148–2156, Aug. 2023, ISSN: 0018-9499, 1558-1578. DOI: 10.1109/TNS.2023.3289945. [Online]. Available: https://ieeexplore.ieee.org/document/10164170/ (visited on 05/03/2024).

[112] P. P. Guss, T. G. Stampahar, S. Mukhopadhyay, A. Barzilov, and A. Guckes, "Scintillation properties of a cs $_2$ LiLa(br $_6$)90%(cl $_6$)10%:ce (CLLBC) crystal," presented at the SPIE Optical Engineering + Applications, G. P. Grim and H. B. Barber, Eds., San Diego, California, United States, Sep. 4, 2014, p. 921 505. DOI: 10.1117/12.2060204. [Online]. Available: http://proceedings.spiedigitallibrary.org/proceeding.aspx?doi=10.1117/12.2060204 (visited on 09/04/2024).

[113] J. Glodo, A. Gueorguiev, U. Shirwadkar, *et al.*, "Integrated neutron detector for handheld systems," *IEEE Transactions on Nuclear Science*, vol. 60, no. 2, pp. 903–907, Apr. 2013, ISSN: 0018-9499, 1558-1578. DOI: 10.1109/TNS.2013.2252020.

[Online]. Available: http://ieeexplore.ieee.org/document/6496293/ (visited on 09/04/2024).

[114] J. Glodo, M. McClish, R. Hawrami, *et al.*, "Temperature behavior of CLYC/MPPC detectors," presented at the SPIE Optical Engineering + Applications, M. Fiederle, A. Burger, L. Franks, and R. B. James, Eds., San Diego, California, United States, Sep. 26, 2013, p. 88520X. DOI: 10.1117/12.2028235. [Online]. Available: http://proceedings.spiedigitallibrary.org/proceeding.aspx?doi=10.1117/12.2028235 (visited on 09/04/2024).

[115] K. E. Mesick, L. C. Stonehill, J. T. Morrell, and D. D. S. Coupland, "Performance of several solid state photomultipliers with CLYC scintillator," in *2015 IEEE Nuclear Science Symposium and Medical Imaging Conference (NSS/MIC)*, Oct. 2015, pp. 1–4. DOI: 10.1109/NSSMIC.2015.7581936. arXiv: 1512.01155[nucl-ex,physics:physics]. [Online]. Available: http://arxiv.org/abs/1512.01155 (visited on 09/04/2024).

[116] N. Dinar, D. Celeste, M. Silari, V. Varoli, and A. Fazzi, "Pulse shape discrimination of CLYC scintillator coupled with a large SiPM array," *Nuclear Instruments and Methods in Physics Research Section A: Accelerators, Spectrometers, Detectors and Associated Equipment*, vol. 935, pp. 35–39, Aug. 2019, ISSN: 01689002. DOI: 10.1016/j.nima.2019.04.099. [Online]. Available: https://linkinghub.elsevier.com/retrieve/pii/S0168900219305960 (visited on 09/15/2024).

[117] F. Liang, H. Brands, L. Hoy, J. Preston, and J. Smith, "Lithium-loaded scintillators coupled to a custom-designed silicon photomultiplier array for neutron and gamma-ray detection," *IEEE Transactions on Nuclear Science*, vol. 65, no. 8, pp. 2162–2168, Aug. 2018, ISSN: 0018-9499, 1558-1578. DOI: 10.1109/TNS.2018.2820658. [Online]. Available: https://ieeexplore.ieee.org/document/8327632/ (visited on 09/04/2024).

[118] Q. Wang, Y. Yang, X. Tuo, C. Deng, and H. Li, "Design of a compact neutron spectrometer using the CLYC scintillator," in *2017 IEEE Nuclear Science Symposium and Medical Imaging Conference (NSS/MIC)*, Atlanta, GA: IEEE, Oct. 2017, pp. 1–3, ISBN: 978-1-5386-2282-7. DOI: 10.1109/NSSMIC.2017.8533144. [Online]. Available: https://ieeexplore.ieee.org/document/8533144/ (visited on 09/04/2024).

[119] Y. Sakurai, "Project 6 advancement of integrated system for dose estimation in BNCT (r3p6)," Kyoto University Research Information Repository, Project Research Report KURNS Progress Report 2022, 2021: 51-70, 2022. [Online]. Available: http://hdl.handle.net/2433/275842.

[120] R. Song, S. Peng, Y. Tong, *et al.*, "The neutron-gamma pulse shape discrimination of CLLB detector," *EPJ Web of Conferences*, vol. 295, R. De Vita, X. Espinal, P. Laycock, and O. Shadura, Eds., p. 09 031, 2024, ISSN: 2100-014X. DOI: 10.1051/epjconf/202429509031. [Online]. Available: https://www.epj-conferences.org/10.1051/epjconf/202429509031 (visited on 09/15/2024).

[121] B. Budden, L. Stonehill, N. Dallmann, *et al.*, "A cs2liycl6:ce-based advanced radiation monitoring device," *Nuclear Instruments and Methods in Physics Research Section A: Accelerators, Spectrometers, Detectors and Associated Equipment*, vol. 784, pp. 97–104, Jun. 2015, ISSN: 01689002. DOI: 10.1016/j.nima.2014.11.051. [Online]. Available: https://linkinghub.elsevier.com/retrieve/pii/S0168900214013394 (visited on 04/28/2024).

[122] D. Takaku, T. Oishi, and M. Baba, "Development of neutron-gamma discrimination technique using pattern-recognition method with digital signal processing," *Progress in Nuclear Science and Technology*, vol. 1, no. 0, pp. 210–213, Feb. 25, 2011, ISSN: 2185-4823. DOI: 10.15669/pnst.1.210. [Online]. Available: https://www.aesj.net/document/pnst001/210.pdf (visited on 08/26/2024).

[123] H. Klein and S. Neumann, "Neutron and photon spectrometry with liquid scintillation detectors in mixed fields," *Nuclear Instruments and Methods in Physics Research Section A: Accelerators, Spectrometers, Detectors and Associated Equipment*, vol. 476, no. 1, pp. 132–142, Jan. 2002, ISSN: 01689002. DOI: 10.1016/S0168-9002(01)01410-3. [Online]. Available: https://linkinghub.elsevier.com/retrieve/pii/S0168900201014103 (visited on 08/26/2024).

[124] M. Morichi, E. Fanchini, and G. Mangiagalli, "A novel portable device for gamma and neutron spectroscopy with special nuclear material identification," *EPJ Web of Conferences*, vol. 225, A. Lyoussi, M. Giot, M. Carette, *et al.*, Eds., p. 07 006, 2020, ISSN: 2100-014X. DOI: 10.1051/epjconf/202022507006. [Online]. Available: https://www.epj-conferences.org/10.1051/epjconf/202022507006 (visited on 09/04/2024).

[125] M. E. Hammad, H. Kasban, R. M. Fikry, *et al.*, "Digital pulse processing algorithm for neutron and gamma rays discrimination," *Analog Integrated Circuits and Signal Processing*, vol. 101, no. 3, pp. 475–487, Dec. 2019, ISSN: 0925-1030, 1573-1979. DOI: 10.1007/s10470-019-01498-8. [Online]. Available: http://link.springer.com/10.1007/s10470-019-01498-8 (visited on 08/26/2024).

[126] H. Ing, W. Cross, and P. Bunge, "Spectrometers for radiation protection at chalk river nuclear laboratories," *Radiation Protection Dosimetry*, vol. 10, no. 1, pp. 137–145, Jan. 1, 1985, ISSN: 1742-3406, 0144-8420. DOI: 10.1093/oxfordjournals.rpd.a079418. [Online]. Available: https://academic.oup.com/rpd/article/1622931/Spectrometers (visited on 09/04/2024).

[127] N. Zaitseva, A. Glenn, L. Carman, *et al.*, "Pulse shape discrimination in impure and mixed single-crystal organic scintillators," *IEEE Transactions on Nuclear Science*, vol. 58, no. 6, pp. 3411–3420, Dec. 2011, ISSN: 0018-9499. DOI: 10.1109/TNS.2011.2171363. [Online]. Available: http://ieeexplore.ieee.org/document/6074975/ (visited on 09/15/2024).

[128] R. Preston, J. E. Eberhardt, R. Bencardino, and J. Tickner, "Software-based digital pulse processing for silicon photomultiplier radiation detectors," in *2012 IEEE Nuclear Science Symposium and Medical Imaging Conference Record (NSS/MIC)*, Anaheim, CA, USA: IEEE, Oct. 2012, pp. 462–467, ISBN: 978-1-4673-2030-6 978-1-4673-2028-3 978-1-4673-2029-0. DOI: 10.1109/NSSMIC.2012.6551149. [Online]. Available: http://ieeexplore.ieee.org/document/6551149/ (visited on 09/04/2024).

[129] A. Comrie, A. Buffler, F. Smit, and H. Wörtche, "Digital neutron/gamma discrimination with an organic scintillator at energies between 1 MeV and 100 MeV," *Nuclear Instruments and Methods in Physics Research Section A: Accelerators, Spectrometers, Detectors and Associated Equipment*, vol. 772, pp. 43–49, Feb. 2015, ISSN: 01689002. DOI: 10.1016/j.nima.2014.10.058. [Online]. Available: https://linkinghub.elsevier.com/retrieve/pii/S0168900214012157 (visited on 09/04/2024).

[130] M. Długosz-Lisiecka, M. Biegała, and T. Jakubowska, "Activation of medical accelerator components and radioactive waste classification based on low beam energy model clinac 2300," *Radiation Physics and Chemistry*, vol. 205, p. 110 730, Apr.

2023, ISSN: 0969806X. DOI: 10.1016/j.radphyschem.2022.110730. [Online]. Available: https://linkinghub.elsevier.com/retrieve/pii/S0969806X22007939 (visited on 04/23/2024).

[131] D. V. Moiseev and L. I. Lukina, "Improving the accuracy of gamma radiation measurements in radiation monitoring," *IOP Conference Series: Earth and Environmental Science*, vol. 548, no. 3, p. 032 009, Aug. 1, 2020, ISSN: 1755-1307, 1755-1315. DOI: 10.1088/1755-1315/548/3/032009. [Online]. Available: https://iopscience.iop.org/article/10.1088/1755-1315/548/3/032009 (visited on 04/17/2024).

[132] A. H. Alsaab and S. Zeghib, "Analysis of x-ray and gamma ray shielding performance of prepared polymer micro-composites," *Journal of Radiation Research and Applied Sciences*, vol. 16, no. 4, p. 100 708, Dec. 2023, ISSN: 16878507. DOI: 10.1016/j.jrras.2023.100708. [Online]. Available: https://linkinghub.elsevier.com/retrieve/pii/S1687850723001863 (visited on 05/02/2024).

[133] J. Bakshi and B. P. Chu, "Attenuation of gamma radiation using ClearView radiation ShieldingTM in nuclear power plants, hospitals and radiopharmacies," *Health Physics*, vol. 119, no. 6, pp. 776–785, Dec. 2020, ISSN: 1538-5159, 0017-9078. DOI: 10.1097/HP.0000000000001336. [Online]. Available: https://journals.lww.com/10.1097/HP.0000000000001336 (visited on 05/02/2024).

[134] J. Meier and S. C. Kappadath, "Characterization of the energy response and backscatter contribution for two electronic personal dosimeter models," *Journal of Applied Clinical Medical Physics*, vol. 16, no. 6, pp. 423–434, Nov. 2015, ISSN: 1526-9914, 1526-9914. DOI: 10.1120/jacmp.v16i6.5549. [Online]. Available: https://aapm.onlinelibrary.wiley.com/doi/10.1120/jacmp.v16i6.5549 (visited on 04/23/2024).

[135] H. Nishimura, M. Shinohara, T. Miyoshi, *et al.*, "Experimental verification of real-time gamma-ray energy spectrum and dose monitor," *Applied Radiation and Isotopes*, vol. 185, p. 110 226, Jul. 2022, ISSN: 09698043. DOI: 10.1016/j.apradiso.2022.110226. [Online]. Available: https://linkinghub.elsevier.com/retrieve/pii/S0969804322001233 (visited on 04/24/2024).

[136] T. Sanami, S. Sasaki, K. Iijima, Y. Kishimoto, and K. Saito, "Time variations in dose rate and spectrum measured at tsukuba city, ibaraki, due to the accident

of fukushima daiichi nuclear power station," in *Insights Concerning the Fukushima Daiichi Nuclear Accident Vol. 4*. The Atomic Energy Society of Japan, 2021, pp. 11–21, ISBN: 978-4-89047-182-9. DOI: 10.15669/fukushimainsights.Vol.4.11. [Online]. Available: https://www.aesj.net/document/fukushima_vol4/Vol4_03_011_021.pdf (visited on 08/30/2024).

[137] R. Solutions. "Https://www.radiationsolutionsonline.com/what-are-the-area-radiation-survey-and-radiation-survey-meter-requirements-for-fixed-gauges/," Radiation Survey Meters. (), [Online]. Available: https://www.radiationsolutionsonline.com/what-are-the-area-radiation-survey-and-radiation-survey-meter-requirements-for-fixed-gauges/ (visited on 04/17/2024).

[138] C. Rizk, S. Long, H. B. Okyar, *et al.*, "RESULTS OF THE JOINT IAEA/ARPANSA INTERCOMPARISON EXERCISE ON WHOLE BODY DOSEMETERS FOR PHOTONS IN ASIA AND THE PACIFIC REGION," *Radiation Protection Dosimetry*, vol. 187, no. 4, pp. 418–425, Dec. 31, 2019, ISSN: 0144-8420, 1742-3406. DOI: 10.1093/rpd/ncz182. [Online]. Available: https://academic.oup.com/rpd/article/187/4/418/5585861 (visited on 05/18/2024).

[139] W. J. Lee, E. J. Jang, K. S. Kim, and Y. J. Bang, "Underestimation of radiation doses by compliance of wearing dosimeters among fluoroscopically-guided interventional medical workers in korea," *International Journal of Environmental Research and Public Health*, vol. 19, no. 14, p. 8393, Jul. 9, 2022, ISSN: 1660-4601. DOI: 10.3390/ijerph19148393. [Online]. Available: https://www.mdpi.com/1660-4601/19/14/8393 (visited on 05/01/2024).

[140] I. Piotrowski, A. Dawid, K. Kulcenty, and W. M. Suchorska, "Use of biological dosimetry for monitoring medical workers occupationally exposed to ionizing radiation," *Radiation*, vol. 1, no. 2, pp. 95–115, Mar. 31, 2021, ISSN: 2673-592X. DOI: 10.3390/radiation1020009. [Online]. Available: https://www.mdpi.com/2673-592X/1/2/9 (visited on 05/04/2024).

[141] D. Borrego, C. M. Kitahara, S. Balter, and C. Yoder, "Occupational doses to medical staff performing or assisting with fluoroscopically guided interventional procedures," *Radiology*, vol. 294, no. 2, pp. 353–359, Feb. 2020, ISSN: 0033-8419, 1527-1315. DOI: 10.1148/radiol.2019190018. [Online]. Available: http://pubs.rsna.org/doi/10.1148/radiol.2019190018 (visited on 05/18/2024).

[142] W. Elshami, R. U. Erdemir, M. Abuzaid, B. Cavli, B. Issa, and H. Tekin, "Occupational radiation dose assessment for nuclear medicine workers in turkey: A comprehensive investigation," *Journal of King Saud University - Science*, vol. 34, no. 4, p. 102 005, Jun. 2022, ISSN: 10183647. DOI: 10.1016/j.jksus.2022.102005. [Online]. Available: https://linkinghub.elsevier.com/retrieve/pii/S1018364722001860 (visited on 05/18/2024).

[143] V. Koch, L. M. Conrades, L. D. Gruenewald, *et al.*, "Reduction of radiation dose using real-time visual feedback dosimetry during angiographic interventions," *Journal of Applied Clinical Medical Physics*, vol. 24, no. 2, e13860, Feb. 2023, ISSN: 1526-9914, 1526-9914. DOI: 10.1002/acm2.13860. [Online]. Available: https://aapm.onlinelibrary.wiley.com/doi/10.1002/acm2.13860 (visited on 05/18/2024).

[144] L. Bouchet, "A comparative study of deconvolution methods for gamma-ray spectra.," *Astronomy and Astrophysics Supplement Series*, vol. 113, p. 167, Oct. 1, 1995, ADS Bibcode: 1995A&AS..113..167B, ISSN: 0365-0138. [Online]. Available: https://ui.adsabs.harvard.edu/abs/1995A&AS..113..167B (visited on 05/02/2024).

[145] N. Sarzi Amadè, M. Bettelli, N. Zambelli, S. Zanettini, G. Benassi, and A. Zappettini, "Gamma-ray spectral unfolding of CdZnTe-based detectors using a genetic algorithm," *Sensors*, vol. 20, no. 24, p. 7316, Dec. 19, 2020, ISSN: 1424-8220. DOI: 10.3390/s20247316. [Online]. Available: https://www.mdpi.com/1424-8220/20/24/7316 (visited on 05/01/2024).

[146] N. E. Scofield, "A technique for unfolding gamma-ray scintillation spectrometer pulse0heigh distributions," Naval Radiological Defense Lab., San Francisco, NSA-15-002808 USNRDL-TR-447, 1960.

[147] F. Li, Z. Gu, L. Ge, *et al.*, "Review of recent gamma spectrum unfolding algorithms and their application," *Results in Physics*, vol. 13, p. 102 211, Jun. 2019, ISSN: 22113797. DOI: 10.1016/j.rinp.2019.102211. [Online]. Available: https://linkinghub.elsevier.com/retrieve/pii/S2211379718334223 (visited on 05/01/2024).

[148] M.-S. Kim, H.-B. Shin, M.-G. Choi, *et al.*, "Reference based simulation study of detector comparison for BNCT-SPECT imaging," *Nuclear Engineering and Technology*, vol. 52, no. 1, pp. 155–163, Jan. 2020, ISSN: 17385733. DOI: 10.1016/j.

net.2019.07.002. [Online]. Available: https://linkinghub.elsevier.com/retrieve/pii/S1738573319303146 (visited on 08/22/2024).

[149] H. Dombrowski, "GRAVEL unfolding of gamma-ray spectra of CeBr $_3$ detectors and related uncertainties," *Journal of Instrumentation*, vol. 18, no. 7, P07005, Jul. 1, 2023, ISSN: 1748-0221. DOI: 10.1088/1748-0221/18/07/P07005. [Online]. Available: https://iopscience.iop.org/article/10.1088/1748-0221/18/07/P07005 (visited on 05/01/2024).

[150] ICRP, *Conversion coefficients for use in radiological protection against external radiation* (ICRP publication Radiation protection 74), 1. ed. Oxford: Pergamon Press, 1997, 205 pp., ISBN: 978-0-08-042739-3.

[151] T. Otto, "Personal dose-equivalent conversion coefficients for 1252 radionuclides," *Radiation Protection Dosimetry*, vol. 168, no. 1, pp. 1–10, Jan. 2016, ISSN: 0144-8420, 1742-3406. DOI: 10.1093/rpd/ncu316. [Online]. Available: https://academic.oup.com/rpd/article-lookup/doi/10.1093/rpd/ncu316 (visited on 05/02/2024).

[152] C. Sükösd, W. Galster, I. Licot, and M. Simonart, "Spectrum unfolding in high energy gamma-ray detection with scintillation detectors," *Nuclear Instruments and Methods in Physics Research Section A: Accelerators, Spectrometers, Detectors and Associated Equipment*, vol. 355, no. 2, pp. 552–558, Feb. 1995, ISSN: 01689002. DOI: 10.1016/0168-9002(94)01122-2. [Online]. Available: https://linkinghub.elsevier.com/retrieve/pii/0168900294011222 (visited on 05/01/2024).

[153] M. Bouhadida, A. Mazzi, M. Brovchenko, *et al.*, "Neutron spectrum unfolding using two architectures of convolutional neural networks," *Nuclear Engineering and Technology*, vol. 55, no. 6, pp. 2276–2282, Jun. 2023, ISSN: 17385733. DOI: 10.1016/j.net.2023.03.025. [Online]. Available: https://linkinghub.elsevier.com/retrieve/pii/S173857332300133X (visited on 04/26/2024).

[154] S. Tripathy, C. Sunil, M. Nandy, P. Sarkar, D. Sharma, and B. Mukherjee, "Activation foils unfolding for neutron spectrometry: Comparison of different deconvolution methods," *Nuclear Instruments and Methods in Physics Research Section A: Accelerators, Spectrometers, Detectors and Associated Equipment*, vol. 583, no. 2, pp. 421–425, Dec. 2007, ISSN: 01689002. DOI: 10.1016/j.nima.2007.09.028. [Online]. Available: https://linkinghub.elsevier.com/retrieve/pii/S0168900207020682 (visited on 05/01/2024).

[155] V. Suman and P. Sarkar, "Neutron spectrum unfolding using genetic algorithm in a monte carlo simulation," *Nuclear Instruments and Methods in Physics Research Section A: Accelerators, Spectrometers, Detectors and Associated Equipment*, vol. 737, pp. 76–86, Feb. 2014, ISSN: 01689002. DOI: 10.1016/j.nima.2013.11.012. [Online]. Available: https://linkinghub.elsevier.com/retrieve/pii/S0168900213015519 (visited on 08/27/2024).

[156] P. Panikkath, A. Udupi, and P. Sarkar, "Estimation of neutron energy distributions from prompt gamma emissions," *Nuclear Instruments and Methods in Physics Research Section A: Accelerators, Spectrometers, Detectors and Associated Equipment*, vol. 871, pp. 83–89, Nov. 2017, ISSN: 01689002. DOI: 10.1016/j.nima.2017.07.066. [Online]. Available: https://linkinghub.elsevier.com/retrieve/pii/S0168900217308410 (visited on 05/03/2024).

[157] M. H. Woo, J. H. Kim, J. W. Kim, *et al.*, "An application of genetic multi-objective optimization algorithm to neutron spectrum unfolding problem," *Progress in Nuclear Science and Technology*, vol. 6, no. 0, pp. 230–233, Jan. 31, 2019, ISSN: 2185-4823. DOI: 10.15669/pnst.6.230. [Online]. Available: https://www.aesj.net/document/pnst006/data/230_233.pdf (visited on 05/01/2024).

[158] R. A. Meyers, Ed., *Encyclopedia of physical science and technology*, 3rd ed, San Diego: Academic Press, 2002, 18 pp., ISBN: 978-0-12-227410-7.

[159] E. M. Hussein, "The physical and mathematical aspects of inverse problems in radiation detection and applications," *Applied Radiation and Isotopes*, vol. 70, no. 7, pp. 1131–1135, Jul. 2012, ISSN: 09698043. DOI: 10.1016/j.apradiso.2011.11.041. [Online]. Available: https://linkinghub.elsevier.com/retrieve/pii/S0969804311005951 (visited on 05/01/2024).

[160] P. Groer, "Bayesian methods for radiation detection and dosimetry," University of Tennesse, Knoxville, Technical Report DE-FG07-99ID13766, 2002.

[161] S. Iwasaki, "A new approach for unfolding PHA problems based only on the bayes theorem," in *Proceedings of the 9th International Symposium on Reactor Dosimetry:*, A. Hamid and O. Bohumil, Eds., Prague, Czech Republic): American Society for Testing and Materials Euratom Working Group on Reactor Dosimetry & E.N. Society. World Scientific, Sep. 2, 1996, pp. 245–252.

[162] G. Choudalakis, *Fully bayesian unfolding*, May 31, 2012. arXiv: 1201.4612[physics]. [Online]. Available: http://arxiv.org/abs/1201.4612 (visited on 05/17/2024).

[163] G. D'Agostini, "A multidimensional unfolding method based on bayes' theorem," *Nuclear Instruments and Methods in Physics Research Section A: Accelerators, Spectrometers, Detectors and Associated Equipment*, vol. 362, no. 2, pp. 487–498, Aug. 1995, ISSN: 01689002. DOI: 10.1016/0168-9002(95)00274-X. [Online]. Available: https://linkinghub.elsevier.com/retrieve/pii/016890029500274X (visited on 05/17/2024).

[164] H. Dombrowski, "Area dose rate values derived from NaI or LaBr3 spectra," *Radiation Protection Dosimetry*, vol. 160, no. 4, pp. 269–276, Aug. 1, 2014, ISSN: 0144-8420, 1742-3406. DOI: 10.1093/rpd/nct349. [Online]. Available: https://academic.oup.com/rpd/article-lookup/doi/10.1093/rpd/nct349 (visited on 06/02/2024).

[165] A. Laso Garcia, A. Hannasch, M. Molodtsova, *et al.*, "Calorimeter with bayesian unfolding of spectra of high-flux broadband x rays," *Review of Scientific Instruments*, vol. 93, no. 4, p. 043 102, Apr. 1, 2022, ISSN: 0034-6748, 1089-7623. DOI: 10.1063/5.0078443. [Online]. Available: https://pubs.aip.org/rsi/article/93/4/043102/2848733/Calorimeter-with-Bayesian-unfolding-of-spectra-of (visited on 05/17/2024).

[166] R. Kurihara, A. Nohtomi, G. Wakabayashi, Y. Sakurai, and H. Tanaka, "Preliminary design study of a simple neutron energy spectrometer using a CsI self-activation method for daily QA of accelerator-based BNCT," *Journal of Nuclear Science and Technology*, vol. 56, no. 1, pp. 70–77, Jan. 2, 2019, ISSN: 0022-3131, 1881-1248. DOI: 10.1080/00223131.2018.1523757. [Online]. Available: https://www.tandfonline.com/doi/full/10.1080/00223131.2018.1523757 (visited on 09/23/2024).

[167] S. Minato and M. Kawano, "Evaluation of exposure due to terrestrial gamma-radiation by response matrix method," *Journal of Nuclear Science and Technology*, vol. 7, no. 8, pp. 401–406, Aug. 1970, ISSN: 0022-3131, 1881-1248. DOI: 10.1080/18811248.1970.9734709. [Online]. Available: http://www.tandfonline.com/doi/abs/10.1080/18811248.1970.9734709 (visited on 09/09/2024).

[168] Y. Nauchi and S. Iwasaki, "Convergence of unfolded spectrum with response function for single radiation based on bayes' theorem," *Nuclear Instruments and Methods in Physics Research Section A: Accelerators, Spectrometers, Detectors and Associated Equipment*, vol. 735, pp. 437–443, Jan. 2014, ISSN: 01689002. DOI: 10.1016/j.nima.2013.09.064. [Online]. Available: https://linkinghub.elsevier.com/retrieve/pii/S0168900213013077 (visited on 05/01/2024).

[169] M. I. Kobayashi, N. Suzuki, T. Saze, *et al.*, "The evaluation of a simple measurement method using NaI(tl) scintillation survey-meter for radiation safety management of radioactivated armor tiles of LHD vacuum vessel," *Radiation Safety Management*, vol. 20, no. 0, pp. 20–28, 2021, ISSN: 1347-1511, 1884-9520. DOI: 10.12950/rsm.210416. [Online]. Available: https://www.jstage.jst.go.jp/article/rsm/20/0/20_210416/_article (visited on 06/02/2024).

[170] M. Kobayashi, F. Sato, S. Kusaka, and I. Murata, "Feasibility study on real-time -ray spectrum / dose measurement system," *EPJ Web of Conferences*, vol. 153, F. Malvagi, F. Malouch, C. Diop, J. Miss, and J. Trama, Eds., p. 07 014, 2017, ISSN: 2100-014X. DOI: 10.1051/epjconf/201715307014. [Online]. Available: http://www.epj-conferences.org/10.1051/epjconf/201715307014 (visited on 04/23/2024).

[171] C. N. S. Commission, *Radionuclide Information Booklet*. Canadian Nuclear Safety Commission, 2017, ISBN: 978-0-660-06034-7. [Online]. Available: https://publications.gc.ca/site/eng/9.822446/publication.html.

[172] IAEA, Ed., *Decay data of the transactinium nuclides*, Technical reports series / International Atomic Energy Agency 261, Vienna: IAEA, 1986, 173 pp., ISBN: 978-92-0-135086-2.

[173] J. R. Association, *Radioisotope pocket data book (In Japanese)*. Maruzen, 2009, 20 pp.

[174] S. Moriuchi, M. Tsutsumi, and K. Saito, "Construction of response matrices for various cylindrical and spherical NaI(tl) scintillation detectors for gamma rays and the test results," *Japanese Journal of Health Physics*, vol. 44, no. 1, pp. 122–133, 2009, ISSN: 0367-6110, 1884-7560. DOI: 10.5453/jhps.44.122. [Online]. Available: http://www.jstage.jst.go.jp/article/jhps/44/1/44_1_122/_article (visited on 05/12/2024).

[175] M. Tsutsumi, K. Saito, and S. Moriuchi, *Spectrum-dose conversion operators, g(e) functions of NaI(tl) scintillators adapted for effective dose equivalent quantities*, 1991. DOI: 10.11484/jaeri-m-91-204. [Online]. Available: https://doi.org/10.11484/jaeri-m-91-204 (visited on 09/17/2024).

[176] K. Park, "Ambient dose equivalent measurement with a CsI(tl) based electronic personal dosimeter," *Nuclear Engineering and Technology*, 2019.

[177] S. Tsuda and K. Saito, "Spectrum-dose conversion operator of NaI(tl) and CsI(tl) scintillation detectors for air dose rate measurement in contaminated environments," *Journal of Environmental Radioactivity*, vol. 166, pp. 419–426, Pt 3 Jan. 2017, ISSN: 1879-1700. DOI: 10.1016/j.jenvrad.2016.02.008.

[178] S. Tsuda, M. Tanigaki, T. Yoshida, R. Okumura, and K. Saito, "Analyses of h∗(10) dose rates measured in environment contaminated by radioactive caesium: Correction of directional dependence of scintillation detectors," *Journal of Environmental Radioactivity*, vol. Jan, no. 166, pp. 419–426, 2021. DOI: 10.1016/j.jenvrad.2016.02.008.

[179] M. Kowatari, Y. Tanimura, P. Kessler, S. Neumaier, and A. Röttger, "Study on method for simultaneous determination of ambient dose equivalent rates and activity concentration in air for environmental radiation monitoring," *RADIOISOTOPES*, vol. 70, no. 1, pp. 1–18, Jan. 15, 2021, ISSN: 0033-8303, 1884-4111. DOI: 10.3769/radioisotopes.70.1. [Online]. Available: https://www.jstage.jst.go.jp/article/radioisotopes/70/1/70_700101/_article (visited on 06/02/2024).

[180] IAEA, *Radiation protection and safety of radiation sources: international basic safety standards; general safety requirements* (IAEA safety standards series General safety requirements GSR-3). Vienna: Internat. Atomic Energy Agency, 2014, 436 pp., ISBN: 978-92-0-135310-8.

[181] IAEA, *Fundamental safety principles: safety fundamentals* (IAEA safety standards series SF-1). Vienna: Internat. Atomic Energy Agency, 2006, 21 pp., ISBN: 978-92-0-110706-0.

[182] A. Konefał, A. Orlef, M. Łaciak, A. Ciba, and M. Szewczuk, "Thermal and resonance neutrons generated by various electron and x-ray therapeutic beams from medical linacs installed in polish oncological centers," *Reports of Practical Oncol-*

ogy & Radiotherapy, vol. 17, no. 6, pp. 339–346, Nov. 2012, ISSN: 15071367. DOI: 10.1016/j.rpor.2012.06.004. [Online]. Available: https://linkinghub.elsevier.com/retrieve/pii/S1507136712000910 (visited on 08/24/2024).

[183] R. K. Wu and P. H. McGinley, "Neutron and capture gamma along the mazes of linear accelerator vaults," *Journal of Applied Clinical Medical Physics*, vol. 4, no. 2, 2003.

[184] D.-Y. Lee, J.-H. Kim, and E.-T. Park, "Assessment of human exposure doses received by activation of medical linear accelerator components," *Journal of Instrumentation*, vol. 12, no. 8, P08022–P08022, Aug. 31, 2017, ISSN: 1748-0221. DOI: 10.1088/1748-0221/12/08/P08022. [Online]. Available: https://iopscience.iop.org/article/10.1088/1748-0221/12/08/P08022 (visited on 09/06/2024).

[185] H. Dombrowski and R. Nolte, "Quantitative investigation of gamma radiation in accelerator produced ISO neutron fields," *Journal of Radiological Protection*, vol. 44, no. 1, p. 011 507, Mar. 1, 2024, ISSN: 0952-4746, 1361-6498. DOI: 10.1088/1361-6498/ad1fdb. [Online]. Available: https://iopscience.iop.org/article/10.1088/1361-6498/ad1fdb (visited on 06/02/2024).

[186] ORNL, "Gamma-ray dose rates resulting from neutron captures in air," Oak Ridge National Lab. (ORNL), Oak Ridge, TN (United States), ORNL-2462, 1958. [Online]. Available: https://doi.org/10.2172/4310301.

[187] M. S. Gossman, P. H. McGinley, M. B. Rising, and A. J. Pahikkala, "Radiation skyshine from a 6 MeV medical accelerator," *Journal of Applied Clinical Medical Physics*, vol. 11, no. 3, pp. 259–264, Jun. 2010, ISSN: 1526-9914, 1526-9914. DOI: 10.1120/jacmp.v11i3.3032. [Online]. Available: https://aapm.onlinelibrary.wiley.com/doi/10.1120/jacmp.v11i3.3032 (visited on 04/28/2024).

[188] E. de Paiva, "Effect of the skyshine approach on the total cost of concrete shielding in a conventional radiotherapy facility room," 2018.

[189] S. Tamaki, F. Panuntun, K. Uedoi, *et al.*, "Radioactivation analysis of concrete wall in OKTAVIAN facility," *Plasma and Fusion Research*, vol. 17, no. 0, pp. 1 405 001–1 405 001, Jan. 21, 2022, ISSN: 1880-6821. DOI: 10.1585/pfr.17.1405001. [Online]. Available: https://www.jstage.jst.go.jp/article/pfr/17/0/17_1405001/_article (visited on 05/02/2024).

[190] S. Yoshida, R. Morotomi, T. Kondo, I. Murata, and A. Takahashi, "Measurement of secondary gamma-ray skyshine and groundshine from intense 14 MeV neutron source facility," *Journal of Nuclear Science and Technology*, vol. 37, pp. 650–654, sup1 Mar. 2000, ISSN: 0022-3131, 1881-1248. DOI: 10.1080/00223131.2000.10874969. [Online]. Available: https://www.tandfonline.com/doi/full/10.1080/00223131.2000.10874969 (visited on 04/28/2024).

[191] S. Yoshida, T. Nishitani, K. Ochiai, *et al.*, "Measurement of radiation skyshine with d–t neutron source," *Fusion Engineering and Design*, vol. 69, no. 1, pp. 637–641, Sep. 2003, ISSN: 09203796. DOI: 10.1016/S0920-3796(03)00196-0. [Online]. Available: https://linkinghub.elsevier.com/retrieve/pii/S0920379603001960 (visited on 04/28/2024).

[192] M. F. Uddin, M. Begum, M. Ahmed, *et al.*, "Radiation safety and shielding evaluation of newly installed medical LINAC facility in bangladesh," *Journal of Radiation Research and Applied Sciences*, vol. 17, no. 2, p. 100 844, Jun. 2024, ISSN: 16878507. DOI: 10.1016/j.jrras.2024.100844. [Online]. Available: https://linkinghub.elsevier.com/retrieve/pii/S1687850724000281 (visited on 09/06/2024).

[193] S. Green, H. Koivunoro, and H. Kumada, "Considerations for a dosimetry code of practice for BNCT," *Health and Technology*, vol. 14, no. 5, pp. 1017–1021, Sep. 2024, ISSN: 2190-7188, 2190-7196. DOI: 10.1007/s12553-024-00852-9. [Online]. Available: https://link.springer.com/10.1007/s12553-024-00852-9 (visited on 09/06/2024).

[194] R. L. Moss, F. Stecher-Rasmussen, K. Appelman, *et al.*, "Radioprotection for patients and staff during BNCT at the HFR petten," in *Frontiers in Neutron Capture Therapy*, M. F. Hawthorne, K. Shelly, and R. J. Wiersema, Eds., Boston, MA: Springer US, 2001, pp. 635–639, ISBN: 978-1-4613-5478-9 978-1-4615-1285-1. DOI: 10.1007/978-1-4615-1285-1_91. [Online]. Available: http://link.springer.com/10.1007/978-1-4615-1285-1_91 (visited on 09/23/2024).

[195] L. Porra, T. Seppälä, L. Wendland, *et al.*, "Accelerator-based boron neutron capture therapy facility at the helsinki university hospital," *Acta Oncologica*, vol. 61, no. 2, pp. 269–273, Feb. 1, 2022, ISSN: 0284-186X, 1651-226X. DOI: 10.1080/0284186X.

2021.1979646. [Online]. Available: https://www.tandfonline.com/doi/full/10.1080/0284186X.2021.1979646 (visited on 06/03/2024).

[196] European Commission. Joint Research Centre. Institute for Energy., *Requirements for boron neutron capture therapy (BNCT) at a nuclear research reactor.* LU: Publications Office, 2009. [Online]. Available: https://data.europa.eu/doi/10.2790/11743 (visited on 04/23/2024).

[197] N. Matsubayashi, H. Tanaka, T. Takata, K. Okazaki, Y. Sakurai, and M. Suzuki, "Development of real-time neutron detectors with different sensitivities to thermal, epithermal, and fast neutrons in BNCT," *Radiation Measurements*, vol. 140, p. 106 489, Jan. 2021, ISSN: 13504487. DOI: 10.1016/j.radmeas.2020.106489. [Online]. Available: https://linkinghub.elsevier.com/retrieve/pii/S1350448720302638 (visited on 04/23/2024).

[198] H. Tanaka, T. Takata, Y. Sakurai, *et al.*, "Development of real-time thermal neutron monitor array for boron neutron capture therapy," *Therapeutic Radiology and Oncology*, vol. 2, pp. 51–51, 2018, ISSN: 26162768. DOI: 10.21037/tro.2018.10.10. [Online]. Available: http://tro.amegroups.com/article/view/4655/5439 (visited on 04/23/2024).

[199] K. Akita, "Evaluation of neutron fluence measurement system utilizing a LiCAF scintillator - optical fiber detector for BNCT," The 58th Annual Conference of the Particle Therapy Co-Operative Group, Manchester, United Kingdom, 2019.

[200] R. L. Moss, O. Aizawa, D. Beynon, *et al.*, "The requirements and development of neutron beams for neutron capture therapy of brain cancer," vol. 33, pp. 27–40, 1997.

[201] M. Kim, B. H. Hong, I. Cho, *et al.*, "Design of a scintillator-based prompt gamma camera for boron-neutron capture therapy: Comparison of SrI2 and GAGG using monte-carlo simulation," *Nuclear Engineering and Technology*, vol. 53, no. 2, pp. 626–636, Feb. 2021, ISSN: 17385733. DOI: 10.1016/j.net.2020.07.010. [Online]. Available: https://linkinghub.elsevier.com/retrieve/pii/S1738573320302205 (visited on 04/23/2024).

[202] S. Kirschenmann, M. Bezak, S. Bharthuar, *et al.*, "Quality assessment of cadmium telluride as a detector material for multispectral medical imaging," *Journal of Instrumentation*, vol. 17, no. 1, p. C01070, Jan. 1, 2022, ISSN: 1748-0221. DOI:

10.1088/1748-0221/17/01/C01070. [Online]. Available: https://iopscience.iop.org/article/10.1088/1748-0221/17/01/C01070 (visited on 06/02/2024).

[203] K. Hiramatsu, S. Yoshihashi, S. Kusaka, F. Sato, E. Hoashi, and I. Murata, "Gamma-ray dose measurement with radio-photoluminescence glass dosimeter in mixed radiation field for BNCT," *EPJ Web of Conferences*, 2017.

[204] W. Ministry of Health Labour, "Report on the deliberation results: Treatment planning program for boron neutron capture therapy," Medical Device Evaluation Division Ministry of Health, Labour and Welfare, 2020.

[205] E. Bavarnegin, H. Khalafi, A. Sadremomtaz, Y. Kasesaz, and A. Khajeali, "Investigation of dose distribution in mixed neutron-gamma field of boron neutron capture therapy using n -isopropylacrylamide gel," *Nuclear Engineering and Technology*, vol. 49, no. 1, pp. 189–195, Feb. 2017, ISSN: 17385733. DOI: 10.1016/j.net.2016.07.012. [Online]. Available: https://linkinghub.elsevier.com/retrieve/pii/S1738573316301371 (visited on 06/03/2024).

[206] R. Kakino, N. Hu, H. Tanaka, *et al.*, "Out-of-field dosimetry using a validated PHITS model and computational phantom in clinical BNCT," *Medical Physics*, vol. 51, no. 2, pp. 1351–1363, Feb. 2024, ISSN: 0094-2405, 2473-4209. DOI: 10.1002/mp.16916. [Online]. Available: https://aapm.onlinelibrary.wiley.com/doi/10.1002/mp.16916 (visited on 06/04/2024).

[207] H. Jarahi, Y. Kasesaz, and S. M. Saleh-Koutahi, "Evaluation of the effective dose during BNCT at TRR thermal column epithermal facility," *Applied Radiation and Isotopes*, vol. 110, pp. 134–137, Apr. 2016, ISSN: 09698043. DOI: 10.1016/j.apradiso.2016.01.012. [Online]. Available: https://linkinghub.elsevier.com/retrieve/pii/S0969804316300124 (visited on 09/08/2024).

[208] M. Golshanian, A. A. Rajabi, and Y. Kasesaz, "Evaluation of the medical staff effective dose during boron neutron capture therapy using two high resolution voxel-based whole body phantoms," *Nuclear Engineering and Technology*, vol. 49, no. 7, pp. 1505–1512, Oct. 2017, ISSN: 17385733. DOI: 10.1016/j.net.2017.06.011. [Online]. Available: https://linkinghub.elsevier.com/retrieve/pii/S1738573316302522 (visited on 04/23/2024).

[209] C. Magni, I. Postuma, M. Ferrarini, *et al.*, "Design of a BNCT irradiation room based on proton accelerator and beryllium target," *Applied Radiation and Isotopes*,

vol. 165, p. 109 314, Nov. 2020, ISSN: 09698043. DOI: 10.1016/j.apradiso.2020.109314. [Online]. Available: https://linkinghub.elsevier.com/retrieve/pii/S0969804320304644 (visited on 06/03/2024).

[210] ORTEC/AMETEK, *MCA8000d multichannel analyzer*. [Online]. Available: https://www.amptek.com/products/multichannel-analyzers/mca-8000d-digital-multichannel-analyzer.

[211] E. JAPAN. "Hōshasen sokuteiki kaihatsu hanbai EMF japan kabushiki gaisha [radiation measurement devices development and sales EMF japan co., ltd.]" (), [Online]. Available: https://www.emf-japan.com (visited on 05/06/2023).

[212] K. N. Vincent, S. Mahapatra, I. Poddar, and S. Verma, "Improving the resolution and light yield in CsI(tl) scintillators," *Nuclear Instruments and Methods in Physics Research Section A: Accelerators, Spectrometers, Detectors and Associated Equipment*, vol. 1056, p. 168 624, Nov. 2023, ISSN: 01689002. DOI: 10.1016/j.nima.2023.168624. [Online]. Available: https://linkinghub.elsevier.com/retrieve/pii/S0168900223006149 (visited on 04/23/2024).

[213] J. Wang, Z. Wang, J. Peeples, H. Yu, and R. P. Gardner, "Development of a simple detector response function generation program: The CEARDRFs code," *Applied Radiation and Isotopes*, vol. 70, no. 7, pp. 1166–1174, Jul. 2012, ISSN: 09698043. DOI: 10.1016/j.apradiso.2011.11.003. [Online]. Available: https://linkinghub.elsevier.com/retrieve/pii/S0969804311005380 (visited on 05/02/2024).

[214] J. Goorley, "MCNP5 to MCNP6 migration notes," LA-UR-13-23338, 1079560, Jun. 26, 2013, LA–UR–13–23 338, 1 079 560. DOI: 10.2172/1079560. [Online]. Available: https://www.osti.gov/servlets/purl/1079560/ (visited on 05/02/2024).

[215] D. N. Grozdanov, N. A. Fedorov, V. M. Bystritski, *et al.*, "Measurement of angular distributions of gamma rays from the inelastic scattering of 14.1-MeV neutrons by carbon and oxygen nuclei," *Physics of Atomic Nuclei*, vol. 81, no. 5, pp. 588–594, Sep. 2018, ISSN: 1063-7788, 1562-692X. DOI: 10.1134/S106377881805006X. [Online]. Available: http://link.springer.com/10.1134/S106377881805006X (visited on 04/17/2024).

[216] A. E. S. of Japan, *Dose Conversion Factor for Radiation Shielding Calculation [Hōshasen shēkei keisan no tame no senryō kansan keisū]* (AESJ-SC-R002:2010). Atomic Energy Society of Japan, 2010, ISBN: 978-4-89047-336-6.

[217] A. El Hamli, A. Bazza, A. Moussa, M. Hamal, M. Zerfaoui, and M. Ouchrif, "Data and simulation studies on the influence of scintillation crystal dimensions on spectrometric parameters," *Applied Radiation and Isotopes*, vol. 181, p. 110 053, Mar. 2022, ISSN: 09698043. DOI: 10.1016/j.apradiso.2021.110053. [Online]. Available: https://linkinghub.elsevier.com/retrieve/pii/S0969804321004449 (visited on 05/11/2024).

[218] M. Jeong, B. Van, B. T. Wells, L. J. D'Aries, and M. D. Hammig, "Comparison between pixelated scintillators: CsI(tl), LaCl 3(ce) and LYSO(ce) when coupled to a silicon photomultipliers array," *Nuclear Instruments and Methods in Physics Research Section A: Accelerators, Spectrometers, Detectors and Associated Equipment*, vol. 893, pp. 75–83, Jun. 2018, ISSN: 01689002. DOI: 10.1016/j.nima.2018.03.024. [Online]. Available: https://linkinghub.elsevier.com/retrieve/pii/S0168900218303590 (visited on 05/15/2024).

[219] I. Lab. "Domestic producer and developer of sodium iodide crystals and cesium iodide crystals i.s.c.lab. co., ltd [youka natoriumu kesshou・youka seshiumu kesshou no kokunai seisan ・kaihatsu kigyou | i.s.c.lab. kabushikigaisha]." (), [Online]. Available: http://www.isc-lab.com (visited on 05/03/2023).

[220] Y. Ogawa, T. Iida, K. Sumita, and C. Ichihara, "Measurement of radioactivity in aluminum alloys and stainless steel irradiated by 14-MeV d-t neutrons," *Journal of Nuclear Science and Technology*, vol. 21, no. 7, pp. 561–563, Jul. 1984, ISSN: 0022-3131, 1881-1248. DOI: 10.1080/18811248.1984.9731082. [Online]. Available: http://www.tandfonline.com/doi/abs/10.1080/18811248.1984.9731082 (visited on 08/19/2024).

[221] Y. Ikeda, C. Konno, Y. Oyama, K. Kosako, K. Oishi, and H. Maekawa, "Absolute measurements of activation cross sections of 27al(n, p)27mg, 27al(n,)24na, 56fe(n, p)56mn, 90zr(n, 2n)89m+gZr and 93nb(n, 2n)92mnb at energy range of 13.314.9 MeV," *Journal of Nuclear Science and Technology*, vol. 30, no. 9, pp. 870–880, Sep. 1993, ISSN: 0022-3131, 1881-1248. DOI: 10.1080/18811248.1993.9734561.

[Online]. Available: http://www.tandfonline.com/doi/abs/10.1080/18811248.1993.9734561 (visited on 09/08/2024).

[222] M.-M. Bé and Bureau international des poids et mesures, Eds., *Table of radionuclides. Vol. 1: A=1 to 150*, vol. 1, Monographie BIPM 5, Sèvres: BIPM, 2004, 285 pp., ISBN: 978-92-822-2206-5.

[223] N. Nakao, T. Kajimoto, T. Sanami, *et al.*, "Measurements and monte carlo simulations of high-energy neutron streaming through the access maze using activation detectors at 24 GeV/c proton beam facility of CERN/CHARM," *Journal of Nuclear Science and Technology*, vol. 58, no. 8, pp. 899–907, Aug. 3, 2021, ISSN: 0022-3131, 1881-1248. DOI: 10.1080/00223131.2021.1887003. [Online]. Available: https://www.tandfonline.com/doi/full/10.1080/00223131.2021.1887003 (visited on 05/02/2024).

[224] V. P. Chechev and N. K. Kuzmenko, "Decay data evaluation project (DDEP): Updated decay data evaluations for 24 na, 46 sc, 51 cr, 54 mn, 57 co, 59 fe, 88 y, 198 au," *Applied Radiation and Isotopes*, vol. 109, pp. 139–145, Mar. 2016, ISSN: 09698043. DOI: 10.1016/j.apradiso.2015.11.009. [Online]. Available: https://linkinghub.elsevier.com/retrieve/pii/S0969804315302372 (visited on 05/02/2024).

[225] E. M. Epp and H. C. Griffin, "Use of 24na as a -ray calibration source above 3mev," *Nuclear Instruments and Methods in Physics Research Section A: Accelerators, Spectrometers, Detectors and Associated Equipment*, vol. 505, no. 1, pp. 9–12, Jun. 2003, ISSN: 01689002. DOI: 10.1016/S0168-9002(03)01008-8. [Online]. Available: https://linkinghub.elsevier.com/retrieve/pii/S0168900203010088 (visited on 05/02/2024).

[226] N. R. Authority, *Gamma-ray Spectral Analysis Using Germanium Detector in Emergencies* (The series of environmental radioactivity measuring methods 24). 2018.

[227] D. C. Vasconcelos, C. Pereira, S. Gallardo, Z. Rocha, and T. O. Santos, "EFFICIENCY SIMULATION OF a HPGE DETECTOR FOR THE ENVIRONMENTAL RADIOACTIVITY LABORATORY/CDTN USING a MCNP-GAMMAVISION METHOD," 2011.

[228] J. Bolivar, M. García-León, and R. García-Tenorio, "On self-attenuation corrections in gamma-ray spectrometry," *Applied Radiation and Isotopes*, vol. 48, no. 8, pp. 1125–1126, Aug. 1997, ISSN: 09698043. DOI: 10.1016/S0969-8043(97)00034-1. [Online]. Available: https://linkinghub.elsevier.com/retrieve/pii/S0969804397000341 (visited on 09/08/2024).

[229] S. Seltzer, *XCOM-photon cross sections database, NIST standard reference database 8*, 1987. DOI: 10.18434/T48G6X. [Online]. Available: http://www.nist.gov/pml/data/xcom/index.cfm (visited on 09/08/2024).

[230] F. Corvi, A. Prevignano, H. Liskien, and P. Smith, "An experimental method for determining the total efficiency and the response function of a gamma-ray detector in the range 0.5–10 MeV," *Nuclear Instruments and Methods in Physics Research Section A: Accelerators, Spectrometers, Detectors and Associated Equipment*, vol. 265, no. 3, pp. 475–484, Mar. 1988, ISSN: 01689002. DOI: 10.1016/S0168-9002(98)90016-X. [Online]. Available: https://linkinghub.elsevier.com/retrieve/pii/S016890029890016X (visited on 09/17/2024).

[231] C. He, Y. Dang, F. Liu, *et al.*, "Photonuclear reaction study with the (p,gamma) resonance gamma-source," *EPJ Web of Conferences*, vol. 239, Z. Ge, N. Shu, Y. Chen, W. Wang, and H. Zhang, Eds., p. 01 014, 2020, ISSN: 2100-014X. DOI: 10.1051/epjconf/202023901014. [Online]. Available: https://www.epj-conferences.org/10.1051/epjconf/202023901014 (visited on 09/23/2024).

[232] I. Murata, S. Nakamura, M. Manabe, H. Miyamaru, and I. Kato, "Characterization measurement of a thick CdTe detector for BNCT-SPECT –detection efficiency and energy resolution," *Applied Radiation and Isotopes*, vol. 88, pp. 129–133, Jun. 2014, ISSN: 09698043. DOI: 10.1016/j.apradiso.2014.01.023. [Online]. Available: https://linkinghub.elsevier.com/retrieve/pii/S0969804314000360 (visited on 06/03/2024).

[233] D. Grozdanov, N. Fedorov, Y. Kopatch, *et al.*, "Semi-empirical gamma-ray response function of BGO, NaI(tl) and LaBr 3 (ce) scintillation detectors," *Nuclear Instruments and Methods in Physics Research Section A: Accelerators, Spectrometers, Detectors and Associated Equipment*, vol. 1014, p. 165 741, Oct. 2021, ISSN: 01689002. DOI: 10.1016/j.nima.2021.165741. [Online]. Available: https:

//linkinghub.elsevier.com/retrieve/pii/S0168900221007269 (visited on 09/24/2024).

[234] F. Andreoli, M. Angelone, A. Colangeli, *et al.*, "Comparison between measurement and calculations for a 14 MeV neutron water activation experiment," *EPJ Web of Conferences*, vol. 239, Z. Ge, N. Shu, Y. Chen, W. Wang, and H. Zhang, Eds., p. 21 002, 2020, ISSN: 2100-014X. DOI: 10.1051/epjconf/202023921002. [Online]. Available: https://www.epj-conferences.org/10.1051/epjconf/202023921002 (visited on 06/02/2024).

[235] I. Murata, Y. Otani, and F. Sato, "Neutron intensity monitor with activation foil for p-li neutron source for BNCT –feasibility test of the concept," *Applied Radiation and Isotopes*, vol. 106, pp. 75–77, Dec. 2015, ISSN: 09698043. DOI: 10.1016/j.apradiso.2015.07.034. [Online]. Available: https://linkinghub.elsevier.com/retrieve/pii/S0969804315301147 (visited on 09/04/2024).

[236] D. J. Thomas, P. Kolkowski, N. J. Roberts, B. D'Mellow, and M. J. Joyce, "Investigation of a possible replacement for cadmium as a thermal neutron absorbing material in neutron instruments," Lancaster, DQL-RN 017, 2006.

[237] AMPTEK, *Complete gamma ray spectrometer GAMMA-RAD5*, 2015. [Online]. Available: https://www.amptek.com/internal-products/obsolete-products/gamma-rad5-gamma-ray-detection-system.

[238] J. A. Brown, B. L. Goldblum, J. M. Gordon, T. A. Laplace, T. S. Nagel, and A. Venkatraman, "Proton discrimination in CLYC for fast neutron spectroscopy," *Nuclear Instruments and Methods in Physics Research Section A: Accelerators, Spectrometers, Detectors and Associated Equipment*, vol. 1069, p. 169 859, Dec. 2024, ISSN: 01689002. DOI: 10.1016/j.nima.2024.169859. arXiv: 2406.15730[physics]. [Online]. Available: http://arxiv.org/abs/2406.15730 (visited on 09/24/2024).

[239] J. Zhu, T. Xue, G. Gong, Z. Cao, L. Wei, and J. Li, "Prototype of integrated pulse digitalization and readout electronics for CLYC detector," in *2018 IEEE Nuclear Science Symposium and Medical Imaging Conference Proceedings (NSS/MIC)*, Sydney, Australia: IEEE, Nov. 2018, pp. 1–4, ISBN: 978-1-5386-8494-8. DOI: 10.1109/NSSMIC.2018.8824287. [Online]. Available: https://ieeexplore.ieee.org/document/8824287/ (visited on 09/24/2024).

[240] A. Gottardo, G. Andreetta, and R. Lombardi, "The CLYC-7 scintillator as a fast neutron spectrometer: Pulse-shape discrimination for different neutron-induced reaction channels," *Nuclear Instruments and Methods in Physics Research Section A: Accelerators, Spectrometers, Detectors and Associated Equipment*, vol. 1041, p. 167 332, Oct. 2022, ISSN: 01689002. DOI: 10.1016/j.nima.2022.167332. [Online]. Available: https://linkinghub.elsevier.com/retrieve/pii/S0168900222006489 (visited on 09/04/2024).

[241] K. Kondo, "Experimental studies on fusion neutron-induced charged-particle emission reactions of light elements," Doctoral Dissertation, Osaka University, 2008.

9 | List of Publications and Academic Achievements

Publications (First or second authorship)

1. N. Voulgaris, T. Miyoshi, S. Tamaki, S. Kusaka, and I. Murata, '**Development of Real-Time Gamma-Ray Spectrum and Dose Monitor Investigation of True Real-Time Convergence**', in *Proceedings of the 37th Workshop on Radiation Detectors and their uses*, Tsukuba, Ibaraki, Japan: High Energy Accelerator Research Organization (KEK), 2024, pp. 30–42. https://www.i-repository.net/il/meta_pub/G0000128Lib_202325001 [16].

2. N. Voulgaris, H. Nishimura, S. Tamaki, S. Kusaka, and I. Murata, '**Balancing Performance and Portability: A Study on CsI(Tl) Crystal Sizes for Real-Time Gamma-Ray Spectrum and Dose Monitoring**', *Radiation*, vol. 4, no. 3, pp. 213–223, Jul. 2024, doi: https://doi.org/10.3390/radiation4030016. [15].

3. I. Murata, N. Voulgaris, T. Miyoshi, M. Shinohara, H. Nishimura, M. Kobayashi, S. Kusaka, S. Tamaki and F. Sato, '**Real-time gamma-ray energy spectrum / dose monitor with k–α method based on sequential Bayesian estimation**' , *Applied Radiation and Isotopes*, vol. 212, p. 111454, Oct. 2024, doi: https://doi.org/10.1016/j.apradiso.2024.111454. [14].

4. (Under Review, second review round) N. Voulgaris, S. Tamaki, J. Qiu, S. Kusaka, and I. Murata, '**Simultaneous Measurement of Gamma-ray Energy Spectrum and Dose in Real-time up to 3 MeV with Sequential Bayesian Estimation and CsI(Tl) Scintillator-based Prototype Monitor**', *Jpn. J. Appl. Phys.*

Publications (3rd or Later Authorship)

5. H. Nishimura, S. Moe, M. Takaaki, N. Voulgaris, S. Kusaka, S. Tamaki, F. Sato, and I. Murata, '**Experimental verification of real-time gamma-ray energy spectrum and dose monitor**', *Applied Radiation and Isotopes*, vol. 185, p. 110226, Jul. 2022, doi: 10.1016/j.apradiso.2022.110226. [135]

Additional Research Contributions

6. S. Kusaka, N. Voulgaris, K. Onishi, J. Ueda, S. Saito, S. Tamaki, I. Murata, T. Takata, and M. Suzuki, '**Therapeutic Effect of Boron Neutron Capture Therapy on Boronophenylalanine Administration via Cerebrospinal Fluid Circulation in Glioma Rat Models**', *Cells*, vol. 13, no. 19, Sep. 2024, doi: https://doi.org/10.3390/cells13191610.

7. J. Qiu, D. Hatano, Y. Ge, N. Voulgaris, K. Sagara, Z. Qiao, S. Tamaki, S. Kusaka and I. Murata, '**Preliminary study of a compact epithermal neutron absolute flux intensity measurement system for real-time in-vivo dose monitoring in boron neutron capture therapy**', *Radiation Measurements*, p. 107308, Oct. 2024, doi: https://doi.org/10.1016/j.radmeas.2024.107308.

Presentations

1. Voulgaris N., Miyoshi T., Tamaki S., Kusaka S., and Murata I., 'Development of Real-time Gamma-ray Spectrum and Dose Monitor', Young Researcher's BNCT Meeting, November 2022

2. Voulgaris N., Miyoshi T., Tamaki S., Kusaka S., and Murata I., ' 'Development of Real-time Gamma-ray Spectrum and Dose Monitor - Investigation of True Real-time Convergence', 37th Workshop on Radiation Detectors and Their Uses, High Energy Accelerator Research Organization (KEK), January 2023

3. Voulgaris N., Sumi H., Kusaka S., Tamaki S., and Murata I., 'Experimental verification of real-time gamma-ray energy spectrum and dose monitor up to 3 MeV gamma-rays', 11th International Symposium on Radiation Safety and Detection Technology (ISORD), Hanyang University, Innovative Technology Center for Radiation Safety (iTRS) and Korean Association for Radiation Protection, July 2023

4. Voulgaris N., Miyoshi T., Tamaki S., Kusaka S., and Murata I., 'Development of Real-time Gamma-ray Spectrum and Dose Monitor: Investigation of application in BNCT', 19th Congress on Neutron Capture Therapy, Yokohama, Japan, July 2023

5. Voulgaris N., Tamaki S., Kusaka S., and Murata I., ' 医療現場（加速器施設）にお

けるリアルタイム　線スペクトル・線量測定装置開発', 第 32 回放射線利用総合シンポジウム, 大阪ニュークリアサイエンス協会, January 2024

Awards

1. Japanese Government (MEXT) Scholarship, Oct 2021, Japan Ministry of Education, Culture, Sports, Science and Technology.
2. Eight-University Engineering Consortium "Doctoral Forum" Core Member, Mar. 2024, Osaka University.

A | Prototype Monitor Related Developmental Aspects

A.1 EMF Japan and Commercialization of Prototype Monitor

Early developmental components and details associated wit the actual development and commercialization of the prototype monitor are introduced below kindly provided by EMF Japan Co., Ltd. [211].

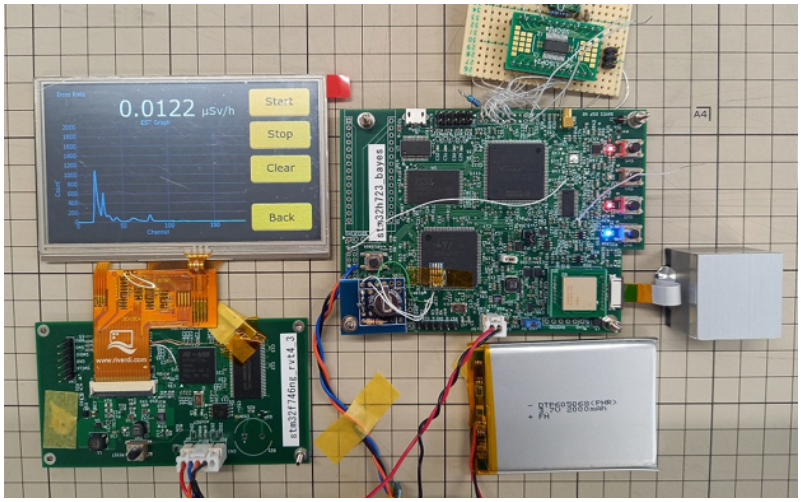

Figure A.1: Early Developmental Process for Commercialization, courtesy of EMF Japan co.ltd.

Table A.1: Specifications of the Prototype Monitor

Item	**Specifications**
Computation	Real-time gamma-ray spectrum and dose measurement based on Bayesian estimation. Pulse processing is done after 40MSPS AD conversion.
Dose Rate Measurement Range	0.05 Sv/h ∼1mSv/h
Sensor	CsI(Tl) 25 × 25 × 12.5mm I.S.C.Lab. MPPC S14161-2302 (13mm square)
MPPC Power Supply	Standard rated 40V, adjustable. Temperature compensation available. (Hamamatsu Photonics MPPC power supply (board-mounted type) is discontinued, so new development is required.)
Maximum Count Rate	10,000cps (target value). Dead-time correction above this.
Display	LCD 2.4 inches - 2.8 inches TFT 240×320, 4.3 inches TFT 480×272, Display size 95mm × 53.8mm.
Touch Panel	Available. Touch panel. Operable with stylus.
Operation Switch	Power switch only. Other functions controlled via touch panel.
DAC Analog Output	12bit 40MSPS 10bit 25MSPS 1ch, Internal FPGA digital processing waveform is output as analog.
Communication	USB (requires separate dedicated PC software development). Wifi (under consideration.
Data Storage	Up to approximately 2GB SD card. Shared with response function file storage. Data can be read via USB or SD card.
Battery Life	2000mAh for 4 hours (Power save mode and auto power-off feature under consideration.)
Dimensions	122mm × 94mm × 30mm. The part that is currently 30mm thick can potentially be reduced to around 26mm by standardizing the detector connector board.

A.2 Complementary Investigations of True Real-time Measurements

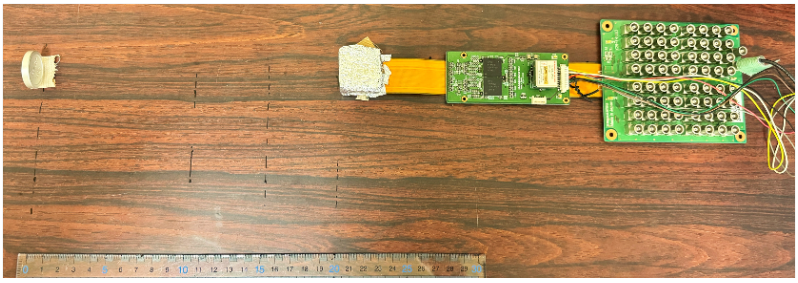

Figure A.2: Experimental setup for 20 cm measurements with standard gamma-ray sources

Table A.2: Comparison of theoretical and measured dose rates at 20 cm for various isotopes using the prototype monitor and NaI detector. Results are mainly in line with other investigations

Isotope	**Theoretical value**	**Prototype Monitor**	**NaI**
Cs	1.61	1.64	1.74
Co	1.59	1.61	1.45
Ba	0.56	0.48	0.70
Na	0.26	0.39	0.44

Table A.2 compares the theoretical dose rate values at a distance of 20 cm with the measurements obtained using both the prototype monitor and an NaI survey meter (Aloka TCS 171 Hitachi). For ^{137}Cs, the prototype monitor closely matches the theoretical value, indicating accurate calibration and performance. However, the NaI shows a slightly higher reading. For ^{60}Co the prototype monitor is again very close to the theoretical value, while the NaI results varies. For ^{133}Ba and ^{22}Na, both detectors overestimate the dose rates, even more so the survey meter. The prototype monitor remains closer to the theoretical values than the NaI. This suggests that the prototype monitor maintains a better overall accuracy across different energy ranges. The overestimations and underestimations of the survey meter are in line with what is seen throughout this thesis.

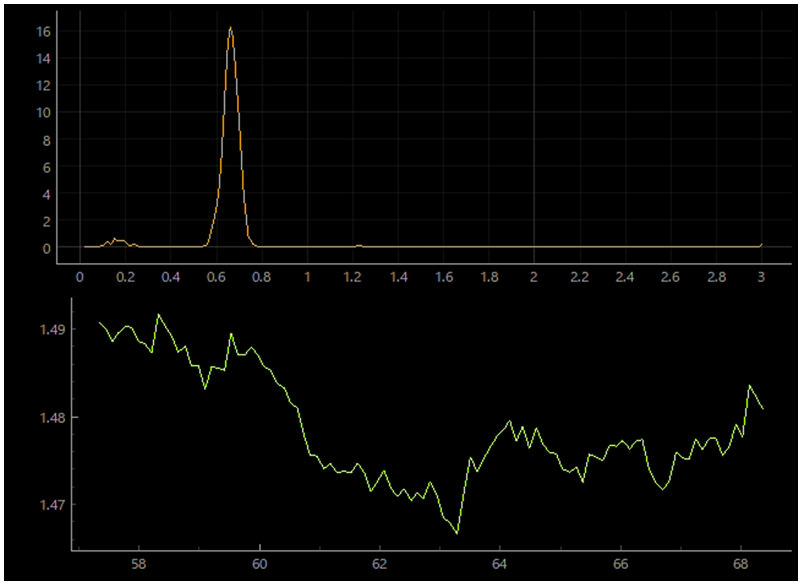

Figure A.3: Estimation of ^{137}Cs spectrum for $k = 10^{-4}$ at 20cm

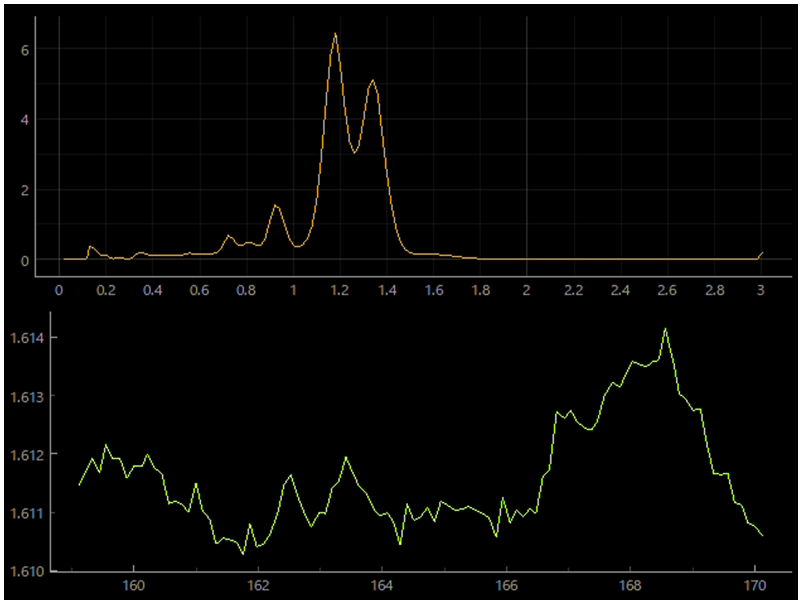

Figure A.4: Estimation of ^{60}Co spectrum for $k = 10^{-4}$ at 20cm

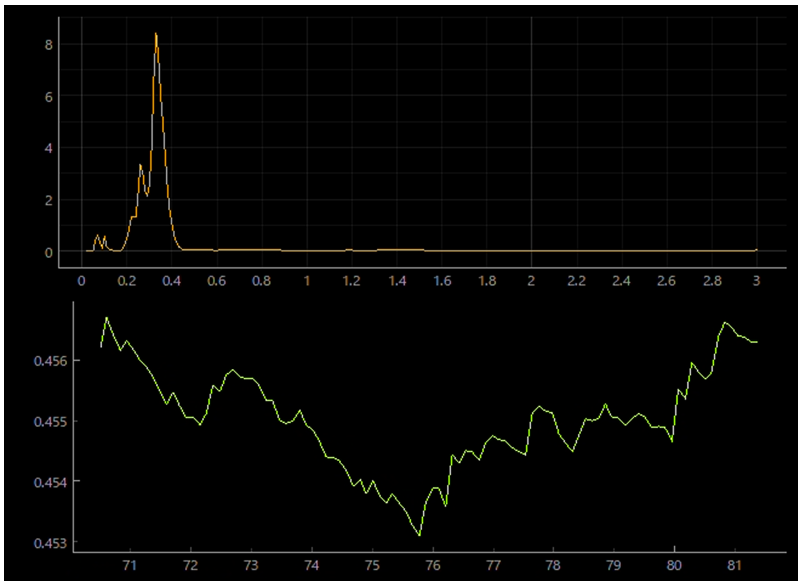

Figure A.5: Estimation of ^{133}Ba spectrum for $k = 10^{-4}$ at 20cm

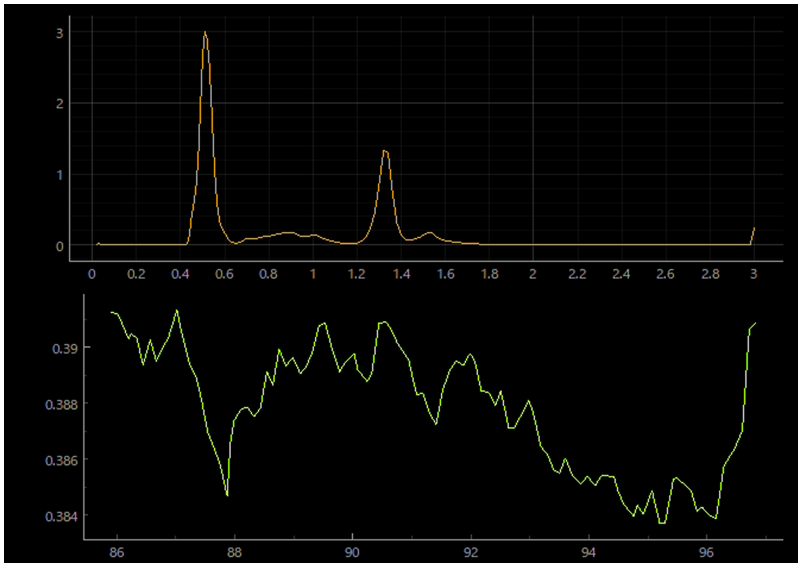

Figure A.6: Estimation of ^{22}Na spectrum for$k = 10^{-3}$ at 20cm

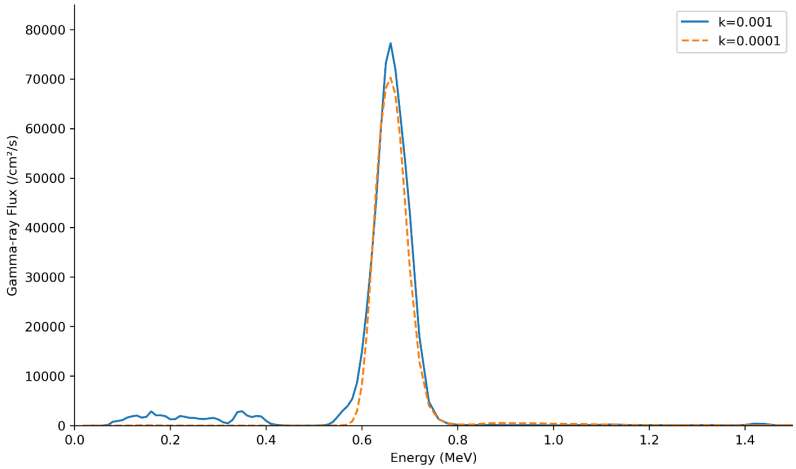

Figure A.7: Unfolded energy spectra of ^{137}Cs for k=10-3 and k=10-4, same time elapsed

Figure A.7 illustrates the degree of stability between a converged Cs energy spectrum when $k = 10^{-3}$ and when $k = 10^{-4}$

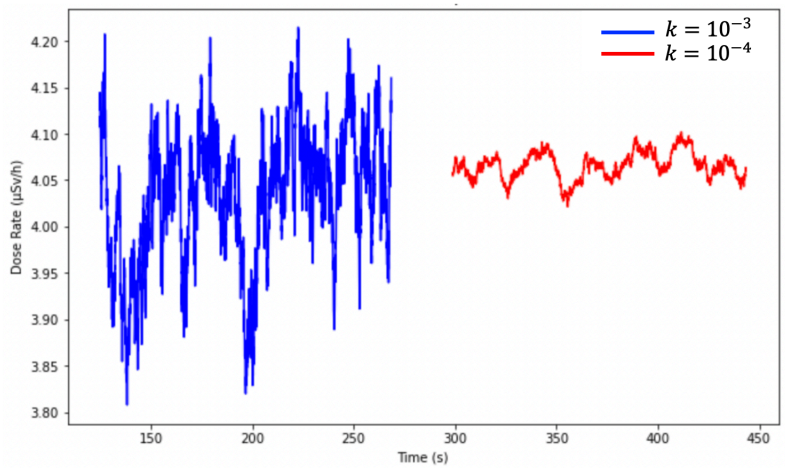

Figure A.8: Dose rate of ^{24}Na source for k= 10-3 and 10-4, post convergence

Figure A.8 illustrates the difference in deviation between the estimated dose rate when $k = 10^{-3}$ and when $k = 10^{-4}$.

A.3 Investigation of convergence

During real-time measurement, convergence is easily identifiable visually, by observing the time dependent change of the gamma-ray spectrum and dose-rate. However, it is beneficial to incorporate an algorithm to check the convergence process as measurement progresses. From the introduction to the convergence parameter I, an investigation methodology into developing more comprehensive ways to judge the convergence of the estimation. Two criteria are considered for assessing convergence:

1. *Variance* of the energy spectrum: smaller variance indicates convergence.
2. *Residual* between estimated and theoretical spectra: smaller residuals indicate convergence.

The *unbiased variance* $S_{c,j}$ of the estimated spectrum at the c-th revision is defined as:

$$S_{c,j} = \frac{1}{c-1} \sum_{x=1}^{c} \left(\phi_{\mathrm{est},x,j} - \overline{\phi_{\mathrm{est},c,j}} \right)^2 \tag{A.1}$$

Sequential calculation of variance can be performed using:

$$S_{c+1,j} = \frac{c+1}{c} \cdot \sigma^2_{c+1,j} \tag{A.2}$$

The *summed variance* over all energy bins $S_{\text{sum},c}$ is used to track convergence:

$$S_{\text{sum},c} = \sum_{j=1}^{n} S_{c,j} \tag{A.3}$$

As I increases, $S_{\text{sum},c}$ initially increases, reaches a maximum, and then decreases, indicating that the spectrum has converged. This behavior is consistent for different k values when normalized by I. The *Normalized Absolute Error (NAE)* is introduced to evaluate the convergence of the estimated energy spectrum by comparing it to the true spectrum obtained from measurements. Specifically, NAE is calculated as the normalized difference between the true pulse height distribution y_{true} and the estimated pulse height distribution y_{est} between the estimated and true pulse-height distributions, and is given by the following Equation:

$$NAE = \frac{\|(y_{\text{true}}) - (y_{\text{est}})\|_1}{\|(y_{\text{true}})\|_1} \tag{A.4}$$

A smaller NAE value indicates that the estimated distribution closely matches the true distribution, suggesting better convergence. Initially, NAE follows the statistical error in the true pulse height distribution. As counts (c) increase, NAE typically decreases, reflecting improved accuracy in the estimated spectrum. NAE stabilizes at a certain point, indicating that the energy spectrum has effectively converged. This stabilization corresponds to a specific value of the convergence parameter I. Apart from the above, investigating the rate of change in the spectrum and dose rate data during measurement by the first derivative of the dose rate or spectrum values, and a rolling average over a sliding window. If the average rate of change within the window consistently falls below a predefined threshold, it might suggest convergence.

A.4 Programs of *k*-α Method

A short introduction and key parts of the methods introduced in Sections 5.5 and 5.9 are given below:

gccDppConsolewin:

This code processes the amplified and time list data (binary data) and sends it in the following format:

DATA[0]	DATA[1]	DATA[2]	DATA[3]	DATA[4]	...	DATA[2n-1]	DATA[2n]
RECORDS	amplifier[0]	time[0]	amplifier[1]	time[1]	...	amplifier[n-1]	time[n-1]

Where:

- **RECORDS**: size of the data list (‘unsigned long long‘)
- **amplifier**: detected channel (0 to 16383)
- **time**: 16-bit + 14-bit count (100 ns per count)

SequentialBayes:

This code receives amplifier and time list data from the above program and executes the k—α method, allowing for the visualization and saving of spectrum and dose rate data. At the same time, the received amplitude and timestamp values are saved in a file for developmental usage if needed. Excerpts and portions of the code are shared below. Some crucial parts have been redacted as the method is utilized in future commerical development as mentioned above.

```
#include <iostream>
#include <Eigen/Dense>
#include <vector>
#include <fstream>
#include <random>
#include <algorithm>

#include <nlohmann/json.hpp>
```

```
using json = nlohmann::json;

#include <filesystem>

namespace fs = std::filesystem;
using namespace Eigen;

#include "include/SharedMemory.h"
#include "include/EventOpen.h"
#include "include/EventCreate.h"
#include <thread>
#include <mutex>
#include <queue>
std::mutex mtx_dp5;  // Mutex to control access to DP5 shared memory
#include "include/UDPSend.h"
std::mutex mtx_graph;  // Mutex to control access to graph data

#include <atomic>
std::atomic<bool> sig_received = false;  // Atomic flag for signal handling
#include <signal.h>

// Function to load CSV data into an Eigen vector
template<typename M>
M load_csv(const std::string &path, unsigned int start_row = 0) {
    std::ifstream indata;
    indata.open(path);
    std::string line;
    std::vector<double> values;
    unsigned int rows = 0;
    unsigned int header_row = 0;
    while (std::getline(indata, line)) {
        std::stringstream lineStream(line);
        std::string cell;
        if (start_row != header_row) {
            ++header_row;
            continue;
        }
        while (std::getline(lineStream, cell, ',')) {
            values.push_back(std::stod(cell));
```

```
48          }
49          ++rows;
50      }
51      return Map<const Matrix<typename M::Scalar, M::RowsAtCompileTime,
            M::ColsAtCompileTime, RowMajor>>(values.data(), rows, values.size() /
            rows);
52  }
53
54  // Signal handler function to catch SIGINT and SIGTERM signals
55  void signalHandler(int sig) {
56      if (sig == SIGINT) {
57          std::cout << "received SIGINT" << std::endl;
58      } else if (sig == SIGTERM) {
59          std::cout << "received SIGTERM" << std::endl;
60      }
61      sig_received.store(true);  // Set the atomic flag to stop all threads
62  }
63
64  // Implementation for signal handling
65  // (Original code replaced for privacy reasons)
66
67
68  // Thread function to read amplitude and timestamp data from DP5 shared memory
69  void threadReadDP5(std::queue<unsigned int> &amplitude, std::queue<unsigned
        long long> &time_tag,
70                     const int max_wait_time, json settings) {
71      const unsigned int BUF_SIZE = 40000;  // Buffer size for shared memory
72      // Implementation details have been redacted
73        ...
74
75          // Lock DP5 mutex for thread safety
76          mtx_dp5.lock();
77
78          int records = memoryControl.pBuf[0];  // Number of records in shared
                memory
79
80          fs::path workspace_dir = settings["workspace_dir"].get<std::string>();
81          fs::path amp_and_time_file =
                settings["amp_and_time_file"].get<std::string>();
```

```
82          std::ofstream log_amp_and_time;
83          log_amp_and_time.open((workspace_dir / amp_and_time_file).string(),
                std::ios::trunc);
84
85          // Process the shared memory data
86          for (int i = 0; i < records; i++) {
87              if (memoryControl.pBuf[i * 2 + 1] == 0)
88                  continue;
89
90              // Push amplitude and time data into queues
91              amplitude.push(memoryControl.pBuf[i * 2 + 1]);
92              time_tag.push(memoryControl.pBuf[i * 2 + 2]);
93
94              // Write the amplitude and time data to a CSV log file
95              log_amp_and_time << std::to_string(memoryControl.pBuf[i * 2 + 1])
                    << ","
96                                  << std::to_string(memoryControl.pBuf[i * 2 + 2])
                                      << "\n";
97          }
98
99          log_amp_and_time.close();
100
101         // Release mutex and reset event
102         mtx_dp5.unlock();
103         ReleaseMutex(memoryControl.ghMutex);
104         ResetEvent(memoryControl.hEvent);
105
106         // Set event signal to continue processing
107         SetEvent(ampEventControl.hEvent);
108     }
109 }
110
111 // Interpolation function to match dose factors to the energy bins in the
        primary data
112 MatrixXd interpolate(MatrixXd dose_factor, MatrixXd %primary_data) {
113     MatrixXd interpolated_dose_factor = primary_data;
114
115     // Linear interpolation logic for dose factors
116     for (int i = 0; i < dose_factor.rows(); i++) {
```

```
117         for (int j = 0; j < primary_data.rows(); j++) {
118             if (dose_factor(i, 0) < primary_data(j, 0) %&& primary_data(j, 0) <
                    dose_factor(i + 1, 0)) {
119                 double y0 = dose_factor(i, 1);
120                 double y1 = dose_factor(i + 1, 1);
121                 double x0 = dose_factor(i, 0);
122                 double x1 = dose_factor(i + 1, 0);
123                 double x = primary_data(j, 0);
124                 double y = y0 + (x - x0) * (y1 - y0) / %(x1 - x0);
125                 interpolated_dose_factor(j, 1) = y;
126             } else if (dose_factor(i, 0) == %primary_data(j, 0)) {
127                 interpolated_dose_factor(j, 1) = %dose_factor(i, 1);
128             }
129         }
130     }
131     return interpolated_dose_factor;
132 }
133 // Thread function to run Bayesian estimation using the k-alpha method
134 void threadBayes(std::queue<unsigned int> &amplitude,
135     // Implementation details have been redacted
136       ...
137
138     // Load settings and response function, primary data, and dose factors
            from files
139   // Implementation details have been redacted
140       ...
141
142    double k = settings["/est_data/k"_json_pointer];
143    double receive_area = settings["/est_data/receive_area"_json_pointer];
144    double bin = settings["/est_data/bin"_json_pointer];
145    double A = settings["/calibration_data/A"_json_pointer];
146    double B = settings["/calibration_data/B"_json_pointer];
147
148     // Load response function matrix
149     MatrixXd response_ = load_csv<MatrixXd>((workspace_dir / resource_root_dir
            / response_file).string());
150     MatrixXd response = response_.block(0, 1, 990, 184);  // Crop response
            matrix
151
```

```
152     // Initialize pulse height spectrum
153     pulse_height_spectrum.assign(16384, 0);
154 
155     // Load primary data matrix
156     MatrixXd primary_data_ = load_csv<MatrixXd>((workspace_dir /
            resource_root_dir / primary_file).string(), 2);
157     MatrixXd primary_data = primary_data_.block(0, 0, 184, 2);
158     {
159         std::lock_guard<std::mutex> lg(mtx_graph);  // Lock graph data
160         energy_axis.assign(primary_data.rows(), 0);  // Set energy axis values
161         Map<VectorXd>(&energy_axis[0], primary_data.rows()) =
                static_cast<VectorXd>(primary_data.col(0));
162     }
163 
164     // Load dose factor matrix
165     MatrixXd dose_factor = load_csv<MatrixXd>((workspace_dir /
            resource_root_dir / dose_factor_file).string(), 1);
166 
167     // Normalize the response matrix
168     MatrixXd normalized_response = response.array().rowwise() /
            response.colwise().sum().array();
169 
170     size_t total_measure_size = response.cols();
171     VectorXd est = VectorXd::Constant(total_measure_size, 1. /
            static_cast<double>(total_measure_size));
172     VectorXd est_old = est;
173     VectorXd est_count = VectorXd::Zero(total_measure_size);
174     VectorXd est_flux = VectorXd::Zero(total_measure_size);
175     VectorXd response_sum = response.colwise().sum().transpose();
176 
177     // Interpolate dose factors to match the energy bins
178    // Implementation details have been redacted
179       ...
180     // Main loop for Bayesian estimation
181     while(!sig_received.load()) {
182         int random_row = 0;
183         float time_now = 0;
184         bool is_amplitude_empty = false;
185 
```

```
186         // Implementation details have been redacted
187       ...
188         // Increment the pulse height spectrum for the current amplitude
189         pulse_height_spectrum[amplitude_copy] += 1;
190         if (random_row == -1) continue;
191 
192         // Run k-a method for Bayesian estimation
193         double alpha = (1. + k * (count + 1)) / static_cast<double>(count + 1);
194         alpha = std::min(alpha, 1.0);
195 
196         est_old = est;
197         est =
                normalized_response.row(random_row).transpose().cwiseProduct(est);
198 
199         // Further Implementation details have been redacted
200       ...
201 
202 // Thread function to send estimated data to the fluxGraph process via UDP
203    // Implementation details have been redacted
204       ...
205     }
206         // Prepare JSON data for UDP transmission
207         json j;
208         {
209             std::lock_guard<std::mutex> lg(mtx_graph);
210             j["energy"] = energy_axis;
211             j["flux"] = flux;
212             j["dose"] = dose;
213             j["time"] = time;
214             j["count"] = total_count;
215         }
216 
217         // Send data via UDP
218         std::string s = j.dump();
219         const char *data = s.c_str();
220         sendEstData.sendData(data);
221 
222         // Reset event after sending data
223         ResetEvent(showEventControl.hEvent);
```

```
224     }
225 }
226
227 // Main function
228 int main() {
229     std::queue<unsigned int> amplitude;
230     std::queue<unsigned long long> time_tag;
231     std::vector<double> energy_axis;
232     std::vector<double> flux;
233     std::vector<int> pulse_height_spectrum;
234     float dose = 0;
235     float time = 0;
236     int total_count = 0;
237
238     // Implementation details have been redacted
239       ...
240
241     // Start thread to read data from DP5
242      std::thread th1([&] {
243          threadReadDP5(amplitude,time_tag, max_wait_time, settings);
244      });
245
246      Sleep(1000);  // Small delay to let the first thread start
247
248     // Start thread to run k-a method
249      std::thread th2([&] {
250          threadBayes(amplitude, time_tag, pulse_height_spectrum, energy_axis,
                flux, dose, time, total_count,
251                  max_wait_time, show_graph_time, settings);
252      });
253
254      Sleep(1000);  // Small delay to let the second thread start
255
256      // Start thread to send the estimated data to the fluxGraph process via
            UDP
257      std::thread th3([&] {
258          threadGraph(energy_axis, flux, dose, time, total_count,
                max_wait_time);
259     });
```

```
260
261     // Wait for threads to finish
262     th1.join();
263     th2.join();
264     th3.join();
265
266     // Save the final pulse height spectrum to a CSV file
267     VectorXi pulse_height_spectrum_vec =
            Map<VectorXi>(&pulse_height_spectrum[0], pulse_height_spectrum.size());
268     std::ofstream log_pulse_height_spectrum;
269     log_pulse_height_spectrum.open((workspace_dir /
            pulse_height_spectrum_file).string(), std::ios::trunc);
270     log_pulse_height_spectrum << pulse_height_spectrum_vec;
271     log_pulse_height_spectrum.close();
272
273     std::cout << "task end" << std::endl;
274 }
```

The following .json file contains configuration parameters used in the radiation data processing system. It specifies file paths for resources (such as which response function to use for unfolding and which primary data and dose factor files to utilize), estimation constants like the k value and calibration constants, as well as some runtime settings. Below is a standard example for $k = 10^{-3}$, the response function up to 3 MeV and $2.6 \times 2.6 \times 2.6$ cm^3 CsI(Tl) scintillator.

```
1     {
2     "workspace_dir": "../",
3     "resource_path": {
4         "root_dir": "resources/",
5         "response_file": "response.csv",
6         "primary_file": "primary.csv",
7         "dose_factor_file": "dosefactor.csv"
8     },
9     "est_data": {
10        "k": 1e-03,
11        "receive_area": 2.6,
12        "bin": 5.0
13    },
```

```
    "calibration_data": {
        "A": 137.127,
        "B": 0.0575505,
    },
    "max_wait_time": 1000,
    "show_graph_time": 0.1,
    "pulse_height_spectrum_file": "result/spectrum.csv",
    "amp_and_time_file" : "result/ampandtime.csv"
}
```